Université Paris Nanterre

200 av. de la République
92001 Nanterre Cedex
www.parisnanterre.fr

Membre de l'université Paris Lumières
École doctorale 139 : Connaissance, langage, modélisation
Laboratoire Electromagnétique Mécanique et Energie (LEME)

Tanguy Lopez

Metasurface-based radar stealth solutions over VHF-UHF bands: Tunable absorption and Doppler cloaking

Thèse présentée et soutenue publiquement le 09/10/2024
en vue de l'obtention du doctorat de Electronique, optronique et systèmes de l'Université Paris Nanterre
sous la direction de M. Shah Nawaz Burokur (Université Paris Nanterre),
de M. Thomas Lepetit (ONERA) et de M. Badr Eddine Ratni (Université Paris Nanterre)

Jury :

Président :	M. Julien DE ROSNY	Directeur de recherche, ESPCI Paris
Rapporteur :	M. Renaud LOISON	Professeur, INSA Rennes
Rapporteur :	M. Sergei TRETYAKOV	Professeur, Université d'Aalto (Finlande)
Examinatrice :	Mme Divitha SEETHARAMDOO	Chargée de recherche, Université Gustave Eiffel
Examinateur :	M. Xavier BEGAUD	Professeur, Télécom Paris
Directeur :	M. Shah Nawaz BUROKUR	Maître de conférences/HDR, Université Paris Nanterre
Co-encadrant :	M. Thomas LEPETIT	Ingénieur de recherche, ONERA
Co-encadrant :	M. Badr Eddine RATNI	Maître de conférences, Université Paris Nanterre

ACKNOWLEDGEMENTS

I would first like to express my sincere gratitude to my PhD advisor, Dr Thomas Lepetit, for his continuous support over the past three years. From sharing his expertise with me to thoroughly reviewing my communications, he has always been willing to take the time to provide valuable assistance with the inevitable research difficulties.

I sincerely thank my PhD supervisor, Dr Shah Nawaz Burokur, for his precious guidance throughout this thesis and beyond. I would not have been able to undertake this research to the extent that I have without his essential support, and I am deeply grateful for the many opportunities to publish and communicate my work.

I would also like to thank Dr Badr Eddine Ratni for his technical expertise and for always finding solutions to accommodate me, either for teaching hours or experimental matters.

Finally, I would like to thank my colleagues at ONERA and LEME who have been so willing to help me; and the friends I have made along the way, sharing our office and cups of tea, through our common supervisor and during my visit to Newcastle University.

I would like to extend a special thanks to all the members of the panel for their detailed scrutiny and comments on my thesis. I would particularly like to mention their kind assessment of my work and their heartwarming compliments.

I would like to thank my mother for her forever support and faith in me, my grandmother for her essential help throughout my life, and I have a special thought for my brother and our recent reunion.

Finally, I thank my fiancée for her constant reassurance and motivation, for her dedication to celebrating even the most mundane of achievements and for sharing my life.

CONTENTS

ACKNOWLEDGEMENTS **3**

CONTENTS **5**

RESUME EN FRANCAIS **7**

ETAT DE L'ART 7
ABSORBANT RADAR A METASURFACE RECONFIGURABLE 12
CONVERTISSEUR DE FREQUENCE A METASURFACE MODULEE TEMPORELLEMENT 15
CONCLUSIONS 18

SUMMARY **20**

INTRODUCTION **21**

I. STATE-OF-THE-ART RADAR CAMOUFLAGING METASURFACE-BASED STRATEGIES **25**

1. INTRODUCTION 26
2. SURVEILLANCE RADAR SYSTEMS FOR DETECTION, DISTANCE AND VELOCITY ESTIMATES 26
   2.1. Surveillance radar systems *27*
   2.2. Radar systems for the estimates of a target's parameters *29*
3. SEMINAL RADAR STEALTH SOLUTIONS 32
   3.1. Radar stealth from shape effects *32*
   3.2. Radar stealth from radar absorbing materials *32*
4. REVIEW OF METASURFACE-BASED RADAR STEALTH SOLUTIONS 40
   4.1. Review of metasurface-based radar absorbers *40*
   4.2. Review of time-controlled active metasurface-based radar stealth solutions *46*
5. CONCLUSIONS 49

II. DEVELOPMENT AND EXPERIMENTAL VALIDATION OF A FREQUENCY-TUNABLE METASURFACE-BASED RADAR ABSORBER OVER THE VHF-UHF BANDS **51**

1. INTRODUCTION 52
2. VHF-UHF COAXIAL METASURFACE 53
   2.1. Cartesian-to-polar coordinate mapping *53*
   2.2. Cartesian-to-polar one-dimensional metasurface equivalents *54*
   2.3. Metasurface of interest *55*
3. DEVELOPMENT AND EXPERIMENTAL VALIDATION OF A METASURFACE-BASED RADAR ABSORBER OVER THE VHF-UHF BANDS 56
   3.1. Equivalent circuit analysis an impedance matching metasurface for a radar absorber *56*
   3.2. Design of an impedance matching metasurface *58*
   3.3. Analytical and numerical studies of the metasurface-based radar absorber using the equivalent circuit model, a 2D axisymmetric FEM model and a 3D FEM model *60*
   3.4. Experimental validation of a metasurface-based radar absorber *65*
4. DEVELOPMENT AND EXPERIMENTAL VALIDATION OF A FREQUENCY-TUNABLE METASURFACE-BASED RADAR ABSORBER OVER THE VHF-UHF BANDS 67
   4.1. Frequency-tunability using varactor diodes *67*
   4.2. ECM and 3D FEM simulations of the frequency-tunable metasurface-based radar absorber *68*
   4.3. Experimental validation of the frequency-tunable metasurface-based radar absorber *70*
5. NUMERICAL AND EXPERIMENTAL INVESTIGATIONS INTO A FREQUENCY-TUNABLE METASURFACE-BASED RADAR ABSORBER OF NEAR-PERFECT ABSORPTION AND TIME-BASED WIDEBAND COVERAGE 73
   5.1. Numerical investigation into a near-perfect metasurface-based radar absorber using a joint tuning of capacitance and resistance *73*

5.2. Experimental investigation into an effectively wideband metasurface-based radar absorber thanks to a temporal control of biasing voltage against a frequency-hopping radar 77
6. CONCLUSIONS 79

III. DEVELOPMENT AND EXPERIMENTAL VALIDATION OF A METASURFACE-BASED FREQUENCY CONVERTER OVER THE VHF-UHF BANDS 81

1. INTRODUCTION 82
2. SPECTRUM MANIPULATION USING A TIME-MODULATED METASURFACE 83
2.1. Frequency conversion by time-modulation of a reflecting surface 83
2.2. Analytical studies of frequency converting time-modulated systems 84
3. DEVELOPMENT AND EXPERIMENTAL VALIDATION OF A METASURFACE-BASED FREQUENCY CONVERTER FOR THE FREQUENCY-CONVERSION OF HARMONIC SIGNALS 88
3.1. Design of the metasurface for a metasurface-based frequency converter and modulation of the reflection coefficient 88
3.2. 2D analytical, numerical and semi-analytical studies of the metasurface-based frequency converter for an incident signal of frequency $f0 = 300$ MHz and modulation frequency $fm = 1$ MHz ... 92
3.3. 3D semi-analytical study of the metasurface-based frequency converter for an incident signal of frequency $f0 = 300$ MHz and modulation frequency $fm = 1$ MHz 99
3.4. Experimental validation of a time-modulated metasurface for the frequency-conversion of harmonic waves at $f0 = 370$ MHz 100
4. EXPERIMENTAL VALIDATION OF A METASURFACE-BASED FREQUENCY CONVERTER FOR THE FREQUENCY-CONVERSION OF NON-HARMONIC WAVES 108
4.1. Analytical justification of the existence of a frequency conversion bandwidth 109
4.2. 2D Analytical and numerical studies of the metasurface-based frequency converter for an incident non-harmonic signal of center frequency $f0 = 300$ MHz and modulation frequency $fm = 1$ MHz 110
4.3. Experimental validation of a time-modulated metasurface for the frequency-conversion of non-harmonic waves around $f0 = 370$ MHz 114
5. CONCLUSIONS 115

CONCLUSIONS & OUTLOOKS 117

LIST OF PUBLICATIONS 123

COMMUNICATIONS 123
PUBLICATIONS 124

APPENDIX 125

A. REFLECTION AND TRANSMISSION AT A TEMPORAL BOUNDARY 127
B. SIMULATION SOFTWARES 131
C. TIME-DOMAIN SURFACE IMPEDANCE BOUNDARY CONDITION 133
D. FREQUENCY CONVERSION AND α VALUE 141
E. VARACTOR DIODE'S SERIES RESISTANCE AND PHASE VARIATION REGIME 143
F. FINITE-ELEMENT TIME DOMAIN SIMULATION: BDF VS. GENERALIZED-α IMPLICIT SOLVERS 147

REFERENCES 149

RESUME EN FRANCAIS

Durant cette thèse, je me suis intéressé à des solutions pour la furtivité radar en bandes VHF-UHF grâce à des structures à métasurface actives. En particulier, j'ai développé puis validé expérimentalement un absorbant radar reconfigurable et un convertisseur de fréquence pour une cape Doppler.

Le résumé qui suit est structuré comme le manuscrit. Dans le Chapitre I, j'introduis tout d'abord les concepts fondamentaux du radar, afin de définir la furtivité pour en présenter des réalisations pratiques. Je mets notamment l'accent sur l'existence d'une borne fondamentale qui limite l'utilisation des solutions historiques à basses fréquences, et donc la nécessité de se tourner vers des solutions actives, que les métasurfaces permettent de réaliser facilement. J'introduirai notamment deux solutions que je développerai par la suite : les absorbants radars reconfigurables et les structures modulées temporellement pour la manipulation du spectre. Dans le Chapitre II, je détaille le développement d'un absorbant radar reconfigurable. J'utilise pour cela des outils analytiques et numériques, pour la conception et la validation. Je réalise alors ensuite la métasurface d'intérêt et confirme par mesures son comportement d'absorbant et sa bonne accordabilité sur la gamme de fréquences d'intérêt, agrandissant ainsi sa bande passante effective. Dans le Chapitre III, je détaille le développement d'un convertisseur de fréquence pour une cape Doppler. Il s'agit d'une structure à métasurface dont la modulation permet de compenser le décalage Doppler qui trahit la vitesse d'une cible radar. J'utilise pour cela, à nouveau, des outils analytiques et numériques pour la conception et validation du système dans le cas d'une onde incidente harmonique. La fabrication de la structure est suivie d'une validation expérimentale, confirmant la bonne dissimulation qu'offrirait un tel système. Puis, j'élargis les cas d'applications aux signaux non-harmoniques, plus couramment utilisés par les radars, et que le convertisseur est également capable d'affronter.

Etat de l'art

Dans le Chapitre I, j'introduis le principe de fonctionnement du radar afin de présenter des solutions à la furtivité. Un radar est un système qui utilise les ondes électromagnétiques pour la détection d'objets comme les avions, les bateaux, ou même la pluie. Acronyme de *RAdio Detection And Ranging*, il est également capable d'estimer la distance de ses cibles, en plus d'autres paramètres comme l'altitude, l'angle ou la vitesse. Apparus durant la première moitié du XXe siècle, suite au développement accéléré par les guerres en Europe, ils permettaient la surveillance de l'espace aérien et maritime pour la protection de zones sensibles. L'avantage des radars est leur fonctionnement par tout temps et même la nuit. Les bandes de fréquence basses utilisées permettent la détection de menaces à longue portée, tandis que l'augmentation de la fréquence permet une plus grande précision.

Le métal est aux ondes électromagnétiques ce qu'un miroir est à la lumière visible. Un radar exploite donc ce comportement, en émettant une onde électromagnétique qui se réfléchit alors sur la cible métallique. Si cette réflexion est captée, alors la détection est enregistrée, comme illustrée en Figure 0-I.1. En revanche, la mesure de la réflexion dépend de nombreux paramètres. Il s'agit en réalité d'une mesure de la puissance portée par l'onde réfléchie. Et cette puissance réfléchie par la cible est fonction de la puissance émise à l'origine par le radar, de la distance de la cible au radar, parcourue à l'aller puis au retour, et d'une quantité propre à la cible appelée surface équivalente radar (SER). Il s'agit là d'une quantité qui mesure la réflexion d'un objet dans différentes directions, pour différents angles d'incidence de l'onde émise, et permet de caractériser sa détectabilité par une quantité homogène à une surface. Ainsi, plus un avion renvoie

de puissance lorsqu'il est illuminé par une onde, plus il est détectable. En pratique, puisque la détection d'une cible est dépendante de sa distance au radar, ces systèmes sont caractérisés par leur portée maximale. La réduction de la SER d'une cible se traduit alors comme la réduction de la portée du radar, permettant de s'approcher au plus près des zones sensibles avant d'être repéré. L'ensemble des stratégies mises en place pour mettre en échec la détection radar est alors plus couramment appelé furtivité.

En plus d'enregistrer la présence de cibles, l'utilisation de formes d'onde spécifiques permet également d'estimer d'autres paramètres de la cible. Deux paramètres de la plus haute importance, en plus de l'angle et de l'altitude, sont la distance et la vitesse de l'objet. En effet, une fois la cible détectée, et l'alerte levée, il faut alors prévoir sa trajectoire pour la poursuivre. Pour cela, une onde électromagnétique particulière est exploitée. Je me suis intéressé tout particulièrement à une onde émise en continue et modulée en fréquence, ou *frequency-modulated continuous waveform* (FMCW). Celle-ci permet en effet l'estimation simultanée de la vitesse et de la distance. Il s'agit en fait de la répétition sans interruption d'une onde dont la fréquence varie linéairement avec le temps. Cela introduit alors des marqueurs temporels dans le signal, *i.e.* la fréquence instantanée, qui permet donc d'estimer le temps écoulé entre l'émission et la réception. Pour une propagation à la vitesse de la lumière de l'onde, il est donc facile de remonter à l'information distance. En plus de cela, une cible en mouvement, par effet Doppler, modifie la fréquence de l'onde réfléchie à sa surface. Ce décalage fréquentiel est proportionnel à la vitesse de l'appareil, et sa mesure trahit donc l'information vitesse de la cible. Cette mesure peut se faire directement sur la fréquence instantanée du signal FMCW, mais la méthode usuelle en traitement radar repose sur la dérivation de la différence des phases des signaux émis et reçu. Le traitement de la scène complète illuminée par le radar permet alors de réaliser une carte distance-vitesse.

La mise en échec des radars constitue donc en réalité un domaine plus large que la seule dissimulation, et peut également faire appel à certaines stratégies de leurrage et de guerre électronique.

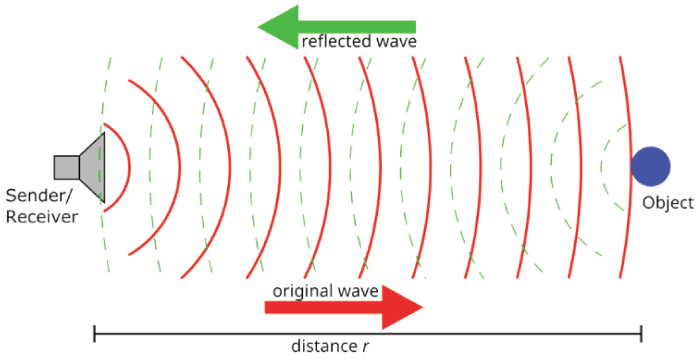

Figure 0-I.1 : Détection d'une cible par un radar : mesure de la puissance réfléchie sur la cible et renvoyée au radar [Georg Wiora (Dr. Schorsch) - Self drawn with Inkscape, CC BY-SA 3.0, https://commons.wikimedia.org/w/index.php?curid=353362].

Afin d'améliorer la furtivité des cibles, il est alors nécessaire de recourir à des solutions de réduction de la SER. Le choix des solutions à privilégier est extrêmement dépendant de la mission envisagée, des conditions d'utilisation et de l'état de l'art.

La solution historique, et la plus couramment utilisée, est celle des effets de forme. Il s'agit d'intégrer à la conception même du corps de l'appareil des stratégies de réduction de la visibilité électromagnétique. Cela passe par l'utilisation de formes profilées pour la redirection des ondes incidentes dans d'autres directions *poubelles* de l'espace, ou par la minimisation d'aspérités en

surface qui réfléchissent fortement la puissance vers le radar. Ces choix de conception sont particulièrement manifestes sur le bombardier B-2, inaugurés à la fin des années 80 par les Etats-Unis, et l'avion de combat F-117. Cependant, cette solution présente des limites, notamment en basses fréquences, où les effets d'atténuation sont altérés. En réalité, les appareils furtifs ne se contentent pas d'intégrer une unique solution de réduction de la SER, mais embarquent plusieurs d'entre elles, afin de compenser les faiblesses de chacune.

Notamment, parmi les solutions les plus utilisées, car les plus faciles à mettre en place, on retrouve les absorbants radars, ou *radar absorbing materials* (RAM). Les RAM sont généralement classés en deux familles : les solutions non-résonantes et les solutions résonantes. Les premières utilisent les propriétés de dissipation de la puissance de certains matériaux, tandis que les deuxièmes se rapprochent de filtres électromagnétiques. Dans les deux cas, le principe premier de conception est l'*adaptation d'impédance*. Il s'agit d'une notion fondamentale qui caractérise l'interface entre deux milieux. L'impédance est une caractérisation du milieu de propagation d'une onde, analogue à la résistance d'une piste de circuit imprimé. Notamment, on parle de désadaptation d'impédance à une interface lorsque les deux milieux présentent un écart d'impédance. La transmission de l'onde du milieu d'origine vers le second n'est alors que partielle, et une partie de la puissance incidente est réfléchie à l'interface. Dans le cas de la furtivité, il s'agit de l'interface entre l'air, où se propage l'onde radar, et le RAM. Un RAM est donc une couche à appliquer sur la surface à dissimuler, qui assure la bonne transmission sans réflexion de l'onde incidente. Cela a donc pour effet de supprimer l'écho sur la cible, et d'empêcher sa détection.

Parmi les solutions non-résonantes, on retrouve alors quelques solutions historiques toujours d'actualité aujourd'hui. Ces solutions maximisent l'atténuation de l'onde incidente avant d'atteindre le fuselage à dissimuler par dissipation de sa puissance. Pour cela, elle utilise des éléments qui présentent des pertes diélectriques et/ou magnétiques, qui transforment l'énergie électromagnétique en chaleur, à la manière d'une résistance. Il est alors possible d'envisager plusieurs structures, d'un unique bloc monolithique (absorbant de Dallenbach), à un gradient continu d'augmentation d'éléments dissipateurs, en passant par des structures composites à couches. Si la solution idéale à gradient est difficile à réaliser en termes de propriétés électromagnétiques, il s'agit du principe exploité par les cônes tapissant les chambres anéchoïques, dont l'efficacité n'est plus à démontrer. En revanche, pour utilisation sur plateforme mobile, on privilégiera l'utilisation de peintures magnétiques par exemple, ou bien de filtres grâce aux solutions résonantes.

Parmi les solutions résonantes, on retrouve en particulier une solution historique, et ses nombreuses itérations, optimisations et variations : l'écran de Salisbury. Il s'agit d'un film résistif situé à une hauteur de $\lambda/4$ du conducteur à dissimuler. Utilisant un film parfaitement adapté en impédance à l'air, il est alors possible d'absorber parfaitement l'onde de longueur d'onde λ. Afin d'élargir la largeur de bande et donc les longueurs d'onde absorbées, l'écran de Jaumann propose d'utiliser plusieurs écrans de Salisbury en cascade. Cependant, la contrainte de dimension devient problématique à basses fréquences où les longueurs d'onde deviennent grandes, et il est impossible de recouvrir un avion d'une couche absorbante de 25 cm d'épaisseur. C'est alors que les métasurfaces sont pour la première fois envisagées pour la conception d'absorbants radars fins.

Une métasurface est une structure planaire composée de résonateurs disposées de manière périodique. Le choix du résonateur, ainsi que l'arrangement global, permettent alors de réaliser des structures artificielles. Dans leurs versions 3D, on retrouve parmi les réalisations exemplaires des milieux de propagation à indice de réfraction négatif, ce qui n'existe pas naturellement. L'avantage des métasurfaces est donc leur versatilité : une variété de comportements électromagnétiques peut être émulés, grâce à une impédance de surface à la fois résistive et réactive. C'est d'ailleurs grâce à la réactivité offerte par ces surfaces qu'il est possible

de réduire l'épaisseur des absorbants radars : sous $\lambda/4$, la distance entre l'écran et le conducteur introduit un comportement équivalent à la présence d'une inductance, que la capacité d'une métasurface peut alors compenser, tout en offrant la résistance nécessaire à l'adaptation d'impédance à l'air. Le principe d'absorbant radar à métasurface est illustré en Figure 0-I.2.

Cependant, les solutions non-résonantes et résonantes, même à métasurfaces, en tant que réseaux d'adaptation d'impédance, sont bornées en termes de bande passante. C'est en fait leur nature *linéaire, passive et invariante dans le temps* qui est en cause. Désignée sous le terme de borne de Bode-Fano dans le cas général, et borne de Rozanov pour les RAM particulièrement, elle indique l'existence d'une borne physique infranchissable du rapport bande passante-épaisseur. Ainsi, un RAM ne peut être fin et large bande à la fois. Ce qui est particulièrement problématique à basse fréquence, où les effets de forme ne suffisent plus, les peintures magnétiques ne sont pas assez performantes, et les solutions résonantes sont épaisses ou à bande étroite.

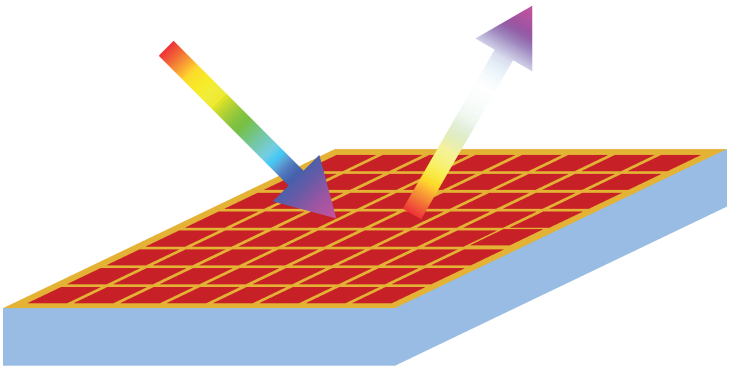

Figure 0-I.2 : Absorbant radar à métasurface, filtrant une partie de la gamme de fréquence incidente.

C'est alors que les RAM à métasurfaces deviennent d'autant plus intéressant. En réalité, à épaisseur équivalente, ceux-ci présentent une plus large bande que l'écran de Salisbury historique. Et le contrôle précis de leur impédance de surface permet de minimiser la perte de bande passante avec la réduction de l'épaisseur. L'ingénierie de leur impédance est d'ailleurs grandement facilitée par la technologie circuit imprimée, ou *printed circuit board* (PCB), et sa haute compatibilité avec les composants électroniques discrets. Cela facilite grandement la réalisation de métasurfaces, pour lesquelles des motifs moins complexes peuvent être compensées par l'électronique pour offrir l'impédance désirée. L'utilisation d'électronique passive notamment permet d'ajouter facilement les éléments résistifs et capacitifs sur la structure pour réaliser l'adaptation d'impédance et l'électronique active permet finalement de briser le caractère *passif* qui soumet ces RAM à la borne de Rozanov-Bode-Fano (RBF). Il devient alors possible de réaliser des absorbants ultra large bande, nécessitant l'utilisation de circuits complexes (non-Foster), ou d'offrir des mécanismes de reconfigurabilité au RAM. Cette reconfigurabilité peut être classée en deux familles : les structures à métasurface commutables et les structures à métasurface accordable. La commutation permet à une unique structure de fonctionner selon différents régimes. Le cas classique est celui d'une surface transmissive ou absorbante, qui permet d'alterner entre écran filtrant et écran transparent. Il est également possible d'envisager d'autres fonctionnalités. L'accordabilité, quant à elle, permet à une unique structure de déplacer son comportement absorbant le long de l'axe des fréquences par exemple. Cela offre donc aux RAM une bande passante effective plus large, pour lesquels la fréquence à laquelle est garantie l'adaptation d'impédance peut être pilotée. Ce comportement peut ensuite être rendue plus ou moins autonome, par des capteurs et boucles de réaction, pour une reconfiguration automatique permise par l'analyse de la menace. Avec la reconfigurabilité, une

certaine dimension temporelle accompagne donc le développement de structures à métasurface actives.

En réalité, le contrôle temporel des propriétés électromagnétiques n'est pas un nouveau concept. Théorisée dans les années 50, les premiers travaux se sont intéressés à l'existence d'interfaces *temporelles*, en tant qu'analogues des interfaces spatiales précédemment introduites avec le concept d'adaptation d'impédance. En particulier, il apparaît que le changement brutal des caractéristiques du milieu (permittivité et perméabilité), génère une interface temporelle qui perturbe la propagation de l'onde. Cette perturbation se manifeste par l'existence d'ondes réfléchie et transmise, tout comme une interface spatiale, mais également par l'accélération/le ralentissement de l'onde dans tout le milieu, ce qui se caractérise par un changement de fréquence. Un tel milieu *variant dans le temps* peut être exploité pour rompre un autre critère d'application de la borne de RBF et réaliser une absorption très large bande, mais il n'existe pas encore de réalisations pratiques dans les gammes radiofréquence (en dehors de certains plasmas). C'est pourquoi la communauté s'est tournée vers d'autres solutions à bases de métasurfaces actives, pour lesquelles la dimension *variant dans le temps* est plus facilement accessible. La réalisation de solutions pour la furtivité doit donc faire appel à d'autres approches que l'utilisation d'interfaces temporelles, et est limité à un cas d'application précis : la modulation doit être lente. Cela est essentiel pour garantir que le système variant dans le temps est vu par l'onde incidente comme statique à tout moment. Il devient alors possible d'utiliser un RAM accordable pour s'adapter en temps réel et continument aux signaux radars incidents. Pour élargir les cas d'utilisation en dehors des RAM, il devient également possible d'envisager de nouvelles stratégies de furtivité et/ou de guerre électronique. Une structure à métasurface commutable dans le temps peut agir comme un déflecteur, à la manière des effets de forme, ou bien peut étaler le spectre réfléchi (*spread spectrum*) répartissant ainsi la puissance sur une large bande de fréquences. Enfin, une structure à métasurface accordable dans le temps peut être modulée en continu pour compenser le décalage Doppler induit par le mouvement de sa plateforme (*Doppler cloaking*), illustré en Figure 0-I.3.

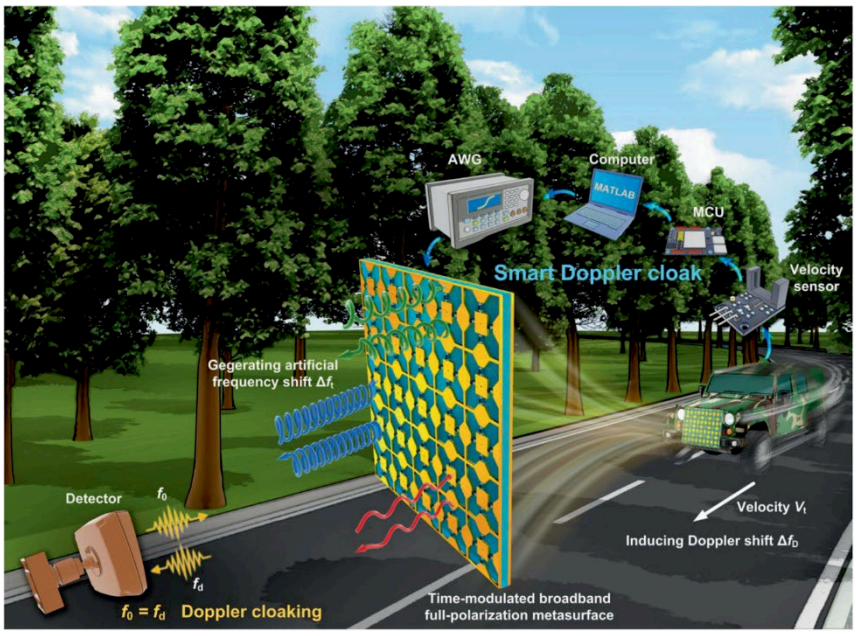

Figure 0-I.3 : Illustration du principe de fonctionnement d'une cape Doppler intelligente à métasurface : le décalage Doppler du véhicule en mouvement est estimé par mesure de la vitesse pour compensation en temps réel par un convertisseur de fréquence à métasurface [B. Liu, Y. He, S.-W. Wong, and Y. Li, "Experimental demonstration of a time-domain digital-

coding metasurface for a Doppler cloak," Opt. Express, vol. 29, no. 2, pp. 740–750, Jan. 2021, doi: 10.1364/OE.414408].

Dans le cadre de mes travaux, la métasurface étudiée est un disque métallique présentant une ouverture centrale. Il s'agit en fait d'une astuce qui permet de réduire la taille du dispositif qui mesurerait plusieurs mètres carrés sinon. La métasurface ainsi fabriquée est conçue pour fonctionner en géométrie coaxiale. Cette métasurface peut ainsi accueillir des composants électroniques discrets, montés à travers l'ouverture circulaire centrale. Il est prévu d'accueillir huit composants, séparés angulairement de 45° sur la métasurface.

En revanche, bien que cela permette une réduction drastique des dimensions, une telle manipulation oblige à ne plus considérer dans la suite qu'une incidence normale et une absence de polarisation de l'onde incidente.

Absorbant radar à métasurface reconfigurable

Dans le Chapitre II, je me suis concentré sur la réalisation d'un absorbant radar à métasurface (ou MBRA pour *metasurface-based radar absorber*) fonctionnant en bandes VHF-UHF. Comme précédemment introduit, la métasurface est avant tout utilisée afin de garantir l'adaptation d'impédance à l'onde radar incidente. Il s'agit donc d'établir les conditions permettant cela, pour lesquelles l'ajout des composants électroniques nécessaires. Je réalise pour cela une analyse circuit équivalent, qui met en évidence deux critères : une adaptation d'impédance résistive et une adaptation d'impédance réactive. Comme précédemment évoquée, il s'agit alors bien de faire appel à un écran résistif permettant de supprimer la réflexion de l'onde incidente au moment de l'impact, combiné à un écran réactif capable de compenser les effets inductifs dus à la faible épaisseur du dispositif. J'ai décidé pour cela de troquer l'absorption large bande pour une absorption à une fréquence unique, offerte par un écran capacitif, bien plus facile à mettre en œuvre. Cette étude permet alors de déterminer que l'adaptation d'impédance est garantie par une métasurface qui est à la fois résistive et capacitive. En pratique, ces éléments sont ajoutés sur la métasurface, à travers l'ouverture, de manière alternée, la symétrie étant un élément crucial dans la conception de métasurfaces. Positionnée au-dessus du conducteur à dissimuler dont la proximité amène le comportement inductif à compenser, ce MBRA forme donc un filtre RLC. Il s'agit là d'un filtre coupe-bande dont la fréquence de résonance est dépendante des éléments réactifs uniquement. L'inductance étant fixée par la géométrie, le seul degré de liberté offert est donc la capacité à utiliser. La fréquence d'absorption est donc une fonction de la capacité de la métasurface.

Afin de valider ce modèle analytique du circuit équivalent (ECM), je le compare à un modèle numérique pour simulation par éléments finis (FEM). Je m'intéresse à ce moment à une métasurface non-reconfigurable afin de valider le protocole de conception. J'utilise donc tout d'abord un modèle 2D axisymétrique, pour sa simplicité de mise en œuvre et rapidité de simulation. En revanche, un tel modèle ne peut rendre compte que d'une configuration invariante par rotation, et supprime donc la notion de localité dans la disposition des composants électroniques. Les résultats de simulation confirment en effet la bonne absorption du signal incident à $f_0 = 300$ MHz prédite par l'ECM et ses composants électroniques, autant en termes de fréquence qu'en termes de minimum d'amplitude obtenu et de bande passante. Afin de continuer la validation de l'ECM, je compare ensuite ces résultats à un modèle 3D FEM, pour lequel la structure exacte de la métasurface est reproduite. Les résultats de simulation mettent alors en évidence certaines différences en ce qui concerne le spectre d'absorption du MBRA. On observe notamment un décalage de la fréquence d'absorption vers $f_0 = 230$ MHz, et une réduction de l'absorption, *i.e.* une amplitude du coefficient de réflexion plus élevé. Il s'agit en fait des effets

induits par l'interaction de la métasurface avec des modes de propagation d'ordre élevé, qui change en partie le comportement général de la métasurface. Le décalage de fréquence laisse penser à une modification du comportement réactif, et la réduction de l'amplitude à une modification du comportement résistif. Malgré tout, ces résultats permettent de mettre en évidence que l'ECM, malgré une certaine imprécision, permet une bonne approximation du comportement du MBRA tout en restant très simple d'utilisation.

La métasurface pour le MBRA a ensuite été réalisée. La nature coaxiale de la métasurface oblige à travailler dans un guide d'ondes élargi qui émule l'illumination radar en propageant une onde avec un mode TEM. La métasurface est introduite en bout de guide, proche du court-circuit faisant office de conducteur à dissimuler. A l'autre bout du guide coaxial, un analyseur de réseau vectoriel (VNA) est utilisé pour la mesure des paramètres de dispersion. En particulier, cela permet la mesure du coefficient S_{11}, rapport de la puissance reçue sur la puissance incidente, qui caractérise ainsi le coefficient de réflexion du MBRA sur la plage $[100, 700]$ MHz d'intérêt. La mesure met alors en évidence une absorption de l'onde à $f_0 = 230$ MHz, avec une amplitude minimale et bande passante similaire aux résultats de simulation 3D.

Le protocole de conception ainsi validé, je me suis donc tourné vers un MBRA reconfigurable. Comme précédemment précisé, la fréquence d'absorption du MBRA est fonction de la capacité de la métasurface à travers ses composants électroniques. Ainsi, avec un composant qui agit comme une capacité variable, il est possible d'obtenir un MBRA dont la fréquence d'absorption est également variable. Pour cela, j'ai utilisé une diode varactor. Il s'agit d'un élément à jonction PN, dont la polarisation permet de générer une certaine gamme de valeurs de capacités. En revanche, ce principe de fonctionnement est nécessairement sujet à une certaine résistance qui accompagne la capacité, et la mise en boîtier du dispositif ajoute des éléments réactifs au composant à monter sur la métasurface. Alors que les éléments réactifs ne sont pas forcément problématiques, en plus de rester suffisamment faible, même de faibles de valeurs de l'élément résistif peut avoir de grandes conséquences sur l'efficacité du système. La diode varactor choisie ici est la diode SMV1249 de Skyworks®, dont la gamme de capacités pour une polarisation (inverse) $V_r \in [0, 5]$ V convient à mes besoins. L'ECM du MBRA est donc modifié suite à l'introduction des diodes varactors, et la comparaison aux résultats de simulation FEM 3D permet de mettre en évidence l'écart de prédiction. En particulier, l'ECM surestime la bande passante effective et montre une amélioration croissante de l'absorption avec l'augmentation de la tension de polarisation, alors que le FEM 3D met en évidence une variation de l'adaptation d'impédance avec la tension de polarisation qui trouve un optimal aux tensions intermédiaires, mais dégradées aux valeurs basses et hautes. Malgré ce comportement, le MBRA reconfigurable est fabriqué et mesuré. Les diodes sont polarisées par une source de tension externe et la mesure se fait toujours grâce au VNA. Le coefficient de réflexion obtenu à chaque tension sur la plage $[100, 700]$ MHz met alors à nouveau en évidence le comportant absorbant et reconfigurable de la métasurface, mais un certain écart aux simulations 3D du FEM. Il apparaît notamment que le prototype de MBRA offre une plus large bande passante effective. Cette différence est attribuée à une sensibilité accrue de la variation de la fréquence d'absorption aux écarts de capacités à haute tension par rapport aux spécifications du fabricant. Une certaine différence au niveau du régime de variation des amplitudes minimales est également observée. Celle-ci est attribuée à la probable présence d'éléments résistifs non contrôlés, et à un manque de précisions des données du constructeur pour la simulation fidèle du comportement du MBRA sous toute tension et toute fréquence. Malgré cela, le MBRA fabriqué présente une absorption sous -10 dB sur $[300, 600]$ MHz, ce qui couvre tout de même une partie de la gamme désirée. Ces résultats, ainsi que la métasurface utilisée, sous présentés en Figure 0-I.4.

Afin d'améliorer ce système, je me suis ensuite tourné vers deux études. Une première étude numérique sur la possibilité d'une absorption (presque) parfaite sur la gamme envisagée,

puis une étude expérimentale sur l'utilisation du MBRA dans une configuration de reconfigurabilité continue face à des radars agiles en fréquence.

En ce qui concerne tout d'abord l'étude numérique, comme également mis en évidence précédemment, il est clair que l'introduction d'éléments résistifs parasites introduit une variation non-désirée de l'amplitude du coefficient de réflexion. Un système idéal couvrirait la plage de fréquences d'intérêt avec une absorption (presque) constante, et surtout sous le critère des -10 dB. Pour cela, il est donc nécessaire de minimiser l'impact négatif de cette résistance supplémentaire. Puisqu'il n'est pas possible de la supprimer, il faut donc trouver des solutions pour en compenser les effets. Pour cela, je propose de changer les résistances fixes utilisées jusqu'à présent par des composants électroniques à résistance variable. Puisque le critère résistif de l'adaptation d'impédance n'est plus celui de l'ECM d'égaler l'impédance du milieu de propagation de l'onde incidente, il faut pouvoir adapter cette résistance au nouveau critère émergeant avec la combinaison tension-fréquence de chaque diode. En particulier, dans le cas de la diode SMV1249, j'ai réalisé une première optimisation analytique de la valeur de la résistance. Cela me permet d'avoir un ordre de grandeur, malgré l'imprécision du modèle ECM, afin de définir un point de départ pour l'optimisation suivante sur le FEM 3D. Les résultats ainsi obtenus offrent une amplitude du coefficient de réflexion de -20 dB à -40 dB avec une résistance optimisée qui s'étale de $5000\ \Omega$ à $40\ \Omega$, soit un ratio de plus de 100. Seule la courbe d'absorption à la tension $V_r = 0$ V n'est pas améliorée par l'optimisation. Le ratio élevé invite cependant à faire un choix sur la plage de tensions à privilégier, ou à envisager l'utilisation d'autres diodes varactor pour un tel absorbant. Cependant, comme démontré, les diodes à large gamme de capacités semblent plus souvent mener à ce genre de compromis, que les diodes à faible gamme de capacités. Il y a donc un compromis entre couverture et qualité de l'absorption à trouver.

En ce qui concerne l'étude expérimentale, la reconfigurabilité est essentielle face aux radars modernes et leur agilité en fréquence. En effet, certains radars, dont la bande passante est assez étroite à basses fréquences, optent pour une opérabilité à plusieurs fréquences, afin d'élargir leur bande et donc leurs chances de détection face à des systèmes plus ou moins robustes à certaines longueurs d'onde. L'analyse automatique de la menace par un système de capteurs et de boucles de rétroaction pourrait alors permettre à un MBRA reconfigurable de balayer la plage de fréquences en question, à la vitesse de commutation du radar afin de toujours y présenter son absorption la plus forte. Pour cela, je me sers du VNA à la fois comme source du balayage en fréquence et comme moyen de mesure de la réponse du MBRA pour lequel l'accordabilité ne se fait plus de manière discrète mais continue. Il est alors possible d'obtenir une couverture fréquentielle en absorption très large. J'ai notamment alors expérimenté plusieurs vitesses de reconfiguration, définies comme fractions de la vitesse de balayage du VNA. Cependant, la relation entre tension de polarisation et fréquence de résonance n'est pas linéaire. Les résultats d'absorption alors obtenus mettent en évidence la possibilité d'élargir la gamme de fréquences couvertes, mais mettent également en évidence la grande variété de courbes d'absorption pour de faibles variations de vitesse. La vitesse de reconfiguration idéale, dans le cas linéaire, nécessite donc un compromis favorisant certaines portions du profil d'absorption idéal. Par manque de temps, je n'ai pas pu étudier la possibilité d'une variation non-linéaire de la tension de polarisation, mais il s'agit de la solution à privilégier pour approcher au mieux le profil idéal. Il suffirait pour cela d'associer chaque paire de tension polarisation – fréquence d'absorption afin de compenser par le signal de polarisation les non-linéarités de la fréquence d'absorption.

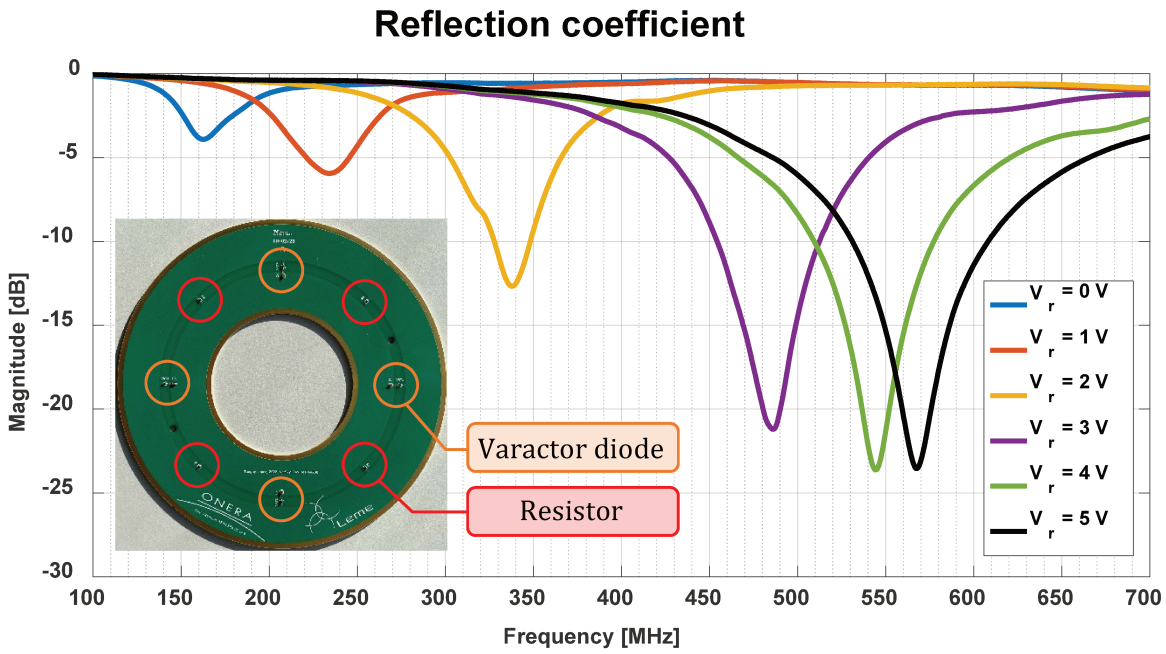

Figure 0-I.4 : Amplitude du coefficient de réflexion face à un absorbant radar à métasurface accordable en fréquence par polarisation des diodes varactor, pour absorption sur la plage [100, 700] MHz.

Convertisseur de fréquence à métasurface modulée temporellement

Dans le Chapitre III, je me suis concentré sur la réalisation d'un convertisseur de fréquence à métasurface (ou MBFC pour *metasurface-based frequency converter*) fonctionnant en bandes VHF-UHF. Comme détaillé plus haut, l'accordabilité d'une métasurface peut être utilisée pour ajouter une dimension temporelle à la structure. Dans ce cas-ci, il s'agit d'une modulation temporelle, pour une reconfiguration continue et périodique. Ce MBFC est alors envisagé comme brique d'une cape Doppler. Il s'agit d'une stratégie apparue avec les métasurfaces à modulation temporelle, dont l'objectif est de supprimer le décalage Doppler d'une cible mouvante. En effet, le décalage en fréquence induit sur le signal est proportionnel à la vitesse de la cible par rapport au radar, ce qui, avec sa position, permet alors d'estimer la trajectoire de l'appareil pour interception. La compensation du décalage Doppler supprime donc l'information vitesse, la cible apparaissant alors comme un objet immobile de la scène illuminée. Or, le traitement des formes d'onde FMCW fait appel à un filtre anti-fouillis qui supprime la réponse des cibles immobiles, afin de ne pas constamment saturer la carte distance-vitesse avec les informations provenant du relief, des bâtiments, des éoliennes… Ainsi, une cape Doppler permettrait, au mieux, de disparaître de la carte distance-vitesse, au pire de fausser l'estimation de trajectoire.

Pour exploiter la manipulation de spectre offerte par la modulation temporelle d'une métasurface, il est crucial de travailler dans le cadre de la modulation lente. Cette ségrégation des deux temps (lent et rapide) permet alors d'écrire le champ électrique réfléchi comme le produit d'un champ électrique incident et du coefficient de réflexion de la métasurface. Ainsi, dans le domaine fréquentiel, le spectre du champ réfléchi devient la convolution des spectres du champ incident et du coefficient de réflexion. Et un coefficient de réflexion qui présente un module unitaire et une rampe de phase dans le temps devient alors un Dirac dans le domaine fréquentiel, réalisant la conversion en fréquence du champ incident au moment de sa réflexion. En assurant ce régime, je présente donc ensuite les spectres attendus de convertisseurs de fréquence idéal et non-idéal. Dans le cas idéal, la rampe de phase parcourt 2π durant la période de modulation T_m et

transpose donc parfaitement la spectre du champ incident de la fréquence de modulation f_m, vers les hautes ou basses fréquences selon le profil de phase. En revanche, dans le cas plus réaliste d'une convertisseur non-idéal, seulement une fraction α de la rampe de phase est possible, ce qui génère dans le spectre du champ réfléchi une infinité d'harmoniques, espacées de la fréquence de modulation f_m. En réalité, la fréquence vers laquelle la conversion s'effectue principalement est l'harmonique la plus proche de $f_0 \pm |\alpha| f_m$. Ce qui indique une absence de conversion pour $|\alpha| < 0.5$.

Après avoir prévenu ce comportement, je m'intéresse à la conception de la métasurface nécessaire pour le MBFC. Une analyse circuit équivalent me permet de mettre en évidence que l'utilisation d'une métasurface purement réactive est une solution à l'obtention d'un profil de phase dont la variation est continue et lisse sur une gamme de valeurs réactives. Je décide donc d'utiliser une métasurface parfaitement capacitive, formant alors un circuit LC avec le conducteur à dissimuler, donc la modulation spécifique de capacité permet la linéarisation de la phase du coefficient de réflexion. Dans la pratique, je décide alors de proposer deux configurations possibles pour la métasurface. Une première, dite 4VCT, analogue à celle du MBRA, où quatre diodes varactor sont montées en alternance de quatre capacités fixes. Et une seconde, dite 8VCT, où huit diodes varactor sont montées sur la métasurface. Les symétries des deux configurations sont donc différentes, et les profils de phase ainsi obtenus devraient également présenter quelques différences.

Je décide ensuite de vérifier le bon fonctionnement d'un tel MBFC en réalisant trois études en configuration 2D axisymétrique. La première étude est entièrement analytique, et repose sur l'utilisation de l'ECM du circuit LC et la relation des spectres offerte par la modulation lente. La seconde étude est entièrement numérique, réalisée sur COMSOL, dont la simulation FEM permet de déterminer le schéma de modulation nécessaire pour la simulation FETD qui réalise alors la conversion. Enfin, la troisième étude est semi-analytique, et exploite le coefficient de réflexion de la simulation FEM puis la relation des spectres. Dans chacun des trois cas, je compare alors le spectre du champ réfléchi obtenu, dans un cas idéal de capacités variables parfaites, et dans un cas réaliste de diodes varactors, accompagnées de leurs éléments parasites. Je quantifie alors la conversion par trois métriques: CL les pertes de puissance à la conversion, R_0 la réduction du signal à la fréquence incidente (qui porte l'information vitesse) et $\mathcal{E}_{ref}/\mathcal{E}_{inc}$ le rapport des énergies réfléchie et incidente sur une plage de fréquences resserrées autour de la fréquence incidente. Dans les trois études, la conversion de fréquence est bien observée pour un signal incident à $f_0 = 300$ MHz et une fréquence de modulation $f_m = 1$ MHz. De plus, les métriques pour les deux cas de l'étude analytique sont les mêmes que pour l'étude qemi-analytique : l'introduction de diodes varactors accentue les pertes (CL augmente de 3.7 dB jusqu'à 3.8 dB), diminue la puissance à la fréquence incident (R_0 augmente de 3.3 dB jusqu'à 20 dB) et plus de la moitié de l'énergie est dissipée ($\mathcal{E}_{ref}/\mathcal{E}_{inc}$ diminue de 1 à 0.45). Dans l'étude numérique, les pertes sont légèrement plus fortes, la réduction légèrement moins forte et la dissipation est égale. L'accord entre les trois études valide en partie l'ECM, utilisée pour la conception du MBFC, et confirme la viabilité de l'étude semi-analytique, qui peut donc être étendue au cas 3D. En effet, le cas 3D est le plus proche de la réalité, ce qui permettrait de prédire au plus proche le comportement d'une réalisation physique. Par contre, la simulation FETD d'une configuration 3D est particulièrement délicate à mettre en place, en plus de demander des ressources et du temps. En revanche, intégrer les interactions haut-niveau dans le coefficient de réflexion même de la métasurface par simulation FEM semble être une solution. Injecté ensuite dans la relation des spectres, le coefficient de réflexion ainsi obtenu et modulé périodiquement, permet l'étude semi-analytique 3D semi-analytique de convertisseurs de fréquence dans le cas de capacités variables et de diodes varactor. Dans ce cas, je retrouve, en plus d'une bonne conversion, à nouveau plus de pertes dans le cas varactor, une meilleure conversion de la fréquence incidente et une réduction

de la dissipation. En réalité, le passage à la configuration 3D, outre avoir modifié quelque peu le schéma de modulation pour prendre en considération les interactions haut-niveau, présente finalement une fraction α plus élevée que la configuration 2D, d'où la réduction de la dissipation d'énergie, et de pertes en générale.

Je passe donc à la réalisation et à la mesure d'un MBFC. Je présente tout d'abord pour cela les moyens de mesure envisagées : une configuration fréquentielle pour la mesure du coefficient de réflexion, puis une configuration temporelle pour la mesure des spectres. La configuration fréquentielle est une réplique de celle utilisée dans le cadre du MBRA, tandis que la configuration temporelle utilise comme source incidente un générateur de signal harmonique, et comme moyen de mesure un oscilloscope. L'utilisation du guide coaxial, sur lequel se trouve un unique point d'accès, invite donc à séparer les signaux incident et réfléchi à l'entrée et à la sortie du guide par un coupleur bidirectionnel.

Je détaille ensuite ma méthode de conception, notamment sur le choix des composants électroniques. Je présente notamment l'intérêt des deux configurations 4VCT et 8VCT. D'un côté, dans le cas 4VCT, malgré une plage de modulation réduite, l'utilisation des capacités fixes permet de choisir précisément la fréquence d'intérêt à convertir. De l'autre côté, dans le cas 8VCT, la large plage de modulation offerte devrait maximiser la fraction $|\alpha|$, mais la plage de fonctionnement est moins flexible. Pour m'assurer de leur bon comportement, je passe donc à la validation analytique et numérique des deux configurations, en utilisant des diodes varactor SMV1255 de Skyworks®. Comme attendu, il apparaît alors que les profils de phase obtenus par la configuration 8VCT, pour une polarisation $V_r \in [0, 5]$ sur une plage $f_0 \in [100, 550]$ MHz, est une version compressée et décalée vers les basses fréquences des profils de la version 4VCT. Dans les deux cas, une gamme de fréquences assez large présente une fraction $|\alpha| > 0.8$, nécessaire pour une conversion efficace. Les profils de phase obtenus par FEM 3D confirment ce même comportement, mais introduit un décalage des profils de phase vers les basses fréquences. Cela ne compromet en rien la conversion de fréquence. Donc une métasurface en configuration 4VCT et une en configuration 8VCT sont réalisées, dont j'ai mesuré les profils de phase. Sans que je puisse y trouver une explication, je réalise alors une inversion dans les profils de phase espérés, et sélectionne donc la métasurface 8VCT pour le MBFC expérimental, plus flexible. Introduit dans le guide coaxial élargi, j'applique alors le schéma de modulation en termes de tension nécessaire à la linéarisation de son coefficient de réflexion, pour une modulation à $f_m = 100$ kHz et un signal incident harmonique à $f_0 = 370$ MHz. La séparation des champs incident et réfléchi par le coupleur permet alors l'analyse des spectres de chacun, qui confirment la bonne conversion du signal réfléchi vers $f_0 \pm f_m$, ce qui finit de valider expérimentalement le MBFC. Les spectres ainsi obtenus, et la métasurface utilisée, sont présentés en Figure 0-I.5.

Je remarque cependant deux choses. Le spectre du champ réfléchi présente une asymétrie de distribution de puissance aux harmoniques qui ne faisait pas partie des résultats mis en évidence par les différentes études. Deuxièmement, la fréquence de modulation de $f_m = 100$ kHz est choisie car au-delà de $f_m = 200$ kHz, la conversion est dégradée, voir absente. Ces deux éléments sont attribués, pour le premier cas, à une erreur dans la modulation de la métasurface, pour le deuxième cas, à une limitation du PCB réalisé.

Pour conclure cette étude, j'élargis les cas d'application du MBFC du cas harmonique au cas non-harmonique, face à une forme d'onde FMCW. En réalité, suite à la linéarisation du coefficient de réflexion à une fréquence donnée, les profils de phase des fréquences voisines sont également presque linéarisés, ce qui laisse penser à l'existence d'une bande passante de conversion (ou FCB pour *frequency conversion bandwidth*) non-nulle. Je vérifie donc ce comportement avec une étude analytique, puis une étude numérique (2D axisymétrique), qui confirment toutes les deux l'existence de cette FCB, et que la conversion est accompagnée d'une réduction de la puissance de la fréquence initiale d'au moins 10 dB sur $FCB = 25$ MHz autour de

$f_0 = 307$ MHz. Je remplace alors la source harmonique par un générateur de signaux arbitraires, paramétrés pour la génération d'un train de *chirps* autour de $f_0 = 370$ MHz avec $\Delta f = 80$ MHz de bande. Le spectre du signal réfléchi mesuré confirme alors bien la conversion d'une portion du spectre incident, avec une $FCB = 30$ MHz autour de $f_0 = 380$ MHz, comme présenté en Figure 0-I.5. Le MBFC ainsi proposé est donc approprié pour faire face à des signaux harmoniques et non-harmoniques, et ce, sur une plage de fréquence qui s'étend de 290 à 420 MHz.

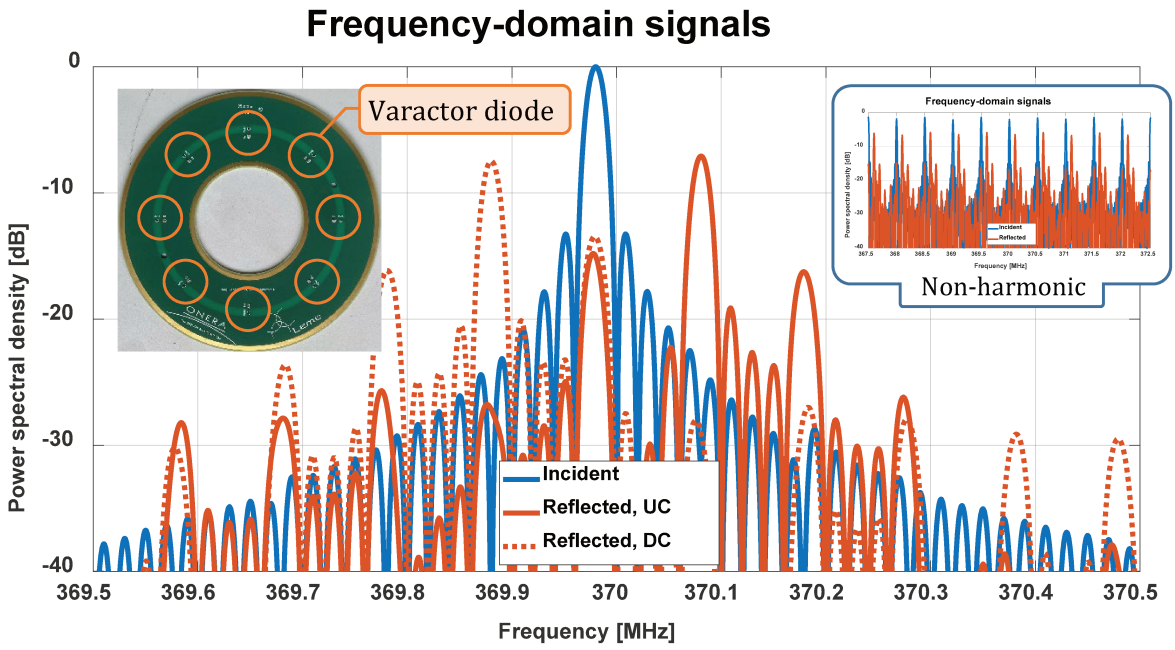

Figure 0-I.5 : Densité spectrale de puissance des champs électriques incident et réfléchi, pour une conversion vers les hautes (*UC*) et basses (*DC*) fréquences d'une onde harmonique, par modulation du convertisseur de fréquence à métasurface de 100 kHz à 370 MHz, accompagné de l'extension au cas non-harmonique.

Conclusions

En conclusion, après avoir introduit les principes de détection et d'estimation des paramètres distance et vitesse du radar, j'ai présenté quelques solutions historiques pour s'en dissimuler. Malgré leurs performances propres, certains cas d'usage comme le camouflage basses fréquences nécessitent de nouveaux développements. L'émergence parallèle des métasurfaces a alors permis la réduction des revêtement absorbants résonants, bien trop encombrants pour être embarqués sur des plateformes mobiles à basses fréquences. De plus, les métasurfaces permettent une intégration simple de composants électroniques, notamment actifs, qui permettent alors de dépasser la limite fondamentale en bande passante de la borne de Rozanov-Bode-Fano. Les métasurfaces actives deviennent donc centrales dans les nombreux développements pour la furtivité. Je me suis alors en effet concentré sur deux aspects essentiels du contrôle de tels dispositifs : leur accordabilité et leur modulation.

Je me suis donc, dans un premier temps, intéressé à l'élargissement effectif de la bande passante des absorbants radars qu'offre l'accordabilité. Grâce à des diodes varactor, pilotées par des signaux DC, je suis en mesure de modifier la fréquence d'absorption, et couvrir ainsi une partie de la bande de fréquence d'intérêt. J'ai ensuite élargi cette accordabilité à une étude préliminaire de la bande d'absorption potentielle offerte par la reconfiguration continue de la fréquence d'absorption.

Je me suis ensuite intéressé à une stratégie de suppression de l'information vitesse par modulation de la métasurface. A nouveau grâce à des diodes varactor, pilotées par des signaux AC, je suis en mesure de réaliser un convertisseur de fréquence, permettant ainsi de compenser le décalage Doppler de la cible mouvante. J'ai ensuite élargi le cas d'un signal harmonique à celui d'un signal FMCW, prouvant la viabilité d'un tel système dans un contexte plus proche d'une illumination radar réelle.

Dans les deux études, j'ai alors présenté mon processus de conception, mes outils et modèles d'analyse (circuit équivalent, simulations 2D axisymétrique, 3D…) et mon protocole de validation expérimentale.

SUMMARY

In this thesis, I am interested in metasurface-based solutions to stealth. The use of active metasurfaces is particularly appropriate to overcome the bandwidth limitations of passive devices, in particular due to the reconfigurability of the electromagnetic properties. These properties can then be exploited to adapt the absorption regime to the threat, or to conceal certain information from the opposing radar.

In Chapter I, I introduce the working principle of radars, in order to look more closely at the strategies used to counter detection and thus improve target stealth. Radar, by reflecting an electromagnetic wave off the target, can estimate the presence, distance and speed of an object, among other parameters. Techniques for reducing the Radar Cross Section (RCS) include the use of specific shapes in the design of the aircraft and the use of radar absorbing materials (RAM). RAMs, whether resonant or non-resonant, ensure impedance matching to the incident wave, minimizing reflection back to the radar. Metasurfaces have made it possible to reduce the bulkiness of traditional solutions at low-frequency, but remain limited by a maximum bandwidth. However, their compatibility with electronics makes them an ideal medium for moving away from the *passive* regime, thanks to active components that enable broadband absorption or reconfigurability. This feature makes it possible to control the metasurface to tune its absorption frequency, or to modulate its properties to manipulate the spectrum of interacting waves.

In Chapter II, I develop a metasurface-based radar absorber (MBRA) operating in the VHF-UHF bands. Highlighted by an equivalent circuit analysis, the metasurface providing impedance matching to the incident radar wave must be both resistive and reactive. The use of such a capacitive screen, despite its narrowband absorption, facilitates the design of the device. The model is then validated by FEM simulation (2D axisymmetric and 3D) and manufactured. Measurements of its reflection coefficient with VNA confirm good agreement with the simulations. A frequency-tunable MBRA using varactor diodes is then designed to expand the effective impedance matching range. Experimental validation confirms absorption below -10 dB from 300 to 600 MHz, despite some deviations from the simulations. Then, a numerical study is carried out for a tunable high-absorption MBRA. Finally, a preliminary experimental study highlights the possibility of broadband absorption in the face of frequency-agile radars by continuous reconfiguration of the metasurface.

In Chapter III, I develop a metasurface-based frequency converter (MBFC) for the VHF-UHF bands. Thanks to the time modulation of the metasurface, it is possible to compensate for the Doppler shift of moving targets. Three studies are carried out (analytical, digital and semi-analytical) to compare equivalent circuit models and 2D axisymmetric and 3D digital models. These highlight the good frequency conversion offered by capacitance modulation, as well as the losses due to the resistive behavior of the varactor diodes. Two configurations of metasurfaces are then manufactured and compared in terms of phase profiles, where the decision criterion is the maximum phase range explored at each frequency. Measurement of the MBFC output spectrum against a harmonic wave at 370 MHz confirmed the 100 kHz conversion, validating the proposed MBFC. This validation is then extended to the case of FMCW (non-harmonic) signals, a portion of which can effectively be converted to suppress the velocity information.

INTRODUCTION

The manipulation of electromagnetic waves is a critical feature to the modern developments of many civil and military applications. Harnessing the fundamental Maxwell's equations from the late 19th century, the first antennas for long-distance communications and remote sensing came to life within the first half of the 20th century. Accelerated by WWII, a variety of land and airborne radars were developed for early warning, maritime patrol, or strategic bombing. Afterwards, subsequent developments of radar systems helped perfect detection hardware, tracking algorithms, and imaging systems to serve civil and military purposes alike. Nowadays, over-the-horizon radars are used for monitoring coastal areas, long-range radars for en-route air traffic control, while short-range radars are integrated into autonomous vehicles for collision avoidance.

In a defense context, radars are essential sensors since they are operational in all weather conditions and at night, unlike infrared-optical sensors: offensively, with airborne radars for target identification, strategically, with spaceborne radars for topography mapping, and defensively, with ground-based radars for sensitive areas protection. In the last case, it is usual to resort to multiple radars at once, each in a different frequency band, to make the most of each strengths and thus multiply chances of detection. For instance, low frequency radars are used for early warning detection in combination with high frequency radars for tracking and targeting.

Camouflaging from radar systems, better known as stealth, is a multifaceted domain of research. It primarily aims at reducing the electromagnetic signature of aircrafts, hiding their presence long enough to penetrate adversary defenses. Bordering on electromagnetic warfare via range/bearing/velocity deception, it can also extend beyond the radiofrequency realm to infrared and visible wavelengths.

Research on stealth solutions led in the 1980's to some of the most famous designs from the USA, such as the F-117 attack aircraft. Integrated into the very specifications of aircrafts, such design choices can be identified by their low-profiled, delta-winged or smooth-surfaced and combat-ready features. However, these geometrical solutions are dependent on the incidence angles, and large wavelengths are not as strongly affected. Therefore, other solutions are necessary to cover such weaknesses, such as reflectionless coatings.

To suppress the reflection upon the surface of the structure to hide, absorbing layers using magnetic and dielectric inclusions have been developed, and the historical principles of electromagnetic screens have gone through many iterations, optimizations and variations. However, some solutions are more appropriate for particular applications, and despite the combination of multiple solutions in practical cases, their mechanical performance and durability in operational conditions are key factors to take into account. In the end, design choices and specific developments are primarily dependent on the designated mission, on-board platform, and state of the art.

Meanwhile, the electromagnetic community at large started to work on a new technology for extraordinary wave manipulations with novel artificial materials, the so-called *metamaterials*. Using three-dimensional arrangements of specifically designed resonant scatterers, called *meta-atoms*, their composite nature can lead to artificial electromagnetic properties beyond those naturally occurring. First conceptualized by Prof. V. G. Veselago in the 1960's, it was demonstrated in the early 2000's by Prof. D. R. Smith and Prof. J. B. Pendry that specific patterns can create media of negative permittivity and/or permeability, and therefore negative refraction index, which was never achieved before. Despite a fast-growing interest for these new materials, bulkiness quickly emerged as a major obstacle to practical realizations. Therefore, research turned to their two-

dimensional counterpart, called *metasurfaces*, enabling the design of a wide variety of electromagnetic behaviors in a compact format. Harnessing the scatterers' resonance, their equivalent surface impedance/admittance can be carefully tailored both in the resistive and reactive regimes.

The extreme versatility of metasurfaces can be even increased with the introduction of electronic components. In the radiofrequency domain, the printed circuit board technology generally used for manufacturing is particularly well-suited to the loading of lumped elements. In radar stealth context, metasurfaces offer a much-needed thickness reduction, compared to seminal resonant radar absorbing structures (Salisbury screen), for similar performances, which is especially valuable at low frequencies.

The versatility of metasurfaces really is their strongest asset. In recent years, more and more electronics has been integrated onto metasurfaces, most notably active electronic components. Active metasurfaces have been designed for resonance frequency tunability, surface impedance control, electronically steerable antennas/reflectors, etc... In the radar stealth context, active metasurfaces have the potential to reach broadband coverage as well as provide several functionalities with a single metasurface. Tunable properties, switchable modes, autonomous operation and temporal control are among the most notable features to be exploited for stealth. In particular, metasurfaces constitute the perfect radiofrequency platform for time-based electromagnetic manipulation.

This PhD thesis focuses on the development and validation of metasurface-based radar stealth devices at VHF-UHF frequencies. I specifically focused on active metasurfaces, whose behavior can be reconfigured. This allows tunability of the reflection properties in real-time to serve two essential purposes: the circumvention of detection and velocity-reading deception. This manuscript therefore consists in three chapters and is structured as follows.

In Chapter I, I start by presenting the fundamental background on radar systems to motivate the current need for better stealth solutions, where metasurface-based devices can offer the necessary thickness reduction for low-frequency applications. Then, I detail how passive radar absorbing devices are constrained in bandwidth by physical limitations that only active elements can overcome.

In Chapter II, I thus focus on broadening the absorption bandwidth through absorption tuning. This approached is based on the use of DC voltage controls in time. Thanks to an equivalent circuit model for the design and full-wave simulations for behavior validation, I fabricate and experimentally validate a metasurface-based *radar absorber*. I then extend the previous design to escape from the fundamental bandwidth limitations on *passive* absorbers by using varactor diodes, and numerically and experimentally validate a voltage-tunable metasurface-based *radar absorber* over the VHF-UHF bands. Then, I turn to a numerical investigation into a near-perfect tunable absorber thanks to capacitance- and resistance-tuning. Finally, I perform an experimental validation of a real-time voltage-sweeping absorber to face frequency-hopping radars.

In Chapter III, I turn to the time-modulation of metasurfaces to compensate the Doppler shift of a moving target, such that it appears as a mere static element of the illuminated scene. This approach is based on the use of AC voltage controls in time. Harnessing the time-modulation of varactor diodes, I design a metasurface-based *frequency converter* and use analytical (equivalent circuit), numerical (simulation) and semi-analytical models to validate its behavior. I then conduct an experimental validation against harmonic impinging signals, demonstrating the suppression of the Doppler frequency. Finally, I extend the validation to non-harmonic impinging signals, an entire portion of which can effectively be frequency-shifted.

Finally, I draw conclusions on the contribution of my works on the design, simulation and measurement of active metasurface-based stealth solutions. In particular, I detail the thought,

validation and measurement processes for a voltage-tunable radar absorber and time-modulated frequency converter over the VHF-UHF bands. I finally provide some outlooks for both cases, arising from unexpected behaviors and time management-driven choices, for future developments.

I. State-of-the-art radar camouflaging metasurface-based strategies

CONTENTS

I. STATE-OF-THE-ART RADAR CAMOUFLAGING METASURFACE-BASED STRATEGIES 25

1. INTRODUCTION 26
2. SURVEILLANCE RADAR SYSTEMS FOR DETECTION, DISTANCE AND VELOCITY ESTIMATES 26
   2.1. Surveillance radar systems 27
      2.1.1. Radar equation 27
      2.1.2. Radar cross section 28
      2.1.3. Maximum radar range 28
      2.1.4. Probability of detection 29
   2.2. Radar systems for the estimates of a target's parameters 29
      2.2.1. Range estimate 30
      2.2.2. Velocity estimate 30
      2.2.3. Simultaneous range and velocity estimates 30
      2.2.4. Range-Doppler map and anti-clutter filter 31
3. SEMINAL RADAR STEALTH SOLUTIONS 32
   3.1. Radar stealth from shape effects 32
   3.2. Radar stealth from radar absorbing materials 32
      3.2.1. Impedance/Admittance matching 33
      3.2.2. Non-resonant radar absorbing materials 33
         3.2.2.1. Impedance matching of non-resonant radar absorber materials 34
         3.2.2.2. Magnetic and conductive composite radar absorbing materials 34
         3.2.2.3. Dallenbach screen 35
      3.2.3. Resonant radar absorbing materials 35
         3.2.3.1. Salisbury screen 35
         3.2.3.2. Jaumann screen 35
         3.2.3.3. Metasurface-based radar absorber 36
      3.2.4. Bode-Fano and Rozanov bounds 37
         3.2.4.1. Bode-Fano bound: impedance matching bandwidth of arbitrary loads 37
         3.2.4.2. Rozanov bound: impedance matching bandwidth of metal-backed dielectrics 38
         3.2.4.3. Bode-Fano and Rozanov bounds equivalence 39
4. REVIEW OF METASURFACE-BASED RADAR STEALTH SOLUTIONS 40
   4.1. Review of metasurface-based radar absorbers 40
      4.1.1. Metasurface-based radar absorber *by design* 41
      4.1.2. Passive-electronic-loaded metasurface based radar absorber 42
      4.1.3. Active-electronic-loaded metasurface-based radar absorber 43
         4.1.3.1. Metasurface-based radar absorber using non-Foster elements 43
         4.1.3.2. Reconfigurable metasurface-based radar absorber 44
   4.2. Review of time-controlled active metasurface-based radar stealth solutions 46
      4.2.1. Time-varying metasurface-based radar stealth solutions 47
      4.2.2. Time-switched metasurface-based radar stealth solutions 47
      4.2.3. Time-modulated metasurface-based radar stealth solutions 47
5. CONCLUSIONS 49

1. Introduction

In this Chapter I, I introduce the working principles of modern radars as well as traditional radar camouflaging techniques, *i.e.* radar stealth. After a presentation of range and velocity estimates, I turn to a discussion about countermeasure techniques such as shape design and absorbing materials. However, some of these traditional solutions fall short for applications in the lower VHF-UHF frequency bands, where wavelengths are around 1 m long. Thanks to the development of metasurfaces, *i.e.* electromagnetic manipulation platforms, the necessary breakthrough technology to devise new camouflaging strategies seems to have emerged. Therefore, I will take particular interest in metasurface-based solutions. In particular, active metasurfaces, which can be used to design controllable systems, such as time-tuned absorbers, time-switched power dissipators and time-modulated spectrum manipulators.

In Section 2, I deal with the topic of radar systems and their operating principles. Foremost, they are used as detection devices: if the power backscattered by an illuminated target reaches a certain threshold above the noise upon reception, detection is triggered. Furthermore, depending on the radar's waveform bank and signal processing algorithms, these systems can also estimate a handful of the target's parameters, such as elevation, bearing, range and velocity.

In Section 3, I introduce some of the most widespread radar stealth solutions. I first take interest in shape design, and then turn to radar absorbing materials (RAM), which can either be non-resonant or resonant. Still, all RAM are but impedance matching devices and are thus limited in their bandwidth by the Rozanov-Bode-Fano (RBF) bound. To be more specific, all RAM have a limited bandwidth-to-thickness ratio rendering these devices rather bulky at lower frequencies. Fortunately, the first developments on metasurfaces highlighted that these planar structures can act as resistive and reactive screens all at once, thereby compensating for the inductive behavior induced by the conductor plane of low-profiled RAM. However, all passive RAM are constrained by the RBF bound, metasurfaces included. Nonetheless, since they usually use PCB technology, they are most suitable for the integration of electronic elements, where active elements can free metasurface-based RAM from the RBF bound, thus providing the potential to reach broader bandwidths than ever obtained before.

In Section 4, I introduce some recent concepts for stealth based on the temporal control of waves. I first introduce the concept of temporal modulation of the propagation medium, highlighting particularly interesting concepts. However, such solutions rely on the modulation of the entire propagation channel, which is technologically unavailable at the moment at radiofrequencies outside of plasma-based solutions. Research has recently expanded towards the time control of surfaces, thanks to active loaded metasurfaces. On top of expanding the use cases of active absorbers to time-base reconfigurations, it also led to the emergence of other radar stealth strategies, such as the reflection in other direction, dissipation of power over frequencies or frequency conversion.

2. Surveillance radar systems for detection, distance and velocity estimates

In this Section 2, I first introduce the concept of surveillance radar, used for the detection of targets [1], [2], [3], [4]. Its entire working principle revolves around the measurement of the power backscattered from the illuminated target, and its comparison to a signal-to-noise ratio

(SNR) threshold. Then, I detail additional functionalities of radar systems, especially for the estimation of some of the target's parameters such as range and velocity, using specific waveforms.

2.1. Surveillance radar systems

A radar is an electromagnetic system used for the detection and estimation of the distance of objects, as the name suggests – RAdio Detection And Ranging. In civil application, it is used for air traffic control, meteorology or to prevent collisions. In military context, it is rather used for the detection of targets, should it be airborne, seaborne or on ground-based, to allow for the protection of sensitive areas, monitoring of air, sea, land, or space. A radar system is comprised of a transmitter, for the generation of the waveform of interest, and a receiver – which may be co-localized (monostatic) or not (bistatic) with the transmitter – to measure the energy of the waveform backscattered onto the target.

Historically, radars in the HF and VHF bands (below 300 MHz), are the first to have been developed during World War II. They show very high range, with some even exceeding the radio horizon caused by the Earth's curvature [5]. Despite very large antennas, these systems have recently been regaining interest because stealth technologies are not readily available at such low frequencies, as will be detailed in Section 3. Radars in the UHF range (from 300 MHz to 1 GHz), still show very long range and remain unaffected by the weather, rendering them particularly useful as early warning radars [3].

Even though radars in the L-band (from 1 GHz to 2 GHz) are still qualified as long-range air surveillance radars, they are mostly used in en-route air traffic control. And radar systems at even higher frequencies (S-, C-, X-, K-, V-... bands) present shorter range as they are affected by the increasingly stronger atmosphere attenuations [2], [3]. They however remain some of the most commonly used systems. In practice, low frequency radars do serve as early warning systems but their coarse range gridding does not provide the necessary resolution for pursuit, unlike high frequency radars and their finer range gridding.

In order to better define the characteristics of a radar, and the subsequent concept of stealth, Section 2.1 provides the basic principles behind target detection.

2.1.1. Radar equation

Under free-space propagation and far-field illumination conditions, the entire working principle of surveillance radar systems relies on the radar equation, expressed in the monostatic configuration depicted in Figure I.1 as

$$P_{R_X} = \lambda^2 \frac{P_{T_X} G^2}{(4\pi)^3 R^4} \sigma \tag{I.1}$$

where P refers to the power, with subscripts T_X and R_X referring to the transmitter and receiver, namely, while G is the antenna gain and R the range (or distance) to the target. The variables λ refers to the wavelength and σ is the target's radar cross section (RCS). The $(4\pi)^2 R^4$ numerator of the monostatic case is the product of the areas of the radiation spheres illuminated by the isotropic sources at emission (from the radar) and scattering (by the target). This isotropy is corrected upon emission by the transmitting antenna gain $G_{T_X} = G$ and upon reception by the receiving antenna gain $G_{R_X} = G$. Therefore, narrow beamwidth and high gain antennas are critical to enhance received power.

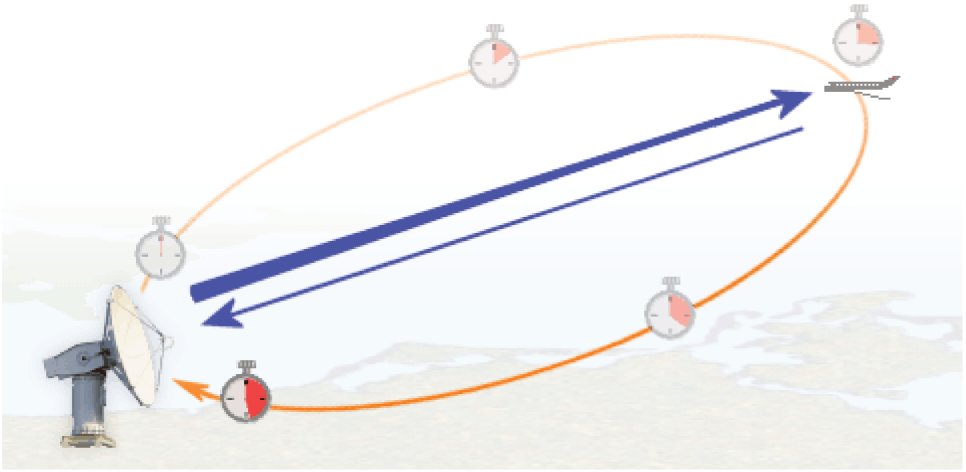

Figure I.1 : Monostatic radar configuration, highlighting the transmitted and received waves [4] (last accessed 28/05/24).

Stealth is therefore defined as the different strategies and techniques used on the target's end to defeat radar detection.

2.1.2. Radar cross section

The RCS σ is specific to every target's geometry and coating [6], [7], [8], which depends on wavelength λ, and quantifies its effective cross-section. Therefore, for an incident power density S_i at the target, the RCS is defined in regards to the scattered power density S_s by the reflector at a distance R as

$$\sigma = \lim_{r \to \infty} 4\pi R^2 \frac{S_s}{S_i} \tag{I.2}$$

2.1.3. Maximum radar range

From Equation (I.1), one may notice that a monostatic radar system is characterized by its maximum range R_{max} such that

$$R_{max} = \sqrt[4]{\lambda^2 \frac{P_{T_X} G^2}{(4\pi)^3 P_{R_X,min}} \sigma} \tag{I.3}$$

with $P_{R_X,min}$ the minimum detectable backscattered power. From Equation (I.1), one may notice the received power P_{R_X}, and from Equation (I.3) the maximum range R_{max}, are strongly dependent on the target's RCS σ. Indeed, the fourth root function requires a drastic σ reduction for significant R_{max} reduction. For instance, halving R_{max} is only possible by dividing σ by 16 (-12 dB).

In the context of airspace surveillance, range is a crucial element to serve early warning purposes. However, since RCS is reduced as little as possible for stealth applications on the target's end, then, according to Equation (I.3), one may notice antenna gains and transmitted power are key elements to optimize. But then practical considerations, such as antenna size and available power, limit design and operational dimensions.

2.1.4. Probability of detection

The detection of a target is conditioned by a statistic test. Indeed, the backscattered signal is mixed with noise upon reception and must reach a significant signal-to-noise ratio (SNR) for detection to be triggered (detection threshold).

If H_0 is the hypothesis that no target is present and H_1 is the hypothesis that a target is present, then by designing the overall received signal by the unknown variable X, one may define the hypothesis test

$$f(X) \gtrless_{H_0}^{H_1} \eta \tag{I.4}$$

where f is the probability density function associated to the overall signal X and η, the decision threshold. Therefore, one may define $A_0 = \{X \leq \eta\}$ as the acceptance set for the null hypothesis H_0 and $A_1 = \{X \geq \eta\}$ as the acceptance set for the alternative hypothesis H_1. Then, the false alarm probability P_{FA} is defined as

$$P_{FA} = P(A_1|H_0) = \int_{A_1} f(X|H_0)dX \tag{I.5}$$

and the detection probability P_D is defined as

$$P_D = P(A_1|H_1) = \int_{A_1} f(X|H_1)dX \tag{I.6}$$

The Neyman-Pearson criterion then allows for the definition of the threshold value η, which maximizes P_D while keeping P_{FA} relatively low. Given the high number of decisions to be made by the surveillance system, P_{FA} is generally set to a low value. For instance, $P_{FA} = 10^{-6}$ and $P_D = 0.8$ is offered by signals of $SNR = 12$ dB [3].

From this statistical hypothesis test, one may also define the missed detection probability $P_{MD} = P(A_0|H_1) = 1 - P_D$ and the correct rejection probability $P_{CR} = P(A_0|H_0) = 1 - P_{FA}$. The statistical test is summarized in Table I-1.

Surveillance radar systems, from the measurement of the signal's power that is backscattered upon reflection on a target, are able to detect the presence of hostile aircrafts They are usually qualified in terms of their range, which is dependent on the transmitted power, antenna gain, frequency used as well as the target's own scattering behavior: its RCS. Besides, a radar, through specific signal processing and associated waveforms, is able to gather additional information beyond the target's simple presence. In particular, it is able to get range, bearing, elevation and velocity readings, which are key pieces of information to deploy defense strategies.

	Target is present $\boldsymbol{H_1}$	**Target is not present** $\boldsymbol{H_0}$
Alarm is raised $\boldsymbol{A_1}$	Detection P_D	False alarm P_{FA}
Alarm is not raised $\boldsymbol{A_0}$	Missed detection P_{MD}	Correct rejection P_{CR}

Table I-1 : Statistical hypothesis test on radar detection.

2.2. Radar systems for the estimates of a target's parameters

Using radar systems, a number of the target's properties can be estimated, such as its range, speed, bearing, and elevation. Though elevation and bearing are crucial elements for the precise positioning of a target, the quantities of interest in this work are range and speed. This Section 2.2 will thus focus on the latter form of target's parameters estimate using a frequency modulated continuous wave (FMCW) radar operating mode. This specific radar system periodically emits a signal whose frequency is a function of time with a pulse repetition period T_p equal to the duration of the frequency modulation T_c, as displayed in Figure I.2(a-b). This waveform allows for the simultaneous estimates of range and velocity of the target.

2.2.1. Range estimate

Range estimate of a target with respect to the radar system, as hinted in Figure I.1, can be performed by measuring the time Δt between transmission and reception of the signal. In fact, knowing this wave travels, back and forth at the constant speed c_0, the light velocity, the range R to the target can be estimated as

$$R = \frac{c_0 \Delta t}{2} \tag{I.7}$$

One may bear in mind this distance is the slant range, *i.e.* the line of sight distance between the radar and target. Ground distance can then only be derived from the target's elevation.

2.2.2. Velocity estimate

Velocity estimate of a target with respect to the radar system relies on measuring the variation in frequency between transmitted and received signals. The method used by radar systems is based on the measurement of the phase difference $\Delta\phi$ between transmitted and received signals from any continuous wave (CW) radar, as displayed in Figure I.2(a). In fact, a time-dependent change of the distance to the target $R(t)$ – hinting at a movement of the target – then a relatively constant change in phase in phase difference offers velocity readings since

$$\frac{\partial \Delta\phi(t)}{\partial t} = -\frac{4\pi}{\lambda}\frac{\partial R(t)}{\partial t} = -\frac{4\pi}{\lambda} v_s \tag{I.8}$$

where v_s is the radial speed of the source. In this case, the Doppler shift f_D, seen in Figure I.2(b), induced by the moving target is

$$f_D = \frac{1}{2\pi}\frac{\partial \Delta\phi}{\partial t} \tag{I.9}$$

2.2.3. Simultaneous range and velocity estimates

Using a FMCW radar, one can get an estimate of both target's range and velocity at once. Indeed, the CW regime allows for measurement of the Doppler shift, while the modulation of frequency introduces time markers for measurement of the round trip, as illustrated in Figure I.2(b). As can be noticed, the round trip time Δt can be calculated by comparison of the times at which the reference and received signals show the same frequency. Then, the target's distance is the same as that of Equation (I.7), or calculated as

$$R = \frac{1}{2}\frac{c_0 |\Delta f|}{df/dt} \tag{I.10}$$

where Δf is the frequency difference due to the travel delay. For a linear dependency of frequency to time as in linear FMCW (LFMCW) radars, then $R \propto \Delta f$.

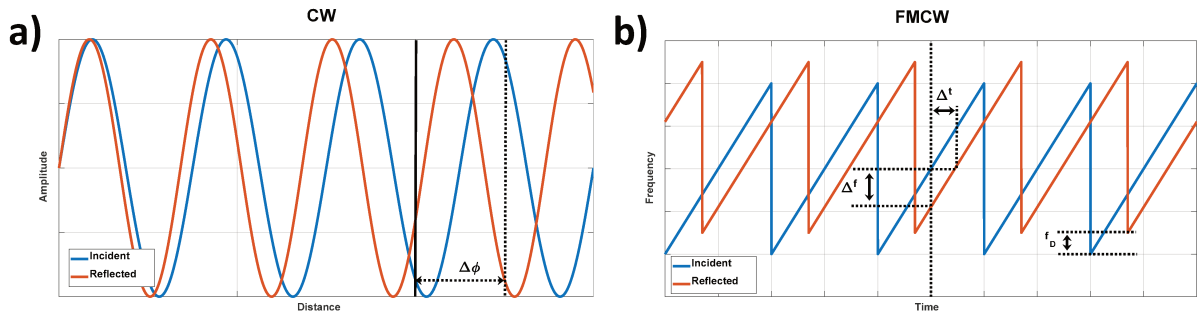

Figure I.2 : (a) Time-domain (blue) transmitted and (red) received signals from a CW radar, highlighting the measurement points for phase shift $\Delta\phi$. (b) Spectrogram of the (blue) transmitted and (red) received signals from a FMCW radar after backscattering onto a target, highlighting the measurement points for the shift in frequency Δf, the round trip time Δt and Doppler shift f_D.

2.2.4. Range-Doppler map and anti-clutter filter

Thanks to the simultaneous measurement of range and Doppler shift, a range-Doppler map can be plotted, as provided in Figure I.3. As can be noticed, power levels around the $v_s = 0$ km/h are high. In fact, these signatures are caused by all elements of the illuminated scene that are not moving, such as mountains, hills, trees, buildings… Therefore, they tend to hide the presence of low-velocity targets and must be removed not to hinder the tracking of slow targets. Doppler radar systems are thus natively equipped with an anti-clutter filter excluding all elements of low velocity, identified thanks to a moving target indicator (MTI) filter [1].

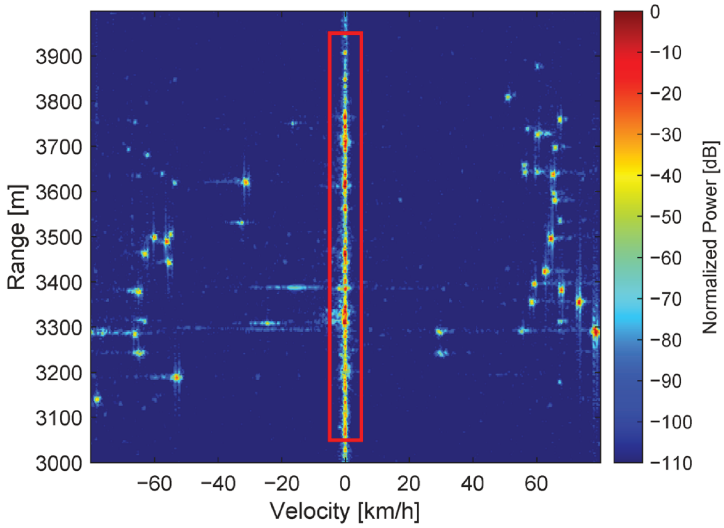

Figure I.3 : Typical range-Doppler map, with highlight of the clutter (red rectangle) to be filtered [9].

As detailed in Section 2, radar systems are used to detect a target and estimate its range, elevation, bearing, and velocity for tracking purposes. In particular, it was highlighted that a radar can be qualified by its maximum range, and that stealth mainly consists in reducing such range by minimizing RCS. Section 3 will review different strategies used for RCS reduction to improve aircrafts' stealth.

3. Seminal radar stealth solutions

Radar stealth is a broad term used to refer to the objective behind the camouflaging strategies designed to avoid detection. In an even broader definition, one may even include electronic warfare strategies under this umbrella term, encompassing other strategies such as the tampering of tracking algorithms, and the overall deception of radar systems. Therefore, radar stealth is multi-faceted, and a one-size-fits-all solution is impossible. In fact, modern radars push the stakes even further with multiple systems working in cooperation (early detection, pursuit…). Combining multiple solutions, each addressing a specific aspect of radar systems, therefore is an absolute necessity to benefit from the advantages of some where others fail.

Therefore, in this Section 3, I will address different strategies for radar stealth. I will first introduce the concept of shape effects for deflection of the reflected power and, then I will focus on radar absorbing materials (RAM) [10]. These RAM consist either in lossy non-resonant, or resonant solutions that provide impedance matching thus suppressing backscattering. However, traditional solutions are rather bulky over the VHF-UHF bands of interest. In the recent years, the development of metasurfaces, as planar structures of unnatural electromagnetic properties, brought interesting candidates to the ever-evolving challenges of stealth. In particular, they allowed for the necessary thickness reduction of modern low-frequency RAM. However, as will be highlighted, that can only be obtained by compromising bandwidth, which is counterproductive in stealth contexts. However, metasurfaces do have the other advantage of being highly compatible with electronic elements, which can offer the necessary features to overcome such physical limitations.

3.1. Radar stealth from shape effects

Based on the working principles of a radar system, the detection of a target can only occur if it backscatters enough power. Therefore, a solution might be to design the aircraft to only minimally reflect power in the incident direction, and favor deflection of power towards forsaken directions. For instance, this is the main thought process behind the design of the Northrop Grumman B-2 Spirit [11]. Its profiled shape, serrated apertures and sawtooth tails are all the results of this mitigation strategy [12].

Even though shape effects are particularly efficient for incident waves on large elements, such as the fuselage, such aircrafts can still suffer from their smallest elements, which may diffract incoming waves into many directions. In general, in stealth contexts, it is better to multiply camouflaging solutions, to improve even further overlapping contributions, and offer counter-strategies to vulnerable elements that one camouflaging solution might not cover.

Shape effects are interesting for dimensions that are large with respect to the radar's wavelength. Therefore, their interest plummets over VHF-UHF bands where wavelength can reach several meters. In these bands, it is particularly interesting to turn to RAM, to create reflectionless coatings.

3.2. Radar stealth from radar absorbing materials

Another solution to backscatter only minimal power towards the radar system is to coat the aircraft with RAM. In fact, dielectric – or magnetic – slabs, of carefully tailored electromagnetic properties can be used to perform absorption of the impinging wave. Resulting RAM are of mostly two natures: non-resonant or resonant [13]. While resonant RAM rely on the bandpass/stopband filtering offered by cavity effects, non-resonant RAM rely on power dissipation from lossy dielectric and/or magnetic structures.

3.2.1. Impedance/Admittance matching

All resonant and non-resonant RAM can be seen as impedance matching devices, *i.e.* they match the impedance of free space to that of a conductor using a lossy device, to render invisible the ground plane to radar waves [14]. Therefore, an equivalent circuit analysis (ECA) of the configuration is particularly appropriate, where dielectric and/or magnetic layers are modeled as transmission lines. Furthermore, given the configuration of having a dielectric slab on top of the conducting plane, as provided in Figure I.4, a derivation in terms of admittances is favored to one in terms of impedances, given the parallel circuits thereby formed. In Figure I.4, Γ is the reflection coefficient and T the transmission coefficient at the interface between free space and the dielectric slab.

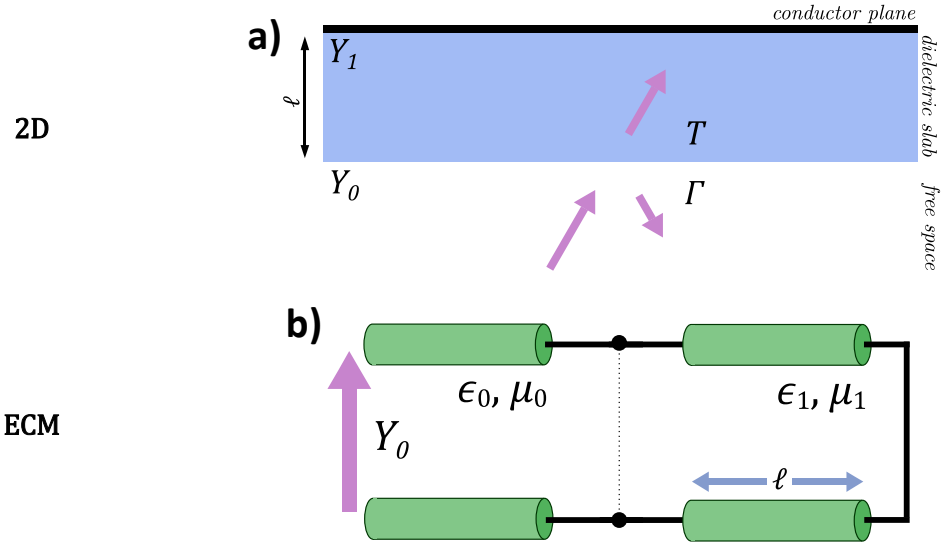

Figure I.4 : (a) 2D cross-sectional illustration of the dielectric slab interface with free space over a conductor plane and (b) associated equivalent circuit model.

In any case, any RAM must be carefully admittance-matched to the impinging wave for proper absorption. More specifically, at the interface between the incident, free space medium of admittance $Y_0 = \sqrt{\epsilon_0/\mu_0} = 1/120\pi = 2.65$ mS, and the RAM medium of admittance Y_1, as illustrated in Figure I.4, one must minimize the reflection coefficient Γ defined as

$$\Gamma = \frac{Y_0 - Y_1}{Y_0 + Y_1} \tag{I.11}$$

In such a case, admittance matching can only be granted by enforcing $Y_1 = Y_0$.

3.2.2. Non-resonant radar absorbing materials

A non-resonant RAM uses lossy dielectric or magnetic materials to dissipate the power of impinging waves. Therefore, they need to simultaneously allow the wave to penetrate the material, by proper admittance matching at the first interface, and absorb it, during a single round trip. However, granting both requirements at once is difficult, and some compromise must be found.

3.2.2.1. Impedance matching of non-resonant radar absorber materials

Non-resonant RAM generally use a lossy propagation medium to perform the absorption of the impinging wave, with an admittance Y_1 such that

$$Y_1 = \sqrt{\frac{\epsilon_1}{\mu_1}} \tag{I.12}$$

where ϵ_1 is the effective permittivity of the medium – accounting for conductivity as well – and μ_1 its permeability. The privileged approach is then to turn to an inhomogeneous slab allowing for admittance matching at the interface with free space as well as absorption of the penetrating wave [15]. Ideally, one would want to use a gradient of conductivity, as displayed in Figure I.5(a)-(b), gradually increasing losses for absorption of the penetrating wave – with minimal internal reflections thanks to a minimal mismatching of the successive, infinitely thin layers.

In practice, this gradient can be achieved geometrically, as is done for foam pyramids and cones used in anechoic chambers [16]. However, slabs with such a precise gradient are hard to fabricate, and one would rather turn to dielectric multilayers to create a discrete conductivity, permittivity or permeability gradient.

3.2.2.2. Magnetic and conductive composite radar absorbing materials

Non-resonant, composite RAM can be manufactured using layers with either conductive or magnetic inclusions, as illustrated in Figure I.5(c)-(d). Composite RAM using magnetic absorbers usually rely on ferrite or iron powders within an insulating layer [15]. This method allows for the fabrication of thin absorbers with relatively high absorption, though only minimal amounts can be used to avoid too heavy a RAM. However, magnetic inclusions-based solutions tend to lose their interesting magnetic properties at high frequencies (above 10 GHz), and still make up for rather thick screens at low frequencies (below 1 GHz) [17]. On the other hand, dielectric layers using conductive inclusions such as carbon-based or metallic elements make up for much lighter [18], though thicker solutions. They also have the advantage of working at higher frequencies, but are less wideband. Despite their drawbacks, these solutions have been used in specific applications, such as carbon black coatings [15], and are still used, such as magnetic paint coatings.

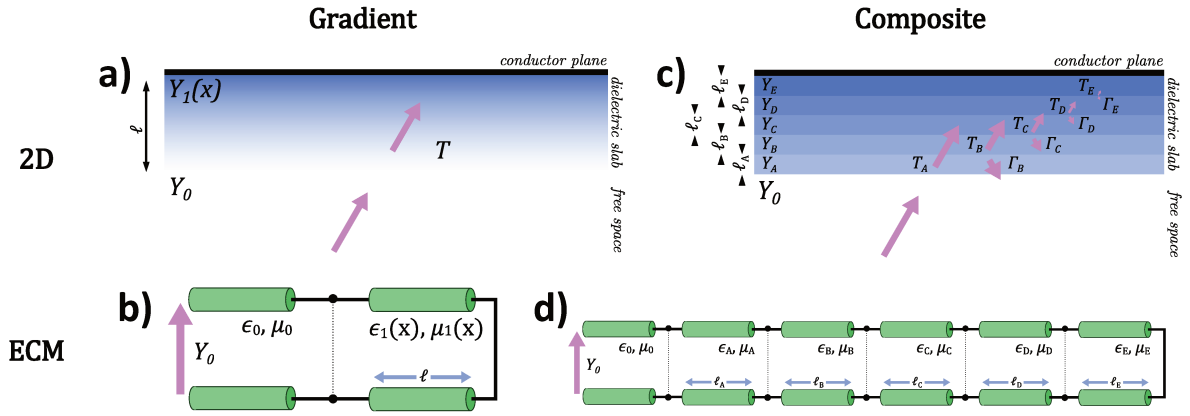

Figure I.5 : (a) 2D cross-sectional illustration of a radar absorbing material impedance-matched to free space using a gradient for gradual absorption and (b) associated equivalent circuit model. (c) 2D cross-sectional illustration of a radar absorbing conductive or magnetic composite material and (d) associated equivalent circuit model of the composite radar absorbing material.

3.2.2.3. Dallenbach screen

On the simpler end of the spectrum of non-resonant RAM, one may find the Dallenbach layer [19]. This solution is but an homogeneous magneto-dielectric slab of thickness ℓ above the ground plane, such as in Figure I.4. In such a case, admittance matching is granted under the condition that

$$-jY_1 \operatorname{cotan}\left(2\pi\ell\sqrt{\mu_1\epsilon_1}/\lambda\right) = Y_0 \tag{I.13}$$

the cotangent function of which leads to a dispersion of the admittance that renders broadband admittance matching hard to reach. Furthermore, because of the Kramers-Krönig relationship, both permittivity and permeability are tightly constrained [20]. Nonetheless, a variety of behaviors can be obtained, by either dielectric or magnetic materials, and thickness-tuning.

3.2.3. Resonant radar absorbing materials

While non-resonant RAM, act as lossy transmission lines, resonant RAM act as filters. They usually rely on lossless spacers and lossy screens to ensure the filtering function.

3.2.3.1. Salisbury screen

The Salisbury is the oldest and most emblematic example of a resonant RAM thanks to its simplicity [21]. In fact, a Salisbury screen is but a resistive screen, located $\ell = \lambda/4$ above the ground plane, separated by a dielectric slab, as illustrated in Figure I.6(a)-(b). The $\ell = \lambda/4$-thick dielectric is essential for the screen to be located at the zone of largest electric field and acts as an admittance inverter [22], turning the null admittance right upon the resistive screen into an infinite admittance at the conductor plane's location. Similar to Equation (I.13), admittance matching is then granted under the condition that

$$1/R_s - jY_1 \operatorname{cotan}\left(\sqrt{\epsilon_1\mu_1}\pi/2\right) = Y_0 \tag{I.14}$$

with R_s the resistance of the screen. Then, with air as a dielectric so that $Y_1 = Y_0$ and $\sqrt{\mu_1\epsilon_1} = 1$, a conductance $1/R_s = Y_0$ ensures admittance matching to free space and suppression of reflection. In the general case of a dielectric spacer, the resistive screen must be placed at $\ell = \lambda/4\sqrt{\epsilon_1\mu_1}$ to physically accommodate for the change in properties.

3.2.3.2. Jaumann screen

A Jaumann screen can be seen as a cascade of Salisbury screens, as illustrated in Figure I.6(c)-(d), harnessing multiple resonances in order to broaden the bandwidth of the RAM [23]. However, though $\ell = \lambda/4$ is a good initial value for the thickness of each slab, the design of an optimal Jaumann absorber requires a complex optimization of the different electromagnetic and geometric parameters [24], [25].

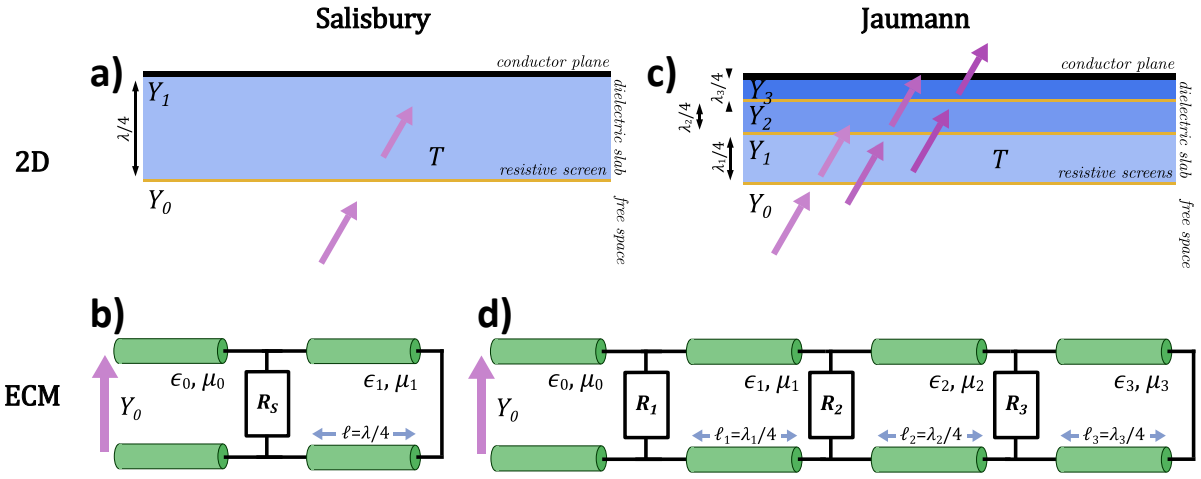

Figure I.6 : (a) 2D cross-sectional illustration of a Salisbury screen and (b) associated equivalent circuit model. (c) 2D cross-sectional illustration of a three-layered Jaumann screen and (d) associated equivalent circuit model. (e) 2D cross-sectional illustration of an arbitrary metasurface-based radar absorber and (f) associated equivalent circuit model.

3.2.3.3. Metasurface-based radar absorber

Pioneered in [26] at the turn of the millenium, metasurface-based radar absorbers (MBRA) were introduced as a solution to reduce the thickness of Salisbury screens. Thanks to their resonators, metasurfaces can be resistive and reactive all at once, and can thus compensate for the effects of reducing the distance to the conductor plane. In fact, before metasurfaces, the required behavior for such a thin absorber was predicted, *e.g.* as *circuit analog* arbitrary screens [27], or *capacitive sheets* [28]. The subsequently devised RAM were most often referred to as *Circuit Analog Absorbers* [29]. In any case, the general configuration of a MBRA, provided in Figure I.7(e-f), is a metasurface-based equivalent to the Salisbury screen, where the resistive screen is a metasurface of both resistive and reactive behavior.

As already introduced in Equation (I.13) and Equation (I.14), changing the dielectric spacer's thickness gives rise to new requirements for admittance matching. From the RAM configuration introduced in Figure I.7(a-b), it therefore appears the metasurface's admittance Y_{MS} must be carefully engineered in order to grant admittance matching such that

$$Y_{MS} - jY_1 \operatorname{cotan}\left(\sqrt{\epsilon_1\mu_1}2\pi\ell/\lambda\right) = Y_0 \qquad \text{(I.15)}$$

Then, a specifically designed metasurface of admittance Y_{MS} can offer admittance matching outside of the zero of the cotangent function. Moreover, the absorption bandwidth of MBRA can be broadened thanks to multiple neighboring absorption frequencies granted by blending multiple resonators. For instance, one may use concentric rings [30]. And metasurfaces can be used jointly with other RAM such as the Dallenbach screen [31].

MBRA thus represent hybrid solutions, drawing from both their resonant and non-resonant predecessors, whose strength relies on their design flexibility, thus minimizing the impact on other design constraints (mechanical, thermal, etc.).

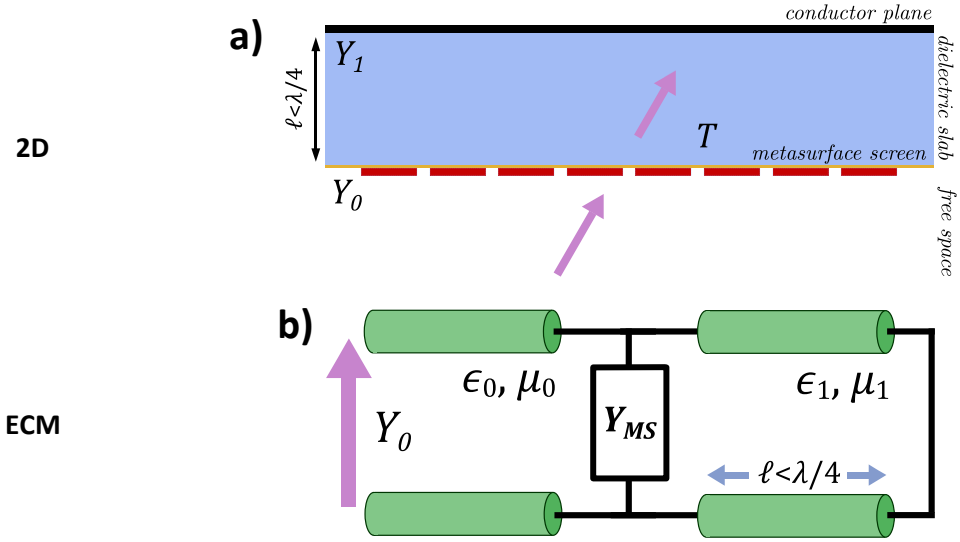

Figure I.7 : (a) 2D cross-sectional illustration of an arbitrary metasurface-based radar absorber and (b) associated equivalent circuit model.

3.2.4. Bode-Fano and Rozanov bounds

As previously stated, all resonant and non-resonant RAM are none other than admittance matching circuits between free space and a ground plane. However, linear, passive and time-invariant admittance matching networks are constrained in terms of bandwidth by purely physical considerations. In fact, this fundamental bound can be expressed in a general manner as the *Bode-Fano bound* [32], for which closed forms of the bound are readily available for canonical loads.

In the radar context, one often turns instead to the *Rozanov bound* [33], to infer an unavoidable bandwidth-to-thickness trade-off for metal-backed structures, *i.e.* RAM.

3.2.4.1. Bode-Fano bound: impedance matching bandwidth of arbitrary loads

According to [32], [34], the bandwidth of an impedance matching network is necessarily finite, and can be devised for any given load. A description of the calculation of the Bod-Fano bound for any arbitrary load is extensively derived, and adopts, in the case of canonical loads closed forms. According to [22], the optimal reflection coefficient is a square-shaped curve in regards to ω, where $|\Gamma| = \Gamma_{min}$ over the desired bandwidth $\Delta\omega$ and $|\Gamma| = 1$ outside. The Bode-Fano bound expression for canonical loads is provided in Table I-2, where one may therefore notice that bandwidth $\Delta\omega$ and minimum reflection coefficient Γ_{min} are necessarily traded-off for a given load. So much so, that $\Gamma_{min} = 0$ can only be reached for $\Delta\omega = 0$, confirming that perfect admittance matching can only be granted at a single frequency.

Load	Bode-Fano bound
Parallel RC	$\int_0^\infty \ln\frac{1}{\lvert\Gamma(\omega)\rvert}d\omega < \Delta\omega \ln\frac{1}{\Gamma_{min}} < \frac{\pi}{RC}$
Series RC	$\int_0^\infty \frac{1}{\omega^2}\ln\frac{1}{\lvert\Gamma(\omega)\rvert}d\omega < \frac{1}{\Delta\omega}\ln\frac{1}{\Gamma_{min}} < \pi RC$
Parallel RL	$\int_0^\infty \frac{1}{\omega^2}\ln\frac{1}{\lvert\Gamma(\omega)\rvert}d\omega < \frac{1}{\Delta\omega}\ln\frac{1}{\Gamma_{min}} < \frac{\pi L}{R}$
Series RL	$\int_0^\infty \ln\frac{1}{\lvert\Gamma(\omega)\rvert}d\omega < \Delta\omega \ln\frac{1}{\Gamma_{min}} < \frac{\pi R}{L}$

Table I-2 : Bode-Fano bounds of typical series and parallel RC and RL circuits.

3.2.4.2. Rozanov bound: impedance matching bandwidth of metal-backed dielectrics

According to [33], by application of the Cauchy theorem to the reflection coefficient Γ over the axis of real wavelengths λ, one can get a similar expression to the Bode-Fano bound for the case of a metal-backed dielectric slab. This case is in fact closer to practical RAM configurations. Once again, for a target minimum magnitude Γ_{min} over the bandwidth $\Delta\lambda$, one gets to the general expression of the Rozanov bound as

$$|\ln\Gamma_{min}|\Delta\lambda < \left|\int_0^\infty \ln|\Gamma(\lambda)|\,d\lambda\right| \leq 2\pi^2\mu\ell \tag{I.16}$$

From this expression, one may notice that a magnetic RAM would always perform better than a non-magnetic one in terms of bandwidth. But as previously stated for multiple RAM solutions, magnetic elements are difficult to integrate. In the case of a single non-magnetic ($\mu = 1$) RAM, such as a Salisbury screen or a dielectric Dallenbach screen, the Rozanov bound can be simply expressed [33], [35] as

$$\frac{\Delta\lambda}{\ell} < \frac{16}{|\ln\Gamma_{min}|} \tag{I.17}$$

linking bandwidth $\Delta\lambda$, minimum reflectance Γ_{min} and thickness ℓ, thereby introducing a bandwidth-to-thickness ratio limitation. To better illustrate this relationship, Figure I.8 provides the Rozanov bound of a non-magnetic, single-layered dielectric as a function of the target minimal reflection coefficient Γ_{min} over the target bandwidth $\Delta\lambda$.

In Figure I.8, one may notice that for low values of Γ_{min}, the bandwidth-to-thickness ratio $\Delta\lambda/\ell$ is also low, meaning that very thick RAM layers are required to obtain a large bandwidth. In other words, the Rozanov bound can be translated as: a RAM cannot be thin and broadband simultaneously. One may notice that in terms of frequency, the Rozanov bound can be expressed as

$$\Delta f = c_0\frac{\Delta\lambda}{\lambda_{max}\lambda_{min}} \leq \Delta\lambda_{RBF} f_{max} f_{min} \tag{I.18}$$

hinting that frequency bandwidth decreases with absolute frequency.

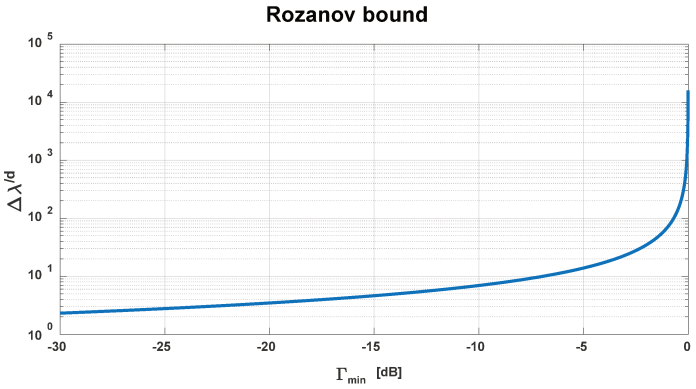

Figure I.8 : Rozanov bound $\Delta\lambda/d$ of a non-magnetic, single-layered dielectric slab as a function of the minimum target reflection coefficient Γ_{min}.

The important takeaway here is that the Rozanov bound proves the existence of a bandwidth limit and gives a value of it, but it does not guarantee it can be reached, nor how. In fact, Fabrice Boust (former research engineer at ONERA) took to classifying different RAM in [36]. Using figures of merit in regards to Rozanov bound (as done in [37]), he compared the bandwidth of both broadband (BFM) and narrowband (RFM) absorbers from the literature, highlighting in Figure I.9 that few MBRA actually perform better than optimized Salisbury RAM. MBRA offer more flexibility than previous concepts but do not guarantee a better performance.

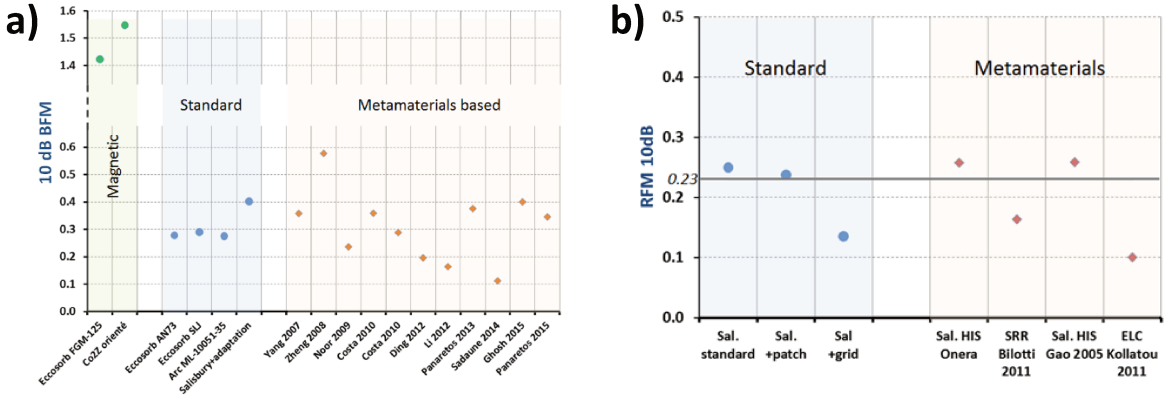

Figure I.9 : Figures of merit of the bandwidth of (a) broadband and (b) narrowband absorbers for comparison of magnetic, Salisbury and metasurface-based passive radar absorbers from selected articles from 2005 to 2015 [36].

3.2.4.3. Bode-Fano and Rozanov bounds equivalence

The Bode-Fano and Rozanov bounds are actually two expressions of the same problem: the maximum allowable bandwidth of an impedance/admittance matching network. In fact, in [33], Rozanov confirms that Equation (I.17) is only a λ-dependent expression to the ω-dependent equivalent from [32]. One may therefore refer to this fundamental limitation in the following as the RBF (Rozanov-Bode-Fano) bound.

However, the RBF bound is defined here for normal incidence. In fact, according to [38], absorption from a linear, passive, time-invariant RAM can be derived from Fano's method from [32] to a generalization of the RBF bound for oblique TE and TM waves. From the ground work of [38], reference [39] extends the application case to multiple oblique incidences and proposes a

tightness investigation to the maximum bound in order to design a corresponding Dallenbach screen.

In Section 3.2, different RAM configurations are presented as a solution to reduce the RCS of a target in order to avoid detection, thereby decreasing the operating range of surveillance radars. However, though one may resort to optimizations, these classical solutions usually remain suboptimal when compared to their RBF bound. Even MBRA, though at equal height, they offer more bandwidth. Furthermore, metasurfaces are highly flexible solutions. So much so that, in Section 4, a review of metasurface-based solutions is proposed. This is done to better pinpoint the current limitations faced by passive MBRA and their subsequent undisputable advantages over traditional solutions when rendered active, thereby breaking the RBF application field.

4. Review of metasurface-based radar stealth solutions

As previously highlighted, metasurface-based solutions are particularly interesting for their versatility. In fact, the development of metamaterials and their 2D counterparts, *metasurfaces*, have recently shown the possibility of conceiving any admittance on demand [40], [41]. Using a regular array of resonators, one may design a variety of admittance functions, paving the way for the renewal of stealth technologies [42]. It is interesting to note some metasurfaces may also exhibit heterogeneous and/or locally uniform distributions of resonators, for wavefront manipulation and holographic purposes for instance [41].

In Section 4, after a review of some MBRA by design, I will then focus on electronics-loaded MBRA. The interest of using lumped elements is that they are insensitive to the impinging frequency. They can thus be used to provide the necessary behavior for admittance matching from a relatively easy design process, on top of alleviating the constraints and sensitivity of equivalent elements. Besides, the active nature of some electronic elements can be harnessed to break the RBF bound for broadband absorption. Then, in Section 4.2, I will present some more recent work on radar deceiving strategies enabled by the continuous control in time of active metasurfaces.

4.1. Review of metasurface-based radar absorbers

On the one hand, the main issue with Salisbury screens and, to a lesser extent with Dallenbach layers, is their thickness over the low VHF-UHF range of interest. For instance, for a wavelength of $\lambda = 1$ m, an admittance inverter is $\ell = \lambda/4 = 25$ cm thick.

On the other hand, even though MBRA were erected as a breakthrough solution, as for any passive RAM they are limited in bandwidth by the RBF bound. Nonetheless, at equal distance to the conductor plane, MBRA can still show a broader bandwidth than Salisbury screens, as illustrated in Figure I.10. In fact, it can be noticed that for the same thickness $\ell = 25$ cm, where a Salisbury screen only reaches 49% of the RBF bandwidth ($\Delta\lambda_{RBF} = 1.74$ m), this MBRA reaches 60 % of it. While not all MBRA do reach such interesting bandwidths, choosing the proper design method is crucial to inch closer to the RBF bound [43], [44].

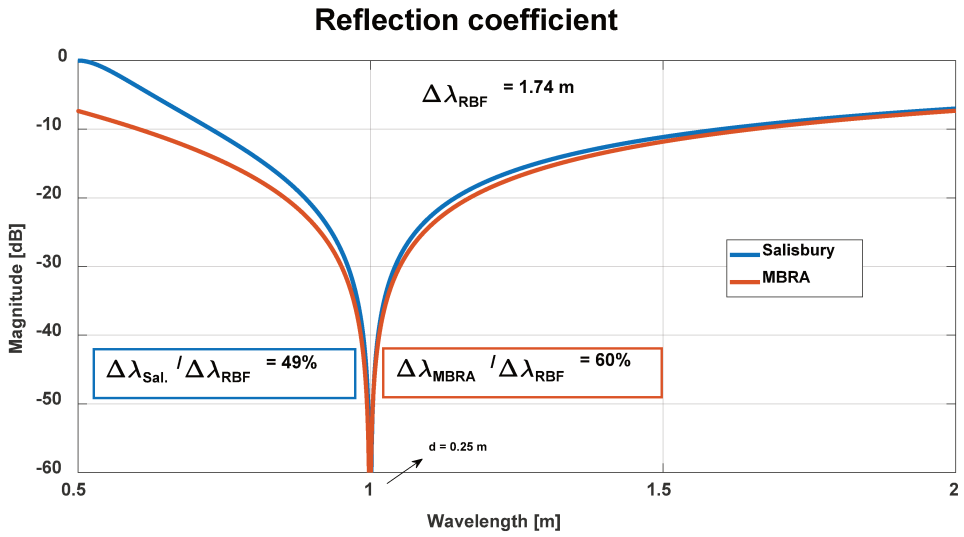

Figure I.10 : Magnitude of the reflection coefficient of a (blue) Salisbury screen and (red) metasurface-based radar absorber for absorption at $\lambda = 1$ m, with value of the RBF bound $\Delta\lambda_{RBF}$ for a $d = 25$ cm RAM, and wavelength bandwidth ratios offered by the Salisbury screen (blue box) and metasurface-based radar absorber (red box).

4.1.1. Metasurface-based radar absorber *by design*

From Equation (I-1), one may notice the resistive elements ensuring proper absorption can be bestowed upon either the metasurface or the dielectric spacer. Therefore, many practical designs can be considered, from non-resonant to resonant, through many hybrid iterations.

For instance, using lossy dielectrics can lead to the results of [45], [46] (Figure I.11(a)), while using air as a spacer can lead to the results of [47]. A particularly outstanding example of an hybrid design is [48] (Figure I.11(b)), which combines the periodicity of metasurfaces with pyramidal dielectrics to reach ultra-wideband. Then, similarly to Salisbury screens, screen-based MBRA rely on the bandstop filter-like behavior of the metasurface to absorb impinging power [49]. This method is widely used, and the printed circuit board (PCB) technology is particularly suitable to manufacture the necessary metasurfaces, ensuring thin device and design flexibility.

However, there is a lack of universal guidelines for the design of MBRA, [50] does provide some guidelines for different thin perfectly absorbing layers, while insisting on the difficulties to reach, all at once, strong absorption, wideband coverage, incidence or polarization insensitivity… Furthermore, going from the desired electromagnetic properties to feasible structures is not always a straightforward process [51], [52], [53]. The design of metasurfaces generally relies on a shortlist of successful patterns and subsequent optimization processes. Recently, artificial intelligence has also been harnessed for this task [54]. In fact, technical constraints and requirements generally enforce different design strategies to reach high absorption [55] (Figure I.11(c)), polarization independency [56], [57] (Figure I.11(d)), wide incidence angle [58], [59], etc.

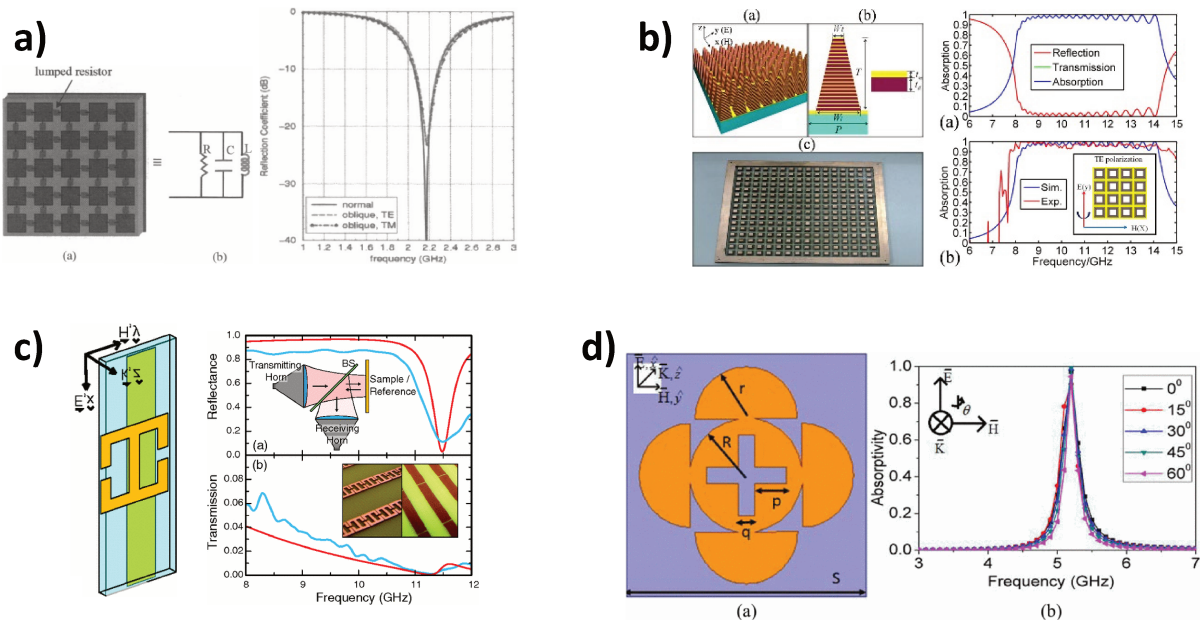

Figure I.11 : (a) Metasurface design, equivalent circuit model and magnitude of the reflection coefficient highlighting simulated absorption at 2.2 GHz below -20 dB for different polarizations [45]. (b) Illustration, photograph and reflection/absorption plots of the periodic array of quadrangular pyramid for measured absorption above 90% over [7.8, 14.7] GHz under TE illumination [48]. (c) Electric split ring and cut wire forming the meta-atom of a metasurface of near perfect measured absorption at 11.5 GHz [55] (d) Metasurface and absorption curve highlighting absorption above 93% at 5.1 GHz from 0° to 60° [57].

4.1.2. Passive-electronic-loaded metasurface based radar absorber

Metasurfaces are particularly suited for the integration of electronic lumped elements thanks to their reliance on PCB technology. The advantage of using lumped elements, instead of equivalent elements, is that their behavior is independent of the wavelength considered due to their deeply subwavelength size, and are readily available off the shelf. In the case of RAM, loading passive lumped elements onto the metasurface of a MBRA helps reach the target absorption and designated absorption frequency – within physical constraints such as the RBF bound. For instance, the reactive metasurfaces of [29], [60] (Figure I.12(a)-(b)) require proper resistive elements to reach admittance matching. Lumped capacitors may also be used, but thanks to the PCB technology, capacitive behavior can be added as capacitive traces, largely used in metagrating-based absorbers [61], [37] (Figure I.12(c)).

The use of lumped elements is also highly compatible with the equivalent circuit analysis used for the design and analysis as metasurfaces. In fact, seen as a discontinuity in the propagation channel of interest, any metasurface pattern can be analyzed using an ECA [62]. Canonical metasurface shapes (rings, slots, patches…) can adopt closed forms [63], [64], but any arbitrary shape's behavior can still be well-approximated. For instance, the modal approach of [65] (Figure I.12(d)) can be used, but because of complex modelling of the metasurface's behavior, it may induce some errors [66]. In any case, using the resulting ECM as a base, one may proceed to the loading of lumped elements, either from a first-order evaluation of the resulting ECM, or through a more tedious and careful integration [67], [68].

By this development stage, MBRA still act as passive RAM, and therefore fall within the application field of the RBF bound, limiting their bandwidth-to-thickness ratio. However, the loading of active elements, on top of offering new functionalities, breaks the RBF ceiling.

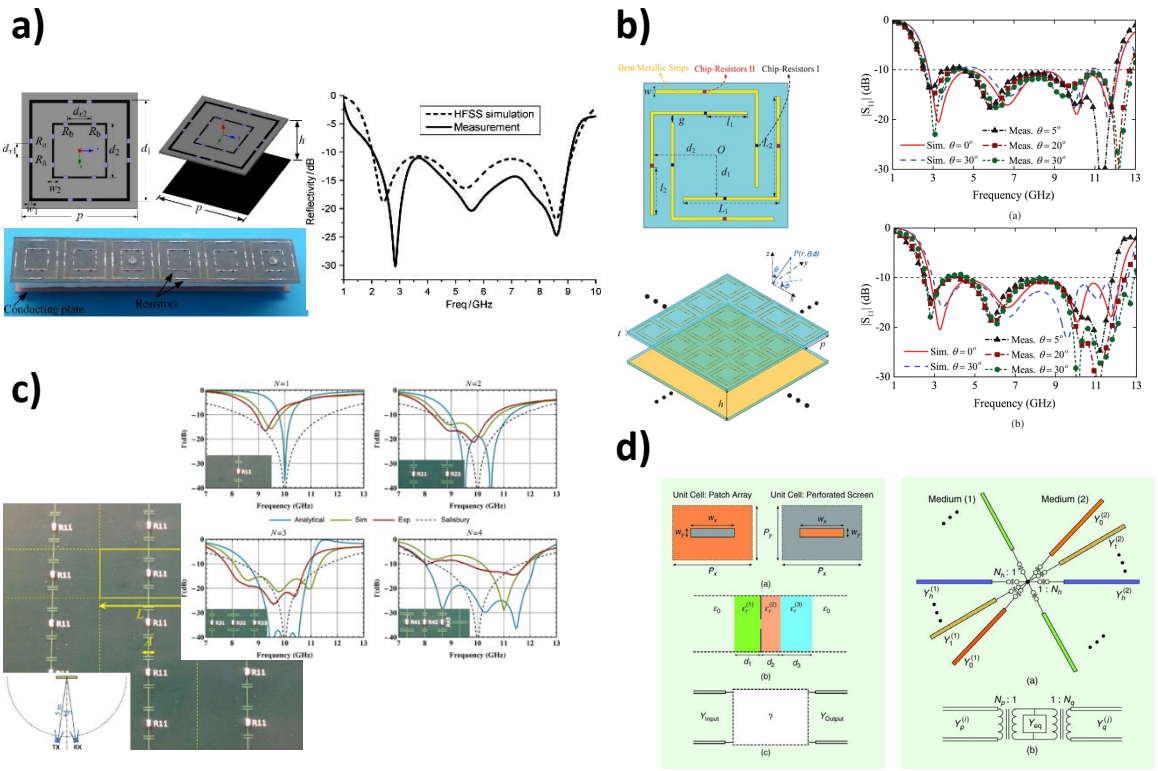

Figure I.12 : (a) Double-square loop metasurface (*circuit analog absorber*) illustration and photograph with highlight of the loaded lumped resistors and associated simulated and measured reflection coefficient for absorption below -10 dB over [2, 9] GHz [29]. (b) Resistor-loaded meta-atom and metasurface and associated measured reflection coefficient below -10 dB over around [3, 13] GHz for incidences from 0° to 30° [60]. (c) Photograph of a metagrating-based absorber (bottom left) and reflection coefficient magnitude (top right) for different topologies [37]. (d) Modelling of the metasurface as a discontinuity in the propagation channel and model expansion illustration [65].

4.1.3. Active-electronic-loaded metasurface-based radar absorber

As previously introduced, the careful design and use of passive electronic elements can offer some optimized MBRA. However, they still are constrained by the RBF bound and more bandwidth must necessarily break free from the *linear, passive and time-invariant* framework. The loading of active lumped elements onto MBRA is a relatively easy solution to that. They can thus reach bandwidth beyond the RBF bound, and may even be granted reconfigurability mechanisms.

4.1.3.1. Metasurface-based radar absorber using non-Foster elements

There exists a previously investigated solution for a thin, wider-than-RBF MBRA: non-Foster circuits. Indeed, taking a look back at Equation (I.15) for a thin RAM, *i.e.* $\ell \ll \lambda$, the imaginary part of the admittance matching condition is given by

$$Im(Y_{MS}) = -\frac{1}{\omega L_{SC}} \tag{I.19}$$

with $L_{SC} = Y_1 c_0 / \ell n_1$. This requires a metasurface that does not respect Foster's reactance theorem [69] : a passive electronic element's reactance is monotonically varying with frequency. In order to create the negative impedance highlighted in Equation (I.19), one must therefore rely on negative impedance converters (NIC) [70] or negative impedance inverters (NII) [71] to create

non-Foster elements. Many researchers have investigated non-Foster MBRA [72], [73], [74], [75] (Figure I.13(a)). However, non-Foster circuits work close to the stability threshold, and are therefore notorious for having stability issues, unwillingly introduced from slight imperfections in the feedback loop. To illustrate the potentially infinite bandwidth offered by a non-Foster metasurface, Figure I.14(a) provides the reflection coefficient's curves from suboptimal solutions where $Im(Y_{MS}) = -1/\omega L_{NF}$ where L_{NF} is a portion of L_{SC}.

Therefore, despite the tremendous advantages of non-Foster admittance matching of MBRA, bandwidth is usually sacrificed in favor of simpler, unconditionally stable circuits. In fact, active electronic elements can still grant an *effective* bandwidth beyond RBF bound through reconfigurability.

4.1.3.2. Reconfigurable metasurface-based radar absorber

Among the so-called *reconfigurable* MBRA, two classes can be defined: switchable MBRA, whose entire behavior can be changed between two or more states, which may not all be absorbing ; and tunable MBRA, whose absorbing behavior can be continuously adapted to the operator's needs. Diodes and transistors oftentimes offer such reconfigurable mechanisms, where biasing voltage or current are the command signals.

On the one hand, switchable metasurfaces are often used to switch between two fundamental states: reflection and absorption [76], [77], [78]. In such cases, PIN diodes are used as variable resistors. Though they are usually highly sensitive to biasing current, they are used in their ON or OFF states – hence the two-state switch –, but proper integration and fine control of current can extend their application to a tri-state metasurface-based device [79] (Figure I.13(b)).

On the other hand, tunable metasurfaces are often used to control absorption, both in frequency and magnitude. With a fine control of PIN diodes, one can continuously tune through multiple reflection coefficient's magnitudes, from reflection to absorption, as in [80]. However, the most widely used feature is the change in absorption frequency enabled by the use of varactor diodes, as in [81], [82], [83] (Figure I.13(c)).

Finally, a special category within reconfigurable MBRA can be called *intelligent*: relying on a variety of sensors and feedback loops to drive the behavior of the MBRA according to its environment. Depending on the function, it can be seen as a closed loop version of either a switchable or tunable metasurface. This makes for an autonomous system, integrating a MCU or FPGA, for software-based continuous, or rapid, reconfiguration [84] (Figure I.13(d)). In a (partially) open loop configuration, it can still offer the operator some control, such as a change of regime [85].

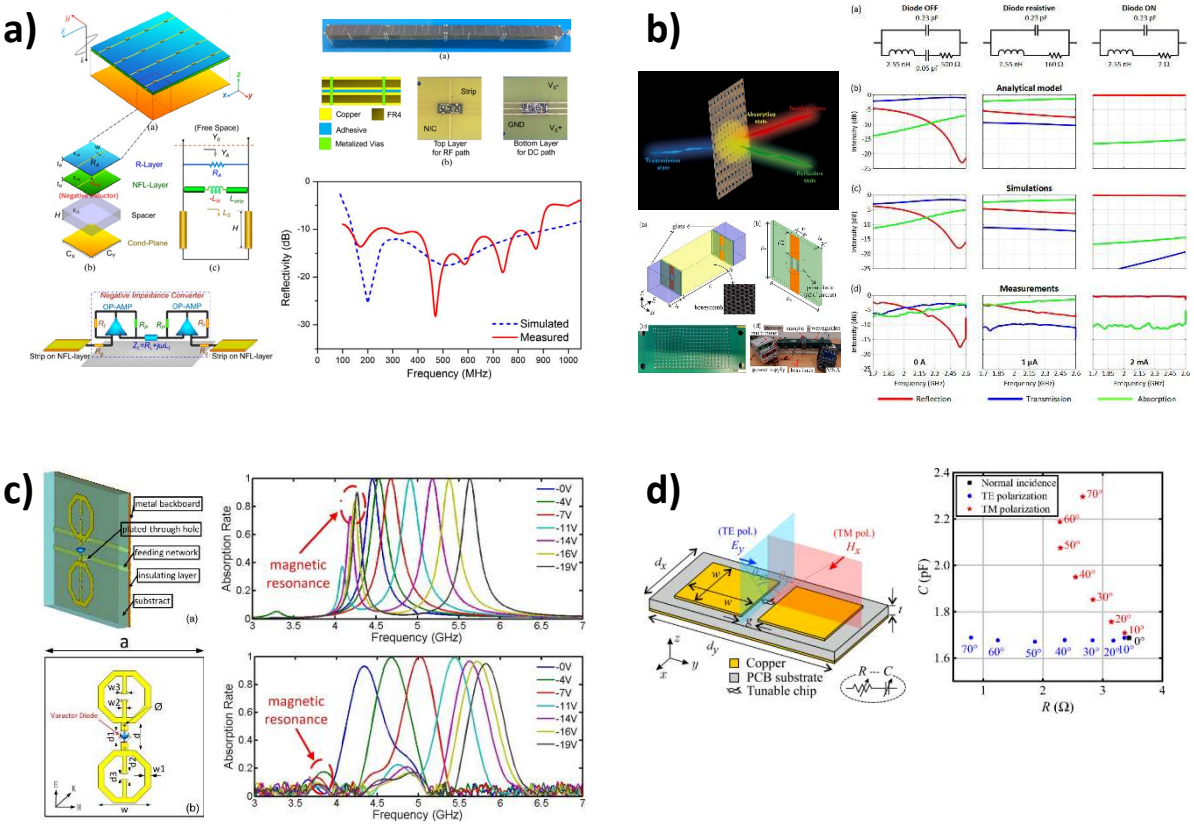

Figure I.13 : (a) Illustration of the non-Foster meta-atom absorber (top left), with topology of the considered NIC (bottom left), photograph of the prototype (top right) and resulting simulated and measured reflection coefficient (bottom right) of magnitude below -10 dB over [150, 900] MHz [74]. (b) Principle illustration (top left), metasurface-base screen with highlight of the PIN diodes (bottom left) and resulting reflection, transmission and absorption states (right) [79]. (c) Meta-atom illustrations with highlight of the varactor diodes for tunability of the absorption frequency confirmed by simulations (top right) and experimental (bottom right) results for an effective bandwidth of 1.5 GHz around 5.1 GHz for absorption above 90% [81]. (d) Capacitance- and resistance-tunable meta-atom and corresponding combinations for perfect absorption (around -60 dB) under TE and TM illumination for incidence angles from 0° to 70° [84].

In the reconfigurable case, one may argue that such an actively tunable MBRA is not exactly going beyond the RBF bound. However, one may distinguish between *instantaneous* bandwidth, which is obtained at each individual state of the tunable range, and *effective* bandwidth, which is the maximum bandwidth offered by combination of all of these states, which may very well exceed the RBF bound. To better highlight the gain in bandwidth, Figure I.14(b) provides the reflection coefficient's curves from a tunable system.

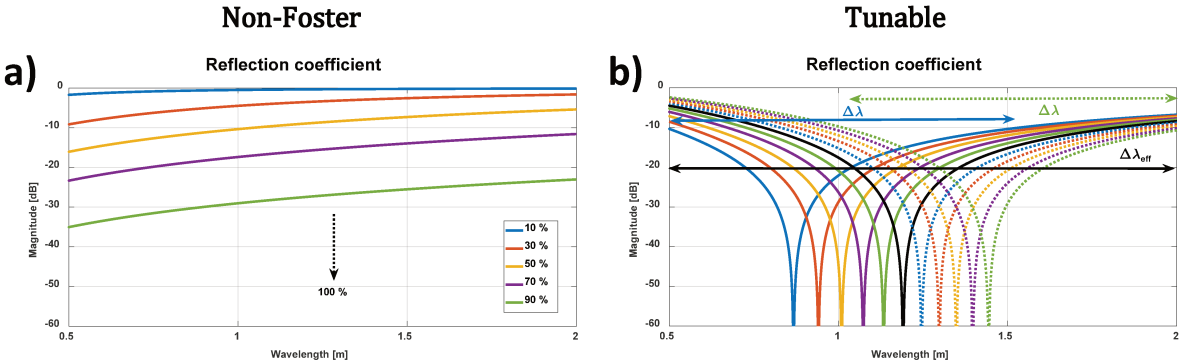

Figure I.14 : (a) Reflection coefficient from a non-Foster metasurface-based radar absorber of suboptimal target inductance to better illustrate the wideband absorption of a perfect system. (b) Reflection coefficient from frequency-tunable metasurface-based radar absorber, highlighting wideband effective bandwidth.

In Section 4.1, MBRA solutions have been extensively reviewed. Using the admittance matching condition as the design basis, purely geometrical metasurface-based screens can be devised in order to bridge the gap between electric and magnetic screens, thereby effectively reducing the distance to the ground plane. The flexibility of metasurfaces does allow for the compensation of the inductive effects arising from low-profiled RAM without compromising the bandwidth. Thanks to their PCB practical implementation, MBRA are especially prone to be used jointly with lumped electronic elements. In particular, the use of active elements leads to an entire new class of MBRA, no longer constrained by the RBF bound. However, once again, no exact guidelines exist to make the most of this lack of bound. Two main avenues of investigation can be distinguished. The use of active elements was previously pointed out to break the *passive* criterion of the RBF bound. Non-Foster elements do grant the desired wideband absorption, but are limited in terms of feasibility, where reconfigurable elements offer a finite effective broadband with simpler implementations. On top of no longer *passive*, the use of active elements can offer the option to free oneself from the *time-invariant* condition of the RAM. The RBF bound could therefore be exceeded without the need for non-Foster elements. Section 4.2 will therefore review some effects of time-modulation, with an intodcution on modulated transmission lines, before turning to metasurface-based structures in order to highlight how it can be harnessed for stealth.

4.2. Review of time-controlled active metasurface-based radar stealth solutions

Research on time-modulated devices started in the 1950's with seminal papers based on the modulation of the propagation medium's electromagnetic properties [86], [87], [88]. Recently, time-modulation has turned into an active field of research [89], [90], [91], [92]. Some more information on time-varying propagation media can be found in Appendix 0.

Many concepts have been put forward, where the sudden change of a medium's properties (ϵ and μ) can grant absorption beyond the RBF bound [93], [94], [95], or be harnessed as a temporal equivalent of an admittance inverter [96]. However, Section 4.2 will focus on time-controlled metasurface-based solutions, which is still allowing for low-profile solutions, where previously introduced concepts have no physical structures yet for experimental validation.

The modulation of metasurfaces through their electronic components is a very simple process, given many basic electronic elements such as diodes can be addressed with AC signals, or at least varying DC signals – though they might exhibit a cut-off frequency. In Section 4.2.1, I

will first introduce an extension of the RAM concept, where the reconfigurable nature of the active MBRA can be continuously changed, adding a temporal dimension to the system. In Section 4.2.3 and Section 4.2.3, I will then introduce concepts beyond the RAM realm, where time-modulation of metasurfaces can exploit key elements of the wave itself (direction of propagation, frequency, amplitude…) or elements of the radar processing chain (Doppler measurement, pulse compression…) in order to deceive radars.

In the works introduced in the following, though not always specified, the times considered for the variation of the structure's properties are much slower than the incident signal's period. In fact, this two-time segregation is a fundamental relationship for the proper time-modulation of devices: *the input [must interact] with the system that is modulated slowly enough such that it can be practically treated as static at all moments of time* [89]. For instance, this feature enables the spectral manipulation of the incident signal upon reflection, and can therefore lead to the many applications detailed in the following.

4.2.1. Time-varying metasurface-based radar stealth solutions

In [97], the proposed absorber, though not exactly a metasurface, can be included in the intelligent RAM category. It adapts in real-time to impinging frequencies thanks to a partially transmitting screen behind which a sensor estimates the incident frequency and sends commands to the reconfigurable screen to match said frequency. When done in an open loop, the absorption is the typical Salisbury resonant filtering response, but working in closed loop, where the source is sweeping the frequency range on interest, brings a wideband absorption. In fact, this resulting absorption is but an overlap of discrete absorption states from a continuously tuned absorber. The two-time segregation here is found in the fast and slow times of the radar operating system. For instance, the analysis of the incident wave can only be performed after a first illumination (fast time) to adapt to the following waveforms (slow time).

4.2.2. Time-switched metasurface-based radar stealth solutions

Time-switched metasurfaces include all devices whose behavior is rapidly switched between two or more states. For instance, the time-domain coding of metasurfaces is a recent development of metasurface-based structures. By referring to the metasurface's states as bits, devised either as a space- or time-based pattern, one can devise a space-time (multi-leveled) checkerboard screen. These states may be offered by PIN or varactor diodes depending on the preferred architecture. Though not all work reviewed here is explicitly designed for radar stealth applications, their results may very well be applicable. For instance, [98] introduced means of RCS reduction thanks to space-modulation to create diffraction patterns, similarly as the forsaken directions from shape effects. In fact, this concept is also proposed in [99], [100], [101], with an additional frequency shift from periodic phase modulations.

The rapid switching of a metasurface's states, also lead to another strategy called *spread spectrum* [102], [103], [104]. Using a pseudorandom modulation of the loaded PIN diodes, the power of the incident signal is spread over a wide frequency range upon reflection, in order to reach sub-noise SNR levels, thereby not triggering detection. The distortion of the backscattered signal does also compromise radar pulse compression.

4.2.3. Time-modulated metasurface-based radar stealth solutions

While in the previous section the modulation is done over discrete states, hence their *coding* character, this section focuses on continuous change of the metasurface-based structure. For instance, this gave rise to the *Doppler cloaking* strategy [105], [106], [107], [108], [109]. Using a time-modulation of the metasurface-based screen offers frequency conversion of the impinging

wave upon reflection, in order to compensate the Doppler shift induced by the target's movement and appear as a mere element of the static scene. In fact, one may notice this modulation is the continuous equivalent to the discrete 2-bit modulation of [101].

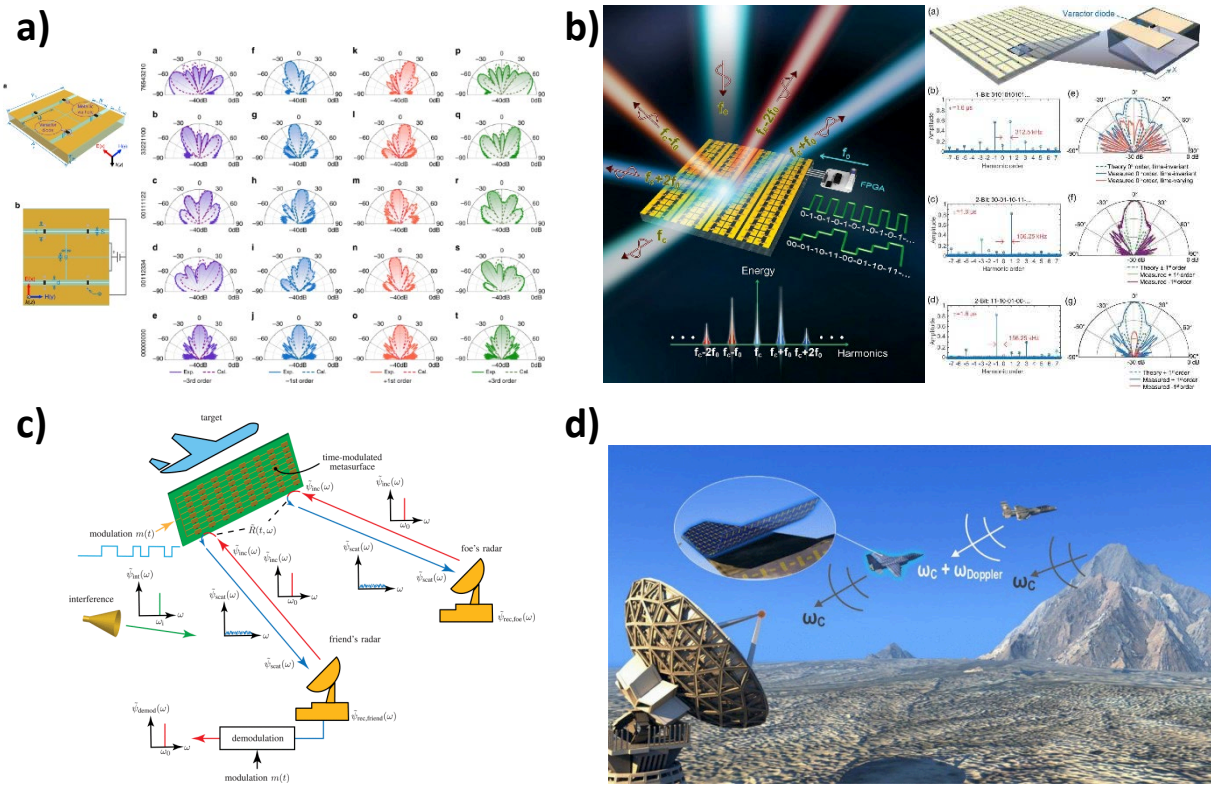

Figure I.15 : (a) (left) Illustration of the varactor-loaded meta-atom and (right) simulated and measured radiation patterns for diffraction orders -3, -1, +1, +3 [100]**.** (b) (left) Illustration of the concept and (right) illustration of the varactor-loaded metasurface and associated measured frequency shifting and radiation patterns [101]**.** (c) Illustration of the spread-spectrum strategy [102]. (d) Illustration of the Doppler cloaking strategy [107].

5. Conclusions

In this Chapter I, I have introduced in Section 2 the working principle of surveillance radar systems: should the received power exceed a SNR threshold value, then detection is triggered. However, the power backscattered by a target is dependent on its signature, defined as its RCS, the reduction of which reduces radar range. Detection avoidance therefore prompted the development of RCS-reducing strategies. But a radar system is not only a sensing unit, it can also be used as a target's parameters estimator, where range and velocity are two crucial elements not to disclose to adversary systems.

As detailed in Section 3.2, on top of body shaping, a number of non-resonant or resonant structures can be used to avoid detection. The carefully chosen lossy elements of Dallenbach layers, and the geometry of Salisbury screens, offer the necessary admittance matching and power dissipating or filtering functions to be used as coatings to face radar illuminations. However, both families of solutions, as *linear, passive and time-invariant* admittance matching networks, suffer from a fundamental bandwidth-to-thickness ratio known as the RBF bound. This bound states that such an electromagnetic absorber cannot be thin and wideband simultaneously, and compromises are inevitable. This limitation is especially damaging over the low-frequency ranges of long-distance, early warning surveillance radars, where their classical designs are necessarily bulky. Erected as the ideal solution to thickness reduction, metasurfaces showed promising results to low-profile equivalents to resonant solutions. In fact, to equivalent height, they can exhibit broader bandwidth compared to their Salisbury screen counterpart. However, they still fall in the RBF application field and therefore still remain constrained in bandwidth by their thickness.

However, the PCB technology used for the manufacture of metasurface is readily compatible with electronic element loading. And this one feature may offer solutions to escaping the applicability perimeter of the RBF bound. On top of simplifying designs, some of these lumped electronic elements can be harnessed for their active nature, thereby breaking the *passive* criterion of the RBF bound. In the case of interest here, active MBRA can thus be manufactured. Though non-Foster active circuits are a particularly interesting solution to broadband absorption, their unstable nature has hindered their development and led research to simpler designs, such as frequency-tunable MBRA. For instance, varactor diodes act as resonance frequency shifters for the filter-like behavior of resonant MBRA, whose effective bandwidth does go beyond the RBF bound of their passive equivalents.

The use of active elements then led to an entirely new paradigm for metasurface-based solutions to stealth, breaking the *time-invariant* clause of the RBF bound. It can be used to broaden the use cases of reconfigurable MBRA, to offer similar solutions to shape effects or to modify the the backscattered wave's spectrum. In particular, energy can be spread in frequency for sub-noise SNR levels, and a moving target's Doppler shift can be compensated by frequency conversion upon reflection, thereby broadening the horizon of radar deceiving techniques.

II. Development and experimental validation of a frequency-tunable metasurface-based radar absorber over the VHF-UHF bands

CONTENTS

II. DEVELOPMENT AND EXPERIMENTAL VALIDATION OF A FREQUENCY-TUNABLE METASURFACE-BASED RADAR ABSORBER OVER THE VHF-UHF BANDS 51

1. INTRODUCTION 52
2. VHF-UHF COAXIAL METASURFACE 53
   2.1. Cartesian-to-polar coordinate mapping 53
   2.2. Cartesian-to-polar one-dimensional metasurface equivalents 54
   2.3. Metasurface of interest 55
3. DEVELOPMENT AND EXPERIMENTAL VALIDATION OF A METASURFACE-BASED RADAR ABSORBER OVER THE VHF-UHF BANDS 56
   3.1. Equivalent circuit analysis an impedance matching metasurface for a radar absorber 56
   3.2. Design of an impedance matching metasurface 58
   3.3. Analytical and numerical studies of the metasurface-based radar absorber using the equivalent circuit model, a 2D axisymmetric FEM model and a 3D FEM model 60
      3.3.1. ECM and 2D axisymmetric FEM simulations of the metasurface-based radar absorber 60
      3.3.2. ECM and 3D FEM simulations in a rotation-invariant configuration of the metasurface-based radar absorber 61
      3.3.3. ECM and 3D FEM simulations of the actual geometry of the metasurface-based radar absorber 63
   3.4. Experimental validation of a metasurface-based radar absorber 65
      3.4.1. Experimental setup for the frequency-domain measurement of the metasurface-based radar absorber 65
         3.4.1.1. Calibration process 66
      3.4.2. Measurement of the metasurface-based radar absorber 66
4. DEVELOPMENT AND EXPERIMENTAL VALIDATION OF A FREQUENCY-TUNABLE METASURFACE-BASED RADAR ABSORBER OVER THE VHF-UHF BANDS 67
   4.1. Frequency-tunability using varactor diodes 67
   4.2. ECM and 3D FEM simulations of the frequency-tunable metasurface-based radar absorber 68
   4.3. Experimental validation of the frequency-tunable metasurface-based radar absorber 70
      4.3.1. Experimental setup for the frequency-domain measurement of the metasurface-based frequency-tunable radar absorber 70
      4.3.2. Measurement of the metasurface-based frequency-tunable radar absorber 70
5. NUMERICAL AND EXPERIMENTAL INVESTIGATIONS INTO A FREQUENCY-TUNABLE METASURFACE-BASED RADAR ABSORBER OF NEAR-PERFECT ABSORPTION AND TIME-BASED WIDEBAND COVERAGE 73
   5.1. Numerical investigation into a near-perfect metasurface-based radar absorber using a joint tuning of capacitance and resistance 73
      5.1.1. Equivalent circuit study of optimal resistance values 74
      5.1.2. Quick 3D FEM optimization of optimal resistance values 75
   5.2. Experimental investigation into an effectively wideband metasurface-based radar absorber thanks to a temporal control of biasing voltage against a frequency-hopping radar 77
      5.2.1. Ideal absorption profile 77
      5.2.2. Experimental validation of the temporally-controlled frequency-tuned metasurface-based radar absorber 78
6. CONCLUSIONS 79

1. Introduction

In this Chapter II, I design and analyze the behavior of a metasurface-based radar absorber (MBRA) operable in the VHF-UHF frequency bands.

In Section 2, I first introduce the Cartesian-to-polar coordinate mapping used throughout this thesis to deal with the impractical dimensions arising from the large wavelengths of the VHF-UHF bands. After exposing the theory of such a translation, I illustrate with canonical one-dimensional arrangements of rectangular patches and finally introduce the actual structure of the metasurface of interest.

To develop the MBRA, I use an equivalent circuit approach for the design process, coupled with a finite-element approach for the validation process. This two-step method is first applied to a MBRA of fixed absorption frequency, as a validation step, before being applied to an absorber of tunable absorption frequency. The reflection coefficient of both radar absorbers is measured and confirms the expected behaviors from the two-step design method. However, the frequency-tunable radar absorber is affected by large magnitude variations, caused by impedance mismatches introduced by the parasitic elements of the varactor diodes. In the last part of this chapter, two investigations are therefore led to overcome these drawbacks and propose solutions to either, grant near-perfect absorption through resistance-tuning or wideband coverage through a temporal control of biasing voltages.

In Section 3, I first introduce the requirements for a MBRA device to be perfectly matched at a single frequency using an equivalent circuit analysis (ECA), resulting in a narrowband absorber. To reach such requirements, a metasurface structure is proposed, along with the necessary passive electronic lumped elements. In order to validate the proper design of the metasurface, the devised equivalent circuit model (ECM) is compared to full-wave simulations using the Finite-Element Method (FEM) simulation solver of COMSOL®. This two-step approach is then validated by the measurement of a real metasurface-based radar absorber, highlighting the ECM is an appropriate design tool for an initial estimation but FEM simulations are necessary for a final validation.

In Section 4, substituting the capacitors of the metasurface for varactor diodes, the MBRA is rendered frequency-tunable. Due to the use of active electronic elements, such an absorber is no longer bound by the RBF constraint, and may therefore reach wideband absorption. However, though acting as variable capacitors, the varactor diodes also bring along some parasitic elements, which, introduce impedance mismatches and cause rather large magnitude variations. Nonetheless a metasurface is fabricated following the two-step approach. The measurement of its reflection coefficient highlights the same general behavior as predicted by FEM simulations: large frequency coverage, but sub-optimal absorption rates.

In Section 5, two different investigations are performed in the search for improved properties of the MBRA. In particular, each section addresses one the two critical properties of a radar absorber: magnitude and bandwidth. In Section 5.1, using an additional tuning of resistance, a compensating mechanism is numerically investigated to correct the large magnitude variations observed on the tunable radar absorber and enable near-perfect absorption over the covered

range. The investigation is led as an optimization of the ideal metasurface resistance for each state of the tunable metasurface. In section 5.2, thanks to a time-dependent tuning of varactor diodes in line with the frequency sweep of the source, the metasurface is experimentally investigated as an effectively wideband absorber.

2. VHF-UHF coaxial metasurface

This thesis tackles the topic of metasurface-based structures over the VHF-UHF frequency bands, the design of which is troublesome because of the size of their constituting elements. I thus decided to first deal with the Cartesian-to-polar coordinates transposition used as a preliminary design step to define the metasurface of interest, whose dimension is drastically reduced from a Cartesian counterpart.

2.1. Cartesian-to-polar coordinate mapping

By definition, a metasurface is an assembly of a sub-wavelength patterns periodically repeated onto a specific material. It is usually manufactured using PCB technology and thus consists in metallic patterns printed onto a substrate. However, the homogenization process, which allows all meta-atoms to act as a single surface impedance, requires all elements to be sub-wavelength [40]. Generally, a meta-atom is considered suitable from $\lambda/5$ and under. This condition can easily be respected with high frequency systems where $\lambda < 20$ cm, so that an arrangement of metallic or dielectric resonators can be deposited or etched onto a substrate and still make up for a metasurface of reasonable dimension. However, as frequency decreases, meta-atoms grow, so much so that at $f_0 = 300$ MHz, the wavelength is $\lambda_0 = 1$ m. Assuming a metasurface can still be manufactured with such dimensions, anechoic chambers wide enough to perform the measurements are extremely rare, on top of the issue with the weight of the carbon black pyramids.

In order to remedy to this issue, it was decided at ONERA to work on a metasurface in the *coaxial* geometry. A coaxial metasurface can be interpreted as the transposition of a one-dimensional arrangement of meta-atoms from the Cartesian space onto the coaxial space. In other words, the (x, y) rectangular coordinates are remapped onto the (ρ, ϕ) polar coordinates, as can be found in [110], [111]. This transposition is possible through conformal mapping, granted by the fact the TEM field considered here can be expressed as the gradient of a scalar potential that satisfies Laplace's equation [112]. In order for such a coordinate mapping to be performed, there needs to exist a relationship F between coordinates (ρ, ϕ) and (x, y) such that

$$F(\rho, \phi) = x + jy \tag{II.1}$$

which ensures the potential Φ satisfies the same equation in both frameworks. Given that in a Cartesian space (u, v), the polar coordinates of a point are $\rho e^{j\phi}$, then the function $F = ln$ is a possible solution leading to

$$F(\rho, \phi) = ln\left(\rho e^{j\phi}\right) = ln(\rho) + j\phi \tag{II.2}$$

where one identifies

$$\begin{cases} x = ln(\rho) \\ y = \phi \end{cases} \tag{II.3}$$

In such a case, as illustrated in Figure II.1(a), one may thus notice that the coaxial disk defined:

- along the ϕ-axis, from $\phi = 0$ to $\phi = 2\pi$;
- along the ρ-axis, from $\rho = a$ the inner radius to $\rho = b$ the outer radius ;

is bound by the curves $S_1 = \{\rho = a, \phi \in [0,2\pi]\}$ and $S_2 = \{\rho = b, \phi \in [0,2\pi]\}$, the inner and outer rims of the disk. Following the transformation F, the disk is thus deployed into the rectangle of Figure II.1(b) defined:

- along the y-axis, from $y = 0$ to $y = 2\pi$;
- along the x-axis, from $x = \ln(a)$ to $x = \ln(b)$;

which remains bound by lateral edges $S_1 = \{x = \ln(a), y \in [0,2\pi]\}$ and $S_2 = \{x = \ln(b), y \in [0,2\pi]\}$. On top of that, though ϕ is defined over $[0,2\pi]$, it actually expands over $[-\infty, \infty]$, offering the one-dimensional periodicity along the y-axis, as hinted in Figure II.1(b).

Regarding the potential Φ, it is defined in the polar coordinates as $\Phi((\rho,\phi) \in S_1) = 0$ V (on S_1) and $\Phi((\rho,\phi) \in S_2) = V_0$ V, and should therefore still verify $\Phi((x,y) \in S_1) = 0$ V and $\Phi((x,y) \in S_2) = V_0$ V after the transformation F, with a periodicity of 2π along y. In such a case, Ref. [112] offers the solution as

$$\Phi(x,y) = \frac{x - ln(a)}{ln(b) - ln(a)} V_0 \tag{II.4}$$

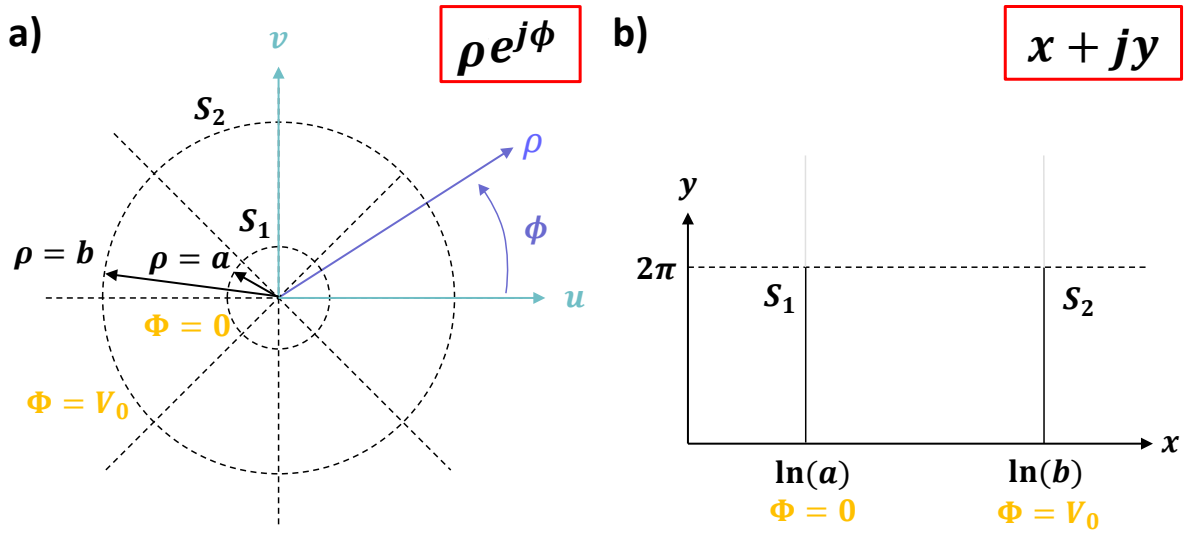

Figure II.1 : (a) Coaxial waveguide cross-section in polar coordinates (ρ,ϕ) defined along bounds $S_1 = \{\rho = a, \phi \in [0,2\pi]\}$ and $S_2 = \{\rho = b, \phi \in [0,2\pi]\}$. (b) Conformally mapped coaxial waveguide in the Cartesian coordinates (x,y) defined by bounds $S_1 = \{x = \ln(a), y \in [0,2\pi]\}$ and $S_2 = \{x = \ln(b), y \in [0,2\pi]\}$.

2.2. Cartesian-to-polar one-dimensional metasurface equivalents

The coordinate projection also applies to any pattern inscribed in one or the other equivalent. For instance, a slit along the y-axis ($y \in [0,2\pi]$) of the Cartesian rectangular patch is matched into a ring aperture in the polar coaxial disk ($\phi \in [0,2\pi]$). This is in fact the case displayed in Figure II.2(a), where the periodic horizontal slit turns into a ring slot once remapped into Figure II.2(b). Equivalently, a slit along the x-axis ($x \in [\ln(a), \ln(b)]$) of the Cartesian rectangular patch is matched into a tapered aperture in the polar coaxial disk ($\rho \in [a,b]$). This is once again the case of Figure II.2(c), where periodic vertical aperture are mapped into tapered grooves once remapped into Figure II.2(d). Finally the irises of Figure II.2(e) are remapped for **Erreur ! Source du renvoi introuvable.**(f), with a clear difference between the top and bottom apertures. These two illustrations are based on the typical irises of meta-atoms [62], thus forming

a capacitive (Figure II.2(a)-(b)), an inductive (Figure II.2(c)-(d)) and mixed (Figure II.2(e)-(f)) Cartesian and coaxial metasurfaces.

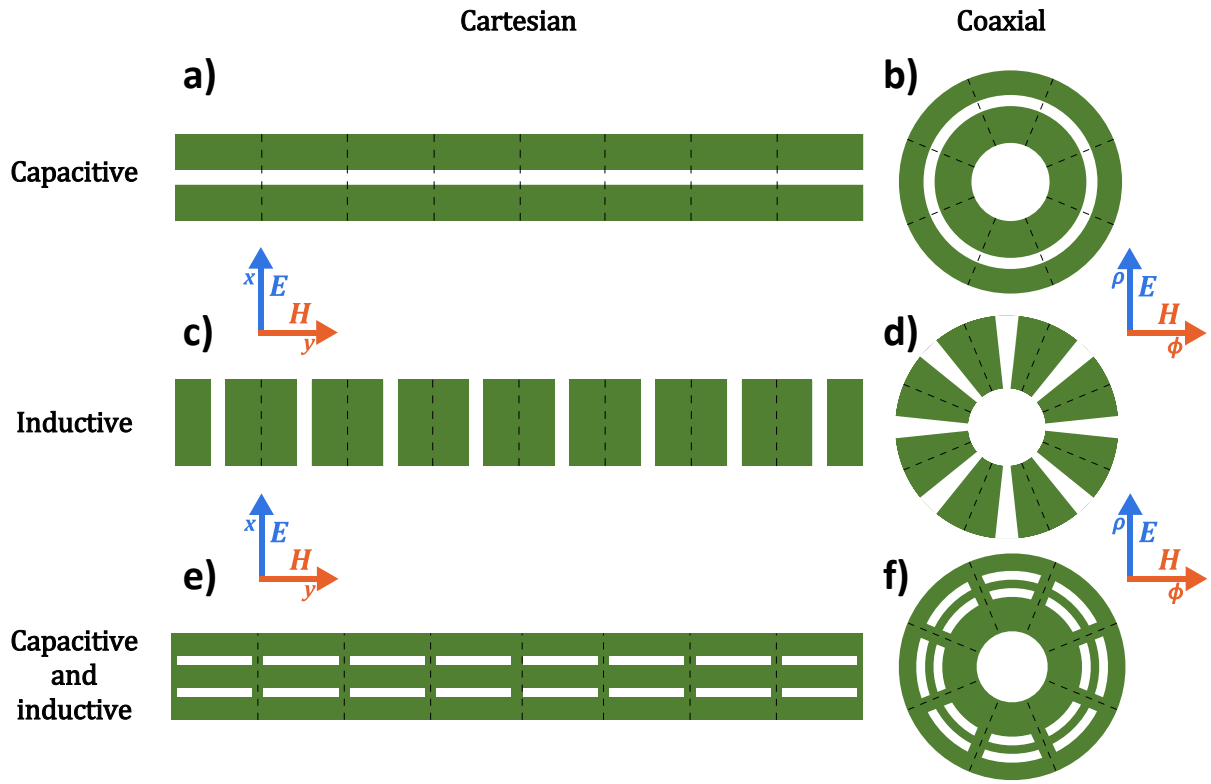

Figure II.2 : (column) Cartesian and coaxial equivalent to a linear arrangement of meta-atoms of (row) capacitive, inductive and mixed behavior.

2.3. Metasurface of interest

The main interest of this transposition lies in the scale factor from Cartesian to polar coordinates, effectively downsizing the metasurface of interest to only 15 cm in diameter, whose entire geometry is provided in Figure II.3. One may finally notice in Figure II.3 the presence of eight rectangular outlines, across the gap, spaced by 45°. These are the placeholders for the addition of lumped electronic elements, depending on the desired applications. In particular, a combination of resistive and capacitive elements for radar absorbing purposes, as detailed in Chapter II, and solely capacitive for frequency conversion purposes, as detailed in Chapter III.

The characteristic impedance of the equivalent coaxial waveguide Z_{coax} is defined from free-space Cartesian impedance $Z_{cart} = \sqrt{\mu_0/\epsilon_0}$ and its geometric dimensions such that

$$Z_{coax} = Z_{cart}\frac{\ln(R_{ext}/R_{int})}{2\pi} \quad \text{(II.5)}$$

In the case of interest, the dimensions ensure $Z_{coax} = 50\ \Omega$. The electronic considerations in this work therefore are 50 Ω-based.

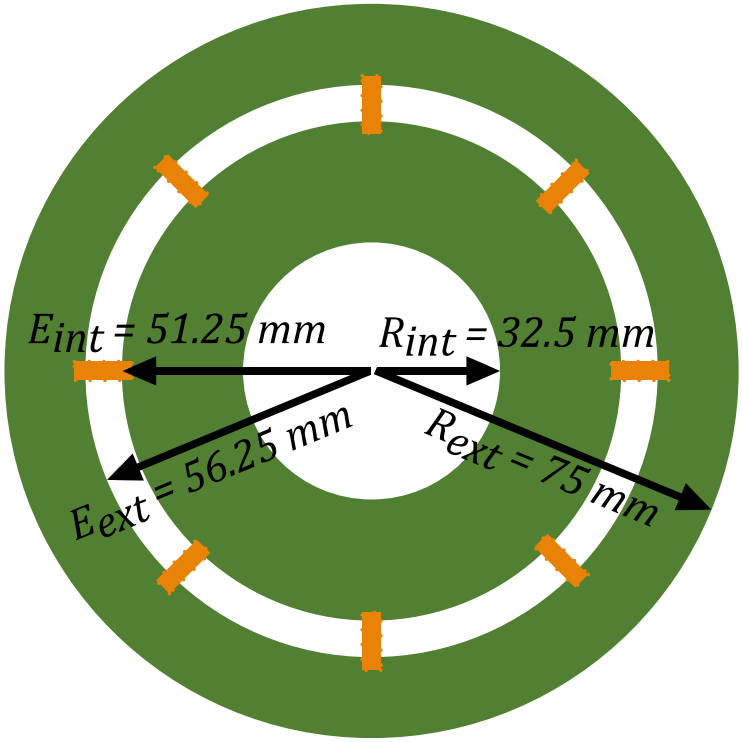

Figure II.3 : Metasurface of interest in the coaxial space of outer conductor's radius $R_{ext} = 75$ mm, inner conductor's radius $R_{int} = 32.5$ mm, outer gap's rim radius $E_{ext} = 56.25$ mm and inner gap's rim radius $E_{int} = 51.25$ mm, with (orange boxes) highlight of the solder pads for lumped electronic elements.

3. Development and experimental validation of a metasurface-based radar absorber over the VHF-UHF bands

In this Section 3, the requirements for a functional MBRA are laid out from an ECA. This leads to the establishment of a target ECM of the configuration, highlighting the admittance requirements bestowed upon the metasurface to grant impedance matching. Confirmed by complementary FEM simulations, the ECM is used as the foundational brick for the design of an actual metasurface. This metasurface is designed to provide impedance matching at a single frequency, leading to a narrowband absorption, whose measured reflection coefficient validates the adequacy of the two-step ECM-FEM method as an appropriate design tool.

3.1. Equivalent circuit analysis an impedance matching metasurface for a radar absorber

Over the VHF-UHF frequency range, wavelengths range from $\lambda_{min} = 43$ cm to $\lambda_{max} = 300$ cm. For instance, at the intermediate frequency $f_0 = 300$ MHz, the wavelength is $\lambda_0 = 100$ cm, which requires an impedance inverter, as found in a Salisbury screen, to be $\lambda_0/4 = 25$ cm, which is rather thick. Using a metasurface screen instead of a resistive screen allows for a drastic reduction of thickness. In fact, to get a device thin enough for practical applications, it was decided to separate the metasurface from the ground plane by a distance $\ell = 20$ mm. Transmission line

theory says the short-circuit's behavior amounts to that of a parallel inductor [22], whose inductance L_{SC} is deduced from

$$Y_{SC}(\ell) = -jY_0 cotan(k_0\ell) \approx \frac{1}{j\omega L_{SC}} \quad \text{(II.6)}$$

where $Y_0 = 0.2$ S is the transmission line characteristic admittance and $k_0 = 2\pi/\lambda_0$ is the wavenumber of the considered TEM wave, leading to an inductance in the coaxial geometry of $L_{SC} = \ell/Y_0 c_0 = \mu_0 \ell \ln(R_{ext}/R_{int})/2\pi \approx 3.35$ nH – see Figure II.3 for the values of R_{ext} and R_{int} the outer and inner radii of the considered coaxial cell.

The metasurface of interest is infinitely thin in regards to the wavelengths over the VHF-UHF bands. Therefore, despite being a quadrupole, it can be described as a single admittance Y_{MS}, in parallel to the transmission line, and not a T or Π circuit [22], as illustrated in Figure I.7. In that case, the reflection coefficient on the short-circuited metasurface Γ of an impinging TEM wave of admittance Y_0 can be expressed as

$$\Gamma = \frac{Y_0 - Y_{in}}{Y_0 + Y_{in}} = \frac{Y_0 - (Y_{MS} + Y_{SC})}{Y_0 + (Y_{MS} + Y_{SC})} \quad \text{(II.7)}$$

where $Y_{in} = Y_{MS} + Y_{SC}$ is the input admittance formed by the short-circuited metasurface, as illustrated in Figure II.4(a).

As would be the case with any other system, absorption is granted when the metasurface is able to provide impedance matching which nullifies the reflection coefficient. The impedance matching conditions in this case are twofold: the nullification of the real and imaginary parts.

On the one hand, one may notice that, outside of the metasurface, only the TEM wave is resistive, of purely real admittance Y_0. Therefore, the real part of the reflection coefficient Γ can be nullified by using a metasurface of resistive behavior opposing that of the TEM wave such that

$$Re(Y_{MS}) = Y_0 \quad \text{(II.8)}$$

On the other hand, one may notice from Equation (II-1) that, outside of the metasurface, only the short-circuit is reactive, of admittance Y_{SC}. Therefore, the imaginary part of the reflection coefficient Γ can be nullified by using a metasurface of reactive behavior able to compensate for the inductive nature of the short-circuit such that

$$Im(Y_{MS}) = \frac{1}{\omega L_{SC}} \quad \text{(II.9)}$$

Therefore, the metasurface can be used as an impedance matching device as long as it is simultaneously able to cancel the resistive elements of the impinging wave and the inductive elements of the short-circuit. As stated in Section 4.1.3.1 of Chapter I, non-Foster elements would be the ideal solutions for broadband admittance matching, but it can still be ensured at a finite number of frequencies through other means (Salisbury, Jaumann screens…). In the case studied here, it was decided to consider impedance matching at a single frequency to ensure a reduced thickness as well as a simple design.

This single-frequency impedance matching can be ensured by the use of a resistive and capacitive metasurface. While resistance matching from an overall resistance R_{MS} is wideband because frequency-independent, reactance matching from an overall capacitance C_{MS} is only reached at the frequency at which $\omega C_{MS} = 1/\omega L_{SC}$. Inserted into the ECM in Figure II.4(a), the resulting MBRA's ECM turns into the RLC parallel circuit provided in Figure II.4(b).

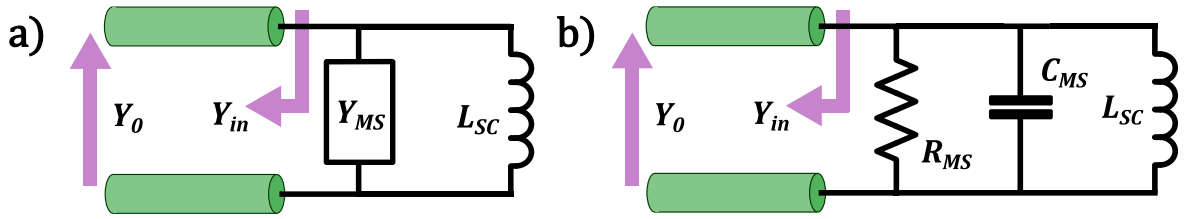

Figure II.4 : (a) Equivalent circuit model of a metasurface-based radar absorber of low thickness. (b) Equivalent circuit model of the ideal metasurface-based radar absorber equivalent to a Salisbury screen.

The equivalent circuit model (ECM) of the MBRA configuration clearly highlights the requirements imposed on the metasurface. In particular, they point out it must provide both resistive and capacitive elements. In Section 3.2, the structure of the metasurface is introduced, before discussing the appropriate electronic elements.

3.2. Design of an impedance matching metasurface

Regardless of the metasurface structure, from the sole resistance matching condition of Equation (II.8) and ECM of Figure II.4, it appears the resistive elements of the metasurface must be chosen to provide an overall resistance $R_{MS} = 1/Re(Y_{MS})$ such that

$$R_{MS} = 1/Y_0 = 50\ \Omega \tag{II.10}$$

Moreover, as shown in Figure II.4, the short-circuited metasurface acts as a RLC circuit with a resonance frequency f_r. In fact, at resonance the reflection coefficient is minimized, which means impedance matching is reached, and subsequently absorption is obtained, at

$$f_r = \frac{1}{2\pi\sqrt{L_{SC}C_{MS}}} \tag{II.11}$$

for $C_{MS} = Im(Y_{MS})/\omega$ the total metasurface's capacitance. Since the inductance is fixed by the distance of the metasurface to the short-circuit, it appears that the absorption frequency can only be set by the metasurface's capacitance. For such a RLC circuit, it is also well-known that the bandwidth Δf is defined as

$$\Delta f = \frac{1}{2\pi C_{MS}R_{MS}} \tag{II.12}$$

Since the resistance is chosen to cancel the impinging wave's resistance, the bandwidth is also set by the metasurface's capacitance.

These electronic considerations now need to be translated into an actual circuit to be integrated onto the metasurface of interest provided in Figure II.3. To maintain as many symmetries as possible, these electronic elements are loaded in an alternating fashion onto these eight different locations, leading to the metasurface illustrated in Figure 2(a).

Now, one should notice that the gap of the metasurface is already slightly capacitive in itself. To evaluate its value, one can resort to the method of [62] – but adapting the given cases to a slit in the middle of the discontinuity in the coaxial case. One may also perform the ECA of [65], which considers the metasurface as a discontinuity coupling with higher-order modes. In fact, this method was used for the same coaxial capacitive metasurface in [66], leading to a self-capacitance of $C_{self} = 4$ pF. Therefore, the admittance of the metasurface is a parallel circuit of this self-capacitance and the admittance of the lumped elements Y_{LE}, leading to the ECM of Figure 2(b).

To clarify the differences between Y_{MS}, the metasurface's overall admittance, and Y_{LE}, the electronic lumped elements' admittance, one should keep in mind that, looking at Figure 2(b), that

$Re(Y_{MS}) = Re(Y_{LE})$ but $Im(Y_{MS}) = Im(Y_{LE}) + j\omega C_{self}$. Therefore, all resistive elements for Equation (II-2) are provided by lumped resistors, while reactive elements to reach Equation (II-3) must take the capacitive gap into consideration. In fact, thanks to additional capacitive elements, natural resonance at $f_r = 1.36$ GHz can be brought down to the range of interest. In this case, the resonance frequency expression of Equation (II.11) can be used to express the required overall capacitance $C_{MS} = C_{LE} + C_{self}$ as

$$C_{LE} = \frac{1}{L_{SC}\omega_r^2} - C_{self} \tag{II.13}$$

Therefore, to bring the resonance down to an intermediate value of $f_r = 300$ MHz requires an additional $C_{LE} = 80$ pF. Spread over four capacitors, each has to exhibit a capacitance $C = 20$ pF, for a total metasurface capacitance be $C_{MS} = C_{LE} + C_{self} = 4C + C_{self} = 84$ pF. Regarding the resistance matching, the use of four parallel resistive elements urges one to use four $R = 4R_{LE} = 4R_{MS} = 200\ \Omega$ resistors. This leads to the final first-order ECM of the MBRA of Figure II.5(c), where all resistive and capacitive elements have been lumped together, for an ECM of equivalent topology to the ideal one of Figure II.4(b).

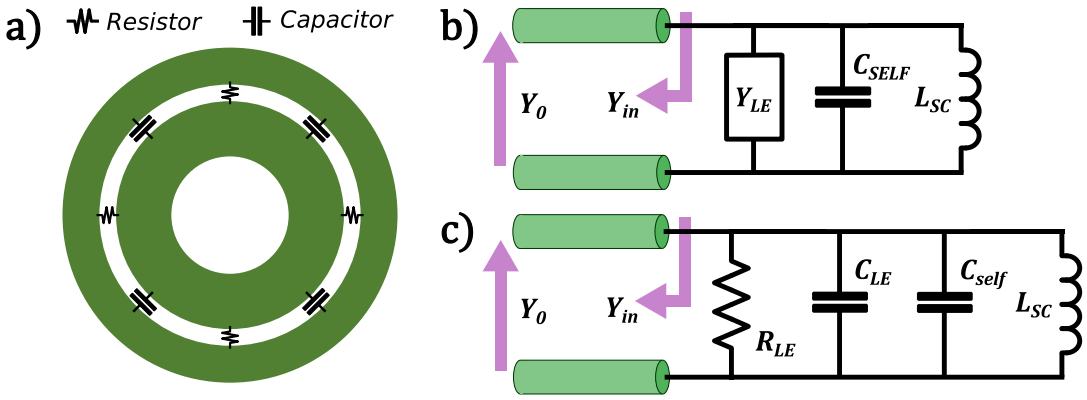

Figure II.5 : (a) Illustration of the impedance matching metasurface for a metasurface-based radar absorber using four capacitors and four resistors in parallel across the capacitive gap. (b) First-order equivalent circuit model to the low-thickness metasurface-based radar absorber using a capacitive host structure of capacitance C_{self} to load electronic elements of equivalent parallel admittance Y_{LE}. (c) Equivalent circuit model to the designed metasurface-based radar absorber, using a capacitive metasurface of capacitance C_{self} along with R_{LE} loaded resistance and C_{LE} loaded capacitance.

During this design process, the ECA is used to quickly apprehend the general behavior of the metasurface. According to [65], the self-capacitance C_{self} here introduced can actually be seen as resulting from the couplings to higher-order coaxial modes *via* the symmetry-breaking metasurface. That explains the precaution used when calling the ECM of Figure II.5 *first-order* – some elements, resulting from unaccounted for higher-order couplings, may be overlooked by this approach. Section 3.3 therefore will provide a comparison between the analytical results of the ECM to two numerical models.

3.3. Analytical and numerical studies of the metasurface-based radar absorber using the equivalent circuit model, a 2D axisymmetric FEM model and a 3D FEM model

In Section 3.3, the numerical models used are an axisymmetric, 2D FEM model and a fully 3D FEM model. This comparison will validate the use of ECM and FEM as a two-step method, allowing for quick designing through the ECM, and numerical validation through the FEM.

3.3.1. ECM and 2D axisymmetric FEM simulations of the metasurface-based radar absorber

In this first comparison between analytical and numerical results, the numerical model is that of a 2D axisymmetric configuration. In fact, in the radar absorbing configuration within a coaxial waveguide, which is of interest in this work (see Figure II.3), the problem is invariant by rotation except for the metasurface itself. In that case, the metasurface's behavior must be extrapolated and affected to a stand-in. In the 2D axisymmetric COMSOL® model, this means the metasurface is now a line across the waveguide onto which only the *Lumped Element* or *Surface Current Density* nodes can be applied to give it the proper behavior. In fact, keeping the gap, as done in the model in Figure II.6(a) offers both possibilities. However, the model of Figure II.6 (b) requires the use a *Surface Current Density* to enforce the proper Surface Impedance Boundary Condition (SIBC) – more information on this matter can be found in Appendix C. In any case, at this stage, the metasurface's behavior can only be described using the ECM of Figure II.5. The *Lumped Element* node is therefore a parallel RC circuit of all lumped elements added to the metasurface, while the *Surface Current Density* is specified to obtain the SIBC of a parallel RC circuit – of all lumped elements for the model of Figure II.6 (a) and adding the gap capacitance for the model of Figure II.6 (b). The advantage of removing the physical gap is that the meshing of the structure is not as constrained by such a small dimension, as can be noticed in Figure II.6 (a-b). This is especially true when considering the smallest wavelength $\lambda_{min} \approx 430$ mm and a gap of only 5 mm wide (86 times smaller).

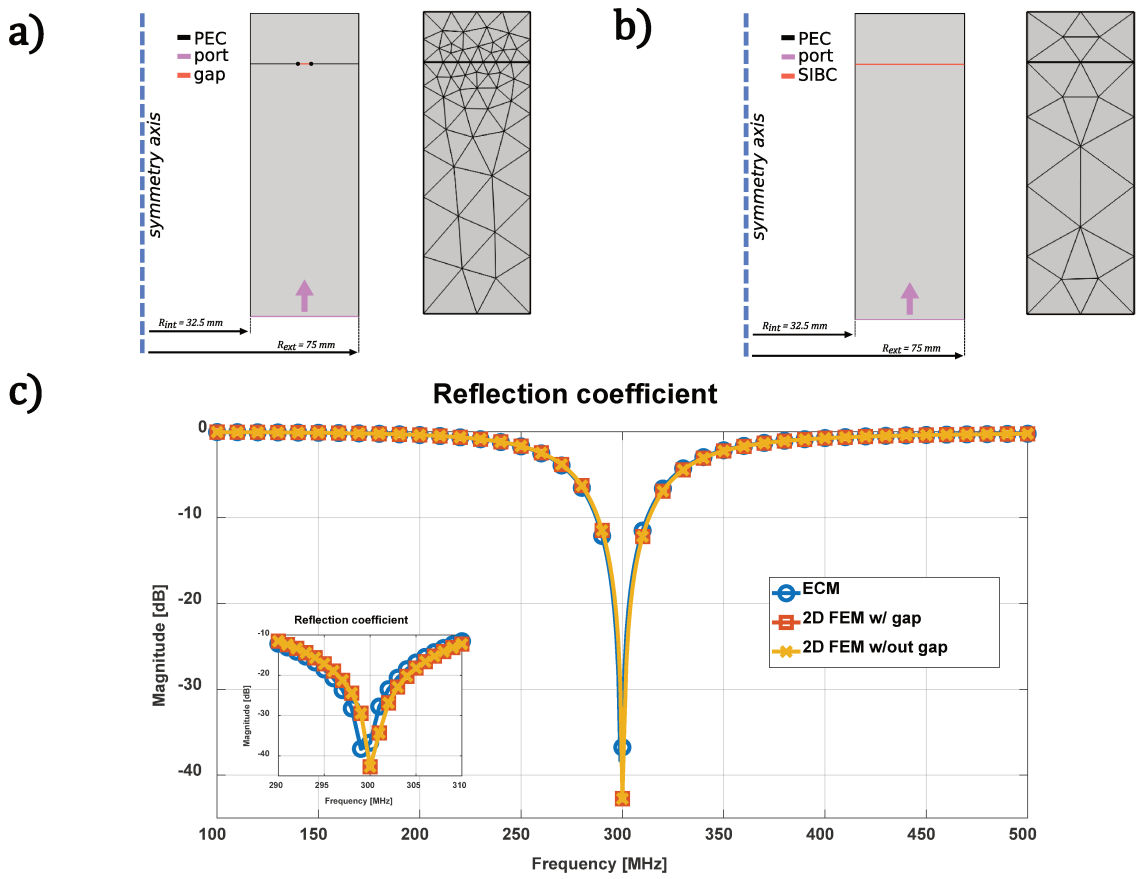

Figure II.6 : (a) 2D axisymmetric numerical models of the metasurface-based radar absorber in the enlarged coaxial waveguide with the metasurface's gap and associated mesh. (b) 2D axisymmetric numerical models of the metasurface-based radar absorber in the enlarged coaxial waveguide with the metasurface's gap and associated mesh. (c) Reflection coefficient of the metasurface-based radar absorber from (blue circles) the ECM and from 2D axisymmetric FEM simulations over $[100, 500]$ MHz using a metasurface with (red squares) and without (yellow crosses) the geometric gap with resistance $R_{MS} = 50\ \Omega$ and capacitance $C_{LE} = 80$ pF.

FEM simulation of the reflection coefficient onto the MBRA can then be performed by simulating the S_{11} parameter of the *Port* node. Since here the only electrical value of interest is the magnitude of the scattering parameter S_{11}, the phase at the *Port* is of secondary importance. Should it be more relevant, it needs to be de-embedded to account for the propagation back and forth within the enlarged waveguide. After simulation, the magnitude of the reflection coefficient in both cases is reported in Figure II.6(c) in comparison to its ECM counterpart.

As can be noticed in Figure II.6, all three curves agree in terms of frequency and magnitude. In fact, both models lead to an absorption at $f_r = 300$ MHz frequency with a minimum reflection coefficient magnitude of around -40 dB and bandwidth of $\Delta f = 35$ MHz. Therefore, these results confirm the ECM can accurately describe the behavior of MBRA of revolution symmetry.

3.3.2. ECM and 3D FEM simulations in a rotation-invariant configuration of the metasurface-based radar absorber

In this second comparison between analytical and numerical results, the numerical model is that of a 3D configuration. In fact, the resulting configuration of Figure II.7(a) can be seen as the rotational extrusion of the model in Figure II.6(a). In this first complexification of the model, the metasurface's gap is therefore entirely filled with a uniform distribution of the lumped elements, showing a ring geometry. The rotation-invariant resulting geometry is a $C_{\infty v}$-symmetric surface [113], and can therefore be simplified to a minimal angular sector thanks to symmetry planes, leading to the geometry of Figure II.7(b) for an angular sector of only 10°. Using a *Perfect Magnetic Boundary* node for the symmetry planes on the cross-sectioned waveguide's faces, this simplification creates an equivalent waveguide which propagates only a portion of the initial power flow. In fact, the angular sector is reduced by a factor 36, but since the voltage differential is unaffected by this transformation, this means the current is also divided by 36. This current reduction therefore increases the input impedance by 36 [114].

The expected results from such model are the same as the 2D axisymmetric model of Figure II.6, given how it was built. The *Surface Current Density* node acts as a uniform distribution of resistive and capacitive elements all around the gap. This distribution therefore means that there is no rotational variance of this model either. Therefore, very few higher-order modes can couple with the metasurface – and those who can are already accounted for in the gap's equivalent capacitance. So no extra behavior from such interactions is expected here, as confirmed in Figure II.7.

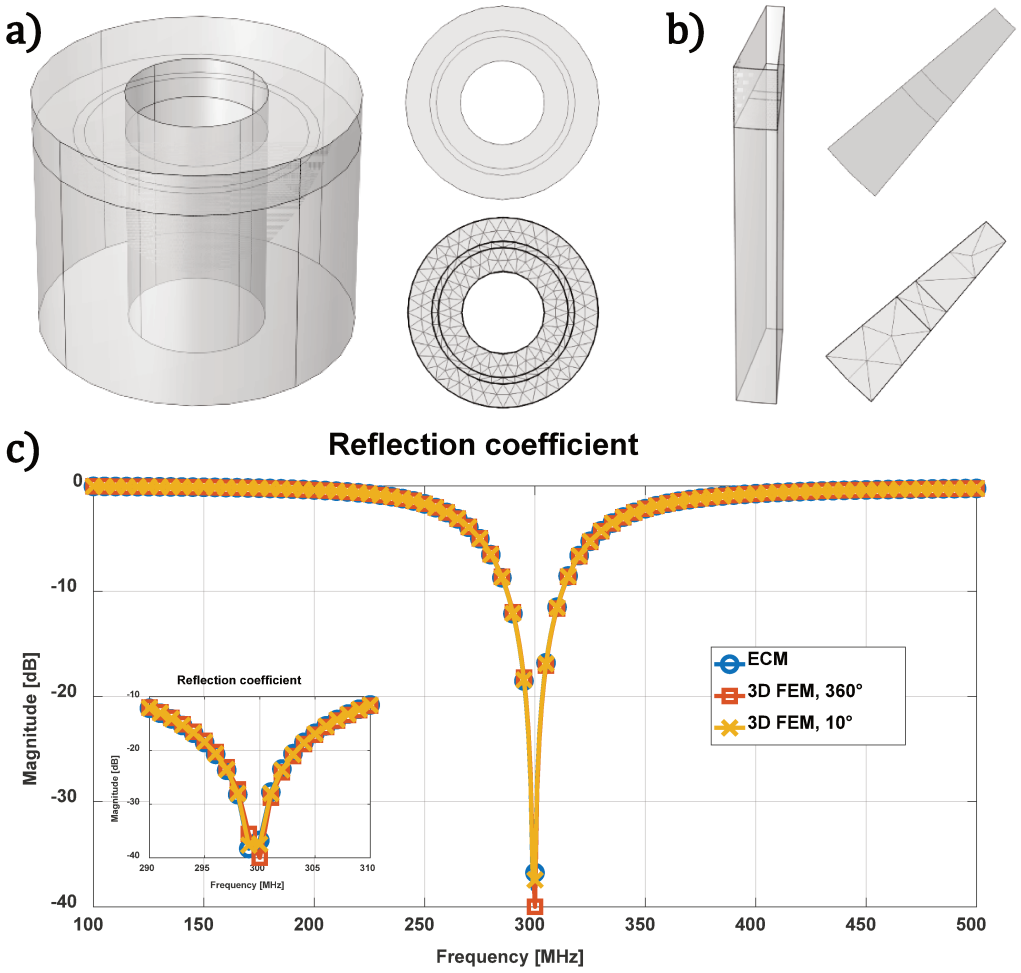

Figure II.7 : (a) Side view of the 3D numerical model of the metasurface-based radar absorber in the enlarged waveguide with an unified metasurface of ring geometry in a 360° angular

sector configurations, with top view of the metasurface and resulting mesh. (b) Side view of the 3D numerical model of the metasurface-based radar absorber in the enlarged waveguide with an unified metasurface of ring geometry in a 10° angular sector configurations, with top view of the metasurface and resulting mesh. (c) Reflection coefficient of the metasurface-based radar absorber from the ECM (blue circles) and 3D FEM simulations over $[100, 500]$ MHz from the (red squares) 360° and (yellow crosses) 10° angular sector configurations for a uniform distribution of the resistance $R_{MS} = 50\ \Omega$ and capacitance $C_{LE} = 80$ pF.

And as can be appreciated in Figure II.7, ECM and FEM simulation results agree on both the resonance frequency and associated minimum magnitude. Once again, absorption is observed at $f_r = 300$ MHz frequency with a minimum magnitude of around -40 dB and bandwidth of $\Delta f = 35$ MHz. These simulation results confirm once more the ECM is a good descriptor for a rotation-invariant configuration, and that symmetric configurations can be efficiently simplified for faster computations.

3.3.3. ECM and 3D FEM simulations of the actual geometry of the metasurface-based radar absorber

In this third and last comparison between analytical and numerical results, the numerical model is that of a 3D configuration, this time using the actual structure of the metasurface, as provided in Figure II.8(a). Compared to the previous model of Figure II.7(a), this model now accounts for the locations of the lumped elements, and the apertures in-between. This structure does account for possible interactions with higher-order modes. In fact, the actual structure of the metasurface exhibits two symmetry planes, running through any two opposing capacitors and through any two resistors, as well as a rotational symmetry of $\pi/2$, making it a surface of C_{4v} symmetry [113].

Given this symmetry, it is not necessary to simulate the entire geometry. In fact, only a fourth of it, cut in the xz- and yz-planes, can be used in combination with symmetry boundary conditions on the quarter's faces. Similarly to the configuration of Figure II.7(b), the resulting geometry is provided in Figure II.8(b). As previously stated, using *Perfect Magnetic Boundary* nodes, this equivalent waveguide only propagates a fourth of the initial power flow, leading to a fourfold input impedance increase [114]. Regarding the lumped elements, it appears the xz- and yz-planes run through two *Lumped Port* nodes, leaving one untouched in the middle of the resulting geometry. Should the split elements be resistors or capacitors, their value need not to be adjusted to the geometry change.

To validate all three approaches to the 3D FEM simulation, as well as to evaluate their differences with the ECM results, the resulting reflection coefficient for all four cases is compared in Figure II.8(c). For the sake of simplicity, the 3D models are referred to as their angular sectors, namely 360° for the model of Figure II.8(a), and 90° for the other model of Figure II.8(b), for which the resistor-affecting transformation is indicated by $R/2$, and equivalently $C/2$ for the capacitor-affecting transformation.

In this case, the simulated results differ from the analytical results of the ECM. Yet, all three 3D models lead to the same reflection coefficient, confirming their equivalence. Despite using the same amount of resistance and capacitance, absorption is now observed for all three FEM simulations at a frequency $f_r = 229$ MHz, which means there is a difference of $\delta f_r = 71$ MHz from ECM predictions. Furthermore, it appears the $R_{MS} = 50\ \Omega$ resistance of the metasurface does not provide a very good impedance matching since the minimum recorded magnitude is now found at around -17 dB instead of -39 dB. As previously stated, these differences are caused by the lower symmetry of such a configuration, allowing the metasurface to couple with higher-order

modes. This change in resonance frequency and minimum reflection coefficient magnitude hints at additional reactive and resistive elements originating from such couplings. In fact, the lower the symmetry, the further the results will drift from the idealized case of the ECM.

In order to further confirm this is not a simulation artifact due to COMSOL®, a similar simulation was performed using another commercial FEM-based software, HFSS®, as provided in Figure II.8(d). As can be noticed, the resulting reflection coefficient curves from COMSOL® and HFSS® agree despite a slight frequency shift. This may be due to a slight geometry discrepancy, or the methods of both softwares to account for circular shapes. Nonetheless, these results confirm the difference between COMSOL® results from the 3D FEM simulations and the ECM calculations only originate from its inability to account for rotational symmetries – in a first-order ECM as provided in Figure II.5(c), since a higher-order model, using [65] for instance, should account for those overlooked interactions.

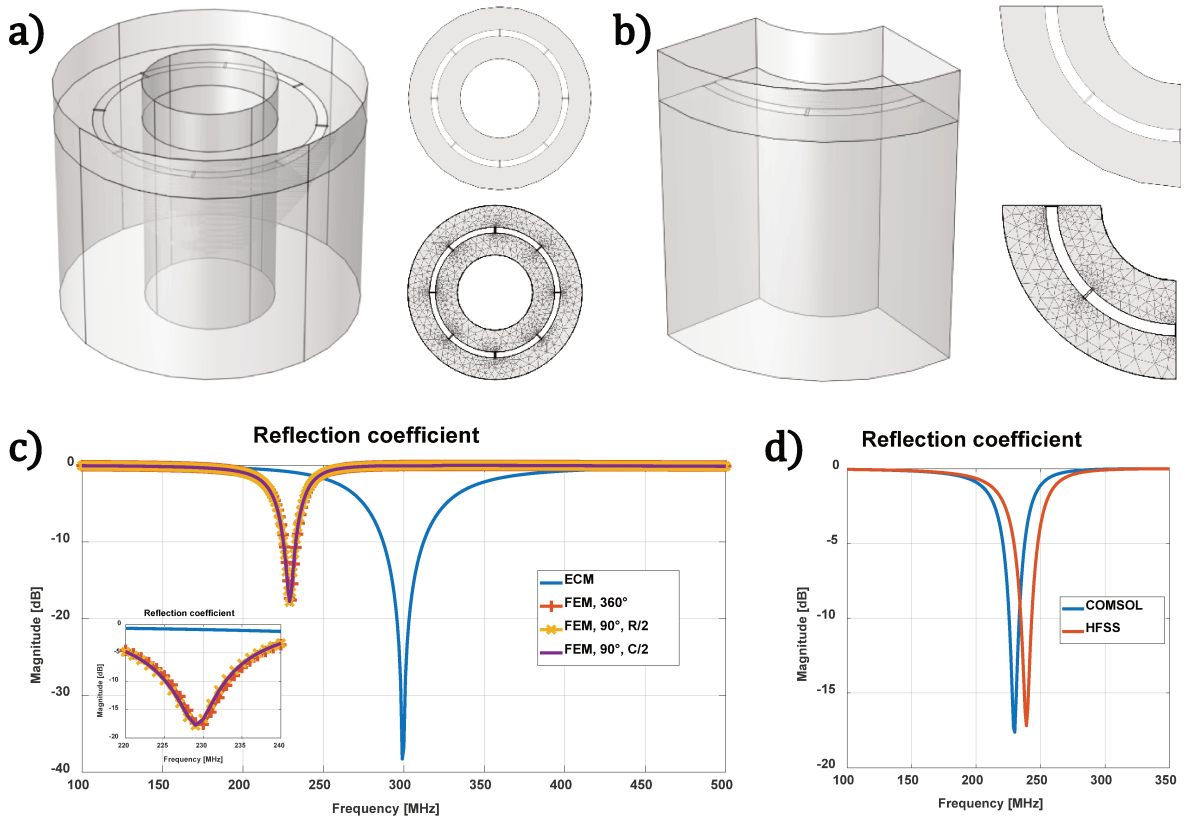

Figure II.8 : (a) Side of the 3D numerical model of the metasurface-based radar absorber in the enlarged coaxial waveguide using the actual structure of the metasurface, with top view of the metasurface and resulting mesh. (b) Side of the 3D numerical model of a fourth of the metasurface-based radar absorber in the enlarged coaxial waveguide using the actual structure of the metasurface, with top view of the metasurface and resulting mesh. (c) Reflection coefficient of the metasurface-based radar absorber from the ECM (blue) and 3D FEM simulations with the (red plusses) 360° configuration and 90° configuration for both the (yellow crosses) resistor-related and (purple) capacitor-related over $[100, 500]$ MHz using the actual geometry of the metasurface with an overall resistance $R_{MS} = 50\ \Omega$ and capacitance $C_{LE} = 80$ pF. (d) Reflection coefficient of the metasurface-based radar absorber from 3D FEM simulations with a metasurface of overall resistance $R_{MS} = 50\ \Omega$ and capacitance $C_{LE} = 80$ pF using (blue) COMSOL® and (red) HFSS® over $[100, 350]$ MHz.

From the results of Figure II.8(c), it appears the ECM is only strictly valid for rotation-invariant metasurfaces. However, even for other configurations, it allows for a fast first estimate. On the other hand, the 3D FEM model is more complex, and resource-intensive, but provides a more accurate prediction of the metasurface behavior. Therefore, both tools will still be used in the following: first the ECM for easy designing, then the 3D FEM model for numerical validation.

3.4. Experimental validation of a metasurface-based radar absorber

3.4.1. Experimental setup for the frequency-domain measurement of the metasurface-based radar absorber

To measure the MBRA's behavior, a Vector Network Analyzer (VNA) is used. From a single endpoint, it can measure both emitted and received powers, magnitudes and phases, to provide the scattering parameters. This is usually performed within an anechoic chamber to suppress parasitic reflections off the walls. However, since the metasurface cannot be measured in our anechoic chamber over the considered frequencies, an enlarged coaxial waveguide was designed at ONERA. Within such waveguide, the fundamental mode is TEM, which emulates free-space plane wave. To be more exact, the waveguide has been designed to exhibit a cut-off frequency around 900 MHz, so the 100 – 700 MHz range only supports the TEM wave of interest. However, within such measurement environment, only the normal incidence can be considered. To better highlight the location of all elements in this measurement setup, Figure II.9(a) provides an illustration. On said illustration, one may notice the VNA is connected to the coaxial waveguide on the left-hand side through a transition ensuring the propagating signal is TEM. On the right-end side, the metasurface is inserted before the short-circuit at a distance $\ell = 20$ mm. In Figure II.9(b-c), pictures of the actual enlarged coaxial waveguide used for measurements are provided.

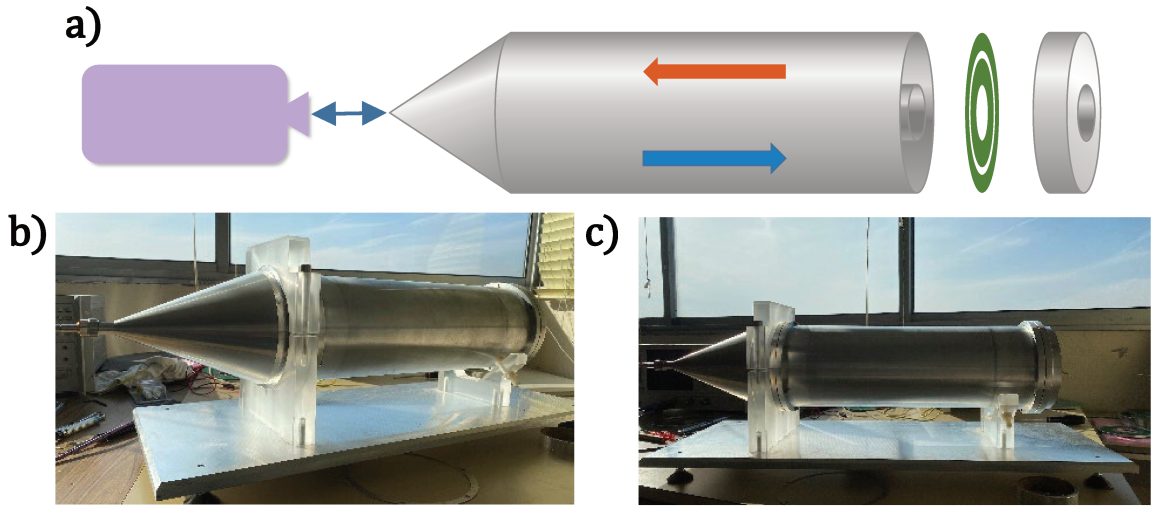

Figure II.9 : (a) Illustration of the experimental setup for measurement of the metasurface-based radar absorber in the frequency-domain using the enlarged coaxial waveguide and a vector network analyzer. (b) Front and (c) side views of the enlarged coaxial waveguide used for measurement of the metasurface-based radar absorber.

The VNA used is the Agilent® 8753ES model and it is addressed using a Matlab® script and the Instrument Control Toolbox® along with a GPIB-USB cable. The VNA can be calibrated in the metasurface plane with an offset short error model as detailed in the following.

3.4.1.1. Calibration process

The offset short error model is a calibration process detailed in [115], which is recalled in the following.

The objective is to correct for the directivity error e_D, source matching error e_{SM} and reflectivity tracking error e_{RT} introduced by the enlarged coaxial waveguide. Considering the enlarged coaxial waveguide as a reciprocal quadrupole $\left(S_{21}^{WVG} = S_{12}^{WVG}\right)$, then $e_D = S_{11}^{WVG}$, $e_{SM} = S_{22}^{WVG}$ and $e_{RT} = S_{21}^{WVG} S_{12}^{WVG}$, where the WVG superscript refers to the waveguide. These errors can then be corrected from the measurement of three offset shorts using the matrix system

$$\begin{pmatrix} e_D \\ e_{RT} - e_D e_{SM} \\ e_{SM} \end{pmatrix} = \begin{pmatrix} 1 & S_{11}^{std_1} & S_{11}^{std_1} S_{11}^{SC_1} \\ 1 & S_{11}^{std_2} & S_{11}^{std_2} S_{11}^{SC_2} \\ 1 & S_{11}^{std_3} & S_{11}^{std_3} S_{11}^{SC_3} \end{pmatrix}^{-1} \begin{pmatrix} S_{11}^{SC_1} \\ S_{11}^{SC_2} \\ S_{11}^{SC_3} \end{pmatrix} \tag{II.14}$$

where the SC_n superscript refers to the considered offset short.

At ONERA, it was decided to measure four short-circuits of different offset lengths: $\ell_1 = 0$ mm, $\ell_2 = 20$ mm, $\ell_3 = 60$ mm and $\ell_4 = 190$ mm, thus resulting in an overdeterminate system. This is done to prevent ill-conditioning of the matrix to be inverted at certain frequencies within the band of interest.

3.4.2. Measurement of the metasurface-based radar absorber

Using the ECM as a design tool, a metasurface is fabricated. Based on the previously introduced design constraints, it is decided to surface-mount four resistors of individual resistance $R = 200\,\Omega$ for an overall resistance $R_{MS} = R/4 = 50\,\Omega$ and four capacitors of individual capacitance $C = 20$ pF for an overall capacitance $C_{MS} = 4C + C_{self} = 84$ pF. The metasurface is provided in Figure II.10(a). This metasurface is then introduced into the enlarged coaxial waveguide of Figure II.9(b-c) for measurement in the frequency-domain. Measurement results are compared to the 3D FEM simulation results used as a reference in Figure II.10(b).

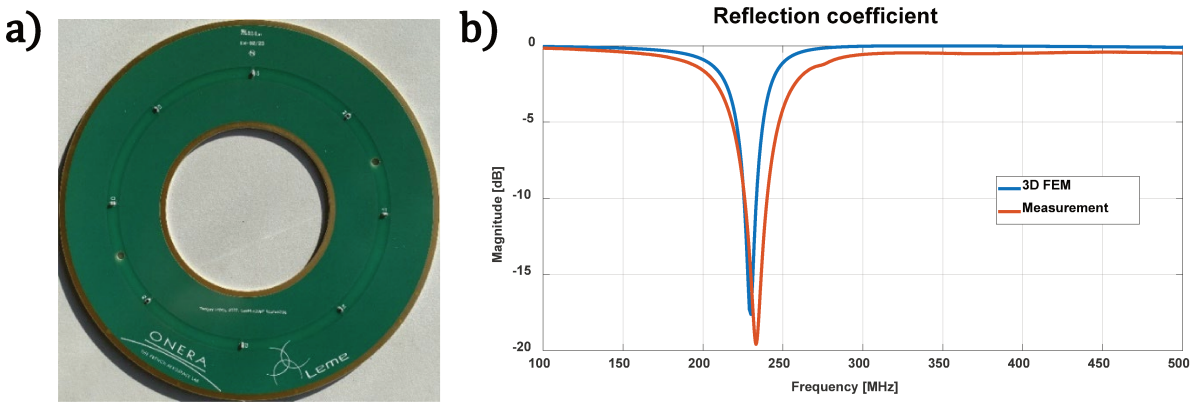

Figure II.10 : (a) Metasurface of overall resistance $R_{MS} = 50\,\Omega$ and capacitance $C_{MS} = 84$ pF. (b) Reflection coefficient of the metasurface-based radar absorber from a 3D FEM simulation (blue) and measurements (red).

In Figure II.10(b), apart from a slight resonance frequency shift and magnitude drop difference, both the measurement and simulation curves of the reflection coefficient agree. In fact, simulations highlight an absorption around $f_r = 229$ MHz that is confirmed by practical measurements of the MBRA.

This also confirms the validity of the two-step design and validation method. In fact, the 3D numerical model leads to accurate predictions of the metasurface built from the ECM design tool.

In this chapter, an ECA was used to highlight the requirements for a MBRA. From such a target ECM, an impedance matching metasurface was proposed, whose own ECM can be approximated by the required RC circuit. The metasurface's ECM is then validated against numerical simulations, highlighting a good first estimate, but a lack in accuracy compared to an exact 3D replica. However, it still constitutes an easy-to-apprehend model that is especially useful for designing. In this case, it has been used to fabricate a metasurface that is impedance-matched at a single frequency $f_r = 300$ MHz, the measurement of which is well predicted by the analytical and numerical models. However, this MBRA has only been designed as a validation step, since it is notoriously limited by the RBF bound. Yet, it has confirmed the validity of the different models. In Section 4, the same design method is applied to a frequency-tunable MBRA, for which the capacitors have been swapped for variable capacitors: varactor diodes.

4. Development and experimental validation of a frequency-tunable metasurface-based radar absorber over the VHF-UHF bands

Based on the previous considerations of Section 0, it was possible to fabricate and experimentally validate a MBRA of fixed absorption frequency. However, as was previously discussed, this MBRA is rather narrowband. To overcome this drawback, it is decided in Section 4 to add frequency-tunability to the impedance matching metasurface. Though the instantaneous bandwidth would remain untouched, the effective bandwidth, *i.e.* frequency coverage, would be greatly improved.

4.1. Frequency-tunability using varactor diodes

Given the resonance frequency's expression of Eq. (II.11), using a capacitive element of variable capacitance can offer a range of absorption frequencies to a single device, without resorting to cascading different metasurfaces to create a Jaumann-like structure. In particular, varactor diodes are a convenient solution to obtain a range of capacitances [116]. The metasurface's illustration of Figure II.5(a) therefore turns into that of Figure II.11(a). However, a varactor diode is not an ideally varying capacitor. In fact, it is a PN junction whose variable depletion width leads to a bias-dependent series resistor. And the packaging of the component also adds reactive elements, such as a series inductance and parallel capacitance, which do alter the reactive behavior of the capacitive diode. Provided in datasheet [117], the SPICE model of a varactor diode is provided in Figure II.11(b) for future reference.

Substituted into the MBRA's ECM of Figure II.5(c) for the fixed capacitors, the new ECM is that of Figure II.11(c). Assuming it still acts as a RLC circuit, using N varactor diodes for frequency tunability, similarly to Equation (II.11), the MBRA exhibits a bias-dependent resonance frequency $f_r(V_r)$ of expression

$$f_r(V_r) = \frac{1}{2\pi\sqrt{L_{SC}C_{MS}(V_r)}} \approx \frac{1}{2\pi\sqrt{L_{SC}\left(N\left(C_d(V_r) + C_p\right) + C_{self}\right)}} \quad \text{(II.15)}$$

As provided in [117], the characteristic curve $C_d(V_r)$ of a varactor diode quickly decreases from its highest value with increasing reverse biasing. As a result, capacitance barely varies beyond the 5 V reverse biasing value. From the provided expression in [117], both the expected resonance frequency and bandwidth can therefore be computed as a function of reverse bias voltage V_r, leading to the curves of Figure II.11(d). To be more precise, there might still be some measurable difference between the resonance frequencies at $V_r = 5$ V and $V_r = 7$ V, but power considerations also come into considerations and lead to the decision to consider only the $V_r \in [0, 5]$ V range.

Since the objective here is to provide the widest coverage, a varactor diode with the largest variation is sought after. It turns out that the SMV1249 model from Skyworks® is an interesting candidate given its [37.35, 2.72] pF range [118]. From the ECM, this would cover the [200, 800] MHz frequency range, which makes up most of the [100, 700] MHz range of interest.

As was previously established, the ECM is not strictly valid in 3D, in both the resonance frequency and impedance matching criteria. In other words, the required capacitive range brought to light just above is probably some ways off the actual requirements. Despite the precautions taken not to get too close to the 100 – 700 MHz range's border, it is thus important to make sure the predictions are not entirely erroneous by a 3D FEM simulation using the varactor diode configuration.

4.2. ECM and 3D FEM simulations of the frequency-tunable metasurface-based radar absorber

Before measurements, the ECM predictions and 3D FEM simulations are compared to numerically validate the choice of components. The resulting reflection coefficient is provided in Figure II.11(e) for reverse biasing voltages of $V_r \in [0,5]$ V. For both the ECM and 3D FEM models, the complete varactor diode's SPICE model is used, including the bias-dependency of the diode's capacitance and resistance using the datasheet values [118].

In Figure II.11(e), one may notice that the ECM and 3D FEM results do not superimpose. The ECM overestimates the resonance frequency at every biasing voltages. In fact, the blueshift observed from the 3D FEM results is still caused by the same couplings with higher-order modes as highlighted in the previous MBRA absorber of Figure II.10. Moreover, the ECM predicts a monotonous improvement of impedance matching, which is not observed in the 3D FEM results. The reflection coefficient from this numerical model is improved for the first biasing values but is degraded from 3 V up.

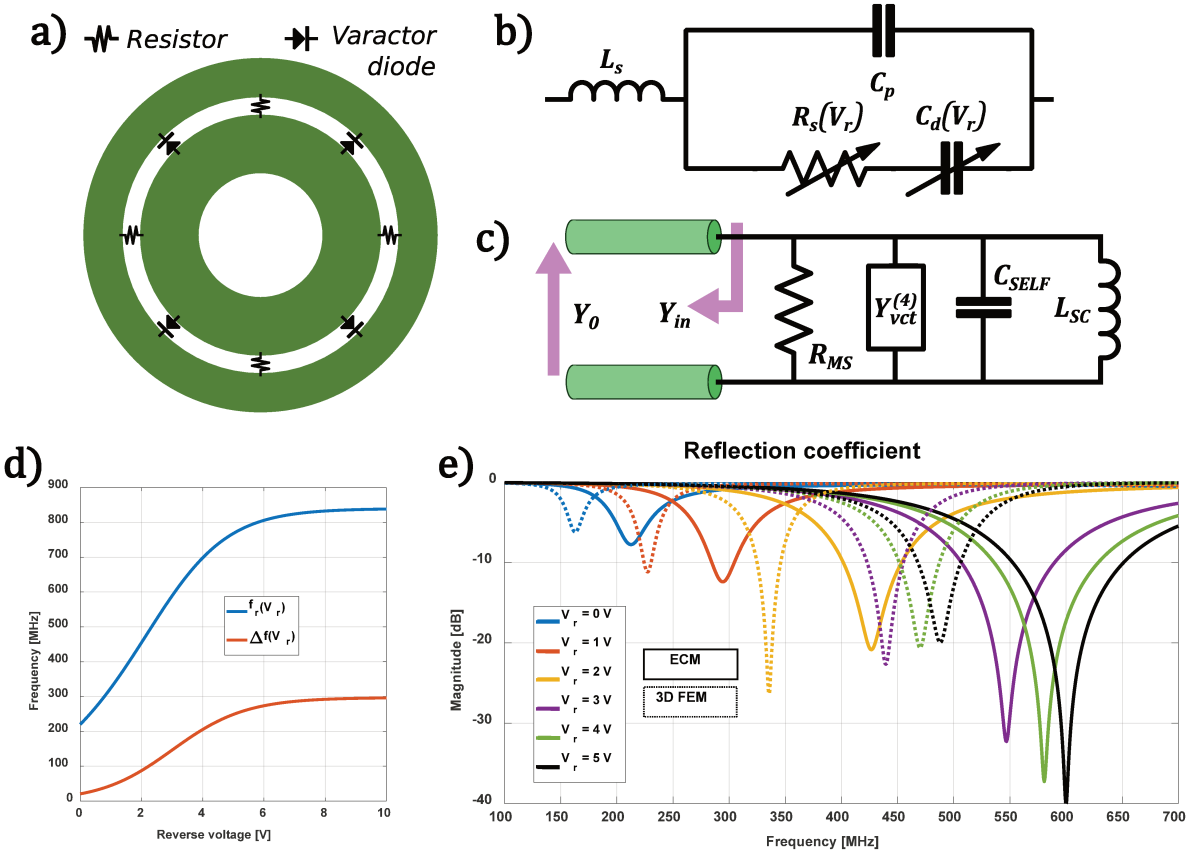

Figure II.11 : (a) Impedance matching frequency-tunable metasurface for a metasurface-based radar absorber using four varactor diodes and four resistors in parallel across the capacitive gap. (b) SPICE model of a varactor diode: C_d is the diode's capacitance, R_s is the diode's series resistor, C_p is the package's parallel capacitance and L_s is the package's series inductance. (c) Equivalent circuit model of the frequency-tunable metasurface-based radar absorber with $Y_{vct}^{(4)}$ the equivalent admittance to four varactor diodes in parallel. (d) Theoretical resonance frequency f_r and resonance bandwidth Δf from the ECM as a function of reverse voltage biasing V_r in the [0, 10] V range for the case of a metasurface-based radar absorber using four SMV1249 varactor diodes and $R_{MS} = 50\,\Omega$. (e) Reflection coefficient of the frequency-tunable metasurface-based radar absorber from the ECM (dashed) and 3D FEM simulations (solid) over [100, 700] MHz for reverse biasing values of $V_r \in [0, 5]$V.

From the results of Figure II.11(e), it appears that, despite discrepancies, the ECM can still provide a good first-estimate of the MBRA's behavior, even with the more complex circuit using varactor diodes. Though discrepancies are larger at higher voltages, the 3D FEM simulation results confirm that the overall behavior with respect to voltage predicted by the ECM still stands an actual metasurface built from it. To validate the behavior of a frequency-tunable MBRA, Section 4.3 will tackle the measurement of a prototype.

4.3. Experimental validation of the frequency-tunable metasurface-based radar absorber

4.3.1. Experimental setup for the frequency-domain measurement of the metasurface-based frequency-tunable radar absorber

The experimental setup for the measurement of this new radar absorber is very similar to that of Figure II.9. The main change is that, now, the metasurface needs to be biased by an external voltage source. An illustration of such a setup is provided in Figure II.12(a). The main issue in this configuration is that the enlarged coaxial waveguide is a sealed enclosure. Therefore, except at the input/output port where the VNA is connected, there is no way to communicate with the exterior. It was therefore decided to add a slit onto the inner conductor of the removable short-circuit used as the sample holder. This slit is barely wide enough to allow a wire to go through, and is actually placed behind the conductor plane not to be seen by impinging waves, as seen in Figure II.12(b)-(c). This enables the metasurface to be connected to an external DC voltage biasing source. The chosen source is an HAMEG© (now Rhode&Schwartz©) HMP4040, and it is addressed using the Instrument Control Toolbox© of Matlab© and a USB cable.

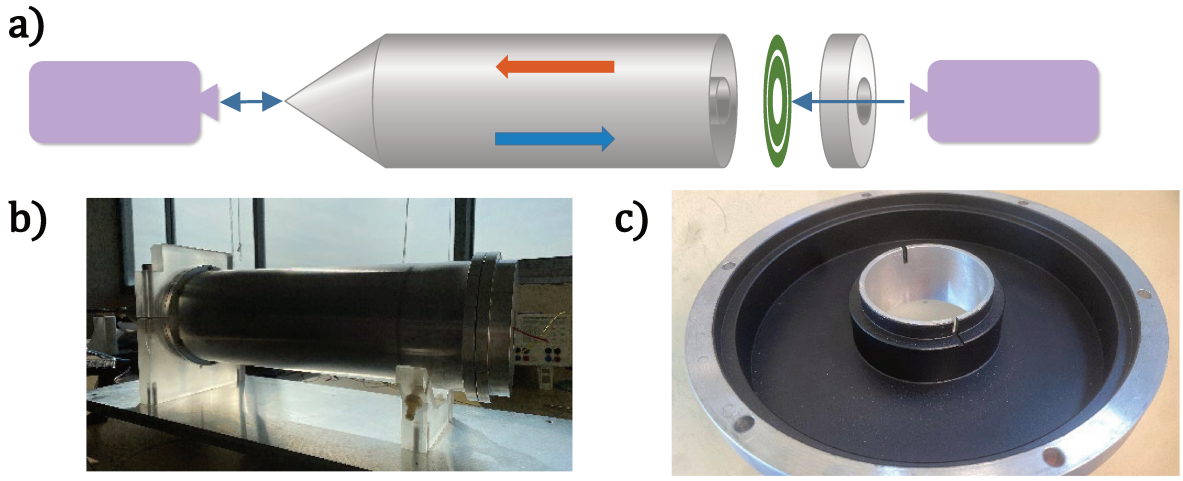

Figure II.12 : (a) Illustration of the experimental setup for measurement of the metasurface-based radar absorber in the frequency-domain using the enlarged coaxial waveguide, a vector network analyzer and a DC voltage biasing source. (b) Picture of the back rear view of the enlarged coaxial waveguide. (c) Picture of the sample-bearing short-circuit with slitted inner conductor.

4.3.2. Measurement of the metasurface-based frequency-tunable radar absorber

From the previous considerations, a metasurface is fabricated. Given the configuration of the enlarged waveguide measurement setup, the biasing voltage is driven up to the varactor diodes from a biasing plane on the back of the metasurface thanks to plated through-hole vias. Figure II.13(a) shows the upper and lower planes of the metasurface, where the routing circuit appears, and the alternating pattern of varactor diodes and resistors can be seen. It was decided to surface-mount the varactor diodes with their cathode to the via to allow for a positive voltage input. The following voltage values are therefore positive values of *reverse biasing*.

Inserted into the coaxial waveguide and wired to an external voltage source, the MBRA's properties can be measured using the VNA from the frequency-domain setup provided in Figure II.12. The measured reflection coefficient is then compared to 3D FEM simulations in Figure II.13(b). One may notice that the overall behavior from the simulations has been observed in the

measured reflection coefficient: frequency-tunability is obtained over most of the [100, 700] MHz range of interest. However, some differences can be noticed, especially regarding the absorption frequencies and impedance matchings, *i.e.* minimal reflection coefficient magnitudes.

First of all, regarding the absorption frequencies, it appears the measured reflection coefficient is minimized at slightly different frequencies than the 3D FEM simulations have predicted. In fact, the differences grow with increasing frequencies. Indeed, at 0 V, the simulated and measured curves agree on the absorption frequency of 160 MHz, but at 5 V, they show a 90 MHz shift. Looking at the varactor diode's datasheet [118], one may notice the capacitance values at higher voltages vary only very slightly, but lead to stronger shifts of resonance frequencies. In fact, from Eq. (II.11), one may notice that the resonance frequency is very sensitive to low capacitance values, as its derivative is

$$\frac{\partial f_r}{\partial C_{MS}} = -\frac{1}{4\pi\sqrt{L_{SC}}\sqrt[3]{C_{MS}}} \tag{II.16}$$

Therefore, a small error on the actual capacitance at high voltages can lead to strong differences. Such an error can be attributed to a dispersion in capacitance (manufacturer's tolerance), or a lack of information from the datasheet regarding a potential dependency of the capacitance value to frequency. It may also be due to a slight voltage drop caused by parasitic resistive elements, introduced by the silver paste used for the electric contact between the metasurface and sample holder.

Secondly, regarding the differences in impedance matchings, it appears simulated and measured reflection coefficients seldom agree on minimal magnitude value reached. To better visualize the issue, seen on both simulated and measured curves, a Smith chart in admittance is provided in Figure II.13(c). This Smith chart is built from 3D FEM simulated results, which exhibit a stronger variation in impedance matching, to better discuss this behavior. On the Smith chart, the resonance frequency associated to each biasing value is highlighted by an asterisk marker. One can notice that the input admittance Y_{in} to the MBRA draws a loop on the upper side of the Smith chart, symptomatic of a resonance. Regarding each individual loop, it appears for $V_r = 0$ V and $V_r = 1$ V, the input admittance loop crosses the resistance matching $Re(Y_{in})/Y_0 = 1$ circle far from the reactance matching line $Im(Y_{in})/Y_0 = 0$. Hence the necessarily lesser observed magnitude drop: admittance matching conditions are only partially met. However, at $V_r = 2$ V, the input admittance almost exactly intercepts the perfect admittance matching point $(Re(Y_{in})/Y_0, Im(Y_{in})/Y_0) = (1, 0)$, leading to the lowest reflection coefficient magnitude observed in Figure II.13(b). Then, despite intercepting the $Re(Y_{in})/Y_0 = 1$ circle, the input impedance for $V_r \in [3, 5]$ V departs from the $Im(Y_{in})/Y_0 = 0$ line, leading to the slow degradation in minimum magnitude. All in all, for $V_r < 2$ V, the metasurface grants neither resistive nor reactive matching, and for $V_r > 3$ V, it grants resistive but not reactive matching.

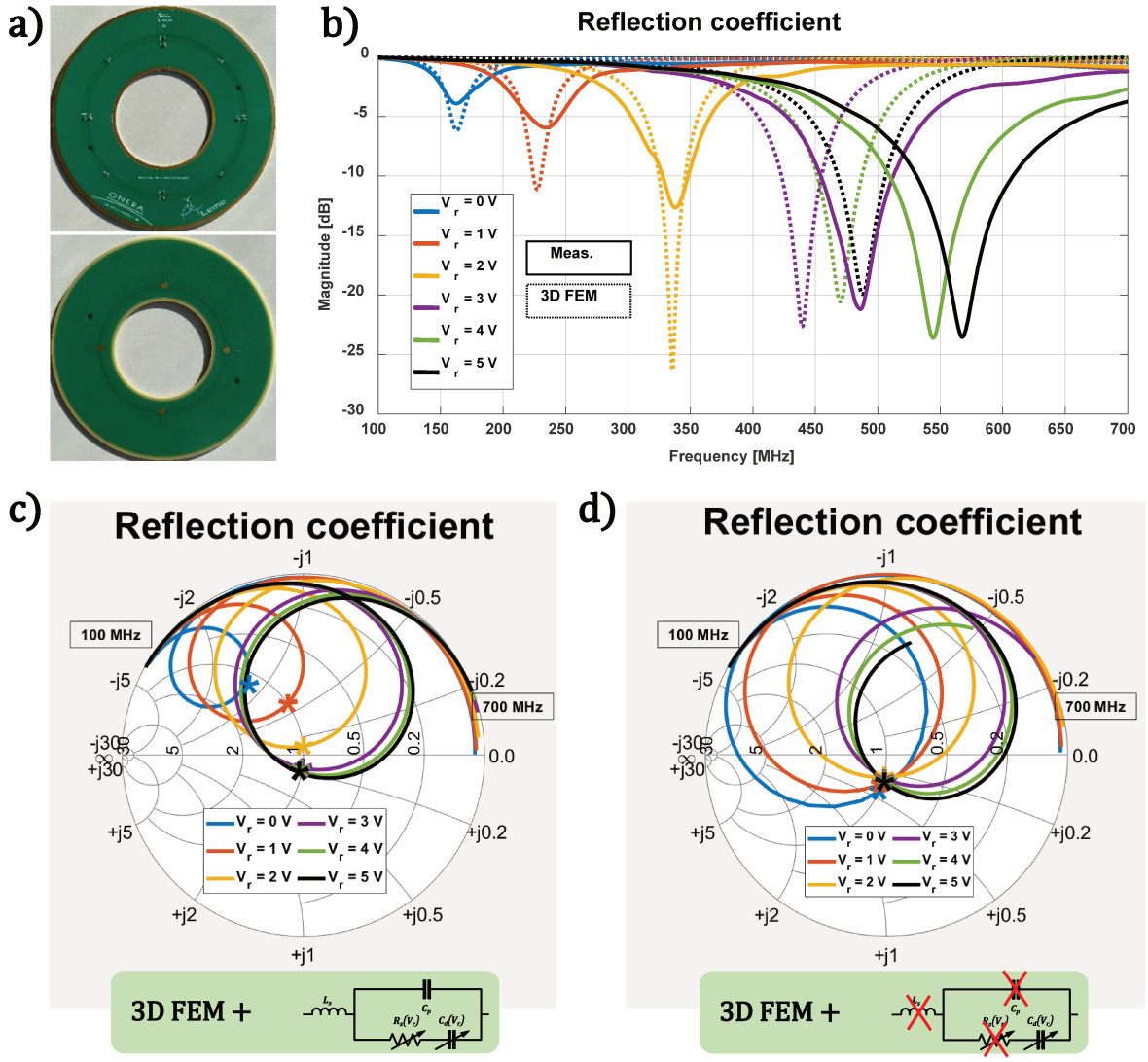

Figure II.13 : (a) Top and bottom views of the metasurface showing the alternating pattern of resistors and varactor diodes on top and the biasing routing strips and location of the vias on the bottom. (b) Reflection coefficient of the frequency-tunable metasurface-based radar absorber from 3D FEM simulations (dashed) and measurements (solid) over [100, 700] MHz for reverse biasing values of [0,5] V. (c) Reflection coefficient of the frequency-tunable metasurface-based radar absorber from 3D FEM simulations as an admittance Smith chart over [100, 700] MHz for reverse biasing values of $V_r \in [0, 5]$V, for the metasurface using all parasitic elements (C_p, L_s, R_s) of the varactor diodes. (e) Reflection coefficient of the frequency-tunable metasurface-based radar absorber from 3D FEM simulations as an admittance Smith chart over [100, 700] MHz for reverse biasing values of $V_r \in [0, 5]$ V, for the metasurface using only the diode's capacitance C_d of the varactor diodes.

In Figure II.13(d), another Smith chart in admittance is provided, based on the same exact configuration, except all parasitic elements of the varactor diodes are removed: the variable varactor diodes are therefore perfect capacitors. As can be observed, for all voltage biasing values, the reflection coefficient curves intercept the $Re(Y_{in})/Y_0 = 1$ circle. Furthermore, they all intercept it around the same value of reactance, which is close to the reactance matching line $Im(Y_{in})/Y_0 = 0$ though not quite. There is therefore a complete absence of minimum reflection coefficient magnitude variation: all curves drop to around -18 dB at resonance. Despite the fact that Figure II.13(b) confirms $R_{MS} = 50\ \Omega$ of overall metasurface's resistance is suboptimal, the

Smith charts of Figure II.13(d) mainly allow to better pinpoint the origin of magnitude variations of the reflection coefficient of the MBRA. Though one may think the reactive element mainly act as resonance frequency shifters, their interaction with the series resistance leads to a complex expression of the metasurface's overall resistance. It therefore clearly appears that the varactor diode's parasitic elements are not to be overlooked when designing the metasurface.

From the results of Figure II.13, it appears that, despite discrepancies between the 3D FEM simulation and measurements, the general frequency-tunable radar absorbing behavior expected from the varactor diode-loaded metasurface is well observed. Such a metasurface can grant absorption on an effective −10 dB bandwidth from around 300 MHz to 600 MHz, though with a wide variety of magnitudes. It has also been highlighted that impedance matching variations are mainly due to the use of varactor diodes, which introduce parasitic elements. In the next Section 5, two investigations are led in order to optimize the two critical elements of a radar absorber: the absorption rate and absorption bandwidth.

5. Numerical and experimental investigations into a frequency-tunable metasurface-based radar absorber of near-perfect absorption and time-based wideband coverage

In Section 5, two investigations are led. The first one is entirely numerical, and consists in granting near-perfect absorption at all considered frequencies thanks to a simultaneous tuning of capacitance and resistance. The goal here is to propose a compensating mechanism for the large magnitude variations observed in Figure II.13, caused by the mismatch introduced by the parasitic resistive elements of the varactor diodes. The second one is entirely experimental, and consists in granting wideband coverage to the absorber by a temporal control of its resonance frequency which closely follows that of the swept-source. The objective is to highlight an appropriate voltage-sweeping time-based pattern to maximize absorption bandwidth, in regards to the frequency-sweeping source.

5.1. Numerical investigation into a near-perfect metasurface-based radar absorber using a joint tuning of capacitance and resistance

In Figure II.13(b), it appears the reflection coefficient of the metasurface-based radar absorber is negatively affected by the parasitic elements of the varactor diodes as they introduce mismatching to the impinging wave. In such a case, using the SMV1249 varactor diode, it appeared perfect impedance matching is reached for a single biasing value found between 2 V and 3 V. However, given the great variance in parasitic elements' values from a varactor diode to another, they can impact the absorber's maximum absorption rates very differently depending on the chosen model. As an illustration, in Figure II.14, the SMV1249 diodes are swapped for SMV1255 [118] and SMV1236 [119] ones, leading to two new distributions of absorptions.

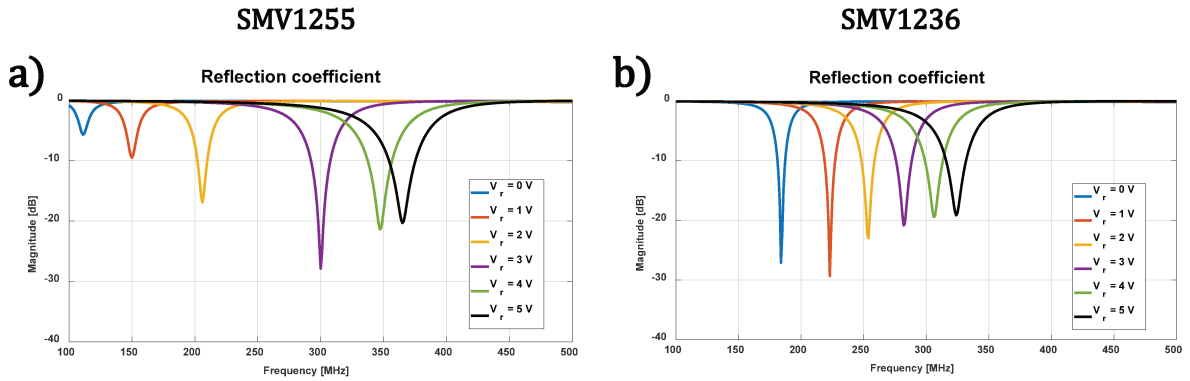

Figure II.14 : Reflection coefficient of the frequency-tunable metasurface-based radar absorber from the ECM (dashed) and 3D FEM simulations (solid) over [100, 700] MHz for reverse biasing values of $V_r \in [0, 5]$ V for a metasurface using (a) SMV1255 and (b) SMV1236 varactor diodes.

In Figure II.14, ECM results are provided mainly as a reference point for expected resonance frequencies. Looking at the solid curves of Figure II.14 produced by 3D FEM simulations, despite the differences in coverage, it appears the impedance matching is reached for different biasing values – namely around 3 V in Figure II.14(a) and around 1 V in Figure II.14(b). Therefore, it appears predicting the effects of the varactor diode on the metasurface's impedance matching may be tedious. To face this issue, instead of optimizing the choice of the varactor diode – strongly constrained on a first-order level by the desired frequency coverage –, a solution might be to resort to using a joint tuning of capacitance and resistance on the metasurface. This may offer the operator with the possibility to adjust the metasurface's overall resistance.

To validate this proposal, a numerical investigation is provided in Section 5.1.1. It consists in, first, performing an optimization on the required resistance value from the ECM. This is in fact a simple process since it is based on an analytical model. In a second time, another optimization is run in COMSOL® to account for the discrepancies between the analytical and numerical model.

5.1.1. Equivalent circuit study of optimal resistance values

During this first step, an optimization is run using Matlab© on the most appropriate resistance value R_{MS} to provide the best impedance matching for each voltage bias using the SMV1249 varactor diode model. The optimization is a least-square regression using R_{MS} as the parameter. In other words, the optimized value R_{opt} is defined as

$$R_{opt} = \underset{R_{MS} \geq 0}{argmin}(|S_{11}(R_{MS})|) \tag{II.17}$$

In Figure II.15(a), the optimized reflection coefficient curves from the optimization process are plotted, along with the associated resistance values R_{opt} in the inset graph. As can be noticed, (almost) every reflection coefficient dip is significantly improved, going from a global minimum magnitude of -26 dB in Figure II.13(b) to -48 dB in Figure II.15(a). As can be noticed in the inset graph, the resistance value associated to these curves is rapidly decreasing with increasing reverse voltage, but finds its asymptote just above 50 Ω. It therefore hints at a suboptimal standard $R_{MS} = 50\ \Omega$ value used for the fabricated metasurface. And it also hints at an increasing sensitivity to the resistance value with increasing capacitance – or decreasing voltage. Regarding the curve obtained for a reverse biasing voltage $V_r = 0$ V, it seems the optimization process could only find a sub-optimal resistance value despite multiple runs. Despite this particular case, it seems this process can greatly improve the absorption abilities of the metasurface-base radar absorber. To pursue the two-step process established throughout this

study, a subsequent optimization of the 3D FEM model must be performed to account for the potential differences.

5.1.2. Quick 3D FEM optimization of optimal resistance values

During this second step, a second optimization is run on the optimal resistance value R_{opt} necessary for the minimization of the reflection coefficient's magnitude. At this stage, the previously highlighted values from the inset graph of Figure II.15(a) are used as a starting point. Then five neighboring resistance values are used in a *Parametric Sweep* node for each biasing voltage: $R_{opt} - R_{opt} * k/10, k \in [\![-2, 2]\!]$. From these simulations, only the resistance providing the stronger absorption is kept. This leads to the results of Figure II.15(b), where the optimized curves (solid lines) are compared to the curves using the standard $R_{MS} = 50\ \Omega$ of Figure II.13(b).

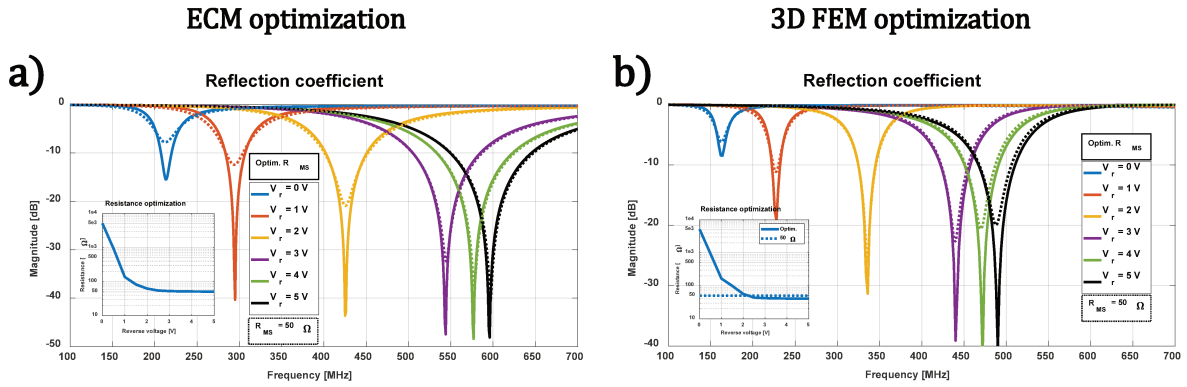

Figure II.15 : (a) Reflection coefficient of the frequency-tunable metasurface-based radar absorber from ECM simulations over $[100, 700]$ MHz for reverse biasing values of $V_r \in [0, 5]$V with (inset) optimized overall resistance R_{MS} value for high absorption (solid) compared to a standard $R_{MS} = 50\ \Omega$ (dashed). (b) Reflection coefficient S_{11} of the frequency-tunable metasurface-based radar absorber from 3D FEM simulations over $[100, 700]$ MHz for reverse biasing values of $V_r \in [0, 5]$ V with (inset) optimized overall resistance R_{MS} value for high absorption (solid) compared to a standard $R_{MS} = 50\ \Omega$ (dashed).

In Figure II.15(b), one can notice that all reflection coefficient curves have improved after optimization compared to the results using the standard $R_{MS} = 50\ \Omega$. However, the improvement is not as striking as that of Figure II.15(a). Nonetheless, a global minimum magnitude of -42 dB is obtained compared to the -27 dB of before, meaning there has been a maximum gain of 15 dB in absorption.

Besides this first analysis, it appears new optimized values R_{opt} have been found compared to the results of Figure II.15(a). They still display the rapidly decreasing curve as before, but this time it crosses the standard $R_{MS} = 50\ \Omega$ line and finds its asymptote just above 40 Ω. Looking at their intersection, one may notice it happens close to $V_r = 2$ V, which is the biasing reverse voltage at which the metasurface's simulation results Figure II.13(b) is the best matched. Which explains why it previously showed the highest absorption rate, along as to why the optimization has not brought much improvement in Figure II.15 – it happens to be already close to the optimal. However, it appears that, from $V_r = 3$ V up, the requirements for impedance matching hint at a smaller resistance of around $R_{opt} = 40\ \Omega$, confirming the effects of the parasitic resistive elements, changing the ideal overall resistance. This is a greatly appreciated improvement. On the other side on the biasing values, it however appears this process has only lead to slight improvements. At $V_r = 0$ V, the ECM optimization had already not been conclusive,

and it is only confirmed here. At $V_r = 1$ V however, absorption improved by around 7 dB nonetheless, which is still halfway to the minimal magnitude of -40 dB hinted by the ECM optimization. This subsequent optimization would probably benefit from a more rigorous methodology and a larger resistance spectrum to evaluate at, which could probably bring the reflection curves at least around the -50 dB average line for biasing values in the $V_r \in [1, 5]$V range. Furthermore, should capacitance be a second parameter for optimization, one may turn to a two-dimension optimization process on both C_d and R_{MS} simultaneously, which may grant better results than the twice one-dimensional optimization here proposed. However, finding the fitting tunable capacitive elements to this 2D optimization may be more tedious.

Regarding practical implementations of such joint tuning of capacitance and resistance, possible solutions for a variable resistance are junction field effect transistors (JFETs). In fact, thanks to a linear relationship between their drain current and drain-source voltage in the ohmic region, may grant the metasurface with the required resistance value range [ref]. In the case of the metasurface using SMV1249 varactor diodes post-FEM optimization, the required values spread from around $R_{opt}(0) = 5$ kΩ to $R_{opt}(5) = 40$ Ω, which are separated by a factor of around 125, which is much too large to be covered by a transistor. Leaving the $V_r = 0$ V particular case aside, even between $R_{opt}(0.5) = 1$ kΩ and $R_{opt}(5)$, the factor of 20 is still too large because the required resistance values for small biasing values are particularly large. Therefore, it appears such solution for this particular metasurface may be limited to the improvement of the absorption obtained at higher biasing values.

While this may still be interesting, Figure II.16 proposes to take a look at the hinted resistance values post-ECM optimization for the other two metasurfaces of Figure II.14 using the SMV1255 and SMV1236 models. One may bear in mind Figure II.16 provides the results from an ECM model of the MBRA, hence the frequency shifts from the 3D FEM results of Figure II.14.

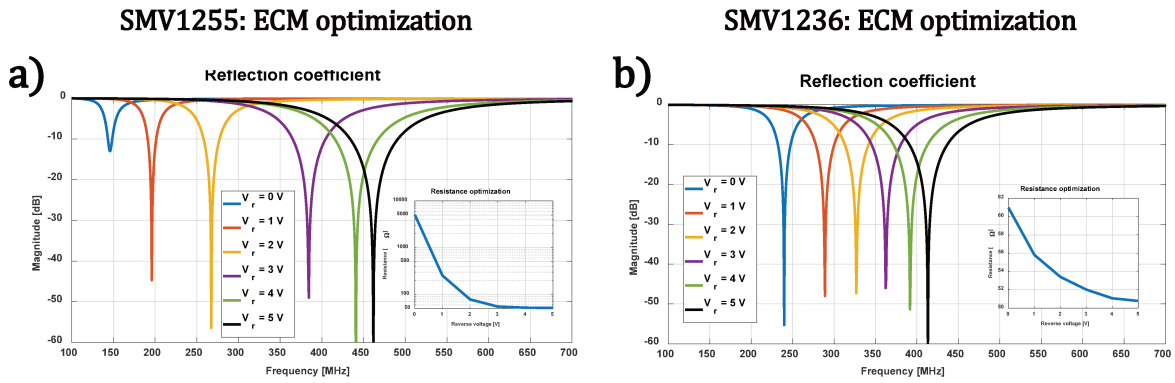

Figure II.16 : Reflection coefficient S_{11} of the frequency-tunable metasurface-based radar absorber from the ECM over [100, 700] MHz for reverse biasing values of $V_r = [0, 5]$ V with the standard $R_{MS} = 50\ \Omega$ (dashed) and optimized overall resistance R_{MS} values (solid) for high absorption for a metasurface using the (a) SMV1255 and (b) SMV1236 models.

It appears that the metasurface using the SMV1255 varactor diode model still exhibits a high ratio $R_{opt}(0)/R_{opt}(5) = 100$, which may still be difficult to cover. However, the metasurface using the SMV1236 model, along with a high-absorption even at $V_r = 0$ V, exhibits a resistance ratio of a mere $R_{opt}(0)/R_{opt}(5) = 1.2$. While losing coverage from a smaller capacitive range, this one metasurface may lead to a highly performing radar absorber in terms of maximum absorption with an average -50 dB reflection coefficient's minimal magnitude.

The results of this numerical study highlight the possibility for a high-performance MBRA using a joint tuning of capacitance and resistance. The impedance matching metasurface using the SMV1249 varactor diode model may not be the most appropriate candidate for a joint tuning of resistance and capacitance because of the high ratio between required resistance values at lower and higher voltages. However, its reflection coefficient may still be greatly improved in terms of absorption rates over a large part of its covered frequency range thanks to a tunable resistance. It also appeared other varactor diode models may be even more suitable as candidates, such as the SMV1236, which is already close to the optimal response from the standard $R_{MS} = 50\ \Omega$. However, such MBRA lacks in effective bandwidth, covering from 260 MHz to 465 MHz, losing around 80 MHz compared to the SMV1249 varactor-loaded MBRA. Therefore, in order to study both absorption magnitude and absorption bandwidth, next Section 5.2 deals with a temporally controlled metasurface for an effectively wideband radar absorber.

5.2. Experimental investigation into an effectively wideband metasurface-based radar absorber thanks to a temporal control of biasing voltage against a frequency-hopping radar

Aware of the design constraints of radar absorbers, radars have been developed to take advantage of the narrow bandwidths: by probing space at different frequencies, some may escape the RAM's operating range and betray the presence of the target. These frequency-hopping radars can be set to periodically explore a range of frequencies, and only wideband RAM solutions can effectively serve as countermeasures. For instance, a frequency-tunable MBRA, thanks to an effective wideband absorption, and under the right temporal control, can be used to oppose such radars.

5.2.1. Ideal absorption profile

From the reflection coefficient curves of the frequency-tunable MBRA from Figure II.13, it appears this system displays a rather wideband effective bandwidth. In fact, as previously stated, the covered range extends from around 300 MHz to 620 MHz, with magnitudes below -10 dB from at least $V_r = 2$ V. Therefore, one may want to benefit from this covered range against a frequency-hopping radar system by continuously adapting to the incoming frequency. From a finer frequency-tuned measurement of the radar absorber, it appears in Figure II.17 the optimized coverage would reach a bandwidth of 71% around 450 MHz.

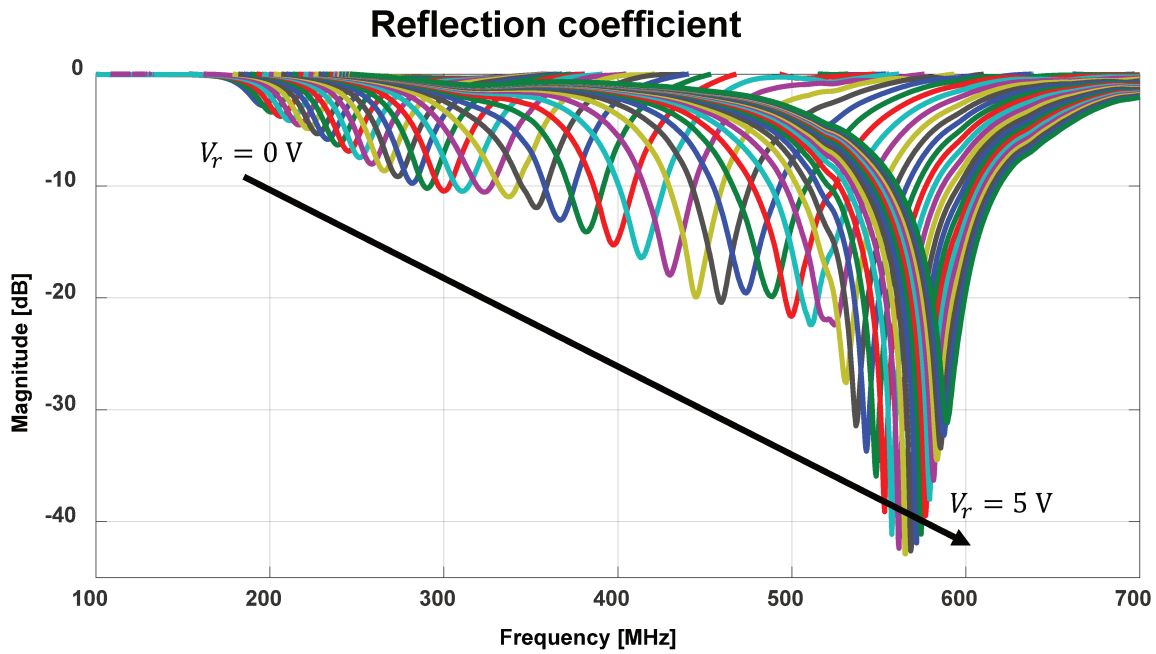

Figure II.17 : Reflection coefficient S_{11} of the frequency-tunable metasurface-based radar absorber from measurements over $[100, 700]$ MHz for reverse biasing values of $[0, 5]$ V with 0.1 V step.

In Figure II.17, the measurements of the reflection coefficient of the frequency-tunable metasurface-based radar absorber using the SM1249 varactor diode model have shifted from the values observed in Figure II.13. This most probably originates from the maintenance the enlarged coaxial waveguide underwent in between both studies. In any case, this does not invalidate this study whose objective is to try and provide a general idea of the potential broadband coverage offered by a time-controlled MBRA.

5.2.2. Experimental validation of the temporally-controlled frequency-tuned metasurface-based radar absorber

In this experimental validation, a working hypothesis is formulated regarding the adversary radar system: it is used in a frequency-sweeping mode, characterized by both its operational frequency range and sweeping time T_{sweep}. In this work, the operational frequency range is supposed to be 100 – 700 MHz, and the sweeping time T_{sweep} is a known variable on the target's end. To be able to reach the maximum bandwidth, the time-based pattern to apply to the frequency-tunable radar absorber must match the changes in operating frequency from the radar system. However, as highlighted in Figure II.18(a), too fast or too slow a change in absorption frequency and the absorption bandwidth is entirely missed. In fact, too fast a voltage-sweeping speed and the associated resonance frequency is way beyond the actual frequency emitted by the radar. Similarly, too slow a voltage-sweeping speed and the resonance frequencies are lagging behind the impinging frequency. Therefore, in order to find the right time-based pattern for voltage-sweeping, a first approach may consist in finding the more appropriate sweeping speeds ratios. In fact, in between the "too slow" and "too fast" speeds of Figure II.18(a), some speeds appear particularly interesting in the bandwidth offered by the linear voltage sweep, as provided in Figure II.18(b).

As can be noticed, the bandwidth offered by such a temporally controlled MBRA is highly sensitive to the voltage-sweeping speed. For instance, the blue curve of Figure II.18(b), though "wideband", only offers below -10 dB reflection over 540 MHz and 610 MHz, where it suddenly

drops. Then, a 5% increase in speed leads to the red curve, which blueshifts this absorption to 500 MHz to 600 MHz, broadening up to 20% of bandwidth at 500 MHz. Finally, another mere 5% speed increase leads to the yellow curve, whose minimum magnitude is slightly increased, but its bandwidth now reaches 35% at 500 MHz, right before it drops under 20% with another 5% speed increase as displayed in the purple curve.

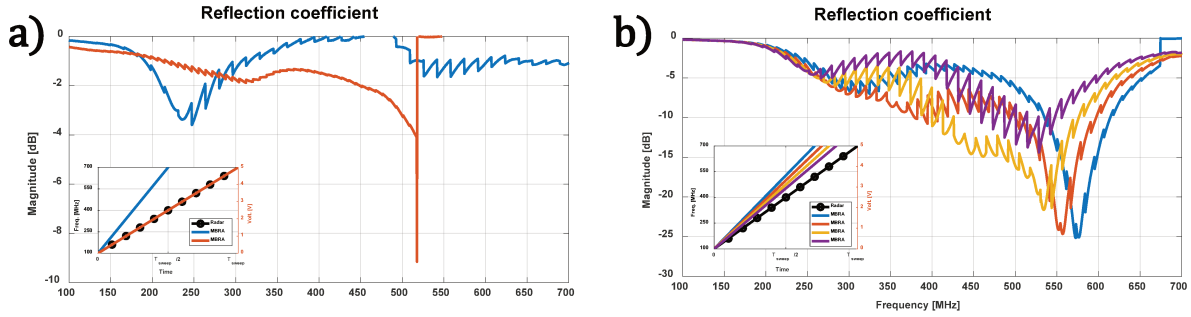

Figure II.18 : (a) Reflection coefficient S_{11} of the time-controlled frequency-tunable metasurface-based radar absorber from measurements over [100, 700] MHz for reverse biasing values of [0, 5] V with 0.1 V step sweeping (blue) too slow (50%) and (red) too fast (100%) in regards to the radar's frequency sweeping speed. (b) Reflection coefficient S_{11} of the time-controlled frequency-tunable metasurface-based radar absorber from measurements over [100, 700] MHz for reverse biasing values of [0, 5] V with 0.1 V step sweeping at (blue) 70%, (red) 75%, (yellow) 80% and (purple) 85% of the radar's frequency sweeping speed.

Obviously, the issue of finding the right voltage-sweeping speed is also rooted in the fact that Figure II.17 highlights the non-linearity of the resonance frequency with biasing voltage. To properly integrate this behavior, one may resort to extracting the (V_r, f_r) couples of Figure II.17, before interpolating the voltage values to a time-based pattern that linearizes the resonance frequency exploration in time. Finding the proper pattern duration to radar frequency-sweeping speed ratio then should offer the wideband absorption hinted at in Figure II.17. This experimental validation could not be performed in the limited time of this thesis.

On top of this fine-tuned time-control of the MBRA, one must bear in mind such frequency-hopping radars do not cover as much bandwidth as investigated here. In fact, at lower frequencies, such as over the VHF-UHF bands, they usually offer some tens of megahertz of operating bandwidth. Therefore, despite the difficulty to properly set the voltage-sweeping speed in regards to the frequency-hopping speed is greatly reduced over such smaller ranges. Indeed, in such a case, the non-linearity of the resonance frequency with respect to the reverse biasing can be better approximated by easy-to-set linear voltage sweeps. However, the electronic to be loaded onto the MBRA must be carefully planned for it to benefit from the maximum absorption over the largest bandwidth, such as from 400 MHz to 575 MHz for the yellow curve of Figure II.18(b).

6. Conclusions

In this Chapter II, I designed and experimentally validated two MBRA over the VHF-UHF frequency bands. The entire design process is based on a two-step approach: an ECA highlights the requirements for the necessary impedance matching metasurface and FEM simulations are used to validate the resulting MBRA. From an increasingly more complex geometry, simulations confirmed the ECM is a good descriptor of a rotation-invariant MBRA, but overlooks some higher-order interactions. This manifests as a slight absorption frequency shift and overestimation of

impedance matching, but still provides a valid and fast first estimate. In fact, the measured reflection coefficient of the MBRA with fixed absorption frequency is in good accordance with 3D FEM simulation results, further validating the two-step approach for the following design of the frequency-tunable MBRA. Substituting capacitors for varactor diodes, the resonance frequency of the RLC circuit of the MBRA can be tuned to the adversary radar's frequency, where absorption can be obtained with levels below -10 dB from around 300 MHz to 600 MHz. However, the introduction of parasitic resistive elements to the metasurface lead to undesired minimum reflection coefficient magnitudes variations, which are strongly dependent on the considered varactor diodes. Thereby, justifying the need for a joint tuning of the metasurface's resistance and capacitance for compensation on the fly and near-perfect absorption over the entire covered range.

This frequency-tunable MBRA here introduced is a relatively common metasurface-based solution to stealth. However, despite the need for some further developments toward operational viability, it is most suitable to the constraints of working over the VHF-UHF bands, thanks to its low-profile and wide effective bandwidth. Moreover, thanks to the use of varactor diodes, the metasurface can be continuously tuned to face different threats, such as frequency-hopping radars. In fact, the use of varactor diodes is particularly appropriate to bridging the gap between reconfigurable and modulated devices, since they can be addressed with biasing and AC signals alike. Changing the equivalent MBRA circuit from RLC to LC, one can use the short-circuited metasurface as a phase-inducing device, no longer serving detection deceiving strategies, but target parameter tempering strategies such as Doppler cloaking, as developed in the next Chapter.

III. Development and experimental validation of a metasurface-based frequency converter over the VHF-UHF bands

CONTENTS

III. DEVELOPMENT AND EXPERIMENTAL VALIDATION OF A METASURFACE-BASED FREQUENCY CONVERTER OVER THE VHF-UHF BANDS 81

1. INTRODUCTION 82
2. SPECTRUM MANIPULATION USING A TIME-MODULATED METASURFACE 83
   2.1. Frequency conversion by time-modulation of a reflecting surface 83
   2.2. Analytical studies of frequency converting time-modulated systems 84
      2.2.1. Analytical model of an ideal frequency converter 84
      2.2.2. Analytical model of a non-ideal frequency converter 86
3. DEVELOPMENT AND EXPERIMENTAL VALIDATION OF A METASURFACE-BASED FREQUENCY CONVERTER FOR THE FREQUENCY-CONVERSION OF HARMONIC SIGNALS 88
   3.1. Design of the metasurface for a metasurface-based frequency converter and modulation of the reflection coefficient 88
      3.1.1. Capacitive metasurface for the metasurface-based frequency converter 89
      3.1.2. Frequency-converting modulation scheme 89
      3.1.3. Geometry of the metasurface 91
   3.2. 2D analytical, numerical and semi-analytical studies of the metasurface-based frequency converter for an incident signal of frequency $f0 = 300$ MHz and modulation frequency $fm = 1$ MHz ... 92
      3.2.1. Analytical study of the metasurface-based frequency converter from an equivalent circuit analysis 94
      3.2.2. Numerical study of the metasurface-based frequency converter from a 2D axisymmetric FETD simulation 97
      3.2.3. Semi-analytical study of the metasurface-based frequency converter from a 2D axisymmetric FEM simulation and analytical conversion computation 98
   3.3. 3D semi-analytical study of the metasurface-based frequency converter for an incident signal of frequency $f0 = 300$ MHz and modulation frequency $fm = 1$ MHz 99
   3.4. Experimental validation of a time-modulated metasurface for the frequency-conversion of harmonic waves at $f0 = 370$ MHz 100
      3.4.1. Experimental setup for the time-domain measurement of the metasurface-based frequency converter 100
         3.4.1.1. Enlarged coaxial waveguide setup for frequency-domain measurement 100
         3.4.1.2. Enlarged coaxial waveguide setup for time-domain measurement 101
         3.4.1.3. Practical constraints of the fabrication of the metasurface 102
      3.4.2. Design of the metasurface and frequency-domain measurement of the reflection coefficient of the metasurface-based frequency converter 103
      3.4.3. Time-domain measurement of the frequency shifting of an harmonic wave at $f0 = 370$ MHz by the time-modulation of the metasurface-based frequency converter 105
         3.4.3.1. Frequency conversion degradation with increasing modulation frequency fm 108
4. EXPERIMENTAL VALIDATION OF A METASURFACE-BASED FREQUENCY CONVERTER FOR THE FREQUENCY-CONVERSION OF NON-HARMONIC WAVES 108
   4.1. Analytical justification of the existence of a frequency conversion bandwidth 109
   4.2. 2D Analytical and numerical studies of the metasurface-based frequency converter for an incident non-harmonic signal of center frequency $f0 = 300$ MHz and modulation frequency $fm = 1$ MHz 110
      4.2.1. Analytical study of the metasurface-based frequency converter from an equivalent circuit analysis for a continuous train of chirp signals 111

4.2.2. Numerical study of the metasurface-based frequency converter from a 2D axisymmetric FETD simulation for a continuous train of chirp signals 112
4.3. Experimental validation of a time-modulated metasurface for the frequency-conversion of non-harmonic waves around $f0 = 370$ MHz 114
5. CONCLUSIONS 115

1. Introduction

In this Chapter III, I design and analyze the behavior of a metasurface-based frequency converter (MBFC) in the VHF-UHF frequency bands. To this end, I use an equivalent circuit approach for the design process, backed by finite-element simulations performed in both the frequency- and time-domains. Under specific conditions, the modulation in time of the MBFC's reflection coefficient leads to frequency conversion, which is intended to serve for Doppler cloaking purposes. Using a purely capacitive metasurface as reference, I first shed light on the undesirable effects from a non-ideal phase shift. Then the undesirable effects from the parasitic elements of varactor diodes are also predicted and quantified with three different models. In the end, a metasurface is manufactured and tested against harmonic and non-harmonic signals, confirming the frequency shifting and highlighting the existence of a non-zero conversion bandwidth. This would prove useful when facing real radar systems, such as FMCW radars.

In Section 2, I first introduce the slow-modulation framework used in this thesis allowing for adiabatic manipulation of electromagnetic fields. In particular, a MBFC with a linearly varying phase in time can offer frequency conversion upon reflection. In practice, however, a practical MBFC hardly ever displays the ideal 2π phase shift, which leads to the existence of an infinite number of non-zero harmonics in the reflected wave's spectrum.

In Section 3, a metasurface loaded with perfectly capacitive elements is introduced as an interesting MBFC candidate, along with an illustrative capacitance modulation. In a first step, such a MBFC is modulated in capacitance in order to linearize the phase at the incident wave's frequency $f_0 = 300$ MHz to confirm the frequency shifting mechanism by $f_m = 1$ MHz. The investigation is led with three models: a purely analytical one using an Equivalent Circuit Model (ECM), a purely numerical one using a Finite Element Model (FEM), and a semi-analytical one, which is the hybridization of the previous two. In all three models, variable capacitive elements are either ideally capacitive or varactor diodes. Studies are performed for a 2D axisymmetric configuration, and extended to the 3D configuration for higher accuracy. Results confirm that parasitic elements of varactor diodes do not compromise the frequency conversion, but introduce an undesired amplitude modulation. Finally, a metasurface is manufactured and the MBFC is measured, confirming the frequency shifting of the incident wave upon reflection.

In Section 4, the same MBFC is used against incident non-harmonic waves, especially those of FMCW radar systems. The existence of a frequency conversion bandwidth is first justified by an analytical study of the phase profiles around the center frequency at which phase is linearized. Confirmed by further analytical and numerical investigations, the incident wave of the experimental setup is changed to a non-harmonic wave to highlight the frequency conversion bandwidth offered by the considered MBFC.

2. Spectrum manipulation using a time-modulated metasurface

In this Section 2, I first introduce the considerations for a time-modulated reflective surface, allowing spectral manipulation through careful tailoring of the reflection coefficient. I then apply these considerations to the analytical study of an ideal frequency converter, in order to highlight the ideal behavior from which the non-ideal frequency converter will depart.[1]

2.1. Frequency conversion by time-modulation of a reflecting surface

In order for a time-modulated system to manipulate the reflected electric fields without significant energy exchange between waves and modulation, the considered system must be seen as static at all times by any impinging wave [89]. In other words, for T_0 the characteristic period of the impinging wave and T_m the modulation period, then, as specified in [102]

$$T_m \gg T_0 \tag{III.1}$$

This scaling ensures the modulated system lies in the stationary regime while undergoing constant modulation. In fact, this grants the existence of two time regimes: a slow time and a fast time. In such a case, at a given frequency ω_0, the incident electric field $\boldsymbol{E_i}$, reflected electric field $\boldsymbol{E_r}$ and reflection coefficient Γ are linked by the relationship

$$\boldsymbol{E_r}(t, \omega_0) = \Gamma(t, \omega_0)\boldsymbol{E_i}(t, \omega_0) \tag{III.2}$$

In this thesis, no polarization is considered, thus Γ is scalar. However, it could be extended to a 2x2 matrix for H, V polarizations. To clear up any confusion: the considered field can be seen as the coaxial equivalent to a linearly polarized electric field as it is orthogonal to the metasurface aperture.

As long as the two-time segregation $T_m \gg T_0$ is ensured, then the time-domain relationship of Equation (III.2) has a simple frequency-domain expression

$$\widetilde{\boldsymbol{E}}_{\boldsymbol{r}}(\omega, \omega_0) = \tilde{\Gamma}(\omega, \omega_0) * \widetilde{\boldsymbol{E}}_{\boldsymbol{i}}(\omega, \omega_0) \tag{III.3}$$

where ~ denotes the Fourier transform.

From Equation (III.3), it therefore appears that from careful time-domain tailoring of the reflection coefficient, the spectrum of the reflected field can be purposefully shaped. In particular, to ensure frequency shifting of the reflected field with respect to the incident field, a reflection coefficient exhibiting a phase ramp over the modulation period T_m is most appropriate due to the existence of the following Fourier transform pair

$$e^{\pm j\omega_m t} \rightleftharpoons \delta(\omega \mp \omega_m) \tag{III.4}$$

The frequency shifting abilities of such a time-modulated MBFC are harnessed in a stealth strategy called *Doppler cloaking*. Indeed, a moving target illuminated by a radar, backscatters a frequency-shifted wave, which bears information on the target's velocity. In fact, even cloaked targets may lose their invisibility when in motion [121]. Therefore, as introduced in [105], compensating the Doppler shift thanks to a frequency converter can solve this issue. Many subsequent developments arose from this concept [106], [107], [108], [109]. In this thesis, only the frequency converting element of the Doppler cloak is studied. A proper deployment would require a platform with an accelerometer, for the velocity information, an impinging frequency sensor, for the radar's central frequency and the frequency shifter, for the Doppler compensation.

[1] The case of a transmissive MBFC is tackled in [120].

From the considerations here exposed, it appears any time-modulated reflective system can be used as a frequency converter under two conditions. First, one has to ensure the two-time segregation by choosing a modulation frequency much smaller than that of the impinging wave, *i.e.* $f_m \ll f_0$. Second, the time-modulated system's reflection coefficient must exhibit a linear phase change of 2π over the modulation period T_m. To be more accurate, this phase change also has to exhibit a monotonous variation over the modulation period. This is a necessary condition to ensure the existence of a unique inverse function.

2.2. Analytical studies of frequency converting time-modulated systems

2.2.1. Analytical model of an ideal frequency converter

An ideal frequency converter is defined as a system that exhibits the required 2π phase shift over the considered modulation range. For a system modulated through its reactance X, then the phase variation of an ideal frequency converter between two values X_1 and X_2 is

$$\angle\Gamma(X_1) - \angle\Gamma(X_2) = \pm 2\pi \tag{III.5}$$

In order to linearize the phase over a modulation period T_m, the phase needs to be smoothly varying over the considered range at the frequency f_0 to alter. Then, the values of X between X_1 and X_2 can be remapped in time to linearize the phase over a modulation period T_m, such that

$$\angle\Gamma(t) = \varphi_1 \pm \frac{2\pi}{T_m} t \tag{III.6}$$

where $\varphi_1 = \angle\Gamma(X_1)$ such that $\angle\Gamma(X_2) - \angle\Gamma(X_1) = +2\pi$ leads to an up-conversion, and $\angle\Gamma(X_2) - \angle\Gamma(X_1) = -2\pi$ to a down-conversion. In such a case, the periodically time-modulated reflection coefficient can be expressed as

$$\Gamma(t) = \left(e^{\pm j\omega_m t} \mathrm{rect}\left(\frac{t - T_m/2}{T_m} \right) \right) * \sum_{n=-\infty}^{+\infty} \delta(t - nT_m) \tag{III.7}$$

where $rect$ is the rectangular window function centered around 0. It was decided to alleviate the notation by assuming the modulation starts at an arbitrary time defined as the time origin and by removing the phase value associated to such a time, given what matters is only the phase variation over T_m.

The resulting reflection coefficient's phase is provided in Figure III.1(a) over a duration of five modulation periods T_m, for both an upward and downward varying phase, granting up- or down-conversion. For illustration purposes, it was decided to consider a system whose phase variation occurs between $\varphi_1 = \pm\pi$ and $\varphi_2 = \mp\pi$, but any two phase values can be used as long as they are separated by $\pm 2\pi$. The resulting modulated reflection coefficient is the serrodyne frequency translating phase modulation [120], [122], [123], [124].

In the frequency-domain, the time-domain reflection coefficient of Equation (III.7) turns into the spectrum

$$\tilde{\Gamma}(\omega) = W(\omega) \sum_{n=-\infty}^{+\infty} \delta(\omega - n\omega_m) \tag{III.8}$$

with W a weighting function such that

$$W(\omega) = \mathrm{sinc}\left(\frac{\omega \mp \omega_m}{2} T_m \right) e^{-j(\omega \mp \omega_m)T_m/2} \tag{III.9}$$

In Figure III.1(b), the normalized amplitudes of the weighting function W, the Dirac comb and resulting frequency-domain reflection coefficient $\tilde{\Gamma}$ are provided for illustration.

As can be observed in Figure III.1(b), for both the up- and down-conversion schemes, the cardinal sine function of the weighting function W finds its zeros at $\omega = (k \pm 1)\omega_m, k \in \mathbb{Z}^*$. As it turns out, this means the only Dirac pulse from the Dirac comb that is not weighted by a zero of the cardinal sine is the one at $k = 0$, *i.e.* $\omega = \pm\omega_m$. Therefore, Equation (III.8) is greatly simplified

$$\tilde{\Gamma}(\omega) = \delta(\omega \pm \omega_m) \tag{III.10}$$

From Equation (III.3), one can then notice that perfect frequency shifting is granted, since

$$\widetilde{\boldsymbol{E}}_{\boldsymbol{r}}(\omega) = \widetilde{\boldsymbol{E}}_{\boldsymbol{i}}(\omega \mp \omega_m) \tag{III.11}$$

After interaction with the time-modulated ideal frequency converter, the reflected electric field is provided in Figure III.1(c), in comparison to the harmonic incident electric field, set at an arbitrary frequency $f_0 \gg f_m$. Both fields are analyzed as power spectral densities (PSD) to highlight the power-bearing frequencies around the incident wave's frequency f_0. Throughout this work, in all PSD figures, the reflected wave's spectrum is normalized in regards to the incident wave's spectrum.

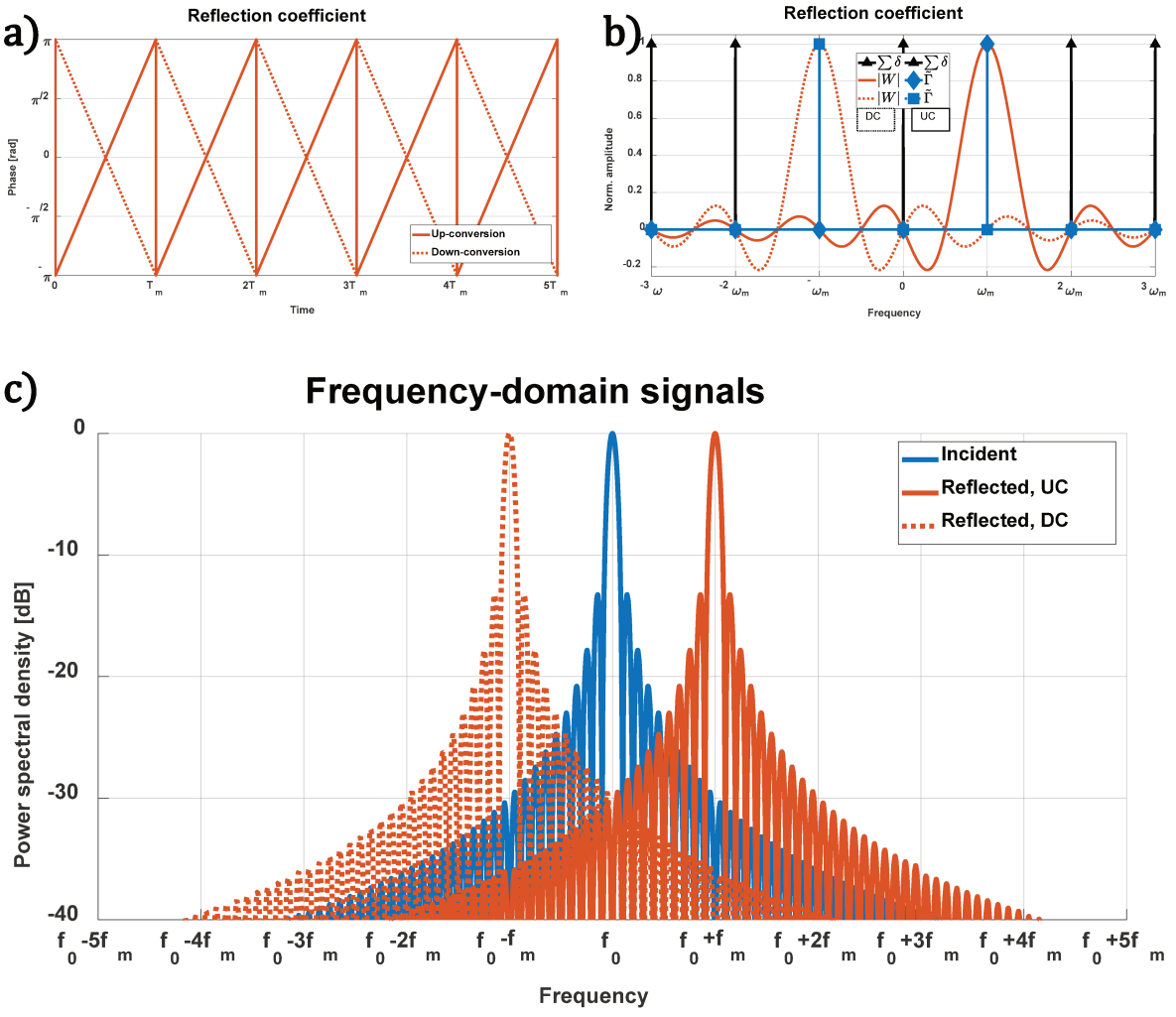

Figure III.1 : (a) Time-domain phase of the reflection coefficient at an arbitrary frequency f_0 for the ideal (solid) up- and (dashed) down-conversion of incident signals. (b) Normalized amplitude (blue) of the frequency-domain reflection coefficient of an ideal frequency converter, with the periodicity-induced Dirac comb (black) and weighting function's module (red), for both (solid) up- and (dashed) down-conversion, namely *UC* and *DC*. (c) Relative power spectral

density of the (blue) incident and (red) reflected signals for an harmonic impinging wave after the ideal (solid) up- and (dashed) down-conversion from f_0 by f_m, namely *UC* and *DC*.

As can be observed in Figure III.1(c), the harmonic incident field at frequency f_0 is entirely shifted up or down by the modulation frequency f_m, without any distortion. This is the ideal behavior of a frequency converting system.

2.2.2. Analytical model of a non-ideal frequency converter

However, frequency-converting devices do not always exhibit this ideal 2π phase shift over a modulation period. In such a case, then Equation (III.5) turns into

$$\angle\Gamma(X_1) - \angle\Gamma(X_2) = \alpha 2\pi \tag{III.12}$$

where $|\alpha| \leq 1$ is a fraction of the ideal phase, whose sign indicates the upward or downward nature of the phase shift. Despite the reduced phase variation, a smoothly varying phase at the considered frequency f_0 can still be linearized in time. This leads to the time-domain periodic reflection coefficient

$$\Gamma(t) = \left(e^{\pm j\alpha\omega_m t}\mathrm{rect}\left(\frac{t - T_m/2}{T_m}\right)\right) * \sum_{n=-\infty}^{+\infty}\delta(t - nT_m) \tag{III.13}$$

In Figure III.2(a), the resulting modulated phase is provided for both up- and down-conversion with a non-ideality coefficient $|\alpha| = 0.9$. Once again, it is arbitrarily decided to consider a system whose phase variation occurs between $\varphi_1 = \left(1 \pm \frac{1-|\alpha|}{2}\right)\pi$ and $\varphi_2 = \left(1 \mp \frac{1-|\alpha|}{2}\right)\pi$, separated by $\alpha 2\pi$.

In the frequency-domain, this reflection coefficient then turns into

$$\tilde{\Gamma}(\omega) = W_\alpha(\omega)\sum_{n=-\infty}^{+\infty}\delta(\omega - n\omega_m) \tag{III.14}$$

with W_α the α-related weighting function such that

$$W_\alpha(\omega) = \mathrm{sinc}\left(\frac{\omega \mp \alpha\omega_m}{2}T_m\right)e^{-j(\omega\mp\alpha\omega_m)T_m/2} \tag{III.15}$$

In the non-ideal case, the Dirac comb, W_α weighting function's cardinal sine and resulting reflection coefficient of Equation (III.14) are provided in Figure III.2(b).

In Figure III.2(b), one may notice that the weighting function's zeros and the elements of the Dirac comb no longer superimpose: the center frequency of the cardinal sine is shifted from ω_m to $\alpha\omega_m$. Therefore, the resulting reflection coefficient $\tilde{\Gamma}$ no longer reduces to a singular element of the Dirac comb, but the entire Dirac comb remains albeit with weights decreasing away from the first harmonic. In such a case, the spectrum of the reflection coefficient cannot be simplified as done in Equation (III.10). From equation (III.3), it therefore appears the reflected field's spectrum is an infinite sum of weighted copies of the spectrum of the incident field, such that

$$\widetilde{\boldsymbol{E}}_{\boldsymbol{r}}(\omega) = \sum_{n=-\infty}^{+\infty} W_\alpha(n\omega_m)\widetilde{\boldsymbol{E}}_{\boldsymbol{i}}(\omega - n\omega_m) \tag{III.16}$$

After interaction with such a time-modulated, non-ideal frequency converter, the reflected electric field is provided in Figure III.2(c), in comparison to the harmonic incident electric field.

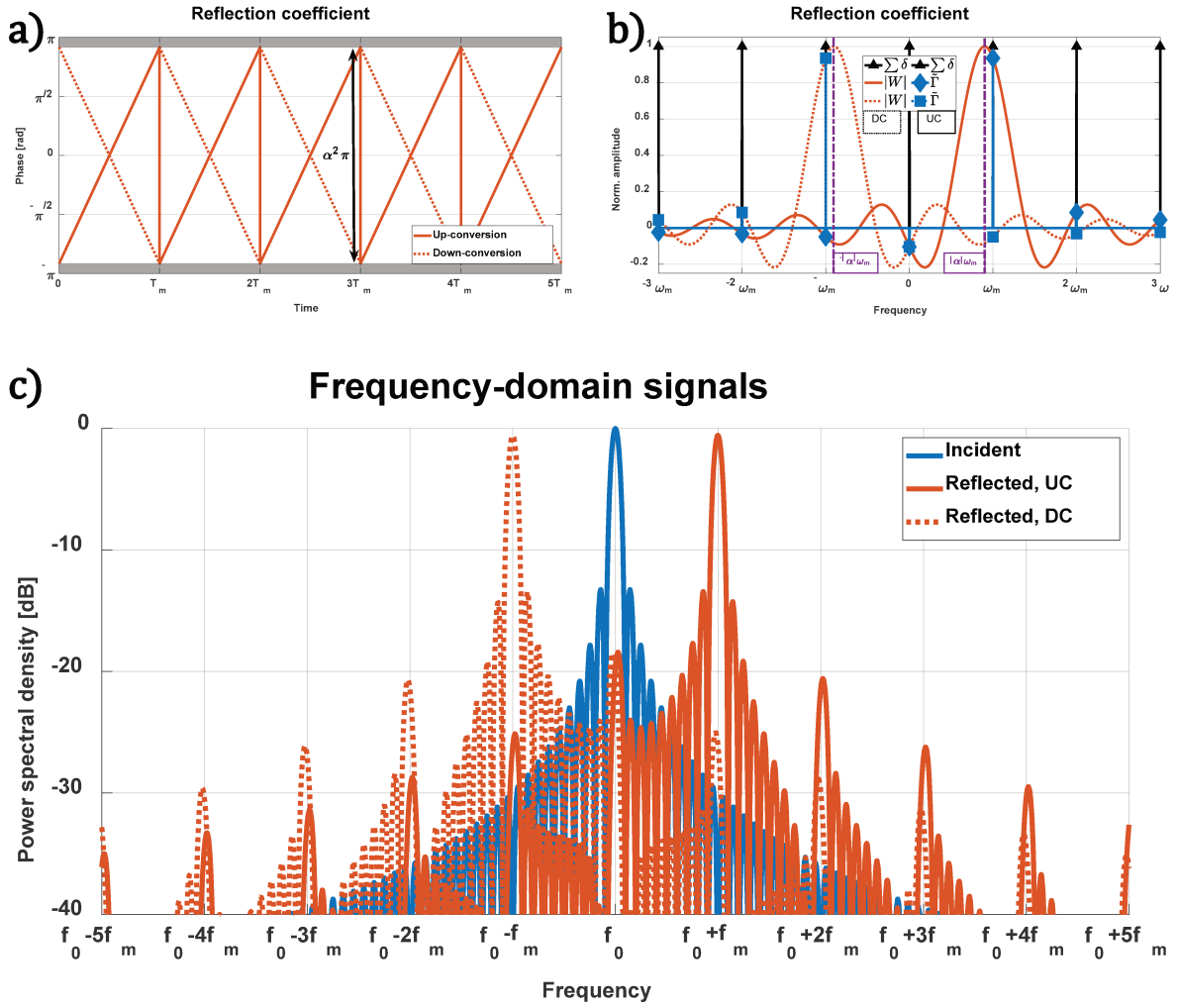

Figure III.2 : (a) Time-domain phase of the reflection coefficient at an arbitrary frequency f_0 for the non-ideal (solid) up- and (dashed) down-conversion of incident signals, with a non-ideality factor $|\alpha| = 0.9$. (b) : Normalized amplitude (blue) of the frequency-domain reflection coefficient of a non-ideal frequency converter of non-ideality factor $\alpha = 0.9$, with highlight of the Dirac comb (black) and weighting function's module (red), for (solid) up- and (dashed) down-conversion , namely *UC* and *DC*. (c) Relative power spectral density of the (blue) incident and (red) reflected fields for an harmonic impinging wave after the non-ideal, $|\alpha| = 0.9$, (solid) up- and (dashed) down-conversion from f_0 by f_m, namely *UC* and *DC*.

As can be observed in Figure III.2(c), both the up- and down-converted signals are not exactly shifted copies of the incident signal. In fact, it appears that both spectra are now plagued by numerous spurious power-bearing harmonics. These harmonics are W_α-weighted copies of the incident spectrum, as predicted in Equation (III.16). In other words, the non-ideal phase variation introduces, in the spectrum of the reflected field, an infinite number of copies of the incident field's spectrum, weighted by a cardinal sine function which prioritizes power shifting to the frequencies closest to $\alpha\omega_m$. The resulting reflected field's spectrum is therefore strongly dependent on the value of α. However, it is important to notice that despite the weight functions being off-centered due to the α coefficient, the power-bearing frequencies of Figure III.2(c) are all still found at harmonics of the modulation frequency, *i.e.* $f_0 + (n \pm 1)f_m, n \in \mathbb{Z}^*$. In fact, taking a look at Equation (III.16), the frequencies onto which the incident field's spectrum is replicated are dictated by the frequency-domain Dirac comb, set to the modulation frequency f_m. Finally, one may notice a slight magnitude imbalance in terms of opposing harmonics around the specular

harmonic. This is caused by the associated coefficients of the weighted Dirac comb of Figure III.2(b): the weights of the even harmonics $f_0 + 2nf_m, n \in \mathbb{Z}^*$ are larger than those of the odd ones $f_0 + (2n+1)f_m, n \in \mathbb{Z}^*$ by definition of the cardinal sine function.

From Equation (III-1), one may notice the α fraction is a critical value in the frequency-shifting process. In fact, as long as $|\alpha| > 0.5$ the conversion favors the harmonic at $f_0 \pm f_m$ and similarly favors f_0 for $|\alpha| < 0.5$. This can also be seen from the curves of Figure III.2(b). More details on this topic can be found in Appendix 0.

From the results of Figure III.1, it clearly appears that, from a reflection phase linearly varying in time, one can achieve perfect frequency shifting of the incident wave. However, frequency converting systems do not always display an ideal 2π phase variation over the considered modulation period, but rather a fraction α of it. Therefore, as it appears in Figure III.2(c), this non-ideality manifests in the reflected field's spectrum as an infinite sum of periodically spaced copies of the incident field. Nonetheless, this does not prevent frequency shifting in any shape or form. In fact, as long as $|\alpha| > 0.5$, most of the power of the reflected field is still found at the desired frequency $f_0 \pm f_m$. In the next Section 3, after introduction of a capacitance-tunable metasurface for the metasurface-based frequency converter, analytical, numerical and semi-analytical investigations are conducted. As established in Chapter II, this is done in order to validate the ECM as a good rotation-invariant descriptor when compared to 2D axisymmetric simulations. All three methods are compared using three distinct metrics, quantifying the frequency conversion and Doppler shift compensation. Finally, a 3D semi-analytical study is led in order to provide a more accurate analysis, using 3D full-wave simulations for the reflection coefficient and the analytical relationship of Equation (III.3).

3. Development and experimental validation of a metasurface-based frequency converter for the frequency-conversion of harmonic signals

In this Section 3, the phase requirements for a functional MBFC are laid out, in order to highlight the suitability of a purely capacitive, but tunable, metasurface from an ECA. The requirements are then transposed to the coaxial metasurface structure (see Figure II.3) using capacitors and/or varactor diodes. The frequency conversion offered by the newly formed *LC* circuit is then validated using an analytical, a numerical and a semi-analytical model for the 2D axisymmetric configuration of the MBFC.

The development of Section 3.1 and validation stage of Section 3.2 of the MBFC are done using either a perfect capacitor or a varactor diode as the modulated component, a varactor diode providing results closer to practical measurements. This is done in order to highlight the impact of parasitic elements introduced by varactor diodes. Finally, a metasurface is manufactured and the MBFC is experimentally validated against an incident harmonic wave set at $f_0 = 300$ MHz for a Doppler compensation of $f_m = 1$ MHz.

3.1. Design of the metasurface for a metasurface-based frequency converter and modulation of the reflection coefficient

In this Section 3.1, an ECA is used in order to clearly highlight the requirements for a functional MBFC. The obtained ECM is then used to model a metasurface with variable capacitance.

3.1.1. Capacitive metasurface for the metasurface-based frequency converter

The MBFC of interest must be designed in the same configuration as in Chapter II: a metasurface is located a short-distance away from its ground plane, which acts as a parallel inductance. Therefore, considering a metasurface of admittance Y_{MS}, the reflection coefficient Γ of the short-circuited metasurface – making up the MBFC of interest – at a given frequency ω_0 is such that

$$\Gamma(Y_{MS}, \omega_0) = \frac{Y_0 - Y_{in}(\omega_0)}{Y_0 + Y_{in}(\omega_0)} = \frac{Y_0 - \left(Y_{MS}(\omega_0) + \frac{1}{j\omega_0 L_{SC}}\right)}{Y_0 + \left(Y_{MS}(\omega_0) + \frac{1}{j\omega_0 L_{SC}}\right)} \tag{III.17}$$

The phase of this reflection coefficient can be expressed as

$$\angle\Gamma(Y_{MS}, \omega_0) = \operatorname{atan}\left(-\frac{Im(Y_{MS}(\omega_0)) - \frac{1}{\omega_0 L_{SC}}}{Y_0 - Re(Y_{MS}(\omega_0))}\right) - \operatorname{atan}\left(\frac{Im(Y_{MS}(\omega_0)) - \frac{1}{\omega_0 L_{SC}}}{Y_0 + Re(Y_{MS}(\omega_0))}\right) \tag{III.18}$$

It appears that, with a purely reactive metasurface, one can simplify the reflection coefficient to

$$\angle\Gamma(Y_{MS}, \omega_0) = -2\operatorname{atan}\left(\frac{\omega_0 L_{SC} Im(Y_{MS}(\omega_0)) - 1}{\omega_0 Y_0 L_{SC}}\right) \tag{III.19}$$

which can be modulated through its reactance $X(\omega_0) = Im(Y_{MS}(\omega_0))$, as introduced in Equation (III.5) and Equation (III.12).

In such a case, the removal of any resistive element from the metasurface ensures the monotony of the phase variation, granted by the arctangent function. Therefore, from variations of the reactive elements of the metasurface, the phase values can be remapped in time to linearize it over the modulation period.

In fact, such a purely reactive metasurface leads to a frequency converter whose phase variation is bound between two extreme values

$$\begin{cases} \lim\limits_{Im(Y_{MS}(\omega_0))\to 0} \angle\Gamma = 2\operatorname{atan}(1/\omega_0 Y_0 L_{SC}) < \pi \\ \lim\limits_{Im(Y_{MS}(\omega_0))\to +\infty} \angle\Gamma = -\pi \end{cases} \tag{III.20}$$

One can notice from Equation (III.20), that increasing $Im(Y_{MS}(\omega_0))$ towards infinity leads to a phase value of $-\pi$, but decreasing $Im(Y_{MS}(\omega_0))$ towards 0 leads to a phase value bound by the considered frequency ω_0, the incident wave's impedance Y_0 and the short-circuit's inductance L_{SC}. Therefore, the ideal 2π phase shift cannot be granted in practice by such a system, though it can get close to it provided that $\omega_0 Y_0 L_{SC} \ll 1$.

For instance, one can use a purely capacitive metasurface, whose admittance is purely imaginary with $Im(Y_{MS}) = \omega C_{MS}$, such that the reflection coefficient's phase is

$$\angle\Gamma(C_{MS}, \omega_0) = -2\operatorname{atan}\left(\frac{\omega_0^2/\omega_r^2 - 1}{\omega_0 Y_0 L_{SC}}\right) \tag{III.21}$$

with $\omega_r = 1/\sqrt{L_{SC} C_{MS}}$ the circuit's resonance frequency. In such a case, the ECM of the MBFC turns into the LC parallel circuit of Figure III.3(a), where C_{MS} is the metasurface's overall variable capacitance, effectively modulating the MBFC's reactance.

3.1.2. Frequency-converting modulation scheme

As an LC parallel circuit, when using capacitance as the modulation parameter, the MBFC's resonance capacitance C_r, at an arbitrary frequency f_r, can be expressed as

$$C_r = \frac{1}{L_{SC}\omega_r^2} \tag{III.22}$$

Using the ECM of Figure III.3(b), the reflection coefficient of the MBFC can be calculated for different arbitrary frequencies. One may notice that, at the resonance, the phase goes through zero, *i.e.* $\angle\Gamma(\mathrm{C}_r) = 0$. The resulting phase profile is provided, as a function of the metasurface's overall capacitance C_{MS}, in Figure III.3(b) over an arbitrary capacitive range from $C_{MS} = 0$ pF to $C_{MS} = 2C_r$ to offer as much phase dynamic before and after resonance. As can be observed in Figure III.3(b), such MBFC exhibits a smoothly varying, monotonous phase profile between any two capacitance values for any frequency. However, the ideal 2π phase shift can never be reached, only allowing a maximum fraction $|\alpha| \approx 0.9$ for two capacitance values far apart. Nonetheless, it is possible to linearize the phase in time for a chosen frequency in order to provide frequency shifting. To do so, the phase values associated to capacitance values must be projected onto the time array spread over a modulation period T_m. To better illustrate this process, Figure III.3(c) compares both the default and linear reflection coefficient, obtained from a linearly varying capacitance and specifically modulated capacitance, respectively, at an arbitrary frequency f_r.

As can be observed in Figure III.3(c), the circle markers on the default phase variation have been stretched into the modulated capacitance range whose corresponding phase values are marked by a square. To better illustrate the time remapping, arrows are provided to highlight the correspondence between default and modulated phase values. For instance, since phase variation is slow from $C_{MS} = 0$ to $C_{MS} = 2C_r/3$, the phase points have been brought a lot closer in the time-remapped capacitance range. On the contrary, the phase values around the resonance at $C_{MS} = C_r$ vary quickly, and thus have been spread far apart by the linearization process.

The modulated capacitance range necessary to the linearization can then be associated to time over the desired modulation period T_m. The resulting time-based capacitance pattern can be periodically repeated, leading to the phase-linearizing modulation provided in Figure III.3(d). This modulation scheme therefore leads to a continuous train of ramp phases, as seen in Figure III.2(a).

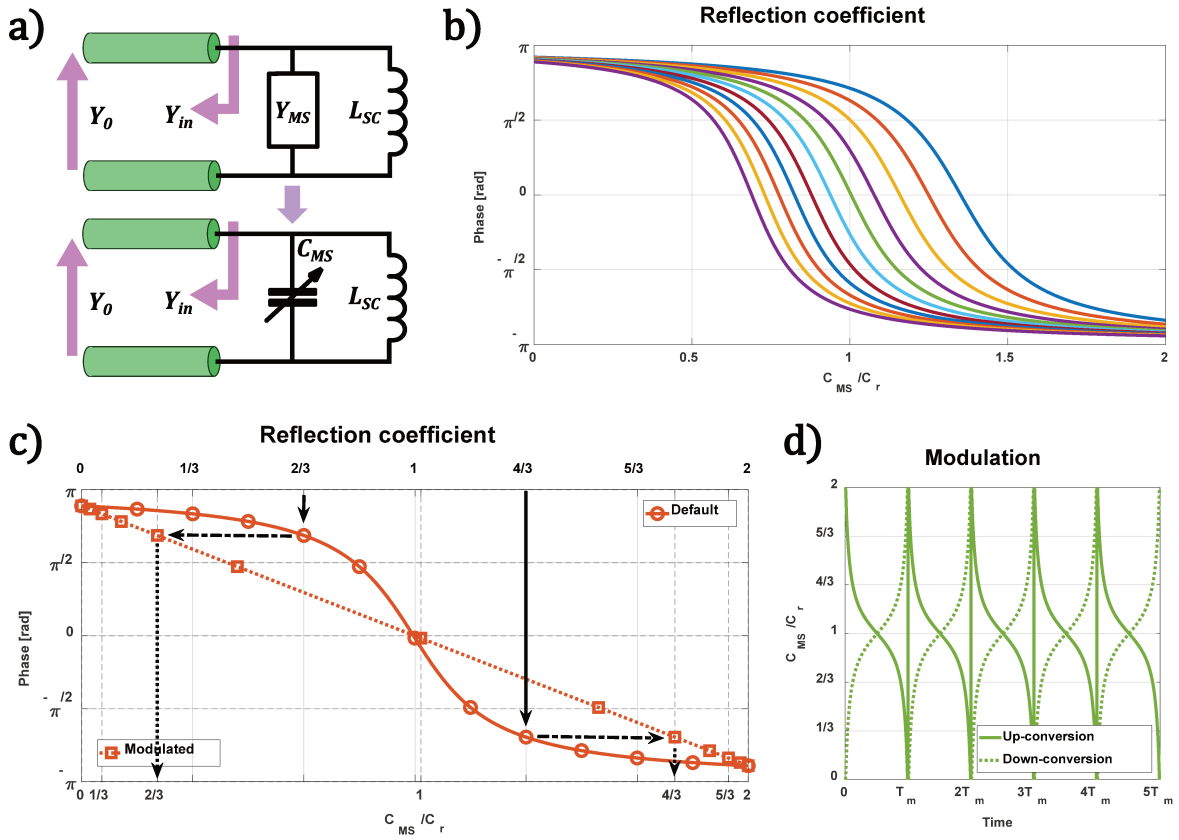

Figure III.3: (a) Equivalent circuit model of the metasurface-based frequency converter using a purely capacitive metasurface acting as a LC parallel circuit, modulated by capacitance. (b) Typical phase profiles of the reflection coefficient of the metasurface-based frequency converter acting as a LC parallel circuit as a function of metasurface's overall capacitance C_{MS} around the resonance capacitance C_r for different arbitrary frequencies (colors). (c) (top, circles) Default and (bottom, squares) modulated phase reflection coefficient of the metasurface-based frequency converter for linearization at an arbitrary frequency f_r as a function of overall metasurface's capacitance C_{MS} around the resonance capacitance C_r. (d) Modulation of the metasurface's overall capacitance C_{MS} for the periodic linearization in time of the reflection coefficient's phase over five modulation periods T_m at an arbitrary frequency f_r.

3.1.3. Geometry of the metasurface

As is the case for the MBRA of Chapter II, the metasurface of interest is the coaxial, capacitive metasurface allowing the loading of eight lumped elements. However, not all of these elements need to be modulated at the same time. Therefore, two main configurations can be considered in the following. The first configuration is the alternating pattern of varying capacitors and fixed capacitors. In such a case, the metasurface is a surface of symmetry C_{4v}, and is referred to as the 4VCT configuration. But a second configuration can be used by substituting all fixed capacitors for varying ones, for a total of eight variable elements, rendering the surface a C_{8v}-symmetric one [113], and is referred to as the 8VCT configuration. Both configurations are illustrated in Figure III.4(a). One may keep in mind that throughout this work, all varying elements are modulated equally. There is no notion of local changes in capacitance, in order not to break symmetries. In any case, since the metasurface's coaxial gap is already slightly capacitive in itself, the ECM of the MBFC is modified accordingly, leading to the ECM of Figure III.4(b).

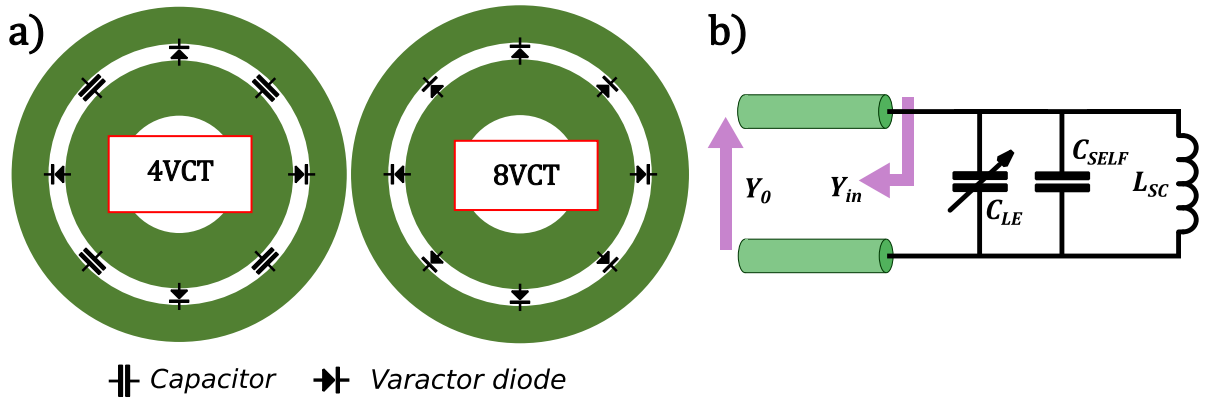

Figure III.4 : (a) Illustration of the (left) C_{8v}-symmetric (8VCT) and (right) C_{4v}-symmetric (4VCT) metasurfaces of interest using varactor diodes and fixed capacitors for the metasurface-based frequency-converter. (b) First-order equivalent circuit model to the designed metasurface-based frequency converter, simplifying varactor diodes into variable capacitors.

In Figure III.4(b), C_{self} is the self-capacitance and C_{LE} the capacitance from the perfectly capacitive varying capacitors, such that $C_{MS} = C_{LE} + C_{self}$. In such a case, the resonance capacitance associated to a frequency f_r is $C_r = 1/L_{SC}\omega_r^2 - C_{self}$. One may keep in mind that, in the 4VCT configuration, $C_{LE} = 4(C_{var} + C_{fix})$ for C_{var} the capacitance of these four varying individual elements and C_{fix} that of the fixed capacitors, and in the 8VCT, $C_{LE} = 8C_{var}$.

One may notice from the phase expression of Equation (III.21) that the existence of this self-capacitance C_{self} bounds the smallest capacitive value, and therefore associated phase value. In other words, even at $C_{LE} = 0$ pF, the metasurface's overall capacitance is $C_{MS} = C_{self} \neq 0$ pF. Therefore, the associated phase value at ω_0 is

$$\angle\Gamma(C_{LE} = 0, \omega_0) = -2\,\mathrm{atan}\left(\frac{\omega_0^2 L_{SC} C_{self} - 1}{\omega_0 Y_0 L_{SC}}\right) < 2\,\mathrm{atan}\left(\frac{1}{\omega_0 Y_0 L_{SC}}\right) < \pi \qquad \text{(III.23)}$$

However, for $C_{self} = 4$ pF, then $\omega_0^2 L_{SC} C_{self} < 1$ over the 100 – 700 MHz frequency range of interest.

From this purely analytical investigation, it appears a capacitive metasurface is an appropriate candidate for the MBFC. By modulation of the loaded capacitance C_{LE}, the reflection coefficient of the system can be periodically linearized in time, granting frequency conversion, as long as $f_m \ll f_0$. In practice, such a metasurface would be loaded with varactor diodes to use capacitance as the modulation parameter. To prepare for the experimental campaign, in the next Section 3.2, the metasurface considered is modulated with perfect variable capacitors and varactor diodes in order to confirm the frequency shifting mechanism and highlight the effects of the parasitic elements of the diodes. To this end, three studies are conducted in the 2D axisymmetric configuration, as detailed in the following.

3.2. 2D analytical, numerical and semi-analytical studies of the metasurface-based frequency converter for an incident signal of frequency $f_0 = 300$ MHz and modulation frequency $f_m = 1$ MHz

In this Section 3.2, the MBFC is studied, either analytically, using the ECM, or numerically, using COMSOL®, or a blend of both. This is a similar process to the one conducted in Chapter II where the ECM is validated by full wave simulations. For all three studies, the frequency

conversion follows the exact same four-step protocol described in the following, as well as summarized in Figure III.5.

Step ① consists in computing the reflection coefficient of the frequency converter as a function of capacitance at the frequency of interest $f_0 = 300$ MHz, *i.e.* $\Gamma(C_{LE}, \omega_0)$. This step relies either on the ECM of Figure III.4(b) or on a 2D axisymmetric FEM simulation.

Step ② consists in linearizing in time the reflection coefficient over the considered modulation period $T_m \gg T_0$ for $f_m = 1$ MHz. Thanks to the appropriate $C_{LE}(t)$ pattern, the reflection coefficient is now time-dependent $\Gamma(t, \omega_0)$, and exhibits a phase ramp. For all three studies, this linearization process is done using a Matlab® script, hence its *analytical* nature in Figure III.5.

Step ③ consists in injecting the modulation pattern for linearization of the reflection coefficient into the metasurface while it is illuminated by the incident field for frequency shifting of the reflected field. This step leads to the generation of the time-dependent reflected electric field from a modulation at ω_0, $\boldsymbol{E_r}(t, \omega_0)$. This process is done either analytically, using Equation (III.3), or with a 2D axisymmetric FETD simulation.

Step ④ consists in processing the time-domain reflected signal into the frequency-domain to analyze the frequency-shifting mechanisms. This leads to the comparison of the power spectral densities of the incident and reflected signals $\widetilde{\boldsymbol{E}}_{\boldsymbol{r}}(\omega, \omega_0)$. For all three studies, this is once again based on a Matlab® script, hence its *analytical* nature in Figure III.5.

As can be noticed:

- In step ① , the numerical and semi-analytical studies share the same numerical FEM tool for simulation of the capacitance-dependent reflection coefficient $\Gamma(C, \omega_0)$.
- In steps ② and ④ , all three studies share the same analytical tools for the time-based linearization of the phase $\Gamma(t, \omega_0)$ (step ②) and Fourier transform analysis of $\widetilde{\boldsymbol{E}}_{\boldsymbol{r}}(\omega, \omega_0)$ (step ④).
- In step ③ , the analytical and semi-analytical share the same analytical tool for the frequency conversion based on the relationship of Equation (III.3) to generate the time-domain reflected signal $\boldsymbol{E_r}(t, \omega_0)$.

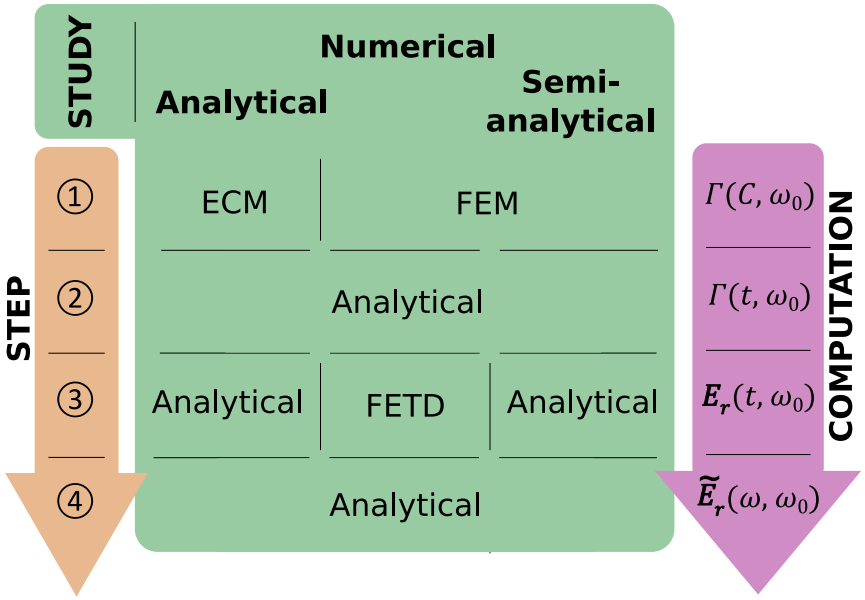

Figure III.5 : Visualization of the four steps (① , ② , ③ , ④) of the three studies (analytical, numerical and semi-analytical) and their associated tools (green) and computation objectives (purple).

3.2.1. Analytical study of the metasurface-based frequency converter from an equivalent circuit analysis

In this analytical study, only the reflection coefficient from the ECM of Figure III.4(c) is used, along with the foundational relationship of Equation (III.3).

In step ① , one has to calculate the phase of the reflection coefficient of the MBFC as a function of capacitance. For a purely capacitive variable element, at the frequency of interest $f_0 =$ 300 MHz, the capacitance associated to the resonance is $C_{MS} = C_0 = 84$ pF, leading to $C_{LE} = C_0 - C_{self} = 80$ pF, *i.e.* $C_{var} = 20$ pF in the 4VCT configuration. However, the reactive elements of the varactor diode – a parallel capacitor C_p and series inductor L_s – and resistive element – the series resistor R_s, alter the perfect LC circuit of the MBFC of Figure III.4(b). The resulting reflection coefficient curves are provided in Figure III.6(a).[2]

As can be observed in Figure III.6(a), the phase of the varactor-loaded MBFC is shifted towards lower capacitance values compared to the capacitor-based MBFC, showing a resonance capacitance at $C_0 = 70$ pF. This shift is mainly caused by the parallel capacitor C_p, whose contribution increases with the number of varactor diodes, but is also only slightly affected by the series inductor L_s. Regarding the magnitude of both reflection coefficients, while the capacitor-loaded MBFC is a perfectly reflective surface, the varactor-loaded one displays some absorption due to the series resistor. Thankfully, the phase of the reflection coefficient is still smoothly varying between two values, meaning it can still be linearized in time to serve frequency conversion purposes. However, the introduction of a non-unitary module to the reflection coefficient turns the ideal Equation (III.13) into this more general expression

$$\Gamma(t,\omega_0) = \left(\gamma(t)e^{\pm j\alpha\omega_m t}\mathrm{rect}\left(\frac{t-T_m/2}{T_m}\right)\right) * \sum_{n=-\infty}^{+\infty}\delta(t-nT_m) \qquad \text{(III.24)}$$

where $\gamma(t)$ is the amplitude of the reflection coefficient.

In such a case, the frequency-domain equivalent of this expression is also modified, going from that of Equation (III.14) to

$$\tilde{\Gamma}(\omega,\omega_0) = \left(\tilde{\gamma}(t) * W_\alpha(\omega)\right)\sum_{n=-\infty}^{+\infty}\delta(\omega-n\omega_m) \qquad \text{(III.25)}$$

As can be noticed, the non-unitary module of the reflection coefficient, caused by the resistance of the varactor diode, changes the weights of the weighting function W_α. This alters the distribution of power amongst undesired harmonics.

In step ② , the linearization process is performed using Matlab®. The reflection coefficient is given as a function of capacitance so that the corresponding phase values can be stretched in time over a modulation period T_m ($f_m = 1$ MHz), leading to the periodic linear phase of the reflection coefficient $\Gamma(t,\omega_0)$ at $f_0 = 300$ MHz of Figure III.6(b) ensured by the modulation of Figure III.6(c). As can be noticed, the linearized reflection coefficient displays predictable, albeit undesired, absorbing behavior.

[2] Since biasing is overlooked here, the resistance value is considered fixed at $R_s = 1.7\ \Omega$, as provided in [118] for the SMV1249 model.

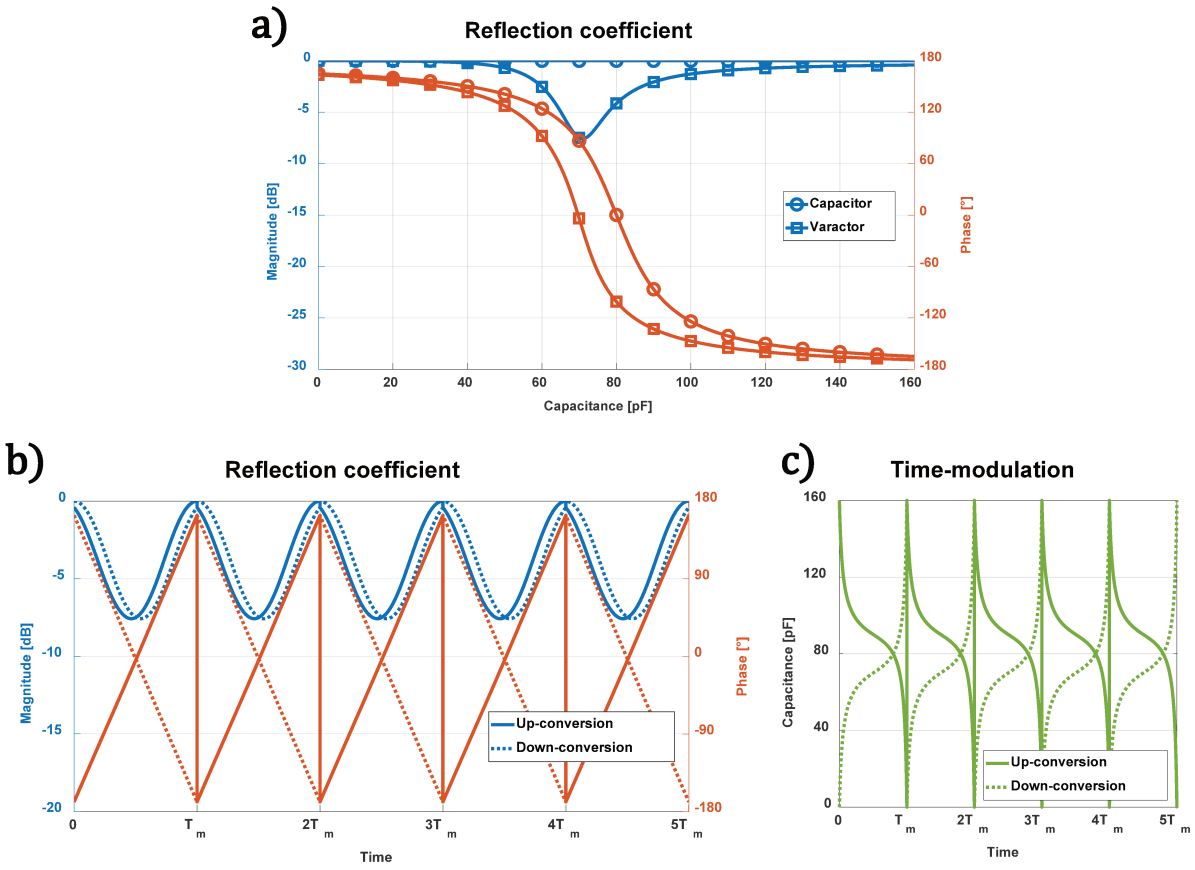

Figure III.6 : (a) (blue) Magnitude and (red) phase of the reflection coefficient from an ECM model of a metasurface-based frequency converter using a 4VCT metasurface with (circles) varying capacitors or (squares) varactor diodes at $f_0 = 300$ MHz. (b) Time-domain (blue) magnitude and (red) phase from an ECM model of a 4VCT varactor-loaded metasurface-based frequency converter using four SMV1249 varactor diodes at $f_0 = 300$ MHz for an (solid) up- and (dotted) down-conversion of any frequency $f_m = 1/T_m$. (c) Time-domain capacitance modulation from the ECM model of the 4VCT metasurface with varactor diodes for an (solid) up- and (dotted) down-conversion.

In step ③ , the foundational relationship of Equation (III.3) is used, with the reflection coefficient from both a capacitor- and a varactor-loaded metasurface. The only two differences between both coefficients is the modulation pattern and the undesired absorption of the varactor-loaded MBFC. This leads to the generation of the time-domain reflected signal $\boldsymbol{E_r}(t, \omega_0)$.

In step ④ , the Fourier transform of the time-domain incident and reflected signals, $\widetilde{\boldsymbol{E}}_{\boldsymbol{i}}(\omega, \omega_0)$ and $\widetilde{\boldsymbol{E}}_{\boldsymbol{r}}(\omega, \omega_0)$, is computed leading to the comparison of PSD in Figure III.7(a) for the capacitor-loaded case and Figure III.7(b) for the 4VCT varactor-loaded one.

As expected, the reflected wave's PSD confirms that the frequency bearing the most power is found at $f_0 \pm f_m$ – since $|\alpha|$ is closer to 1 than to 0. As also expected from the non-ideal phase shift fraction $|\alpha| \approx 0.92$, the PSD are plagued by spurious harmonics. However, these harmonics bear little power compared to the main power-bearing frequency, in both cases, despite a higher power loss during the conversion in the varactor-loaded case. In order to quantify the conversions from all three models in total, three metrics are added to every element of Figure III.7, highlighting similarities and discrepancies. In particular, three metrics are used:

- The conversion loss, CL, which is the difference in maximum magnitude between the incident signal's power at f_0 and the reflected signal's power at the desired $f_0 \pm f_m$ frequency. It quantifies the undesired power loss caused by the frequency shifting.
- The power reduction of the harmonic at f_0, R_0, which is the reduction in power of the reflected wave at the frequency that bears the Doppler shift, *i.e.* the target velocity information. Given the dependency of the Fourier transform to simulation times to obtain the PSD, R_0 is chosen as the power reduction between the lobe centered at f_0 of the incident spectrum and the adjacent lobe(s) to f_0 of the reflected spectrum.
- The total energy spread over the [295, 305] MHz frequency range, $\mathcal{E}_{ref}/\mathcal{E}_{inc}$, which measures the energy dissipation, to be compared with the CL and R_0, especially in the varactor-loaded MBFC case

In the case of the analytical study of Figure III.7(a)-(b), the reduction in power for the capacitor-loaded MBFC of $R_0 = 16.85$ dB is less than that of the varactor-loaded MBFC, which reaches $R_0 = 20$ dB. This is probably due to the general absorption brought by varactor diodes, and is in fact beneficial. However, this absorbing behavior also increases conversion losses, dropping by 3.7 dB in the varactor-loaded case. On top of that, it appears the harmonics at $f_0 \pm 2f_m$ in the varactor case reach around -14 dB, compared to the -20 dB in the capacitor case. This gain of power may originate from the secondary power distribution added by the undesired amplitude modulation. Finally, one may notice the use of varactor diodes, as expected, increases energy dissipation. In the case of the capacitor-loaded, energy is preserved, with $\mathcal{E}_{ref}/\mathcal{E}_{inc}$ equal to one, but turns into a ratio $\mathcal{E}_{ref}/\mathcal{E}_{inc}$ closer to 0.5 when varactor diodes are involved, meaning half of the energy is lost to the resistive elements during conversion.

In order to confirm that the ECM and Equation (III.3) can describe the actual behavior of a MBFC, Section 3.2.2 will be devoted to a fully numerical study.

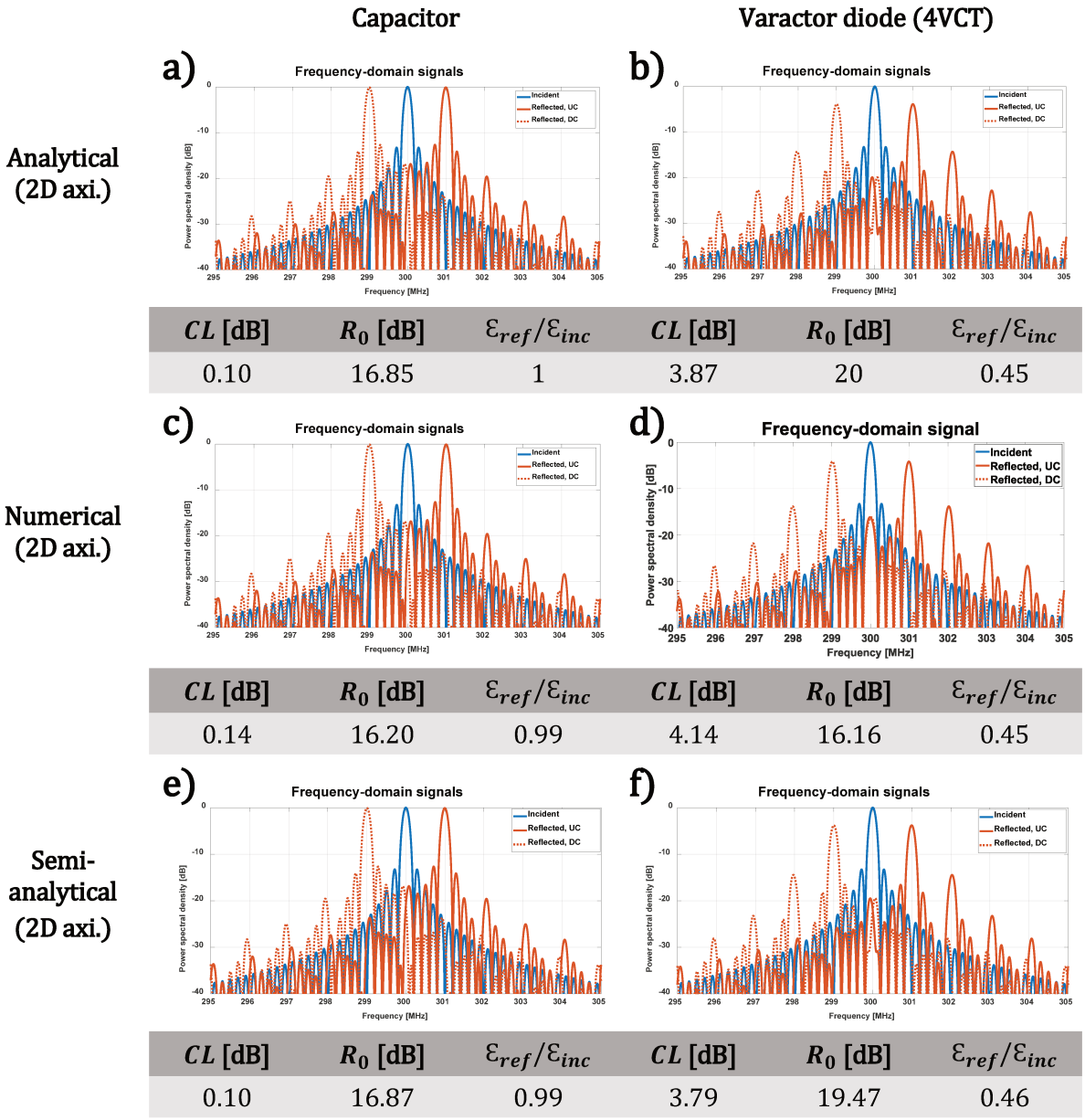

CL [dB]	R_0 [dB]	$\mathcal{E}_{ref}/\mathcal{E}_{inc}$	CL [dB]	R_0 [dB]	$\mathcal{E}_{ref}/\mathcal{E}_{inc}$
0.10	16.85	1	3.87	20	0.45

CL [dB]	R_0 [dB]	$\mathcal{E}_{ref}/\mathcal{E}_{inc}$	CL [dB]	R_0 [dB]	$\mathcal{E}_{ref}/\mathcal{E}_{inc}$
0.14	16.20	0.99	4.14	16.16	0.45

CL [dB]	R_0 [dB]	$\mathcal{E}_{ref}/\mathcal{E}_{inc}$	CL [dB]	R_0 [dB]	$\mathcal{E}_{ref}/\mathcal{E}_{inc}$
0.10	16.87	0.99	3.79	19.47	0.46

Figure III.7 : Relative power spectral density of the (blue) incident and (red) reflected electric signals from (row) one of the three 2D axisymmetric studies of a (column) varying capacitor- or SMV1249 varactor diode-loaded metasurface-based frequency converter in the 4VCT configuration for an impinging wave at frequency $f_0 = 300$ MHz for both an (solid) up- and (dashed) down-conversion of frequency $f_m = 1$ MHz, namely *UC* and *DC*.

3.2.2. Numerical study of the metasurface-based frequency converter from a 2D axisymmetric FETD simulation

In this numerical study, the metasurface is modelled in a 2D axisymmetric configuration in COMSOL®, as done in Figure II.6. The integration of the varactor diodes in a time-domain simulation must be done through the explicit implementation of the SPICE model into the software, because there is no readily available node that can emulate such a circuit.

In step ① , both the *Lumped Element* or *Surface Current Density* nodes can be used to emulate the metasurface. In fact, it is used to simulate the parallel circuit formed by the self-capacitance C_{self} of the metasurface and the loaded capacitance C_{LE}, as provided in Figure III.4(b).

This leads to a simulated capacitance-dependent reflection coefficient at the desired frequency to convert ω_0, $\Gamma(C_{LE}, \omega_0)$.[3] Since the ECM can accurately predict the behavior of a rotation-invariant configuration, the reflection coefficients for the capacitor-loaded and varactor-loaded cases are the same as in Figure III.6(a).

In step ②, as previously specified, the Matlab® script is used for linearization in time, *i.e.* $\Gamma(t, \omega_0)$ through specific modulation $C_{LE}(t, \omega_0)$. This leads to the same periodic reflection coefficient and modulation pattern of Figure III.6(b)-(c).

In step ③, the metasurface is once again emulated, though only the *Surface Current Density* node is compatible with the time-domain expression of lumped elements. The appropriate expression for the time-domain simulation of a varactor diode is provided in Appendix C**.** Once properly set up, the FETD simulation is run for five modulation periods T_m, generating the reflected signal $E_r(t, \omega_0)$ from an harmonic incident signal $E_i(t, \omega_0)$ set at $f_0 = 300$ MHz.

In step ④, the incident and reflected signals are computed in the frequency-domain and their PSD are provided in Figure III.7(c) and Figure III.7(d), for the capacitor- and varactor-loaded cases, namely.

As can be observed, the incident electric field is up- or down-converted by the MBFC from f_0 to $f_0 \pm f_m$, but is also copied to every other harmonics $f_0 + (n \pm 1)f_m, n \in \mathbb{Z}^*$. As previously demonstrated, this is symptomatic of a non-ideal phase variation over a modulation period.

In the capacitor-loaded case of Figure III.7(c), the resulting metrics are very similar to those of the analytical study, with a near-zero CL, conserved energy ratio $\mathcal{E}_{ref}/\mathcal{E}_{inc} = 1$ and $R_0 = 16.5$ dB. However, in the varactor-loaded case of Figure III.7(d), though CL and $\mathcal{E}_{ref}/\mathcal{E}_{inc}$ are unchanged, it seems the power reduction is reduced to $R_0 = 16.16$ dB, which is 4 dB higher than the ECM predicts. This one metric result is debatable: this change might only be due to the single lobe found at f_0 where two were previously found in Figure III.7(a)-(c) and probably merged, thereby bearing more power. Therefore, the analytical and numerical models do coincide on many aspects, but some slight differences do arise.

Accepting this discrepancy, this confirms step ③ of the time-based computation can either be conducted as a FETD simulation, or simply done by applying the foundational relationship of Equation (III.3).

3.2.3. Semi-analytical study of the metasurface-based frequency converter from a 2D axisymmetric FEM simulation and analytical conversion computation

This third and last study of the MBFC is done in a semi-analytical manner, and not a fully numerical one. This method has the advantage of removing the computation-heavy FETD simulation used in step ③ while still maintaining a high level of accuracy.

In step ①, the FEM simulation for the reflection coefficient $\Gamma(C_{LE}, \omega_0)$ is the same as the previous analytical and numerical studies, provided in Figure III.6.

In step ②, the same Matlab® script is used for linearization in time, leading to $\Gamma(t, \omega_0)$ with the same previously established modulation $C_{LE}(t, \omega_0)$.

In step ③, the FETD simulation of the numerical study is swapped for the Equation (III.3) of the analytical study. Thanks to the linearized reflection coefficient, an analytical reflected signal $E_r(t, \omega_0)$ is generated from a harmonic incident signal.

In step ④, the incident and reflected fields' PSD, $\widetilde{\boldsymbol{E}}_{\boldsymbol{i}}(\omega, \omega_0)$ and $\widetilde{\boldsymbol{E}}_{\boldsymbol{r}}(\omega, \omega_0)$, are computed and provided in Figure III.7(e) and Figure III.7(f), for the capacitor- and varactor-loaded cases. In

[3] Once again, since no biasing is considered here, the series resistance is simplified into its average datasheet value $R_s = 1.7\ \Omega$.

both cases, the reflected PSD is the same as that of the analytical model: all three metrics (CL, R_0 and $\mathcal{E}_{ref}/\mathcal{E}_{inc}$) remain the same. To be exact, the R_0 of the varactor case from the semi-analytical is 0.5 dB lower.

These results confirm the analytical frequency conversion based on Equation (III.3) is a good approximation of an actual simulation, but is somewhat simplified. However, one should keep in mind that this only holds true in the slow modulation regime described of Equation (III.1).

In the numerical simulation, the 2D axisymmetric configuration is easily meshed following the recommendations of [125], [126], and leads to FETD computation times of acceptable duration. However, a 3D configuration must be meshed with an even greater deal of caution and the simulation thus inevitably becomes too resource-hungry and time-consuming.

Fortunately, the accuracy of the semi-analytical study in the 2D axisymmetric case has just been proved, and may therefore be applied to the 3D case. Section 3.3 will therefore turn to the semi-analytical study of the MBFC in the 3D configuration, implementing the exact structure of the metasurface, under the same illumination and modulation conditions.

3.3. 3D semi-analytical study of the metasurface-based frequency converter for an incident signal of frequency $f_0 = 300$ MHz and modulation frequency $f_m = 1$ MHz

The previous section confirmed the semi-analytical model is accurate enough to serve as a basis for the design process. Thus, it can be used to take into account all specificities that arise in 3D.

In step ①, the interactions of the metasurface with higher-order modes are embedded into the reflection coefficient from a 3D FEM simulation. This manifests as a blueshift of the reflection coefficient curve of Figure III.6(a) to a resonance at $C_0 = 46$ pF instead of $C_0 = 80$ pF for the capacitor-loaded case and $C_0 = 38$ pF for the varactor-loaded case.

In step ②, the phase being still smoothly varying, this frequency shift has no incidence on the frequency conversion outside of a reduced linearization range for $C_{LE}(t, \omega_0)$. On the contrary, the α fraction is somewhat larger at $|\alpha| = 0.95$, which should grant an even better conversion.

In step ③, as for the previous semi-analytical study, Equation (III.3) is used instead of a full-wave FETD, leading to the time-domain reflected signal $E_r(t, \omega_0)$.

In step ④, the incident and reflected fields' PSD are computed and provided in Figure III.8(a) and Figure III.8(b).

One may notice that conversion is once again happening, and that the obtained reflected PSD is only slightly different from the ones of Figure III.7(e)-(f). In particular, it appears the spurious harmonics do not bear as much power, as expected from the greater $|\alpha|$ fraction. This manifests as some changes in the three metrics. For instance, in the capacitor-loaded case of Figure III.8(a), with a (still) negligible $CL = 0.04$ dB, but an increased $R_0 = 18.70$ dB, which is 2 dB higher than the 2D axisymmetric case (semi-analytical). In the varactor-loaded case of Figure III.8(b), both the conversion loss $CL = 2.88$ dB and the power reduction $R_0 = 20.30$ are 1 dB less than the axisymmetric case, leading to less power dissipation, hence $\mathcal{E}_{ref}/\mathcal{E}_{inc} = 0.56$ instead of $\mathcal{E}_{ref}/\mathcal{E}_{inc} = 0.46$ for the axisymmetric case.

	Capacitor			Varactor diode		
Semi-analytical (3D)	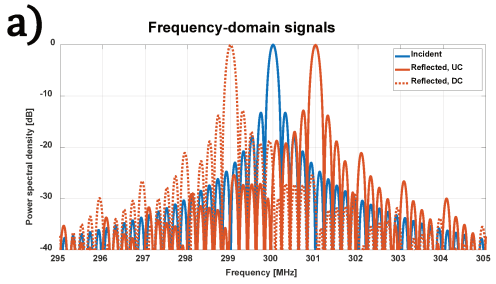			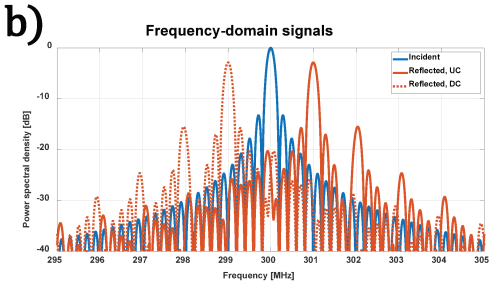		
	CL [dB]	R_0 [dB]	$\mathcal{E}_{ref}/\mathcal{E}_{inc}$	CL [dB]	R_0 [dB]	$\mathcal{E}_{ref}/\mathcal{E}_{inc}$
	0.04	18.70	0.99	2.88	20.30	0.56

Figure III.8 : Relative power spectral density of the (blue) incident and (red) reflected electric signals from the 3D semi-analytical study of a (column) varying capacitor- or SMV1249 varactor diode-loaded metasurface-based frequency converter in the 4VCT configuration for an impinging wave at frequency $f_0 = 300$ MHz for both an (solid) up- and (dashed) down-conversion of frequency $f_m = 1$ MHz, namely *UC* and *DC*.

From the results of all three 2D axisymmetric studies performed in Section 3.2 and the results of the 3D semi-analytical study of Section 3.3, it clearly appears the use of varactor diodes onto the metasurface still enables frequency conversion by modulation, though it introduces some absorption. From the ideal case of only using variable capacitors to the more practical case with varactor diodes, CL generally increases by around 2 to 4 dB, and R_0 increases, suppressing some more the Doppler-shifted backscattered wave. According to the three studies, the experimental measurements of a 4VCT MBFC's reflected signal are expected to be affected by a CL of around 3 dB, with a R_0 of around 20 dB.

3.4. Experimental validation of a time-modulated metasurface for the frequency-conversion of harmonic waves at $f_0 = 370$ MHz

In this Section 3.4, two metasurfaces are fabricated: one with the 4VCT and one with the 8VCT configurations. The resulting MBFC is measured in the frequency-domain with a DC voltage sweep to get the necessary $\Gamma(C)$ of step ① for the subsequent time-domain measurement under modulation of step ③. The experimental setups are introduced in Section 3.4.1, along with the expected behaviors of the manufactured metasurfaces. Both MBFC's reflection coefficients are analyzed to select the most appropriate for the experimental campaign of Section 3.4.3.

3.4.1. Experimental setup for the time-domain measurement of the metasurface-based frequency converter

3.4.1.1. Enlarged coaxial waveguide setup for frequency-domain measurement

For measurement of the reflection coefficient of the MBFC while undergoing DC biasing voltage sweeping, the experimental setup provided in Figure III.9(a) is similar to the one used for the measurement of the MBRA of Chapter II. The main difference is the addition of a dual directional coupler between the VNA and enlarged coaxial waveguide, to be used for the time-domain measurement of the MBFC. The VNA used is the 8753ES model by Agilent®, the DC biasing voltage source is the Hameg® (Rohde & Schwarz®) HMP4040 model, and the coupler is the HP

7780 (0.1-2.0 GHz). One may notice on Figure III.9(a) that the source of modulation is not directly the capacitance of the metasurface, but rather its biasing voltage. In fact, the varactor diode's capacitance being a function of reverse biasing, it is entirely possible to substitute capacitance for biasing voltage as the modulation parameter.

3.4.1.2. Enlarged coaxial waveguide setup for time-domain measurement

For measurement of the incident and reflected signals interacting with the modulated MBFC, the experimental setup provided in Figure III.9(b) is used. Conversely to the frequency-domain setups used so far, this one does not rely on a VNA, but rather on a harmonic signal generator and a high frequency oscilloscope. The incident harmonic signal originating from the signal generator is injected into the enlarged coaxial waveguide, and is probed by the coupler's auxiliary port to feed the oscilloscope. In the enlarged coaxial waveguide, the incident signal is converted upon reflection onto the modulated MBFC, and is sent back to the coupler, once again probing the reflected signal to feed the oscilloscope. The harmonic signal generator is a 2023A Signal Generator by IFR®, the arbitrary waveform generator is the 33120A model by HP® and the oscilloscope is a HDO4054A model by Teledyne Lecroy®.

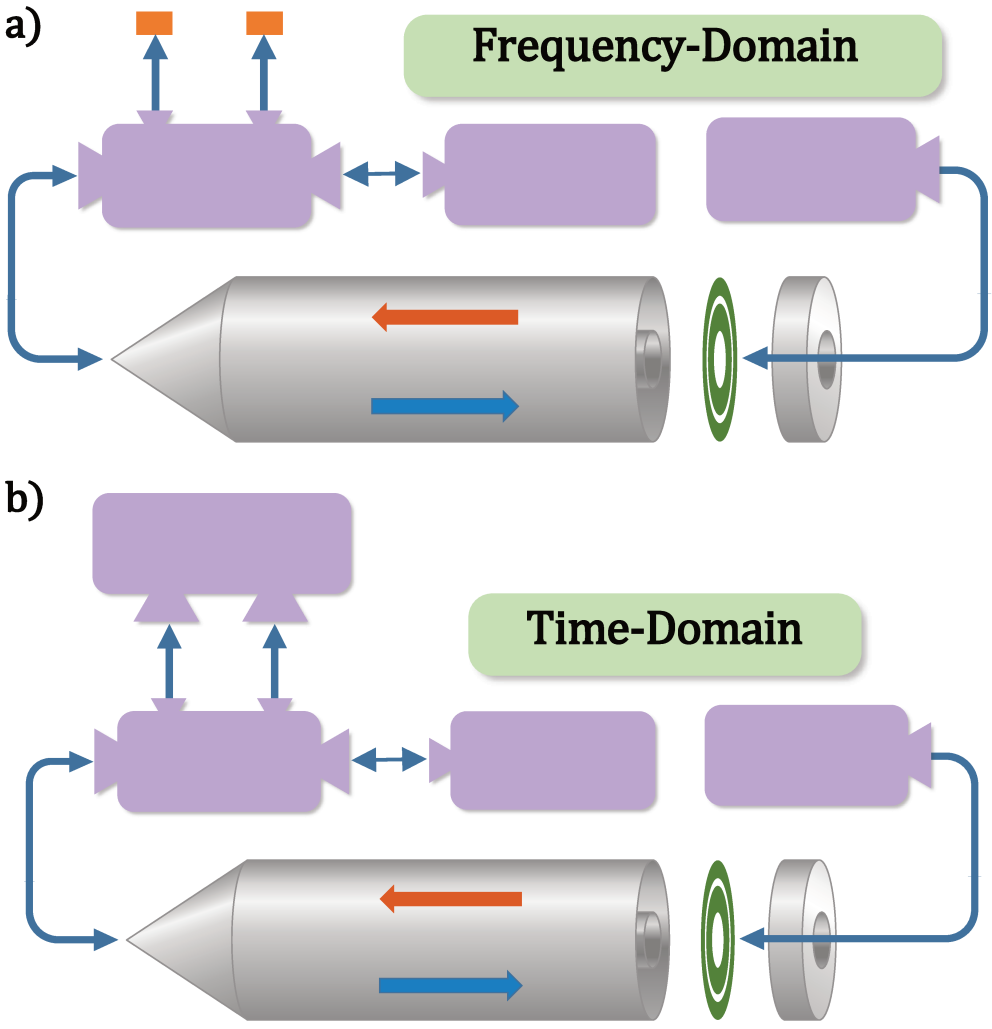

Figure III.9 : (a) Illustration of the experimental setup for measurement of the reflection coefficient of the metasurface-based frequency in the frequency-domain (FD) while undergoing DC biasing voltage sweep, using the enlarged coaxial waveguide, a vector network analyzer, a DC voltage biasing source and a matched loaded coupler. (b) Illustration of the experimental

setup for measurement of the reflection coefficient of the metasurface-based frequency in the time-domain (TD), using the enlarged coaxial waveguide, a harmonic signal generator as the incident signal source, an arbitrary waveform generator as the modulation signal source and a coupler for measurement of the incident and reflected signals thanks to an oscilloscope.

3.4.1.3. Practical constraints of the fabrication of the metasurface

As one may notice, in the ECM of the MBFC in Figure III.4(b), the capacitance from loaded capacitors and varactor diodes is accounted as a single capacitor C_{LE}, used as the modulation parameter. As introduced with the ECM in Figure III.4(b), in the 4VCT configuration $C_{MS} = C_{LE} + C_{self} = 4\left(C_{var} + C_{fix}\right) + C_{self}$ and in the 8VCT configuration $C_{MS} = C_{LE} + C_{self} = 8C_{var} + C_{self}$, with C_{fix} the fixed capacitance and C_{var} the variable capacitance – simplifying the varactor diode to its sole diode capacitance. Therefore, by definition, C_{var} is the one parameter used for the phase exploration.

However, varactor diodes are bound by their smallest capacitance value even at high reverse biasing voltage [117] to a value $C_{var}(V_r = V_{max}) = C_{var}^{min}$, and by their highest capacitance $C_{var}(V_r = V_{min}) = C_{var}^{max}$ for zero reverse biasing voltage. In this case, at the chosen frequency ω_0, the phase varies between two extrema such that

$$\begin{cases} \angle\Gamma(V_r = V_{min}, \omega_0) = -2\,\mathrm{atan}\left(\dfrac{\omega_0^2 L_{SC} C_{MS}^{max} - 1}{\omega_0 Y_0 L_{SC}}\right) > -\pi \\ \angle\Gamma(V_r = V_{max}, \omega_0) = -2\,\mathrm{atan}\left(\dfrac{\omega_0^2 L_{SC} C_{MS}^{min} - 1}{\omega_0 Y_0 L_{SC}}\right) < \pi \end{cases} \quad \text{(III.26)}$$

with $C_{MS}^{max} = 8C_{var}^{max} + C_{self}$ and $C_{MS}^{min} = 8C_{var}^{min} + C_{self}$ in the 8VCT configuration and $C_{MS}^{max} = 4(C_{var}^{max} + C_{fix}) + C_{self}$ and $C_{MS}^{min} = 4(C_{var}^{min} + C_{fix}) + C_{self}$ in the 4VCT configuration. Therefore, the resulting MBFC should be suitable for any frequency f_0 such that

$$\frac{1}{2\pi\sqrt{L_{SC} C_{MS}^{max}}} < f_0 < \frac{1}{2\pi\sqrt{L_{SC} C_{MS}^{min}}} \quad \text{(III.27)}$$

One may thus better appreciate the role of the capacitance range in the frequency range. In the 8VCT configuration, the capacitance range of the varactor diodes provides a wider phase variation. The 4VCT configuration, though with a narrower phase variation from using only four varactor diodes, can be tuned to the frequencies of interest thanks to additional capacitors of fixed capacitance C_{fix}. Figure III.10(a) is provided for illustration of this design principle in the 4VCT case, where the C_{var}^{min} to C_{var}^{max} is crucial to defining the range of frequencies that can be converted. For instance, sacrificing conversion at $f_0 = 500$ MHz, one can get higher α fractions at $f_0 = 400$ MHz, which may better fit the operational requirements.

To nuance the previous explanation, not all frequencies in the range of Equation (III.27) [127]*can* be frequency-converted, only the portions for which $|\alpha| > 0.5$. In the following, a fraction $|\alpha| > 0.8$ is arbitrarily chosen to distinguish between regimes of high conversion and lower conversion rates, thereby further reducing the allowable frequency range.

Finally, the decisive factor in the choice between a 4VCT and 8VCT MBFC is the acceptable variations of the reflection coefficient's magnitude. As already shown in Figure III.6(a), the use of varactor diodes introduces some absorption because of the parasitic series resistor. However, this absorption can be mitigated by using parallel capacitive elements [127], be they capacitors or varactor diodes. In the case of varactor diodes, this is due to the reduction of the total equivalent impedance's real part with the number of equal parallel components. For instance, as seen in

Figure III.10(b), overlooking the C_{fix} value, the 8VCT MBFC exhibits a lesser minimum reflection coefficient's magnitude than its 4VCT counterpart.

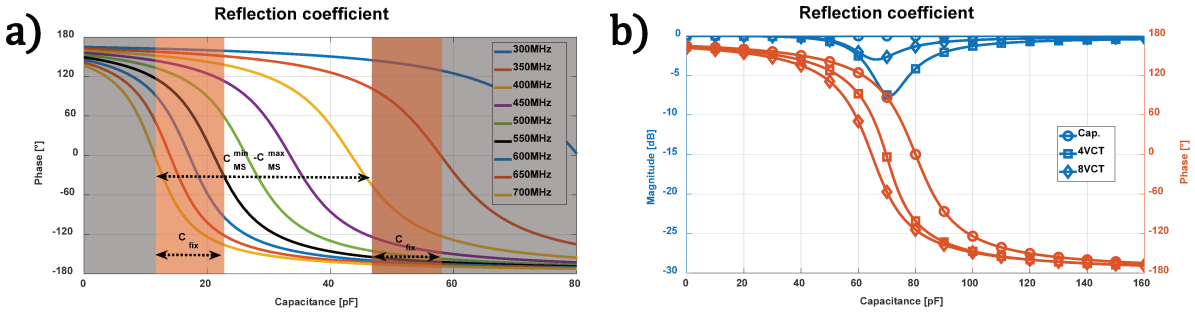

Figure III.10 : (a) Phase profiles from an ECM model of a capacitor-loaded metasurface-based frequency converter using four varying capacitors of capacitance C_{var} and four capacitors of capacitance C_{fix} for frequencies in $f_0 \in [300, 700]$ MHz. (b) (blue) Magnitude and (red) phase from an ECM model of a (circles) 4VCT capacitor-loaded, (squares) 4VCT and (diamonds) 8VCT varactor-loaded metasurface-based frequency converter at $f_0 = 300$ MHz for $C_{var} \in [0, 160]$ pF.

3.4.2. Design of the metasurface and frequency-domain measurement of the reflection coefficient of the metasurface-based frequency converter

Though the SMV1249 varactor diode model has been used until now, as stated in Section 3.4.1.3, the capacitance range is a crucial design element. Given that the objective was to work on a low-frequency MBFC, the low capacitance range can be sacrificed by using a C_{var}^{min} value of relatively high capacitance if C_{var}^{max} is further away. Using the SMV1255 model, capacitance variation from around $C_{var}^{min} = 4.8$ pF to $C_{var}^{max} = 81$ pF offers the much desired large phase exploration. The objective in this section is to validate the decision of using this varactor diode model, and compare the resulting phase profiles from 4VCT and 8VCT configurations. In the 4VCT configuration, four capacitors of capacitance $C_{fix} = 2$ pF are also used. In both cases, the phase profiles are compared for a $V_r \in [0, 5]$ V reverse biasing sweep in the $[100, 550]$ MHz range. Those phase profiles come from an analytical model (2D axisymmetric) in Figure III.11(a)-(b), a numerical model (3D) in Figure III.11(c)-(d) and measurements in Figure III.11(e)-(f) of the 4VCT metasurface of Figure III.11(g) and the 8VCT metasurface of Figure III.11(h). The objective is to confirm design choices (analytical and numerical studies) and which configuration is best suited for measurements. To this end, the decisive criterion is the quality of the phase shift, as a smooth and large variation, measured by the $|\alpha|$ fraction associated to the $V_r \in [0, 5]$ V modulation at each frequency. Therefore, the frequency range over which $|\alpha| \geq 0.8$ is a key indicator.

In the analytical case, the ECM phase profiles are provided in Figure III.11(a) for the 4VCT metasurface and Figure III.11(b) for the 8VCT one. One may notice the 8VCT-related phase map is a frequency-compressed version of the 4VCT-related one since equal phase profiles are explored for lower biasing voltages, *i.e.* the metasurface is more capacitive for the same bias. The sought after smooth and wide ($|\alpha| > 0.8$) phase variations are achievable for $f_0 \in [249, 391]$ MHz in Figure III.11(a) and $f_0 \in [180, 297]$ MHz in Figure III.11(b). Thereby confirming that both configurations seem appropriate for the MBFC, and that they should offer two complementary operable frequency ranges. One may also notice the collapse of $|\alpha|$ over low frequencies, which is due to a phase shift regime change caused by the resistive elements. This phenomenon is hard to predict from datasheet information alone, and can be better appreciated in Appendix E. Aside from that, since the ECM is only a 2D axisymmetric model, a 3D FEM simulation will further validate the design choices.

In the numerical case, the resulting phase profiles are provided in Figure III.11(c)-(d), for the 4VCT and 8VCT configurations, namely. Compared to the analytical results, the phase profiles of both configurations show a general shift toward lower frequency values and greater absolute phase values. The sought after smooth and wide ($|\alpha| > 0.8$) phase variations are achievable for $f_0 \in [160, 325]$ MHz in Figure III.11(c) and $f_0 \in [100, 227]$ MHz in Figure III.11(d). For the 8VCT case, one may notice a suppression of the low $|\alpha|$ values regime (found below 100 MHz) and a second zone of high phase values that was absent in all previous cases manifests itself in this case, with $|\alpha| \geq 0.8$ over $[445, 471]$ MHz. The suitability of both configurations being validated to work over two different frequency ranges, the two metasurfaces are manufactured, photographs of which are provided in Figure III.11(g)-(h). One may notice that, once again, all varactor diodes are routed together through a single trace on the bottom face of the metasurfaces.

In the experimental case, the measured phase profiles are provided in Figure III.11(e) and Figure III.11(f) for the 4VCT and 8VCT MBFC, namely. One may notice an unexpected shift of the allowable frequency range in both cases. In fact, it seems both characteristics are inverted from ECM/FEM simulations: the widest allowable frequency range is offered by the 8VCT MBFC. The 4VCT MBFC's allowable range is $f_0 \in [245, 275]$ MHz, and $f_0 \in [287, 418]$ MHz for the 8VCT MBFC. The 4VCT MBFC exhibits a similar unexpected window at $f_0 \in [396, 404]$ MHz as the results of Figure III.11(d). In the end, the 8VCT MBFC is favored for measurements, for its large $|\alpha| \geq 0.8$, as well as its near zero reflection coefficient's magnitude, which should both minimize the impact of spurious harmonics. The reason behind such a discrepancy could not be identified, and is thought to be due to some elements in the experimental setup that have not been predicted for.

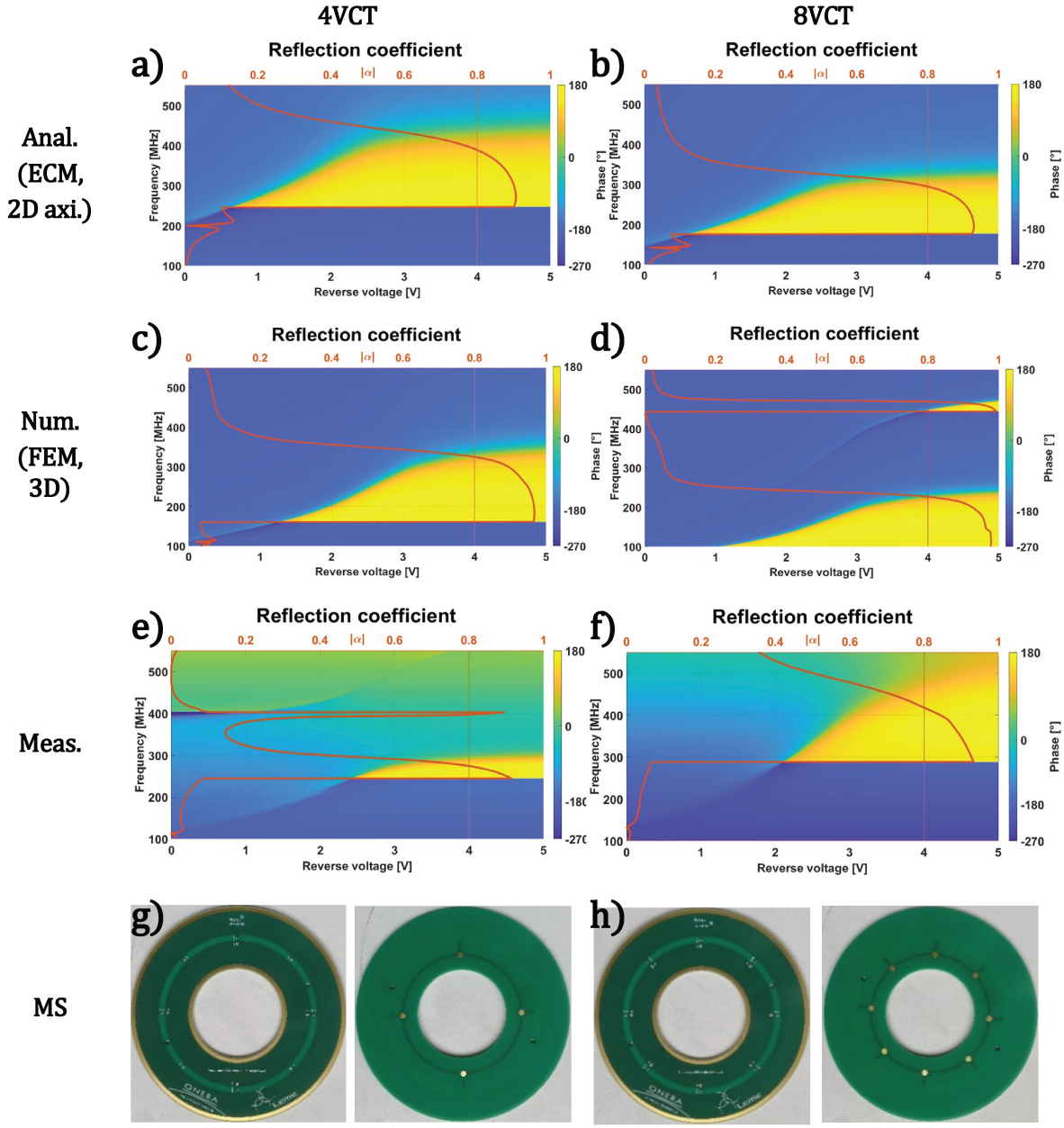

Figure III.11 : Phase of the reflection coefficient (map) and obtained $|\alpha|$ fraction (red line) from (a)-(b) an equivalent circuit model, (c)-(d) a 3D model, and (e)-(f) measurements of 4VCT and 8VCT metasurface-based frequency converters using SMV1255 varactor diodes. (g) Top and bottom faces of the 4VCT metasurface-based frequency converter. (h) Top and bottom faces of the 8VCT metasurface-based frequency converter.

3.4.3. Time-domain measurement of the frequency shifting of an harmonic wave at $f_0 = 370$ MHz by the time-modulation of the metasurface-based frequency converter

From the phase plots of Figure III.11(f), it was decided to use $f_0 = 370$ MHz as the incident wave's frequency. This frequency is favored, instead of the previously used $f_0 = 300$ MHz, because it offers a large $|\alpha| = 0.88$ without being too close to a non-smooth phase variation, at the tip of the upper yellow patch, where absorption is largest. In such a case, the phase is linearized in time over a modulation period T_m for a modulation frequency $f_m = 100$ kHz. In Figure III.12, the PSD of both the incident and reflected signals from measurement are provided from a measurement duration of five modulation periods T_m.

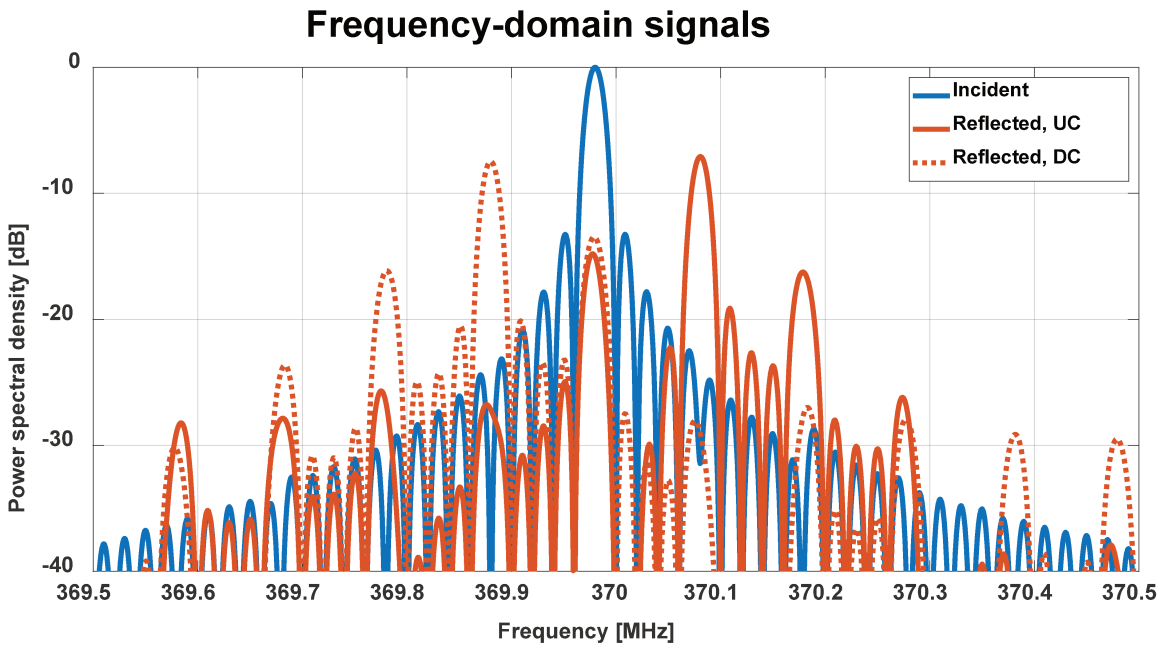

Figure III.12 : Relative power spectral density of the (blue) incident and (red) reflected electric signals from measurements of a varactor-loaded metasurface-based frequency converter using eight SMV1255 varactor diodes for an impinging wave at frequency $f_0 = 370$ MHz and both an (solid) up- and (dashed) down-conversion of frequency $f_m = 100$ kHz, namely *UC* and *DC*.

As can be noticed in Figure III.12, the frequency conversion of the incident harmonic wave at $f_0 = 370$ MHz is observed on the reflected signals' PSD whose specular harmonic is found at $f_0 \pm f_m$ for $f_m = 100$ kHz. One may notice slightly off-centered power-bearing frequencies caused by a slight bias from the signal generator, but that does not impact the frequency conversion process. One may also notice a stronger conversion loss of around $CL \approx 7.25$ dB, and reduced $R_0 \approx 14.2$ dB compared to the metrics of Figure III.8. This may be due to the lesser $|\alpha| = 0.88$, compared to $|\alpha| = 0.90$ in the analytical and numerical studies and $|\alpha| = 0.92$ in the semi-analytical. However, the main source of losses here is ohmic since the reflection coefficient's magnitude, though supposedly reduced from the 4VCT configuration (Figure III.10(b)), is measured to reach a minimum of around -10 dB at $f_0 = 370$ MHz, as seen in Figure III.13.

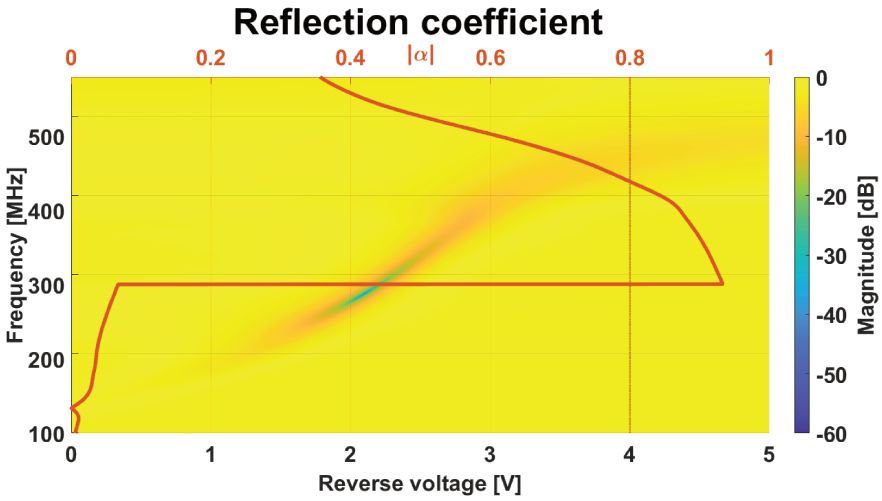

Figure III.13 : Magnitude of the reflection coefficient (map) and obtained $|\alpha|$ fraction (red line) from measurements of the 8VCT metasurface-based frequency converter using SMV1255 varactor diodes

These results confirm the interest in using such a MBFC for Doppler cloaking strategies, but the reduced R_0 value should be addressed in further developments. One may also notice that the measurements here are strongly affected by an asymmetric power distribution upon reflection. Though this behavior was previously noticed, it was never observed to be as marked as here. In fact, looking over a wider frequency range, as provided in Figure III.14, one may notice a strong asymmetry of the reflected spectra, for both up and down-conversion. In fact, it seems there are two regimes: on one side of the reflected wave's PSD, harmonics abruptly lose all power, while on the other side, their power only linearly decreases with distance to the main harmonic. This behavior was never observed in the validation studies of Section 3.2, and might be induced by an undesired element of the reflection coefficient. However, such an element would then by defined as affecting only the side opposed to the direction of the conversion., *i.e.* $f \leq f_0 - 2f_m$ for the up-conversion (Figure III.14(a)) and $f \geq f_0 + 2f_m$ for the down-conversion (Figure III.14(b)). At present, the source of this behavior remains undetermined.

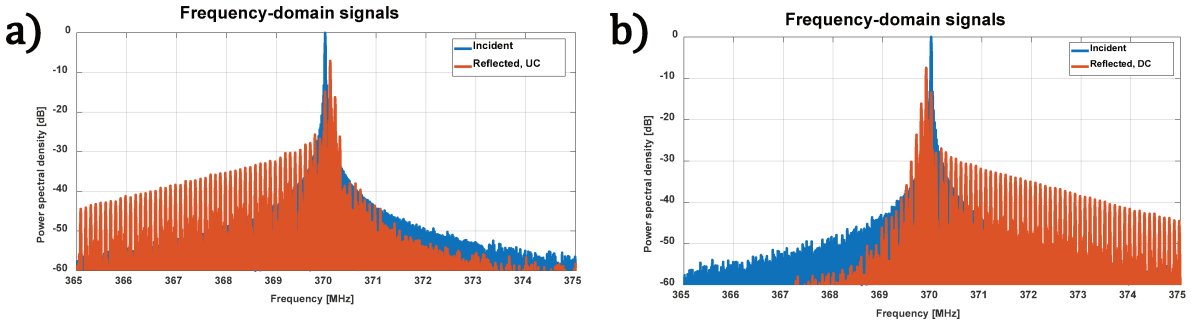

Figure III.14 : Relative power spectral density of the (blue) incident and (red) reflected electric signals from measurements of a varactor-loaded metasurface-based frequency converter for an impinging wave at frequency $f_0 = 370$ MHz and both an (a) up- and (b) down-conversion of frequency $f_m = 100$ kHz.

3.4.3.1. Frequency conversion degradation with increasing modulation frequency f_m

In the simulations of Section 2.2, the $f_m = 1$ MHz modulation frequency was favored to minimize computation times. However, at $f_0 = 300$ MHz, a Doppler shift $f_D = 1$ MHz is equivalent to a velocity superior to Mach 1000, which is unrealistic. On top of that, experimental measurements highlight an inability of the MBFC to properly shift the incident frequency at such a high modulation frequency. Indeed, as can be observed in Figure III.15(a), though harmonics are manifesting, the frequency bearing the most power is f_0. In fact, reducing the modulation frequency does improve results. This is confirmed by the observation of the frequency conversion at $f_m = 100$ kHz (Figure III.15(b)) and $f_m = 10$ kHz (Figure III.15(c)), where the harmonic at $f_0 + f_m$ is bearing the most power. The limiting factor is thought to be the traces on the backside of the metasurface in Figure III.11(g)-(j) that may not allow for the propagation of high frequency signals (cutoff from around $f_m = 500$ kHz). In fact, the reflected wave's PSD from any decreased modulation frequency gives very similar plots, as well as CL and R_0 to the $f_m = 100$ kHz case. This behavior was also experimentally confirmed for $f_m = 50$ kHz to $f_m = 10$ kHz, but is not included for brevity reasons.

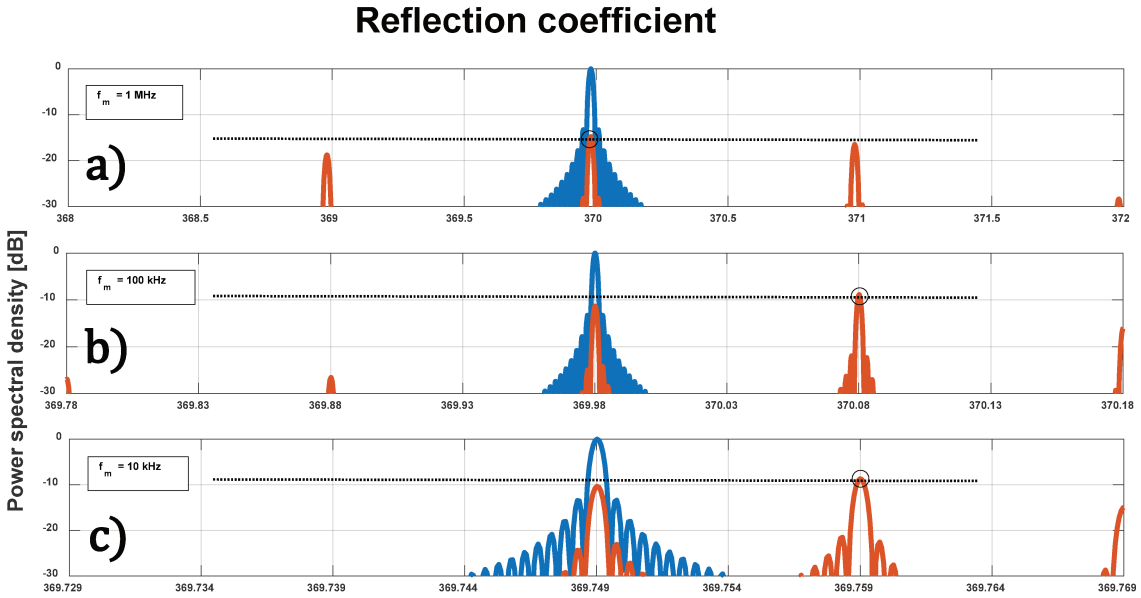

Figure III.15 : Relative power spectral density of the (blue) incident and (red) reflected electric signals from measurements of a varactor-loaded metasurface-based frequency converter using eight SMV1255 varactor diodes for an impinging wave at frequency $f_0 = 370$ MHz for an up-conversion of frequency (a) $f_m = 1$ MHz, (b) $f_m = 100$ kHz and (c) $f_m = 10$ kHz.

4. Experimental validation of a metasurface-based frequency converter for the frequency-conversion of non-harmonic waves

In this Section 4, the previously designed MBFC is used for the frequency shifting of non-harmonic waves. In fact, radar systems usually rely on signals exhibiting some bandwidth, such as FMCW (Frequency Modulated Continuous Wave) radars that rely on chirp signals. In the following, I consider a linear FMCW (LFMCW), which is a continuous train of chirps signals whose frequency is linearly varying with time. In Section 4.1, I analytically describe the existence of a non-zero frequency conversion bandwidth (FCB), and turn in Section 4.2, to analytical and

numerical studies (similarly as Figure III.5) in order to validate this behavior before the experimental campaign of Section 4.3.

4.1. Analytical justification of the existence of a frequency conversion bandwidth

Before using the metasurface for conversion of non-harmonic signals, here I aim at providing a justification for the existence of a non-zero frequency conversion bandwidth (FCB). In fact, around the frequency of interest $f_0 = 300$ MHz, the phase profiles are as depicted in Figure III.16(a). It appears in Figure III.16(b) that the reflection coefficient's phase profiles of the neighboring frequencies to f_0 are also almost linearized during this process, which would imply the existence of a non-zero FCB.

To better understand, these phase profiles can be fitted by different approximations, such as a piece-wise linear approximation, as illustrated in Figure III.16(c). In particular, for the frequencies closest to f_0, the phase profiles can be fitted by a two-piece linear approximation, from which the periodically modulated phase can be expressed as

$$\Gamma(t) = \left(e^{j\alpha_a\omega_a t}\mathrm{rect}\left(\frac{t - T_a/2}{T_a}\right) + e^{j\alpha_b\omega_b t}\mathrm{rect}\left(\frac{t - T_b/2}{T_b}\right)\right) * \sum_{n=-\infty}^{+\infty} \delta(t - nT_m) \qquad \text{(III.28)}$$

where $\alpha_a = (\varphi_0 - \varphi_1)/2\pi$, $\alpha_b = (\varphi_2 - \varphi_0)/2\pi$ and $T_a + T_b = T_m$, as illustrated in Figure III.16(c).

In such a case, by Fourier transform, the frequency-domain expression of the reflection coefficient $\tilde{\Gamma}$ is

$$\tilde{\Gamma}(\omega) = \left(W_{\alpha_a}(\omega) + W_{\alpha_b}(\omega)\right) \sum_{n=-\infty}^{+\infty} \delta(\omega - n\omega_m) \qquad \text{(III.29)}$$

with

$$\begin{cases} W_{\alpha_a}(\omega) = T_a sinc\left(\dfrac{\omega - \alpha_a\omega_a}{2} T_a\right) e^{-j\omega T_a/2} \\ W_{\alpha_b}(\omega) = T_b sinc\left(\dfrac{\omega - \alpha_b\omega_b}{2} T_b\right) e^{-j\omega T_b/2} \end{cases} \qquad \text{(III.30)}$$

From Equation (III.29), it therefore appears the total frequency-domain reflection coefficient is a sum of the periodic reflection coefficient from each piece of the approximation.

One may notice that the Dirac comb is not affected by this approach since it is imposed by the periodicity of the modulation T_m. However, the weighting functions may distribute power to these harmonics differently than what was obtained for the center frequency in Equation (III.14) and Equation (III.15). For instance, since the conversion is favoring the harmonic closest to $\alpha_x\omega_m$, where $x = a$ or $x = b$, and that $\alpha_a + \alpha_b < 1$, then $\alpha_a < 0.5$ and/or $\alpha_b < 0.5$, which should lead to no conversion from the first and/or second half of the approximation. However, since $T_a + T_b = T_m$, then either $\omega_a \geq \omega_m$ or $\omega_b \geq \omega_m$, which will spread the main lobe of the associated cardinal sine function, distributing power to more harmonics around $\alpha_x\omega_m$. For instance, $\alpha_a < 0.5$ but $T_a/T_m < 0.5$ will distribute power to harmonics $-\omega_m$, 0 and ω_m.

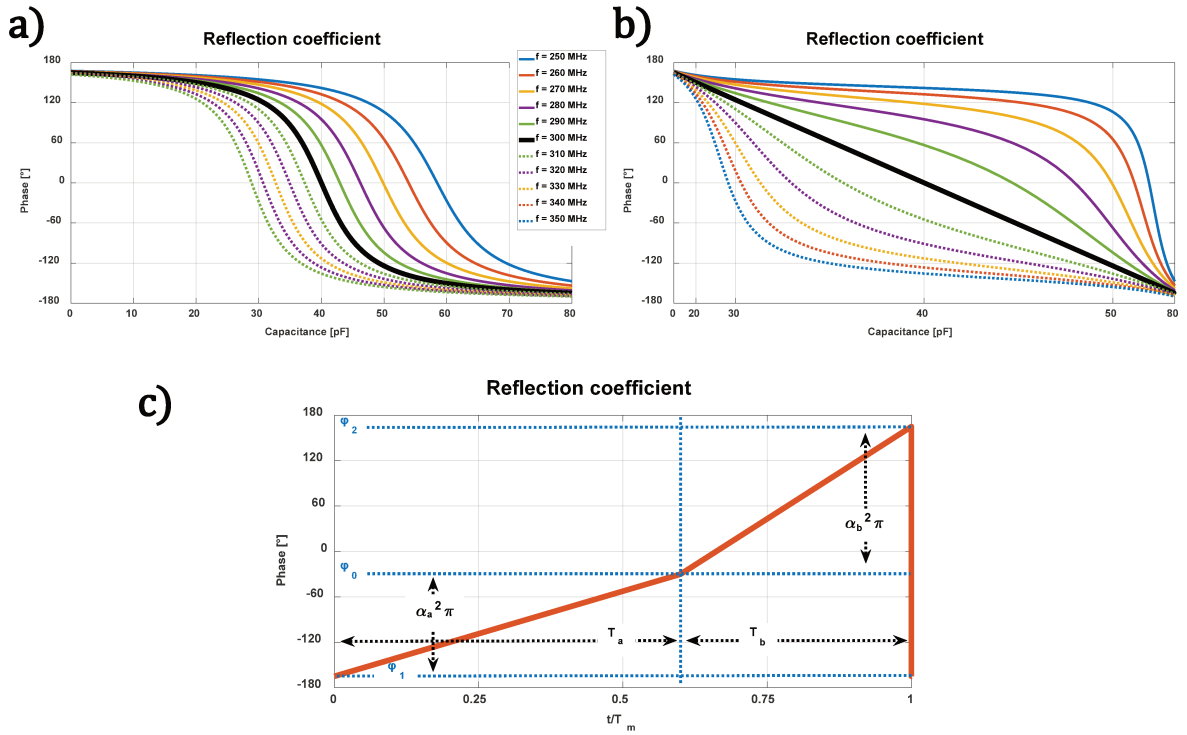

Figure III.16 : (a) Default and (b) modulated phase of the reflection coefficient from a 2D axisymmetric FEM model of a 8VCT metasurface-based frequency converter using varying capacitors for linearization at $f_0 = 300$ MHz, highlighting the curving of the phase profiles of neighboring frequencies in $f_0 \in [250, 350]$ MHz. (c) Illustration of the two-piece linear approximation used for the fitting of the phase of the reflection coefficient of the metasurface-based frequency converter at a frequency f in the close vicinity to the frequency of linearization f_0.

From this explanation, it seems the MBFC considered here can in fact be used for the frequency conversion of non-harmonic signals. Though it was stated a degradation of the frequency shift is expected with distance to the frequency of the phase linearization, an exact FCB is hard to predict for such a purely analytical study. In order to confirm the existence and extent of the non-zero FCB for such a metasurface, it is more appropriate to turn to simulations, where either analytical or numerical, to provide an actual value to the FCB.

4.2. 2D Analytical and numerical studies of the metasurface-based frequency converter for an incident non-harmonic signal of center frequency $f_0 = 300$ MHz and modulation frequency $f_m = 1$ MHz

In this Section 4.2, the signal of interest is a continuous train of chirps with linearly varying frequency, where each individual signal $c(t)$ is defined as

$$c(t) = sin\left(\left(\omega_i + \frac{\omega_f - \omega_i}{2T_c}t\right)t\right) rect\left(\frac{t - T_c/2}{T_c}\right) \quad \text{(III.31)}$$

where $\omega_i = \omega_0 - \Delta\omega/2$ and $\omega_f = \omega_0 + \Delta\omega/2$ and T_c the duration of the chirp. In the case of the FMCW radar operating regime, the chirp duration T_c and pulse repetition period T_p are the same. Therefore, in the frequency-domain, the expected spectrum of the incident signal is such that

$$\tilde{E}_i(\omega) = \left(\tilde{C}(\omega) * T_c sinc\left(\frac{\omega}{2}T_c\right) e^{-\frac{jT_c}{2}}\right) \sum_{n=-\infty}^{\infty} \delta(\omega - n\omega_p) \quad \text{(III.32)}$$

with $\tilde{C}$ the Fourier transform of a sine wave of linearly varying frequency and ω_p, the frequency of the pulse repetition. For large bandwidth-duration product, $\tilde{C}(\omega)$ is a flat-topped spectrum, which is then sampled by the Dirac comb at the pulse repetition frequency. Finally, the finite duration of the simulation convolutes the resulting comb with a cardinal sine wave.

In the case studied here, the chirp signals are centered around $f_0 = 300$ MHz, display a $\Delta f = 80$ MHz bandwidth and a pulse duration $T_c = T_m/5 = T_p$. The considered bandwidth does not reach an exact flat top spectrum since $\Delta f T_c = 16$ is not very large compared to 1. Yet, it is large enough to illustrate the existence of the FCB. Once again, in this Section 4.2, the analytical and numerical studies are conducted according to the process of Figure III.5 in order to predict the behavior expected from the experimental campaign of Section 4.3. The semi-analytical study is not conducted here for brevity.

4.2.1. Analytical study of the metasurface-based frequency converter from an equivalent circuit analysis for a continuous train of chirp signals

From the explanations on the FCB of Section 4.1, the reflected signal's PSD is then expected to be an exact transposition of the incident signal, though only around the center frequency – because of the frequency conversion degradation with distance to the frequency of phase linearization. Using the tools of the analytical study introduced in Figure III.5, the incident and reflected wave's PSD are provided in Figure III.17(a), for five modulation periods T_m, from a 8VCT MBFC using SMV1255 varactor diodes. As done in the preliminary studies of Section 3, a modulation frequency of $f_m = 1$ MHz is chosen to keep the simulation time of the numerical study within reasonable durations.

As can be noticed, the PSD is made up of two families of frequency-bearing harmonics. First of all, as can be identified from the incident signal's PSD, there is the pulse repetition frequency separating the chirp's Dirac-sampled frequencies of $f_p = 5f_m = 5$ MHz. These will be referred to as *FMCW harmonics*. While the reflected signal's PSD is plagued by another family of harmonics, stemming from the modulation, separating power-bearing frequencies by $f_m = 1$ MHz. These will be referred to as *modulation harmonics*. Therefore, one may notice each FMCW harmonic is up-converted by f_m. This can be observed around $f_0 = 300$ MHz, from around 270 MHz to above 350 MHz.

This asymmetry is most probably due to the asymmetry in distribution of the phase profiles as seen in Figure III.16(a). For instance, at $f = 250$ MHz, the resonance capacitance is $\Delta C_0 = 30$ pF higher than that at $f_0 = 300$ MHz, while at $f = 350$ MHz, the difference is only $\Delta C_0 = 25$ pF. Therefore, lower frequencies' phase profiles distance faster from the ideal linearized phase profile at $f_0 = 300$ MHz from Figure III.16(b), than higher frequencies'. Of course, an intermediate modulation can be devised to grant symmetry to the frequency conversion bandwidth, which may simply be shifting the center frequency up for compensation.

Despite this asymmetry, similarly to the harmonic case, the definition of metrics will help quantify the conversion of non-harmonic signals. To this end, two metrics are considered: the frequency conversion bandwidth (FCB) and average conversion loss (ACL). The FCB is an equivalent to R_0, quantifying the bandwidth over which $R_0 \geq 10$ dB for each power-bearing frequencies, while ACL is an equivalent to CL, quantifying the average power loss during conversion over the previously established FCB. In this case, $FCB = 15$ MHz and $ACL \approx 0.68$ dB. In this case, under the definition of the FCB metrics, the asymmetry of phase profiles seems not to have the expected effect on the distributions of power. Furthermore, the absorption cause by the varactor diodes, despite being visible over the lower frequencies, seems surprisingly small over the center frequencies. In order to confirm these values, a numerical study is therefore necessary.

4.2.2. Numerical study of the metasurface-based frequency converter from a 2D axisymmetric FETD simulation for a continuous train of chirp signals

For this numerical, the exact same model used in the 2D axisymmetric numerical studies of Section 3.2.2 is used, with the non-harmonic signal of Equation (III.31). The metasurface used is the 8VCT one using SMV1255 varactor diodes. The frequency-dependent behavior of the reflection coefficient should therefore be well taken into account, in both phase and magnitude. In fact, after simulation, the incident and reflected wave's PSD are provided in Figure III.17(b).

Once again, both the FMCW harmonics and modulation harmonics show up, and confirm the conversion of some frequencies around $f_0 = 300$ MHz. Using the previously defined metrics, this conversion does reduce the original frequency-bearing by at least 10 dB over $FCB = 25$ MHz. And the asymmetry manifests as a centering of the FCB at $f = 307.5$ MHz, instead of the original $f_0 = 300$ MHz. Furthermore, the general absorption brought by the use of varactor diodes is more apparent around the center frequencies, where it seems underestimated in Figure III.17(b). In fact, using the previously defined metrics, the average conversion loss over the FCB is $ACL = 2$ dB. In this case, both the expected asymmetry of conversion and the absorption of center frequencies is observed, and both FCB and ACL are larger than hinted at during the analytical study.

a)

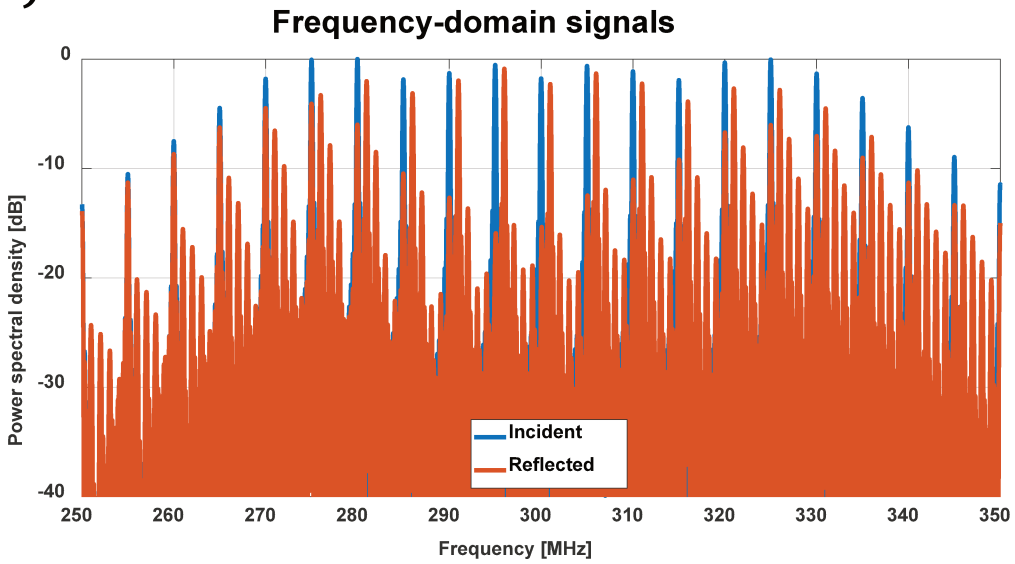

Analytical

FCB [MHz]	ACL [dB]
15	0.68

b)

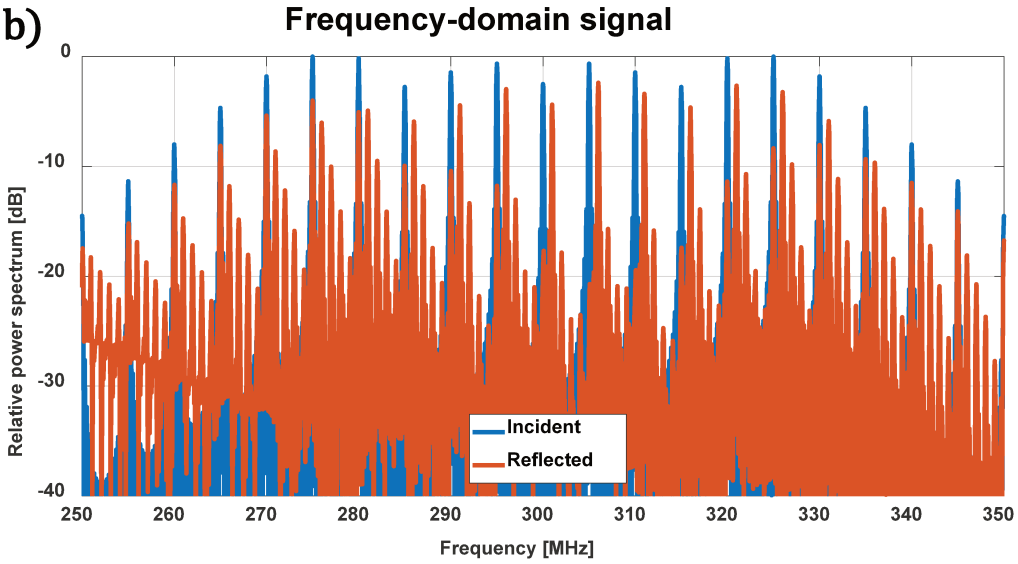

Numerical

FCB [MHz]	ACL [dB]
25	2.0

Figure III.17 : Relative power spectral density of the (blue) incident and (red) reflected electric signals from (a) the analytical and (b) numerical studies from a SMV1255 varactor diode-loaded metasurface-based frequency converter in the 8VCT configuration for an impinging train of chirp signals of center frequency $f_0 = 300$ MHz, bandwidth $\Delta f = 80$ MHz, chirp duration $T_c = T_m/5$ and pulse period $T_p = T_c$, for the up-conversion of frequency $f_m = 1$ MHz.

In both the analytical and numerical studies, the existence of the non-zero FCB is well-observed, despite an inaccuracy from the ECM. Using the numerical study as the standard reference for ulterioir comparisons, it seems a FCB of up to around $FCB = 25$ MHz with $ACL = 2.0$ dB can be expected from a conversion of non-harmonic signals set for $f_0 = 300$ MHz.

4.3. Experimental validation of a time-modulated metasurface for the frequency-conversion of non-harmonic waves around $f_0 = 370$ MHz

From the phase plots of Figure III.11(f), it appears that the 8VCT metasurface using the SMV1255 model makes up for a MBFC whose phase profiles at neighboring frequencies are close enough to offer an interesting frequency conversion bandwidth. To confirm the analytical and numerical results previously presented, the MBFC is used against the same FMCW wave as before – center frequency $f_0 = 370$ MHz and $\Delta f = 80$ MHz – while undergoing a modulation of $f_m = 100$ kHz. In that case, $T_c = T_m/5$ leads to $\Delta f T_c = 160$, which can be argued to produce a flat-topped spectrum.

The experimental setup is the same as Figure III.9(b), only substituting the harmonic waveform generator (2023A Signal Generator by IFR®) for an arbitrary waveform generator (Tektronix® AWG5000 Series) compatible with LFMCW requirements. After five modulation periods T_m, the resulting incident and reflected PSD are provided in Figure III.18. Because of the smaller frequency shift, the frequency range of Figure III.18 is reduced from that of Figure III.17 to better notice the effects of the frequency converter.

As can be noticed, the reflected wave's spectrum is up-shifted from the incident's one by the modulation frequency around $f_0 = 370$ MHz, confirming the existence of the frequency conversion bandwidth from such a MBFC. In fact, it apparently extends from around $f = 348$ MHz to $f = 417$ MHz. Referring to previously defined metrics, despite some exceptions, the conversion granting a reduction of at least $R_0 \geq 10$ dB happens over $FCB = 31$ MHz around $f_0 = 384$ MHz, because of the asymmetry of phase profiles. This is somehow larger than expected, and it is probably due to a more beneficial distribution of phase profiles in the practical case than the numerical one, just like there were differences in simulated and measured profiles in Figure III.11 However, the average conversion loss increases to $ACL = 4.56$ dB, which is larger than expected. However, it is close to the CL observed in the harmonic case in Figure III.12. The discrepancy may therefore be due to the additional absorbing elements in the experimental setup that the analytical and numerical studies did not take into account.

The frequency conversion of the incident signal around the center frequency of phase linearization confirms the existence of a non-zero FCB. This feature is particularly interesting to face practical radar signals, such as FMCW. They are particularly interesting for the simultaneous measurement of range and velocity, the latter being estimated from Doppler shift measurement. Therefore, a MBFC is a practical solution to the frequency compensation necessary for the suppression of the Doppler shift over the impinging chirp signal's bandwidth. Experimentally, 8% to 10% of bandwidth is converted from a signal of center frequency in the $[350, 400]$ MHz range, results of which are not presented here for brevity.

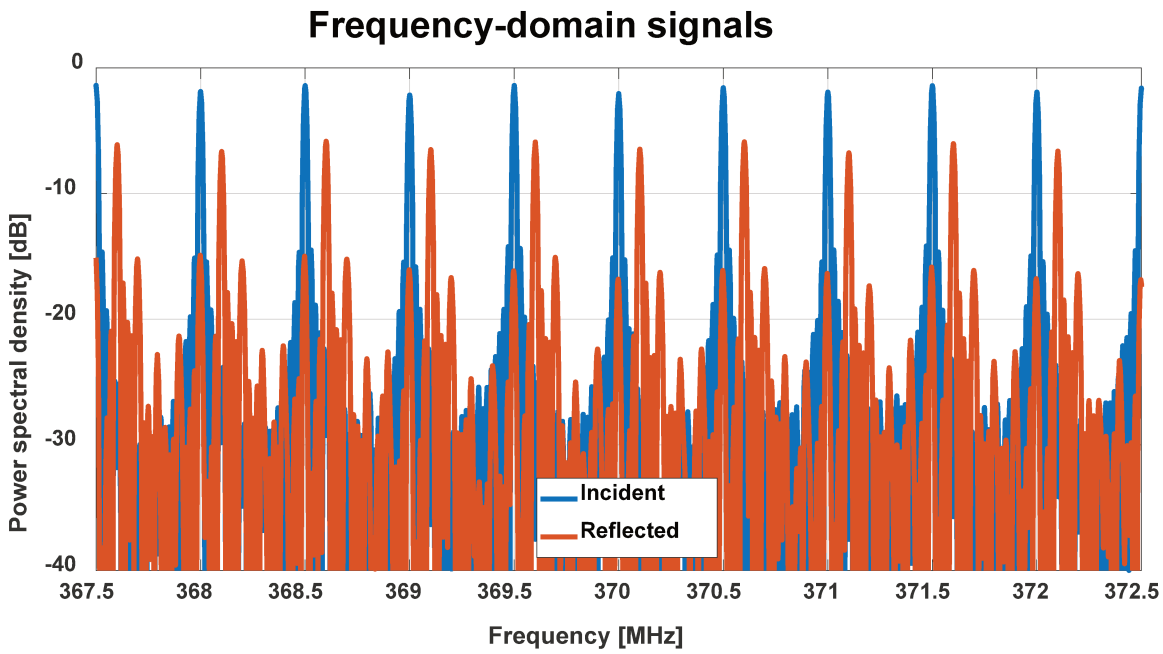

Figure III.18 : Power spectral density of the (blue) incident and (red) reflected electric fields from measurements for an impinging train of chirp signals of center frequency $f_0 = 300$ MHz, bandwidth $\Delta f = 80$ MHz, chirp duration $T_c = T_m/5$ and pulse period $T_p = T_c$, for the up-conversion of frequency $f_m = 100$ kHz using the SMV1255 varactor-diode-loaded metasurface.

5. Conclusions

In this Chapter III, I developed and experimentally validated a metasurface-based frequency converter over the VHF-UHF bands. I first introduced, in Section 2, the underlying principles behind the time-modulation to enable frequency-shifting in a reflective case. In particular, it is crucial to ensure the modulation is slow enough for the system to be seen as static at all times by the impinging wave. Under this two-time segregation, I then introduced analytical results on both an ideal and non-ideal frequency converters, based on the phase-induced frequency-shifting provided by the reflection coefficient's phase ramp, in order to predict the expected behavior in practical cases. In particular, it appears a phase ramp of non-ideal variation $|\alpha|2\pi$, with $|\alpha| < 1$, over the modulation range introduces an infinite number of harmonics in the reflected wave's spectrum. In this case, for any fraction $|\alpha| > 0.5$, frequency shifting is still granted thanks to a weighting function favoring the harmonics $f_0 \pm f_m$, depending on the up- or down-conversion modulation scheme used.

In Section 3, I then tackled the actual design and validation of a MBFC in the case of an impinging harmonic case. I first highlighted the conditions for the design of a practical MBFC. In fact, a purely reactive and short-circuited metasurface, can offer the necessary broad and smooth phase variation through reactance modulation. In practice, these requirements are baked into the metasurface using varactor diodes for capacitance modulation. I then proceeded to the theoretical and numerical validation of the MBFC with analytical, numerical and semi-analytical models in the 2D axisymmetric case, confirming the frequency converting mechanisms of the considered structure. Then, with a semi-analytical model in order to avoid a time-consuming full-wave 3D time-domain simulation, a 3D analysis confirmed the behavior of the actual structure, from which two metasurfaces were built. The phase profiles of both MBFC were studied analytically, numerically and experimentally in order to single out the most appropriate device for the experimental campaign. Under illumination from an incident harmonic wave set at 370 MHz, the

frequency shifting up and down 100 kHz were measured, thereby confirming the suitability of the system for Doppler cloaking. Besides, this campaign also highlighted some limitations such as the maximum usable modulation frequency.

Finally, in Section 4, I demonstrated the suitability of the same MBFC for Doppler cloaking under LFMCW radar illumination. I first justified the existence of a non-zero frequency conversion bandwidth from an analytical standpoint on a simplified case, which I then confirmed with proper analytical and numerical simulations (2D axisymmetric). These simulations highlighted a FCB of around 40 MHz at 370 MHz, at which the frequency is up-converted and the initial frequency is decreased by at least 10 dB. Then, the experimental campaign confirmed this behavior, though with a lesser FCB, confirming for the first time the possibility to effectively shift in frequency an entire portion of an incident train of chirp signals, as used by FMCW radars.

CONCLUSIONS & OUTLOOKS

During this PhD, I have worked on improving active metasurface-based solutions for stealth over the VHF-UHF bands. First, I have used analytical tools, such as equivalent circuit models, and numerical tools, such as full-wave simulations, to design metasurfaces. Then, I proceeded to the fabrication of the designed metasurface-based structures. Finally, I conducted subsequent experimental validations, which confirmed the desired electromagnetic wave manipulation, and I thoroughly discussed the results.

In particular, I tackled two crucial aspects to stealth and electronic warfare at large: detection avoidance, thanks to a radar absorbing structure, and velocity-readings deception, thanks to a frequency-converting Doppler cloak.

In Chapter I, I started by introducing the necessary background on radar systems as well as seminal contributions to stealth. In particular, I detailed the principles behind the detection as well as the range-velocity estimates from radar systems, allowing, with elevation/bearing estimation, for both early warning detection and subsequent tracking. I took particular interest in FMCW radars, which can perform both range and velocity estimations at once using a frequency-modulated waveform, thus providing a concise picture of the entire illuminated scene with a single range-velocity map.

I introduced stealth solutions to defeat adversary radars. I first introduced the concept of target shaping, which is often the number one solution, whereby radar cross-section mitigation strategies define the target's shape. I then turned to impedance/admittance matching devices, *i.e.* radar absorbers, since *the design of a reflectionless structure is equivalent to the problem of matching from free space to a short circuit by means of a lossy transmission line* (Prof. C. G. Montgomery). Harnessing the power-dissipating properties of dielectric and/or magnetic layers, or the filtering behavior of resonant electromagnetic cavities, the conductor plane of the target's fuselage can be efficiently camouflaged from radar illuminations. In the last 25 years, the development of metasurface-based radar absorbers has led to a reduction in thickness without compromising the bandwidth.

However, optimizations notwithstanding, all *linear, passive and time-invariant* radar absorbers are limited in their bandwidth-to-thickness ratio by the Rozanov-Bode-Fano bound. This bound dictates a maximum bandwidth-to-thickness ratio that even metasurface-based solutions cannot overcome. Despite the existence of this bound, there currently exists no guideline on how to reach it, or even if it can be reached at all. At low frequencies, where the thickness of traditional solutions limits bandwidths, escaping the framework of the Rozanov-Bode-Fano bound is therefore essential to broadband absorption. The extreme versatility of metasurfaces therefore emerges as a particularly suitable solution to reach such new horizons.

Metasurfaces, thanks to their relatively simple design, loading of electronic elements, and fabrication, allow for a variety of wave manipulation structures, to be easily iterated over. In particular, active lumped elements can render radar absorbing materials active, thereby breaking the *passive* criterion of the Rozanov-Bode-Fano application field. The resulting active radar absorbers have therefore the potential to reach broader bandwidths. The reconfigurability offered by some active elements also motivated the development of a variety of stealth and radar deceiving solutions. For instance, this can be harnessed for the tunability of absorption frequency, both in open and closed loops, for prescribed or autonomous adaptations to impinging waves. Moreover, the additional temporal dimension can also be exploited for continuous reconfiguration, enabling spectral manipulations.

A metasurface in the VHF-UHF bands of interest is an arrangement of meta-atoms that can amount to a surface of impracticable dimensions. This is a major drawback in both the fabrication and measurement stages. It was therefore decided, at ONERA, to transpose the problem into the coaxial geometry.

In Chapter II, I decided to focus on the reconfigurability offered by active elements loaded onto a metasurface-based radar absorber in the VHF-UHF bands. The metasurface-based radar absorber of interest here was derived from a resonant Salisbury screen, for which the quarter-wave impedance inverter was drastically reduced in thickness thanks to the reactive nature of the metasurface screen. Therefore, the objective was to design the proper impedance/admittance matching metasurface for absorption at the desired frequency. This was done by loading the necessary electronic lumped elements onto the metasurface. The decision was then made to turn away from complex circuits to focus on simpler realizations.

A metasurface-based radar absorber was first designed using an equivalent circuit model, which was validated by 2D axisymmetric FEM simulations. The ECM model is a good descriptor of a rotation-invariant structure, but lacks accuracy for 3D structures. These discrepancies have been attributed to higher-order interactions of the metasurface, which were overlooked in the first-order ECM. 3D FEM simulations were used to validate the final design.

Finally, the experimental measurement of a metasurface-based radar absorber at $f_0 =$ 300 MHz was carried out. Designed with the ECM and confirmed by the FEM simulation results, thereby validating this two-step process for further developments.

I then moved on to the design of a frequency-tunable absorber, substituting the fixed capacitors for varactor diodes. This was intended as a means to provide wideband coverage from the sole reverse bias voltage, the resulting capacitance dictating the absorption frequency. However, the resistive elements brought along by varactor diodes introduced undesired variations of the metasurface's overall resistive behavior. This manifested, in both ECM and FEM simulations as a deterioration of the impedance/admittance matching for some frequency-voltage combinations. This behavior was confirmed to originate from the sole resistive element by comparison with a model of purely reactive varactor diodes, where magnitude variations were entirely absent.

In order to counter this undesired behavior, I then turned to a numerical investigation into a metasurface-based radar absorber with both resistance- and capacitance-tuning. Resistance-tuning can be a way to compensate impedance/admittance mismatches on the fly, granting near-perfect absorption over the covered range.

Finally, I extended this work to a case similar to the *smart radar absorber* of Prof. D. Chambers and Prof. K. L. Ford, to face frequency-hopping radar. Thanks to a continuous reconfiguration, the MBRA can be used for an effectively wideband absorption of incident frequency-sweeping harmonic signals. The linear change of biasing was proven to be only approximating the ideal absorption profile, which would have to be specifically adapted for practical uses.

In Chapter III, I decided to focus on the spectral manipulation offered by the modulation in time of the reflection coefficient of a metasurface-based structure. I took particular interest in a frequency converter to serve Doppler cloaking strategies in the VHF-UHF bands. I first started by an introduction of the slow-modulation framework, enabling spectral modulation upon interaction. Applied to the frequency shifting of the incident wave, I then turned to the analytical study of both an ideal and non-ideal frequency converter. In fact, I predicted the effects of a reduced phase variation over the modulation period. Though not compromising frequency-

shifting, this plagues the reflected signal's spectrum with an infinite number of weighted harmonics of the incident signal's spectrum.

Then, I took to the design of the metasurface-based frequency converter. I first showed that a proper modulation in capacitance can linearize the phase of the reflection coefficient of the metasurface-base structure for frequency shifting. Setting an incident harmonic wave at $f_0 = 300$ MHz and modulation frequency at $f_m = 1$ MHz, I compared the results in frequency shifting, from a purely analytical standpoint, between the use of ideal variable capacitors and varactor diodes. In both cases, the modulation pattern was similar, and the reflected signal's power spectral density was shifted in frequency, up or down by the modulation frequency. Besides, it did confirm the resistive elements bring undesired absorption. I then turned to a fully-numerical approach in a 2D axisymmetric configuration, which minimizes the complexity of the simulation setup compared to a 3D model. Similar results as for the analytical study, in terms of conversion loss and power reduction of the incident harmonic, were observed, as well as the frequency shifting. Then, I blended both approaches into a semi-analytical study to alleviate the duration of the costly time-domain simulation, leading to almost identical results to both the analytical and numerical studies. The validation of this 2D semi-analytical approach confirmed that a 3D semi-analytical could be relied upon for the actual design. The resulting frequency-shifted power spectral densities showed slightly better metrics in 3D, compared to the 2D axisymmetric case, thanks to a wider phase variation.

Two metasurfaces were manufactured, using either four or eight varactor diodes. The measured phase variation profiles indeed confirmed their suitability for frequency conversion over portions of the VHF-UHF bands, though measurements eventually highlighted the metasurface loaded with eight varactor diodes was the most suitable for the experimental campaign.

Under modulation with $f_m = 100$ kHz, the metasurface-based frequency converter was illuminated by a harmonic wave set at $f_0 = 370$ MHz, effectively converted upon reflection, thereby validating the prototype for harmonic wave.

I then took to the experimental validation of that same structure to shift in frequency an entire range of frequencies, which is especially useful in against existing FMCW radars since they have a non-zero bandwidth. Measurements exhibited around 30 MHz bandwidth around $f_0 = 370$ MHz, thereby confirming the adequacy of this metasurface-based frequency in a non-harmonic Doppler cloak system.

To summarize, in my PhD thesis, I introduced the principles behind radar systems in order to shed light on the limitations of seminal solutions to stealth. In fact, I highlighted that even the versatile metasurface-based stealth structures are bounded in their bandwidth-to-thickness ratio as long as they are *linear, passive and time-invariant* in nature. However, their compatibility with active electronic components gives them all the tools to break any, or all, of these three constraints and explore new unbounded regimes. For instance, their active nature confers them reconfigurability mechanisms, to be harnessed for the tunability of the absorption frequency or the temporal control of the reflection coefficient of the metasurface-based structure. I therefore tackled these two topics, using varactor-loaded metasurface-based structures. First, by designing a frequency-tunable radar absorber, providing absorption over $[300, 600]$ MHz. Then, by designing a time-modulated frequency converter for the Doppler cloaking of moving targets from FMCW radars over $[300, 400]$ MHz.

Some outlooks are drawn out for possible further developments. First of all, due to the coaxial nature of the metasurface of interest, only the normal incidence is considered, whereas a

real target would be illuminated under various incidence angles. On top of that, the sole TEM illumination is considered. Though it emulates free space propagation, insensitivity to TE and TM polarizations is central to the development of operational solutions. Now, regarding the two solutions explored in this thesis, some specific outlooks have been laid out.

In the radar absorbing case (MBRA), here is a list of possible items to investigate in the future:

- **Optimized metasurface's resistance**
  The variation in magnitude of the reflection coefficient with reverse bias was confirmed to be due to the resistive element of the varactor diodes. A first approach to reducing these variations might be to find an optimized value for the overall metasurface's resistance, instead of the standard 50 Ω. In fact, even with the metasurface of fixed capacitance, the reflection coefficient magnitude at resonance from 3D simulations and measurements is higher than in analytical results, which overlooks higher-order interactions that have probably shifted around the exact resistance value required for impedance matching.
- **Experimental validation of the joint tuning**
  According to the numerical investigation of the validity of a joint tuning, the dispersion of values of optimized resistances is too high for some varactor diode model to be efficiently averaged with the previous solution. Therefore, the natural subsequent development is the design of a metasurface of joint resistance- and capacitance-tuning using transistors, for reflection coefficient magnitude variations compensation, and varactor diodes, for frequency tunability. Its viability has been proved numerically and applied to three different models. For experimental validation, on top of the integration of the three-pinned JFET on the top plane, the bottom plane of the metasurface must be properly routed to accommodate for two independent signal paths.
- **Closed-loop smart radar absorber**
  As proposed by Prof. Chambers, blending a tunable radar absorber with a frequency sensor into a feedback loop can lead to a smart radar absorber [97]. Though partially investigated in Section 5.2 of Chapter II, the linearly varying voltage signal showed its limitations. In order to reach the ideal phase profile, a voltage-absorption frequency mapping must be done beforehand, in order to use a compensating biasing pattern, as done for the MBFC and the phase ramp.

In the time-modulated frequency converter case (MBFC), I propose some possible items to investigate in the future:

- **Phase profiles discrepancies**
  Though the analytical and numerical simulations of the phase profiles are in accordance, the measured phase profiles exhibit a very different variation regime. The source of this discrepancy could not be identified, but probably is due to some external elements from the experimental setup.
- **Strong absorption**
  As provided in Figure III.13, the metasurface-based frequency converter using eight varactor diodes showed unexpectedly strong absorption depending on the frequency-bias combination. Since the metasurface was designed as a mostly capacitive element, this came as a surprise. A possible source for this absorbing behavior might be the use of silver epoxy paste for the electric contact between the metasurface and the sample-holder, probably introducing some resistive elements.
- **Harmonics decrease regime**

It was highlighted in Figure III.14, at the end of the experimental campaign of the harmonic case, that the measured reflected wave's PSD shows a peculiar behavior. In particular, the harmonics around the shifted frequency decrease in power following two different regimes, on either side. This behavior was never observed during the previous analytical nor numerical simulations, and seems therefore to originate from a purely experimental issue. The most probable cause is the modulation pattern, inducing a supplementary transformation of the spectra.

- **Frequency shifting degradation with frequency**
  It was highlighted in Figure III.15, at the end of the experimental campaign of the harmonic case, that there was a degradation of the frequency shifting mechanism with increasing frequency. It was experimentally confirmed to work with only negligible distortion up to 200 kHz, but the spectra obtained at 500 kHz could already highlight the degradation of the conversion. The microstrip traces for the propagation of the modulation frequency are thought to be the cause for this issue. It is a probably because they have not been designed for such frequencies, and the vias, from the back to the top planes, may have introduced a cut-off frequency. To investigate this point, a wafer probing of the metasurface must be considered.
- **Pulsed regime**
  The pulsed regime is very common among radar systems, which is based on short-lived frequency-modulated pulses emitted with a large period of repetition. However, the synchronization between the source and the Doppler cloak in this case is crucial to the effective deception. Therefore, similarly to the closed-loop radar absorber, a smart feedback loop, analyzing the impinging waveform, can be considered in order to adapt to following illuminations.

LIST OF PUBLICATIONS

COMMUNICATIONS

	FORMAT	REFERENCE
NATIONAL	Poster	T. Lopez, T. Lepetit, and S. N. Burokur, "Analyse circuit équivalent d'une métasurface passive en tant qu'absorbant électromagnétique," GDR Lille, 2021.
	Oral	T. Lopez, T. Lepetit, and S. N. Burokur, "Analyse circuit équivalent d'un absorbant radar à métasurface," JS URSI Paris, 2022.
	Poster	T. Lopez, T. Lepetit, B. Ratni, and S. N. Burokur, "Analyse Circuit Equivalent d'un Absorbant Radar à Métasurface," JNM Limoges, 2022.
	Poster	T. Lopez, T. Lepetit, B. Ratni, and S. N. Burokur, "Métasurface Modulée Temporellement pour Conversion de Fréquence," GDR Marseille, 2023.
	Oral	T. Lopez, T. Lepetit, B. Ratni, and S. N. Burokur, "Sur la Validité de Nouveaux Schémas de Modulation pour la Conversion en Fréquence de Signaux par une Métasurface Modulée Temporellement," JNM Antibes, 2024.
INTERNATIONAL	Oral	T. Lopez, T. Lepetit, B. Ratni, and S. N. Burokur, "Reconfigurable Coaxial Metasurface Radar Absorber Using Varactor Diode Tuning," in *2023 IEEE International Symposium on Antennas and Propagation and USNC-URSI Radio Science Meeting (USNC-URSI)*, 2023, pp. 1775–1776. doi: 10.1109/USNC-URSI52151.2023.10238029.
	Oral	T. Lopez, T. Lepetit, B. Ratni, and S. N. Burokur, "Experimental Validation of a Reconfigurable Coaxial Metasurface Radar Absorber Using Varactor Diode Tuning," in *2023 Seventeenth International Congress on Artificial Materials for Novel Wave Phenomena (Metamaterials)*, 2023, p. X-211-X–213. doi: 10.1109/Metamaterials58257.2023.10289133.
	Oral	T. Lopez, T. Lepetit, B. Ratni, and S. N. Burokur, "Time-Modulated Metasurface for Harmonic Signals Frequency Conversion," in *2024 18th European Conference on Antennas and Propagation (EuCAP)*, 2024, pp. 1–4. doi: 10.23919/EuCAP60739.2024.10501399.

PUBLICATIONS

STATUS	REFERENCE
Published	T. Lopez, T. Lepetit, and S. N. Burokur, "Equivalent circuit analysis of a mode-converting metacell in a coaxial transmission line at microwave frequencies," *Journal of Applied Physics*, vol. 132, no. 5, p. 054901, 2022, doi: 10.1063/5.0096832.
Published	T. Lopez, T. Lepetit, B. Ratni, and S. N. Burokur, "Design and measurement of a tunable metasurface low-frequency radar absorber," Journal of Applied Physics, vol. 135, no. 12, p. 124901, Mar. 2024, doi: 10.1063/5.0196932.
Submitted	T. Lopez, T. Lepetit, B. Ratni, and S. N. Burokur, "Broadband Metasurface-Based Doppler Cloaking over VHF-UHF Bands", 2024.

APPENDIX

CONTENTS

APPENDIX **125**

A. REFLECTION AND TRANSMISSION AT A TEMPORAL BOUNDARY 127
A.1. Reflection and transmission coefficients at a temporal boundary *127*
A.2. Frequency shift at a temporal boundary *128*
A.3. General behavior at a temporal boundary *128*
A.4. Wave manipulation from temporal boundaries for stealth *129*
B. SIMULATION SOFTWARES 131
B.1. COMSOL® *131*
B.1.1. Frequency-domain simulations 131
B.1.2. Time-domain simulations 131
B.2. MATLAB® *132*
C. TIME-DOMAIN SURFACE IMPEDANCE BOUNDARY CONDITION 133
C.1. Frequency- and time-domain expressions of the Surface Impedance Boundary Condition *133*
C.1.1. Frequency-domain expression 133
C.1.2. Time-domain expression 133
C.2. Surface Impedance Boundary Condition of classical electronic components *134*
C.2.1. Frequency-domain expressions 134
C.2.2. Time-domain expressions 134
C.2.3. COMSOL® implementation 134
C.3. Surface Impedance Boundary Condition of classical circuits *135*
C.3.1. Series circuits 135
C.3.1.1. Frequency-domain expressions 135
C.3.1.2. Time-domain expressions 135
C.3.1.3. COMSOL® implementations 136
C.3.2. Parallel circuits 136
C.3.2.1. Frequency-domain expressions 136
C.3.2.2. Time-domain expressions 136
C.3.2.3. COMSOL® implementations 137
C.4. Generalization of the expressions *137*
C.4.1. Particular case of a varactor diode 137
D. FREQUENCY CONVERSION AND α VALUE 141
E. VARACTOR DIODE'S SERIES RESISTANCE AND PHASE VARIATION REGIME 143
F. FINITE-ELEMENT TIME DOMAIN SIMULATION: BDF VS. GENERALIZED-α IMPLICIT SOLVERS 147

A. Reflection and transmission at a temporal boundary

CONTENTS

A.1. Reflection and transmission coefficients at a temporal boundary 127
A.2. Frequency shift at a temporal boundary 128
A.3. General behavior at a temporal boundary 128
A.4. Wave manipulation from temporal boundaries for stealth 129

The propagation of a wave in a time-modulated medium was already formulated in the late 50's [86]. It consists in the abrupt change of the entire medium's electromagnetic properties, ϵ and/or μ, to create a temporal boundary, analogue to a space boundary at the interface between two media. It is important to remember the time boundary is possible thanks to a change happening throughout the entire medium at once, so that there is no notion of locality in space. However, this does not forbid one from introducing hybrid boundaries.

References [89], [90], [91], [92], [128] deal with the general subject of (space-) time modulations and metasurfaces.

A.1. Reflection and transmission coefficients at a temporal boundary

Analogous to a spatial interface, the abrupt change of the medium's properties from a step function of ϵ and/or μ creates a *temporal* interface onto which the impinging wave is both reflected and transmitted [129], as illustrated in Figure App. 1.

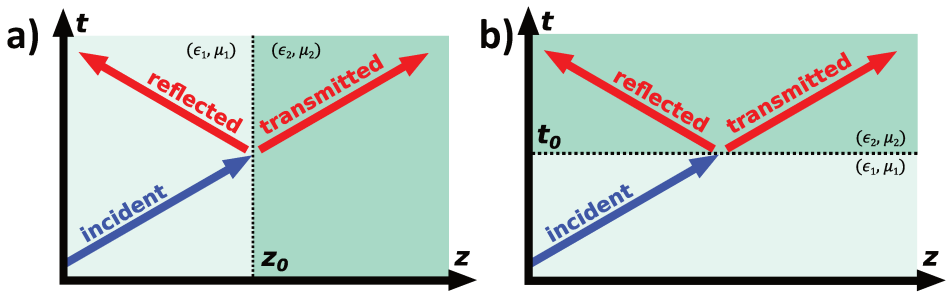

Figure App. 1 : Illustration of (a) spatial and (b) temporal boundaries, with highlight of the incident, reflected and transmitted waves and change of permittivity (ϵ) and permeability (μ).

As specified in [91], the continuity of $\boldsymbol{D}$ and $\boldsymbol{B}$ needs to be ensured at a temporal boundary. For instance, should the medium change with a step function from $\epsilon(t = t_0^-) = \epsilon_1, \mu(t = t_0^-) = \mu_1$ to $\epsilon(t = t_0^-) = \epsilon_2, \mu(t = t_0^-) = \mu_2$, then the electric and magnetic fields $E(t \geq t_0^+)$ and $H(t \geq t_0^+)$, are split into reflected and transmitted waves such that

$$\begin{cases} \epsilon_1 E_i(t = t_0^-) = \epsilon_2 \left(E_t(t = t_0^+) + E_r(t = t_0^+)\right) \\ \mu_1 H_i(t = t_0^-) = \mu_2 \left(H_t(t = t_0^+) - H_r(t = t_0^+)\right) \end{cases} \quad \text{(App.-1)}$$

where the subscripts i, r and t are used for the incident, reflected and transmitted waves, namely. The incident, transmitted and reflected waves of can be observed in the time-domain part representations provided in Figure App. 2.

This finally leads to the ϵ- and μ-related time-based reflection and transmission Fresnel coefficients R_{TD} and T_{TD} for the electric field from [86], [129]. In [91], an equivalent expression is

provided, highlighting the medium's refractive index $n(t \leq t_0^-) = n_1 = \sqrt{\epsilon_1 \mu_1}$, $n(t \geq t_0^+) = n_2 = \sqrt{\epsilon_2 \mu_2}$ and impedance $Z(t \leq t_0^-) = Z_1 = \sqrt{\mu_1/\epsilon_1}$, $Z(t \geq t_0^+) = Z_2 = \sqrt{\mu_2/\epsilon_2}$

$$\begin{cases} R_{TD}^E = \dfrac{E_r(t = t_0^+)}{E_i(t = t_0^-)} = \dfrac{1}{2}\left(\dfrac{\epsilon_1}{\epsilon_2} - \dfrac{\sqrt{\epsilon_1 \mu_1}}{\sqrt{\epsilon_2 \mu_2}}\right) = \dfrac{n_1}{n_2}\dfrac{Z_2 - Z_1}{2Z_1} \\ T_{TD}^E = \dfrac{E_t(t = t_0^+)}{E_i(t = t_0^-)} = \dfrac{1}{2}\left(\dfrac{\epsilon_1}{\epsilon_2} + \dfrac{\sqrt{\epsilon_1 \mu_1}}{\sqrt{\epsilon_2 \mu_2}}\right) = \dfrac{n_1}{n_2}\dfrac{Z_2 + Z_1}{2Z_1} \end{cases} \quad \text{(App.-2)}$$

This alternative expression has the benefits of better highlighting the condition for the lack of reflection onto the temporal boundary: impedance matching $Z_1 = Z_2$.

To better highlight the differences of these time-domain reflection coefficient (TD index) compared to the usual space-domain ones (SD index), [91] and [129] provide the relationship

$$\begin{cases} R_{TD}^E = -sR_{SD} \\ T_{TD}^E = +sT_{SD} \end{cases} \quad \text{(App.-3)}$$

with s the time-dilation factor detailed in [130] expressed as

$$s = n_1/n_2 \quad \text{(App.-4)}$$

Values of R_{TD}^E, T_{TD}^E and s can be found for some illustrative cases in Figure App. 2.

A.2. Frequency shift at a temporal boundary

The change of permittivity ϵ and/or permeability μ induces a change in refractive index n, which leads in turn to a change in velocity c right at the temporal boundary [86]. In a non-dispersive medium, this change of velocity therefore manifests as a dilatation or compression of the propagating wave, better defined as a change in frequency ω. Explicitly detailed in [91] and hinted in [86], [129], the continuity condition at a temporal boundary leads to the frequencies associated to the reflected ω_r and transmitted ω_t waves, time-dilated from the incident's ω_i, such that

$$\begin{cases} \omega_r = -s\omega_i \\ \omega_t = +s\omega_i \end{cases} \quad \text{(App.-5)}$$

One may notice the reflected frequency ω_r is negative, which only hints at a reversal of the reflected wave, as displayed in the time-domain part of the representations of Figure App. 2. Associated frequency-domain spectra are also provided, highlighting the change in frequency offered by a non-unitary time-dilation factor.

The continuity condition at the temporal boundary also confirms that the transmitted k_t and reflected k_r wavevectors are the same as the incident's k_i, though the reflected wave is travelling backward in space [91].

A.3. General behavior at a temporal boundary

From the previously established relationships between incident, reflected and transmitted waves at a temporal boundary, one may notice it allows for a variety of possible electromagnetic waves manipulation. From Equation (App.-5), it appears that, through careful time boundaries, one can perform frequency shifting offered by a dilation factor $s \neq 1$, change the amplitudes of the transmitted and reflected waves and suppress the reflected wave, as illustrated in Figure App. 2(a)-(f).

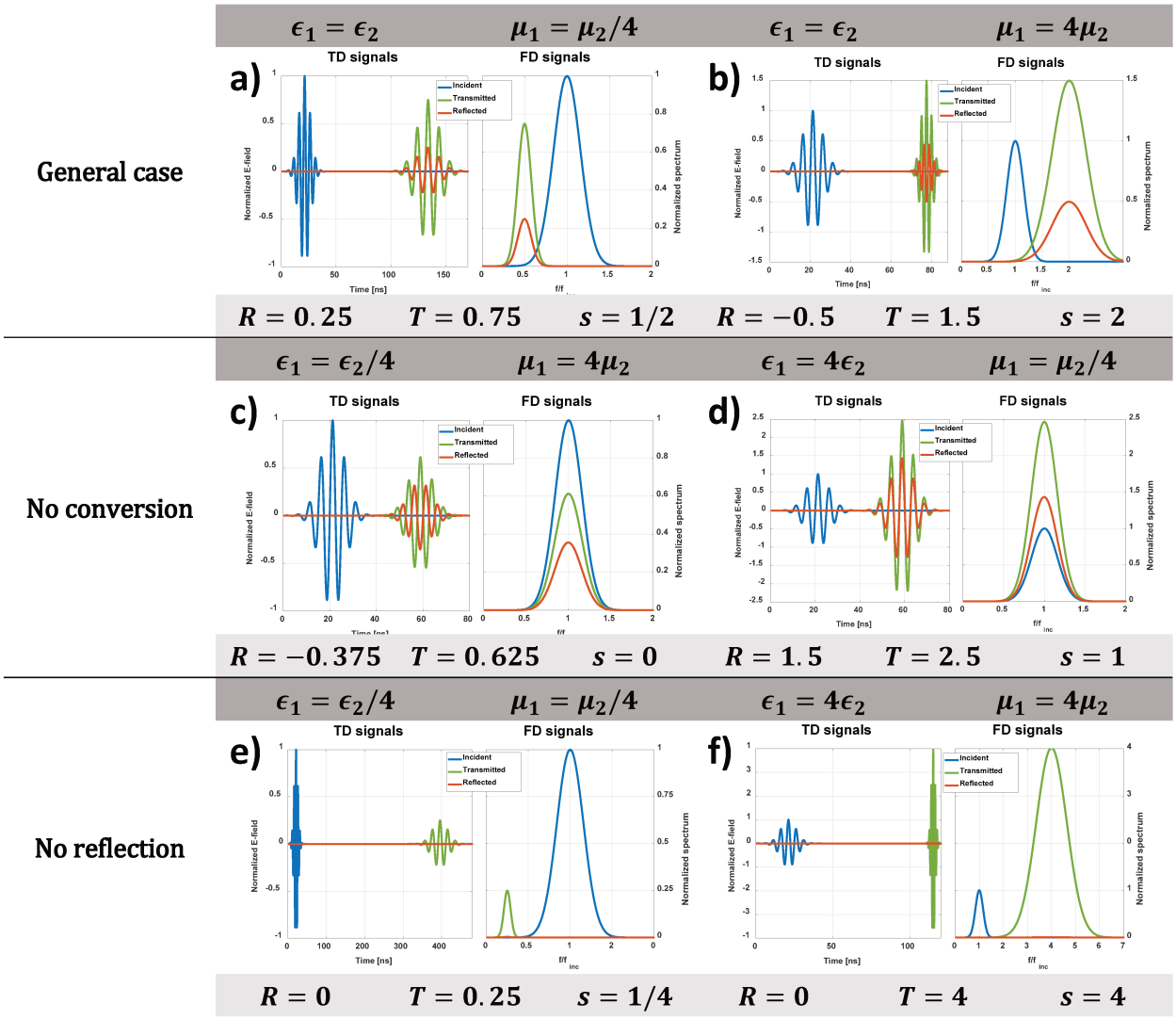

Figure App. 2 : (left) Time- *(TD)* and (right) frequency-domain *(FD)* signals after propagation in a time-varying medium, with (blue) incident, (green) transmitted and (red) reflected waves onto the time boundary. (a) Case for $\epsilon_1 = \epsilon_2$ and $\mu_1 = \mu_2/4$ for down-conversion and attenuation. (b) Case for $\epsilon_1 = \epsilon_2$ and $\mu_1 = 4\mu_2$ for up-conversion and amplification/attenuation. (c) Case for $\epsilon_1 = \epsilon_2/4$ and $\mu_1 = 4\mu_2$ for no conversion and attenuation. (d) Case for $\epsilon_1 = 4\epsilon_2$ and $\mu_1 = \mu_2/4$ for no conversion and amplification. (e) Case for $\epsilon_1 = \epsilon_2/4$ and $\mu_1 = \mu_2/4$ for down-conversion and no reflection. (f) Case for $\epsilon_1 = 4\epsilon_2$ and $\mu_1 = 4\mu_2$ for up-conversion and no reflection.

One may notice that some of the wave manipulations presented in Figure App. 2 lead to transmitted and reflected waves whose total energy is greater than that of the incident wave. In this case, the time-invariance symmetry of the system is broken. Therefore, energy conservation applies to ensemble formed by the wave *and* the medium [131], as specified in [132]. Therefore, there exist some energy exchanges between the wave and the medium itself, providing or depriving waves from power depending on the medium's change. In particular, in stealth contexts, one should avoid amplification through modulation [133], and devise precise effective radar camouflage strategies.

A.4. Wave manipulation from temporal boundaries for stealth

Harnessing the different properties of temporal boundaries, more sophisticated solutions to wave absorp tion have been developed that may be interesting for stealth. First of all, thanks to

the new temporal degree of freedom in such RAM, the *passive, time-invariant* condition for the definition of the Rozanov bound no longer holds, paving the way for absorption bandwidths larger than this limitation. In particular, in [93], it appears that a meticulous switching of the properties of a metal-backed dielectric layer can allow absorption of short-pulsed incident signals, with bandwidths beyond Rozanov's bound. In [94] work is extended beyond the metal-backed case, and [95] delves into the time-modulated Dallenbach screen RAM to highlight broader reachable bandwidths. In a similar vein, [96] introduces a temporal equivalent to quarter-wave impedance inverter, as used in resonant RAM, thereby suppressing the reflected wave.

While all these solutions rely on temporal boundaries, some other solutions turn to periodic temporal modulations of the propagation medium [88], [134]. For instance, one can create a medium of desired effective permittivity [135] from a two-state medium for a finer control of the scattering parameters from the sole duty cycle parameter.

Despite these particularly interesting solutions to reflectionless coatings, they rely on the modulation in time of the very properties of the considered dielectric. Some practical realizations of temporal boundaries within propagation media have recently been proposed for photonic applications [136], such as phase-change materials [137], [138]. However, results on radiofrequency equivalents are few because of the difficulty to have a suitable material in these frequency ranges, and the availability of metasurface-based active devices for the development of surface equivalent concepts, and entirely new strategies.

B. Simulation softwares

CONTENTS

B.1. COMSOL® *131*
B.1.1. Frequency-domain simulations 131
B.1.2. Time-domain simulations 131
B.2. MATLAB® *132*

In this Appendix B, I present the necessary software tools used throughout this thesis. Several metasurface models of increasing complexity are used in order to analyze and design the desired devices before moving on to their manufacturing and measurement. In particular, an ECM and CAD/FEM models are used hand in hand in a two-step approach: the ECM allows for a simple first design and analysis while the CAD/FEM models confirm design choices with their full-wave approach. In particular, the CAD/FEM models are simulated with software COMSOL®, and the ECM is simulated using MATLAB®.

In Section B.1, I therefore introduce COMSOL®, tackling its use in this thesis in both the frequency- and time-domains. Then, in Section B.2, I specify the ways MATLAB® is used in this thesis.

B.1. COMSOL®

COMSOL Multiphysics® [139] is a commercial multiphysics software, based on a finite-element method (FEM). The one module of interest in this work is the RF module [140], for either frequency- or time-domain simulations.

B.1.1. Frequency-domain simulations

In COMSOL®, the RF module's frequency-domain *Physics* is called *Electromagnetic Waves, Frequency Domain*.

In the 2D axisymmetric configuration, the electric field is expressed as $\mathbf{E}(\mathrm{r},\varphi,\mathrm{z}) = \underline{\mathbf{E}}(\mathrm{r},\mathrm{z})\mathrm{e}^{-\mathrm{j}\mathrm{m}\varphi}$, with m the azimuthal mode number, and the *Wave Equation* provided in page 109 of reference [140] turns to

$$\left(\nabla - \mathrm{j}\frac{\mathrm{m}}{\mathrm{r}}\widehat{\boldsymbol{\varphi}}\right) \times \mu_{\mathrm{r}}^{-1}\left(\left(\nabla - \mathrm{j}\frac{\mathrm{m}}{\mathrm{r}}\widehat{\boldsymbol{\varphi}}\right) \times \underline{\boldsymbol{E}}\right) - k_0^2\left(\epsilon_r - \frac{j\sigma}{\omega\epsilon_0}\right)\underline{\boldsymbol{E}} = \mathbf{0} \qquad \text{(App.-6)}$$

with $\widehat{\boldsymbol{\varphi}}$ *the* unit vector in the out-of-plane φ direction. In the case of a structure that is rotation-invariant, then $\mathrm{m} = 0$ and Equation (App.-6) further simplifies.

In the 3D configuration, the *Wave Equation* equation, provided in page 108 of reference [140], is the generalized Helmholtz's equation

$$\nabla \times \mu_{\mathrm{r}}^{-1}(\nabla \times \boldsymbol{E}) - k_0^2\left(\epsilon_r - \frac{j\sigma}{\omega\epsilon_0}\right)\boldsymbol{E} = \mathbf{0} \qquad \text{(App.-7)}$$

B.1.2. Time-domain simulations

In COMSOL®, the RF module's time-domain *Physics* is called *Electromagnetic Waves, Transient*.

In the 2D axisymmetric configuration, the *Wave Equation* is not provided, but can be deduced from the previous expression and the general expression provided in the following to be

$$\left(\nabla - \mathrm{j}\frac{\mathrm{m}}{\mathrm{r}}\widehat{\boldsymbol{\varphi}}\right) \times \mu_{\mathrm{r}}^{-1}\left(\left(\nabla - \mathrm{j}\frac{\mathrm{m}}{\mathrm{r}}\widehat{\boldsymbol{\varphi}}\right) \times \boldsymbol{A}\right) + \mu_0\sigma\frac{\partial \boldsymbol{A}}{\partial t} + \mu_0\frac{\partial}{\partial t}\left(\epsilon_0\epsilon_r\frac{\partial \boldsymbol{A}}{\partial t}\right) = \boldsymbol{0} \qquad \text{(App.-8)}$$

In the 3D configuration, the *Wave Equation* is provided in page 237 of reference [140]

$$\nabla \times \mu_{\mathrm{r}}^{-1}(\nabla \times \boldsymbol{A}) + \mu_0\sigma\frac{\partial \boldsymbol{A}}{\partial t} + \mu_0\frac{\partial}{\partial t}\left(\epsilon_0\epsilon_r\frac{\partial \boldsymbol{A}}{\partial t}\right) = \boldsymbol{0} \qquad \text{(App.-9)}$$

for $\boldsymbol{A}$ the magnetic vector potential such that $\nabla \times \boldsymbol{A} = \mu\boldsymbol{H}$ and $-\partial\boldsymbol{A}/\partial t = \boldsymbol{E}$ (using the gauge whereby the scalar electric potential vanishes (page 237 of reference [140])).

In this work, the *Electromagnetic Waves, Transient Physics node is used with an implicit generalized-α solver as suggested in* [125], [126]. This method requires careful configuration of the geometry, meshing and data management of the problem to solve for, which creates resource- and time-hungry computations. Nonetheless, work has been conducted with this method, based on the provided official COMSOL recommendation. However, around the end of this thesis work, some time-domain simulations were conducted using the implicit BDF solver, instead of the generalized-α one, and showed similar results from more flexible configurations, as given in Appendix 0.

B.2. MATLAB®

MATLAB® [141] is a high-level programming language and environment especially developed for the numeric computation of matrix-based operations. In this work, it is used for the computation of equivalent circuit model's behaviors, LiveLink™ cross-platform simulation with COMSOL® and instrument control during experimental campaigns. Thanks to the *Instrument Control Toolbox*, most of the instruments setting and data collecting is done from the software using *Standard Commands for Programmable Instruments* (SCPI) [142], [143].

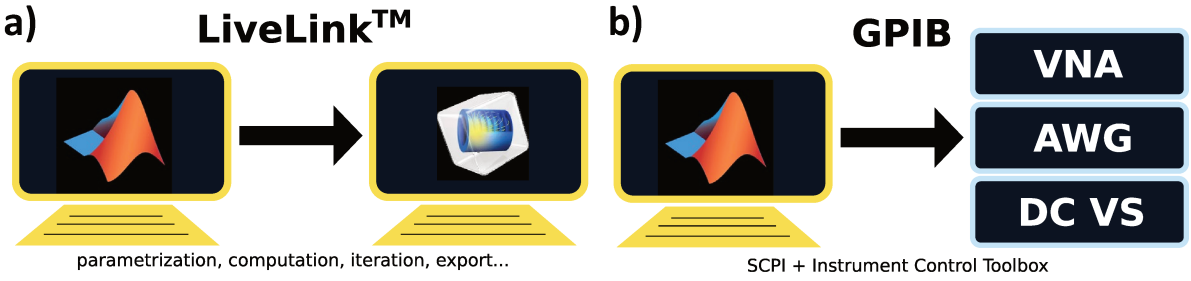

Figure App. 3 : (a) Matlab® used for the parametrization of models, computation of simulations, iterations and results export from COMSOL® using LiveLink™ for cross-platform. (b) Matlab® used with the Instrument Control Toolbox to address instruments thanks to SCPI commands.

C. Time-domain surface impedance boundary condition

CONTENTS

C.1. Frequency- and time-domain expressions of the Surface Impedance Boundary Condition 133
C.1.1. Frequency-domain expression 133
C.1.2. Time-domain expression 133
C.2. Surface Impedance Boundary Condition of classical electronic components 134
C.2.1. Frequency-domain expressions 134
C.2.2. Time-domain expressions 134
C.2.3. COMSOL® implementation 134
C.3. Surface Impedance Boundary Condition of classical circuits 135
C.3.1. Series circuits 135
C.3.1.1. Frequency-domain expressions 135
C.3.1.2. Time-domain expressions 135
C.3.1.3. COMSOL® implementations 136
C.3.2. Parallel circuits 136
C.3.2.1. Frequency-domain expressions 136
C.3.2.2. Time-domain expressions 136
C.3.2.3. COMSOL® implementations 137
C.4. Generalization of the expressions 137
C.4.1. Particular case of a varactor diode 137

C.1. Frequency- and time-domain expressions of the Surface Impedance Boundary Condition

C.1.1. Frequency-domain expression

According to [144], the Leontovich surface impedance boundary condition (SIBC), is a derivative of the usual relationships between electromagnetic fields at an interface, this time showing a surface impedance Z_s, that can be expressed in the frequency-domain as

$$\boldsymbol{E}(\omega) - (\boldsymbol{E}(\omega) \cdot \boldsymbol{n})\boldsymbol{n} = Z_s(\omega)\boldsymbol{n} \times \boldsymbol{H}(\omega) \quad \text{(App.-10)}$$

for E and H the electric and magnetic fields at the interface, and n the normal vector to the surface such that

$$\boldsymbol{E}(\omega) - (\boldsymbol{E}(\omega) \cdot \boldsymbol{n})\boldsymbol{n} = \boldsymbol{E_t}(\omega) \quad \text{(App.-11)}$$

with $\boldsymbol{E_t}$ the electric field tangential to the surface. On the other hand, one may notice that at the interface between two media, then

$$\boldsymbol{n} \times \boldsymbol{H}(\omega) = \boldsymbol{j_s}(\omega) \quad \text{(App.-12)}$$

for $\boldsymbol{j_s}$ the surface current onto the surface. In the end, the SIBC is simply expressed as

$$\boldsymbol{E_t}(\omega) = Z_s(\omega)\boldsymbol{j_s}(\omega) \quad \text{(App.-13)}$$

or equivalently, the surface admittance boundary condition (SABC) is expressed as

$$\boldsymbol{j_s}(\omega) = Y_s(\omega)\boldsymbol{E_t}(\omega) \quad \text{(App.-14)}$$

C.1.2. Time-domain expression

As confirmed in [145], the jump from a frequency- to a time-domain expression of the SIBC is only a matter of a Fourier transform. In the general case, for a surface impedance Z_s showing both a resistive R_s and reactive X_s part, then

$$Z_s(\omega) = R_s(\omega) + j\omega X_s'(\omega) \rightleftharpoons \tilde{Z}_s(t) = \tilde{R}_s(t) + \frac{\partial}{\partial t}\tilde{X}_s'(t) \qquad \text{(App.-15)}$$

with $X_s = \omega X_s'$. Despite Chapter III using $\sim$ to denote frequency-domain counterparts to time-domain variables, $\sim$ will be used here for *time-domain* variables out of habits and conventional expressions of impedances. Therefore, the time-domain expression of the SIBC is

$$\widetilde{\boldsymbol{E}}_{\boldsymbol{t}}(t) = \tilde{Z}_s(t) * \tilde{\boldsymbol{j}}_{\boldsymbol{s}}(t) \qquad \text{(App.-16)}$$

and the SABC is

$$\tilde{\boldsymbol{j}}_{\boldsymbol{s}}(t) = \tilde{Y}_s(t) * \widetilde{\boldsymbol{E}}_{\boldsymbol{t}}(t) \qquad \text{(App.-17)}$$

C.2. Surface Impedance Boundary Condition of classical electronic components

C.2.1. Frequency-domain expressions

Component	Surface impedance $\boldsymbol{Z_s}$	SIBC $\boldsymbol{E_t(\omega) = Z_s(\omega) j_s(\omega)}$	Surface admittance $\boldsymbol{Y_s}$	SABC $\boldsymbol{j_s(\omega) = Y_s(\omega) E_t(\omega)}$
Resistor	R	$\boldsymbol{E_t}(\omega) = R\boldsymbol{j_s}(\omega)$	$1/R$	$\boldsymbol{j_s}(\omega) = \boldsymbol{E_t}(\omega)/R$
Capacitor	$1/j\omega C$	$j\omega C\boldsymbol{E_t}(\omega) = \boldsymbol{j_s}(\omega)$	$j\omega C$	$\boldsymbol{j_s}(\omega) = j\omega C\boldsymbol{E_t}(\omega)$
Inductor	$j\omega L$	$\boldsymbol{E_t}(\omega) = j\omega L\boldsymbol{j_s}(\omega)$	$1/j\omega L$	$j\omega L\boldsymbol{j_s}(\omega) = \boldsymbol{E_t}(\omega)$

Table App. 1 : Frequency-domain expressions of the surface E_t and j_s impedance boundary conditions equivalent to a resistor, a capacitor and an inductor.

C.2.2. Time-domain expressions

Component	Surface impedance $\boldsymbol{Z_s}$	SIBC $\boldsymbol{E_t(\omega) = Z_s(\omega) j_s(\omega)}$	Surface admittance $\boldsymbol{Y_s}$	SABC $\boldsymbol{j_s(\omega) = Y_s(\omega) E_t(\omega)}$
Resistor	R	$\widetilde{\boldsymbol{E}}_{\boldsymbol{t}}(t) = R\tilde{\boldsymbol{j}}_{\boldsymbol{s}}(t)$	$1/R$	$\tilde{\boldsymbol{j}}_{\boldsymbol{s}}(t) = \dfrac{\widetilde{\boldsymbol{E}}_{\boldsymbol{t}}(t)}{R}$
Capacitor	$1/j\omega C$	$C\dfrac{\partial \widetilde{\boldsymbol{E}}_{\boldsymbol{t}}(t)}{\partial t} = \tilde{\boldsymbol{j}}_{\boldsymbol{s}}(t)$	$j\omega C$	$\tilde{\boldsymbol{j}}_{\boldsymbol{s}}(t) = C\dfrac{\partial \widetilde{\boldsymbol{E}}_{\boldsymbol{t}}(t)}{\partial t}$
Inductor	$j\omega L$	$\widetilde{\boldsymbol{E}}_{\boldsymbol{t}}(t) = L\dfrac{\partial \tilde{\boldsymbol{j}}_{\boldsymbol{s}}(t)}{\partial t}$	$1/j\omega L$	$\dfrac{\partial \tilde{\boldsymbol{j}}_{\boldsymbol{s}}(t)}{\partial t} = \dfrac{\widetilde{\boldsymbol{E}}_{\boldsymbol{t}}(t)}{L}$

Table App. 2 : Time-domain expressions of the surface E_t and j_s impedance boundary conditions equivalent to a resistor, a capacitor and an inductor.

C.2.3. COMSOL® implementation

To be implemented in COMSOL®, the behavior of the desired components (and subsequent circuits) can be specified in a *Surface Current Density* node. To allow for more flexibility, it can be coupled to a *Coefficient Form PDE* physics. In this case, the PDE adopts a general expression provided in pages 1273-1274 of reference [146]

$$e_a \frac{\partial^2 u}{\partial t^2} + d_a \frac{\partial u}{\partial t} + \nabla \cdot (-c\nabla u - \alpha u + \gamma) + \beta \cdot \nabla u + au = f \qquad \text{(App.-18)}$$

where u is the variable to solve for and f the source term, while the coefficients are: e_a the mass, d_a the damping, c the diffusion, α the conservative flux convection, γ the conservative flux source, β the convection and a the absorption.

The surface current density can then be implemented be translating the SIBC of Table App. 2 into the expression of Equation (App.-18), leading to the coefficients of Table App. 3.

	u	f	e_a	d_a	c	α	γ	β	a
R	j_s	$\boldsymbol{E_t}$	0	0	0	R	0	0	0
C	j_s	$\partial \boldsymbol{E_t}/\partial t$	0	0	0	$1/C$	0	0	0
L	$\partial j_s/\partial t$	$\boldsymbol{E_t}$	0	0	0	L	0	0	0

Table App. 3: Example for the definition of R, L and C equivalent surface current densities to the *Coefficient Form PDE* formulation of partial differential equations.

C.3. Surface Impedance Boundary Condition of classical circuits

C.3.1. Series circuits

For series circuits, since impedances are summed, the $\boldsymbol{E_t}$ SIBC is easier to specify.

C.3.1.1. Frequency-domain expressions

Circuit	Surface impedance $\boldsymbol{Z_s}$	Surface Impedance Boundary Condition $\boldsymbol{E_t(\omega) = Z_s(\omega) j_s(\omega)}$
R-C	$R + 1/j\omega C$	$j\omega \boldsymbol{E_t}(\omega) = (j\omega R + 1/C)\, \boldsymbol{j_s}(\omega)$
R-L	$R + j\omega L$	$\boldsymbol{E_t}(\omega) = (R + j\omega L)\boldsymbol{j_s}(\omega)$
L-C	$j\omega L + 1/j\omega C$	$j\omega \boldsymbol{E_t}(\omega) = ((j\omega)^2 L + 1/C)\boldsymbol{j_s}(\omega)$
R-L-C	$R + j\omega L + 1/j\omega C$	$j\omega \boldsymbol{E_t}(\omega) = ((j\omega)^2 L + j\omega R + 1/C)\boldsymbol{j_s}(\omega)$

Table App. 4 : Frequency-domain expressions of the $\boldsymbol{E_t}$ surface impedance boundary conditions equivalent to the series circuit formed by the associations of a resistor, a capacitor and an inductor.

C.3.1.2. Time-domain expressions

Circuit	Surface impedance $\boldsymbol{Z_s}$	Surface Impedance Boundary Condition $\boldsymbol{E_t(\omega) = Z_s(\omega) j_s(\omega)}$
R-C	$R + 1/j\omega C$	$\frac{\partial}{\partial t}\widetilde{\boldsymbol{E}}_{\boldsymbol{t}}(t) = \left(R\frac{\partial}{\partial t} + \frac{1}{C}\right)\tilde{\boldsymbol{j}}_{\boldsymbol{s}}(t)$
R-L	$R + j\omega L$	$\widetilde{\boldsymbol{E}}_{\boldsymbol{t}}(t) = \left(R + L\frac{\partial}{\partial t}\right)\tilde{\boldsymbol{j}}_{\boldsymbol{s}}(t)$
L-C	$j\omega L + 1/j\omega C$	$\frac{\partial}{\partial t}\widetilde{\boldsymbol{E}}_{\boldsymbol{t}}(t) = \left(L\frac{\partial^2}{\partial t^2} + \frac{1}{C}\right)\tilde{\boldsymbol{j}}_{\boldsymbol{s}}(t)$

R-L-C	$R + j\omega L + 1/j\omega C$	$\frac{\partial}{\partial t}\tilde{\boldsymbol{E}}_t(t) = \left(L\frac{\partial^2}{\partial t^2} + R\frac{\partial}{\partial t} + \frac{1}{C}\right)\tilde{\boldsymbol{j}}_s(t)$

Table App. 5 : Time-domain expressions of the $\boldsymbol{E_t}$ surface impedance boundary conditions equivalent to the series circuit formed by the associations of a resistor, a capacitor and an inductor.

C.3.1.3. COMSOL® implementations

	u	f	e_a	d_a	c	α	γ	β
R-C	j_s	$\partial \boldsymbol{E_t}/\partial t$	0	R	0	$1/C$	0	0
R-L	j_s	$\boldsymbol{E_t}$	0	L	0	R	0	0
L-C	j_s	$\partial \boldsymbol{E_t}/\partial t$	L	0	0	$1/C$	0	0
R-L-C	j_s	$\partial \boldsymbol{E_t}/\partial t$	L	R	0	$1/C$	0	0

Table App. 6 : Equivalent surface current densities as the *Coefficient Form PDE* to the series circuit formed by the associations of a resistor, a capacitor and an inductor.

C.3.2. Parallel circuits

For parallel circuits, since the admittances are summed, the $\boldsymbol{j_s}$ SABC is easier to specify.

C.3.2.1. Frequency-domain expressions

Circuit	Surface admittance $\boldsymbol{Y_s}$	Surface Admittance Boundary Condition $\boldsymbol{j_s(\omega) = Y_s(\omega)E_t(\omega)}$
R/C	$1/R + j\omega C$	$\boldsymbol{j_s}(\omega) = (1/R + j\omega C)\boldsymbol{E_t}(\omega)$
R/L	$1/R + 1/j\omega L$	$j\omega\boldsymbol{j_s}(\omega) = (j\omega/R + 1/L)\boldsymbol{E_t}(\omega)$
L/C	$1/j\omega L + j\omega C$	$j\omega\boldsymbol{j_s}(\omega) = ((j\omega)^2 C + 1/L)\boldsymbol{E_t}(\omega)$
R/L/C	$1/R + 1/j\omega L + j\omega C$	$j\omega\boldsymbol{j_s}(\omega) = ((j\omega)^2 C + j\omega/R + 1/L)\boldsymbol{E_t}(\omega)$

Table App. 7 : Frequency-domain expressions of the $\boldsymbol{j_s}$ surface admittance boundary conditions equivalent to the series circuit formed by the associations of a resistor, a capacitor and an inductor.

C.3.2.2. Time-domain expressions

Circuit	Surface admittance $\boldsymbol{Y_s}$	Surface Admittance Boundary Condition $\boldsymbol{j_s(\omega) = Y_s(\omega)E_t(\omega)}$
R/C	$1/R + j\omega C$	$\tilde{\boldsymbol{j}}_s(t) = \left(\frac{1}{R} + C\frac{\partial}{\partial t}\right)\tilde{\boldsymbol{E}}_t(t)$
R/L	$1/R + 1/j\omega L$	$\frac{\partial}{\partial t}\tilde{\boldsymbol{j}}_s(t) = \left(\frac{1}{R}\frac{\partial}{\partial t} + \frac{1}{L}\right)\tilde{\boldsymbol{E}}_t(t)$
L/C	$1/j\omega L + j\omega C$	$\frac{\partial}{\partial t}\tilde{\boldsymbol{j}}_s(t) = \left(C\frac{\partial^2}{\partial t^2} + \frac{1}{L}\right)\tilde{\boldsymbol{E}}_t(t)$
R/L/C	$1/R + 1/j\omega L + j\omega C$	$\frac{\partial}{\partial t}\tilde{\boldsymbol{j}}_s(t) = \left(C\frac{\partial^2}{\partial t^2} + \frac{1}{R}\frac{\partial}{\partial t} + \frac{1}{L}\right)\tilde{\boldsymbol{E}}_t(t)$

Table App. 8 : Time-domain expressions of the $\boldsymbol{j_s}$ surface admittance boundary conditions equivalent to the series circuit formed by the associations of a resistor, a capacitor and an inductor.

C.3.2.3. COMSOL® implementations

	$\boldsymbol{u}$	$\boldsymbol{f}$	$\boldsymbol{e_a}$	$\boldsymbol{d_a}$	$\boldsymbol{c}$	$\boldsymbol{\alpha}$	$\boldsymbol{\gamma}$	$\boldsymbol{\beta}$
$\boldsymbol{R/C}$	$\boldsymbol{E_t}$	j_s	0	C	0	$1/R$	0	0
$\boldsymbol{R/L}$	$\boldsymbol{E_t}$	$\boldsymbol{\partial j_s/\partial t}$	0	$1/R$	0	$1/L$	0	0
$\boldsymbol{L/C}$	$\boldsymbol{E_t}$	$\boldsymbol{\partial j_s/\partial t}$	C	0	0	$1/L$	0	0
$\boldsymbol{R/L/C}$	$\boldsymbol{E_t}$	$\boldsymbol{\partial j_s/\partial t}$	C	$1/R$	0	$1/L$	0	0

Table App. 9: Equivalent surface current densities as the *Coefficient Form PDE* to the parallel circuit formed by the associations of a resistor, a capacitor and an inductor.

C.4. Generalization of the expressions

For more complex circuits – integrating both parallel and series electronic elements –, then the SIBC equivalent to such circuits can be obtained be the following generalization of the their expression. For instance, in the case of a circuit exhibiting two series elements of impedance Z_1 and Z_2, then the overall surface impedance is $Z_s = Z_1 + Z_2$, leading to the expression of the tangential field

$$\boldsymbol{E_t} = Z_s \boldsymbol{j_s} = (Z_1 + Z_2)\boldsymbol{j_s} = \boldsymbol{E_1} + \boldsymbol{E_2} \tag{App.-19}$$

Therefore, for $i \in \{1,2\}$, who may notice

$$\boldsymbol{E_i} = Z_i \boldsymbol{j_s} = Z_i \frac{\boldsymbol{E_t}}{\boldsymbol{E_t}} \boldsymbol{j_s} = \frac{1}{Y_i} \frac{\boldsymbol{E_t}}{\boldsymbol{E_t}} \boldsymbol{j_s} = \frac{\boldsymbol{E_t}}{\boldsymbol{j_i}} \boldsymbol{j_s} = \boldsymbol{E_t} \frac{\boldsymbol{j_s}}{\boldsymbol{j_i}} \tag{App.-20}$$

Which leads to the total tangent electric field E_t to

$$\boldsymbol{E_t} = \boldsymbol{E_1} + \boldsymbol{E_2} = \boldsymbol{E_t} \frac{\boldsymbol{j_s}}{\boldsymbol{j_1}} + \boldsymbol{E_t} \frac{\boldsymbol{j_s}}{\boldsymbol{j_2}} = \boldsymbol{E_t} \frac{\boldsymbol{j_1} + \boldsymbol{j_2}}{\boldsymbol{j_1 j_2}} \boldsymbol{j_s} \left(= Z_s \boldsymbol{j_s}, Z_s = \boldsymbol{E_t} \frac{\boldsymbol{j_1} + \boldsymbol{j_2}}{\boldsymbol{j_1 j_2}} \right) \tag{App.-21}$$

In other words, the equivalent surface current $\boldsymbol{j_s}$ to this series circuit is

$$\boldsymbol{j_s} = \frac{\boldsymbol{j_1 j_2}}{\boldsymbol{j_1} + \boldsymbol{j_2}} \tag{App.-22}$$

with $\boldsymbol{j_1} = Y_1 \boldsymbol{E_t}$ and $\boldsymbol{j_2} = Y_2 \boldsymbol{E_t}$.

For a parallel circuit, one may notice a similar process. Indeed, the overall surface admittance $Y_s = Y_1 + Y_2$ leads to the surface current

$$\boldsymbol{j_s} = Y_s \boldsymbol{E_t} = (Y_1 + Y_2)\boldsymbol{E_t} = \boldsymbol{j_1} + \boldsymbol{j_2} \tag{App.-23}$$

which leads to $\boldsymbol{j_i} = \boldsymbol{j_s E_t / E_i}$ for $i \in \{1,2\}$, and therefore

$$\boldsymbol{E_t} = \frac{\boldsymbol{E_1 E_2}}{\boldsymbol{E_1} + \boldsymbol{E_2}} \tag{App.-24}$$

For $\boldsymbol{E_i} = Z_i \boldsymbol{E_t}$.

C.4.1. Particular case of a varactor diode

For a varactor diode, the SPICE model is such that the equivalent impedance Z_{vct} is

$$Z_{vct}(\omega, V_r) = Z_{L_s}(\omega) + \frac{1}{\frac{1}{Z_{C_p}(\omega)} + \frac{1}{Z_{C_d}(\omega, V_r) + Z_{R_s}(V_r)}} \quad \text{(App.-25)}$$

One may notice this impedance is the sum of two impedances, such that Z_{vct} as $Z_s = Z_1 + Z_2$ with $Z_1 = Z_{L_s}$ and

$$Z_2 = \frac{1}{\frac{1}{Z_{C_p}(\omega)} + \frac{1}{Z_{C_d}(\omega, V_r) + Z_{R_s}(V_r)}} \quad \text{(App.-26)}$$

Therefore, the total surface current density j_s equivalent to a varactor diode in the frequency-domain will adopt the expression of Equation (App.-22), with

$$\boldsymbol{j_1}(\omega) = Y_1 \boldsymbol{E_t} = (j\omega(C_d + C_p) + (j\omega)^2 C_d C_p R_s)\boldsymbol{E_t}(\omega) \quad \text{(App.-27)}$$

and

$$\boldsymbol{j_2}(\omega) = Y_2 \boldsymbol{E_t} \Leftrightarrow j\omega L_s \boldsymbol{j_2} = \boldsymbol{E_t}(\omega) \quad \text{(App.-28)}$$

And in the time-domain

$$\boldsymbol{j_1}(t) = ((C_d + C_p)\frac{\partial}{\partial t} + C_d C_p R_s \frac{\partial^2}{\partial t^2})\boldsymbol{E_t}(t) \quad \text{(App.-29)}$$

and

$$L_s \frac{\partial}{\partial t}\boldsymbol{j_2}(t) = \boldsymbol{E_t}(t) \quad \text{(App.-30)}$$

In the case here considered, where the incident signal is transmitted into the time-domain some ways away from the metasurface, then one may notice the zero-current initial values of j_1 and j_2. However, looking at Equation (App.-22), this is not an acceptable possibility. Therefore, when implementing this method into COMSOL®, it is necessary to define small but non-zero initial values for the surface currents. Furthermore, when taking a look at the time-domain signals, it appears this method introduces difficulties. Indeed, as observed in Figure App. 4, the solver seems to have trouble finding suitable solutions during the early times. Hopefully, this is far from keeping the simulation from converging and to have any noticeable effect on a long simulation.

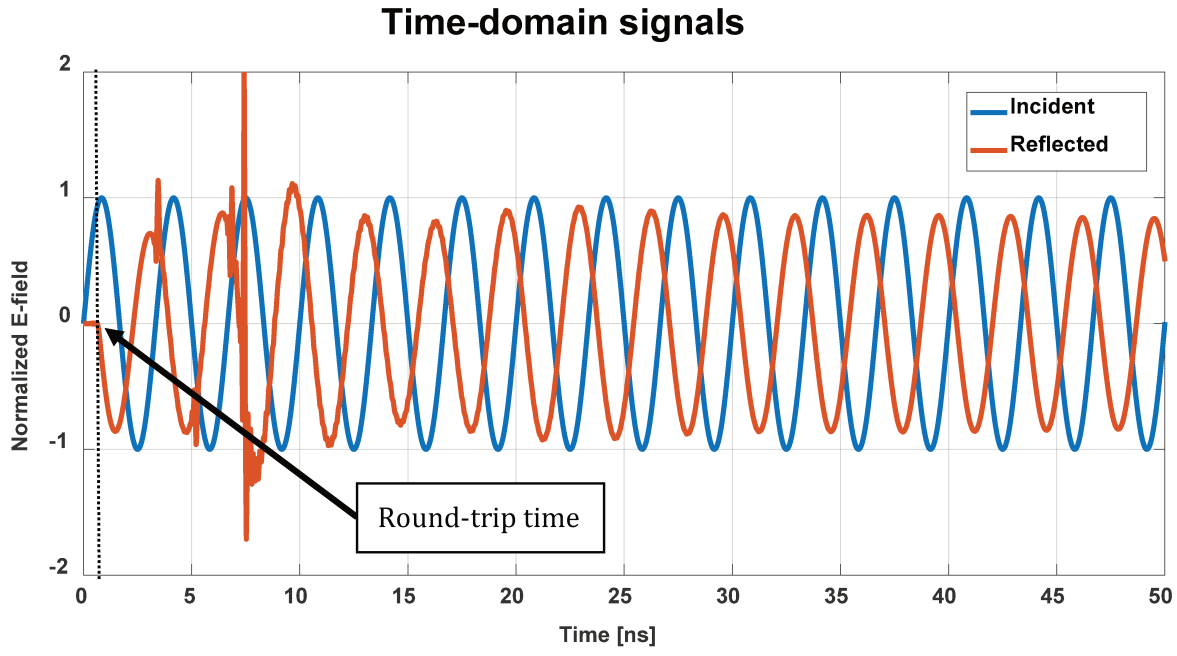

Figure App. 4 : Early-time (blue) incident and (red) reflected signals from a FETD simulation where the surface current density definition requires the use of the general SIBC expression and a non-zero initial value for the surface currents.

D. Frequency conversion and α value

As defined in Equation (III.12), the α fraction is defined as the portion of the ideal phase variation 2π that is explored by the MBFC over a given modulation range. As highlighted in Figure III.2, this α value shifts the cardinal sine function of the weighting function W_α defined in Equation (III.15). Since $|\alpha| \leq 1$, then the weighting function can be shifted to any intermediate value from the ideal conversion case ($|\alpha| = 1$) to the conversion-less case ($\alpha = 0$). What is important to notice here is that W_α, as a cardinal sine function, is found the strongest at its center of symmetry, *i.e.* at $\alpha\omega_m$. The subsequent sampling provided by the Dirac comb of Equation(III.14) then only extracts the cardinal sine values found at $nf_m, n \in \mathbb{Z}$, creating the weighting coefficients of the infinite sum of incident field's copies of Equation (III.16). Therefore, different distributions of power to this infinite sum are expected from different values of α. In particular, the strongest coefficient will be associated to the harmonics found the closest to the center of the cardinal sine function of W_α. In other words, a non-ideal frequency conversion favors the conversion to the harmonics closest to $\alpha\omega_m$. Therefore, any frequency conversion of $|\alpha| < 0.5$ cannot provide the desired conversion to $f_0 \pm f_m$. And on top of that, should $|\alpha| \neq 0$, it would still plague the reflected wave's spectrum with infinite copies of the incident's. Unlike a frequency conversion of $|\alpha| > 0.5$, which will provide the desired frequency conversion.

For illustration, Figure App. 5(a)-(c) provides resulting spectra from phase modulations of conversion-less α fractions, with highlight of the W_α cardinal sine function and resulting $\tilde{\Gamma}$ coefficients as PSD. In these examples, the phase ramp is always centered around $\Gamma = 0$ and α is obtained by altering the maximum and minimum values of Γ equally. As can be noticed, no conversion is happening because the weighting function's main lobe's symmetry axis is found in the $f \in [f_0, f_0 + f_m/2[$ range, favoring distribution of power to the closest harmonic: f_0. Similarly, Figure App. 5(d)-(f) provides mirroring cases for frequency-converting α values, along with the W_α cardinal sine function and resulting $\tilde{\Gamma}$ coefficients as PSD. Similarly as before, in Figure App. 5(d)-(f), frequency conversion is observed conversion thanks to the shifting of the weighting function's main lobe's symmetry axis to the $f \in]f_0 + f_m/2, f_0 + f_m]$ range, favoring distribution of power to the closest harmonic: $f_0 + f_m$.

As can be observed in Figure App. 5, the closest $|\alpha|$ is to 1, the more power is distributed to the desired harmonic, and the less power is given to parasitic harmonics. Furthermore, any distribution of power obtained from an α value can find its mirror image in the mirrored fraction value in regards to the $|\alpha| = 0.5$ axis. So much so, that the weighting coefficients associated to the frequencies f_0 and $f_0 + f_m$, as functions of α, follow the curves provided in Figure App. 6 for an up-conversion. In Figure App. 6, the coefficients are power-related and normalized. As can be observed, both curves follow the same exact pattern, but mirrored at the $\alpha = 0.5$ axis. For instance, 100% of the power is provided to the harmonics at f_0 for $\alpha = 0$ and 100% is provided to $f_0 + f_m$ for $\alpha = 1$, as previously established. This behavior is also observed for a down-conversion. And this even leads to a particular point where, at $|\alpha| = 0.5$ axis, power is neither distributed to f_0 nor $f_0 \pm f_m$. However, this specific topic could not be thoroughly studied in the time of this thesis.

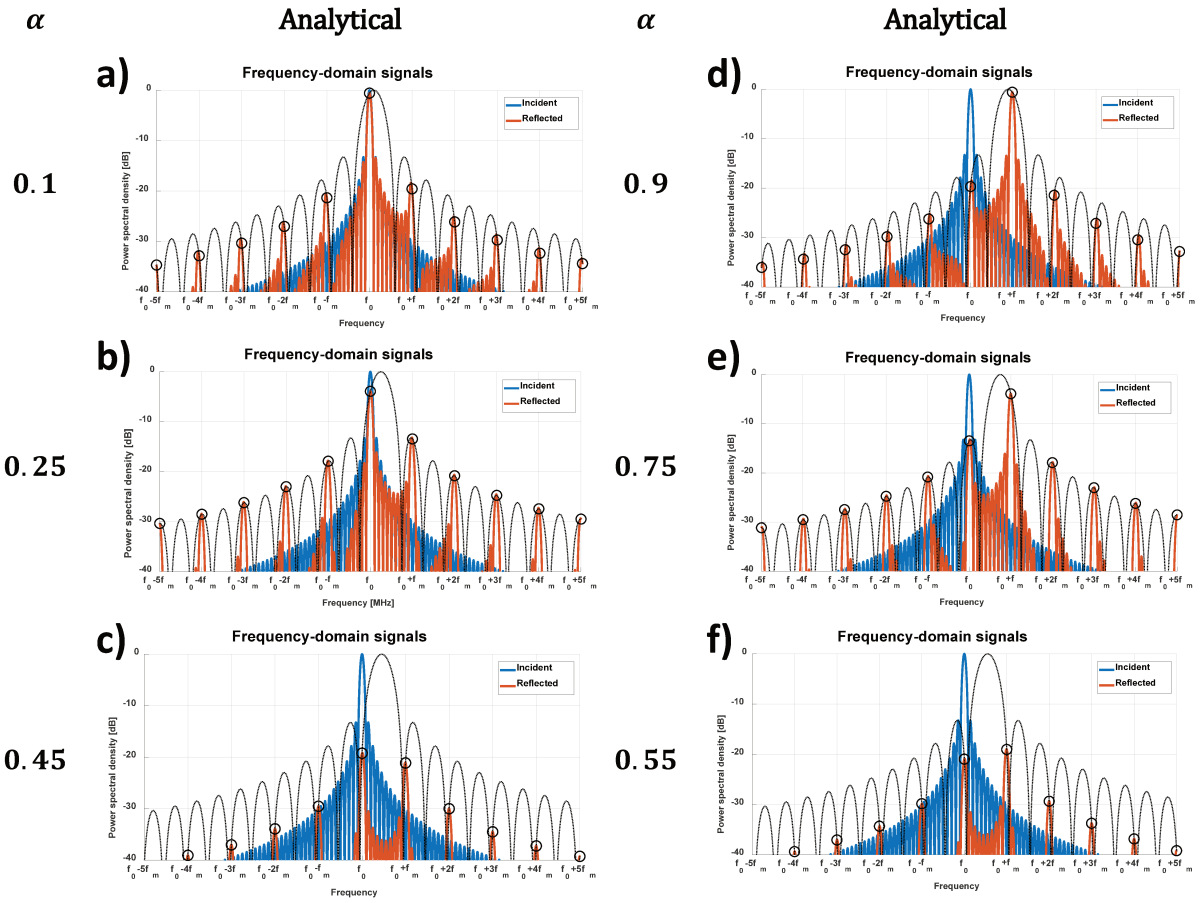

Figure App. 5 : Relative power spectral density of the (blue) incident and (red) reflected fields for an harmonic impinging wave undergoing an (a) $\alpha = 0.1$, (b) $\alpha = 0.25$ and (c) $\alpha = 0.45$ phase modulation with mirroring (d) $\alpha = 0.9$, (e) $\alpha = 0.75$ and (f) $\alpha = 0.55$ cases for an up-conversion from f_0 by f_m, with highlight of the (dotted lines) weighting function and (circles) weighting coefficients.

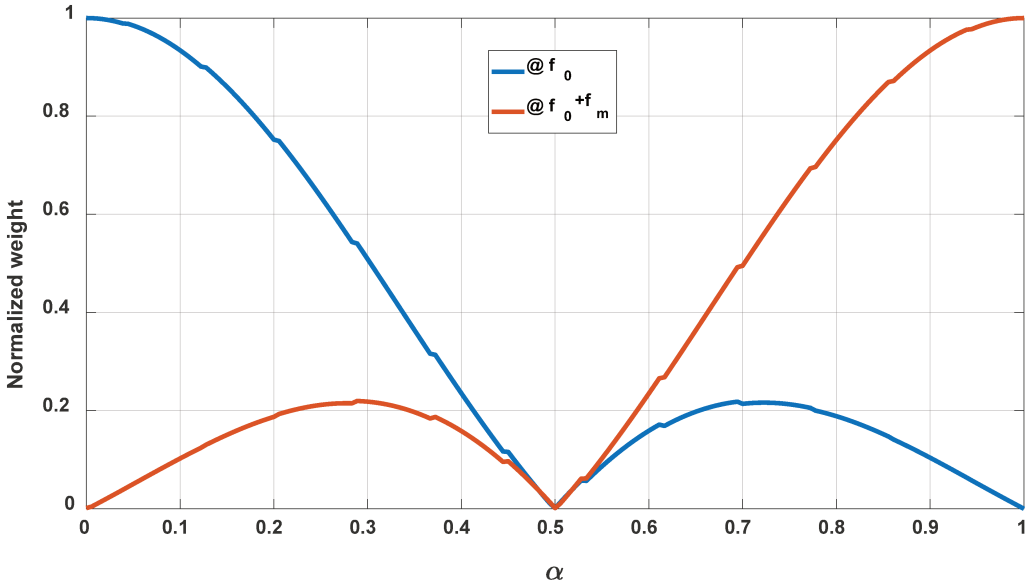

Figure App. 6 : Normalized weight distributed to the frequency f_0 (blue) and $f_0 + f_m$ for an up-conversion depending on the value of the fraction α.

E. Varactor diode's series resistance and phase variation regime

From Equation (III.18), one may notice that, at ω_0, the phase of the MBFC can be expressed as a function of capacitance $\angle\Gamma(\mathrm{C}) = -(\theta_1(C) + \theta_2(C))$ where

$$\begin{cases} \theta_1(C,\omega_0) = \operatorname{atan}\left(\dfrac{Im(Y_{MS}(C,\omega_0)) - 1/\omega_0 L_{SC}}{Y_0 - Re(Y_{MS}(C,\omega_0))}\right) \\ \theta_2(C,\omega_0) = \operatorname{atan}\left(\dfrac{Im(Y_{MS}(C,\omega_0)) - 1/\omega_0 L_{SC}}{Y_0 + Re(Y_{MS}(C,\omega_0))}\right) \end{cases} \quad \text{(App.-31)}$$

where $Y_{MS}(C,\omega_0)$ is the capacitance-dependent admittance of the varactor-diode-loaded metasurface. Both resulting curves are provided in Figure App. 7 as a function of capacitance, with a broader range of resistance values R_s to better highlight the two regimes.

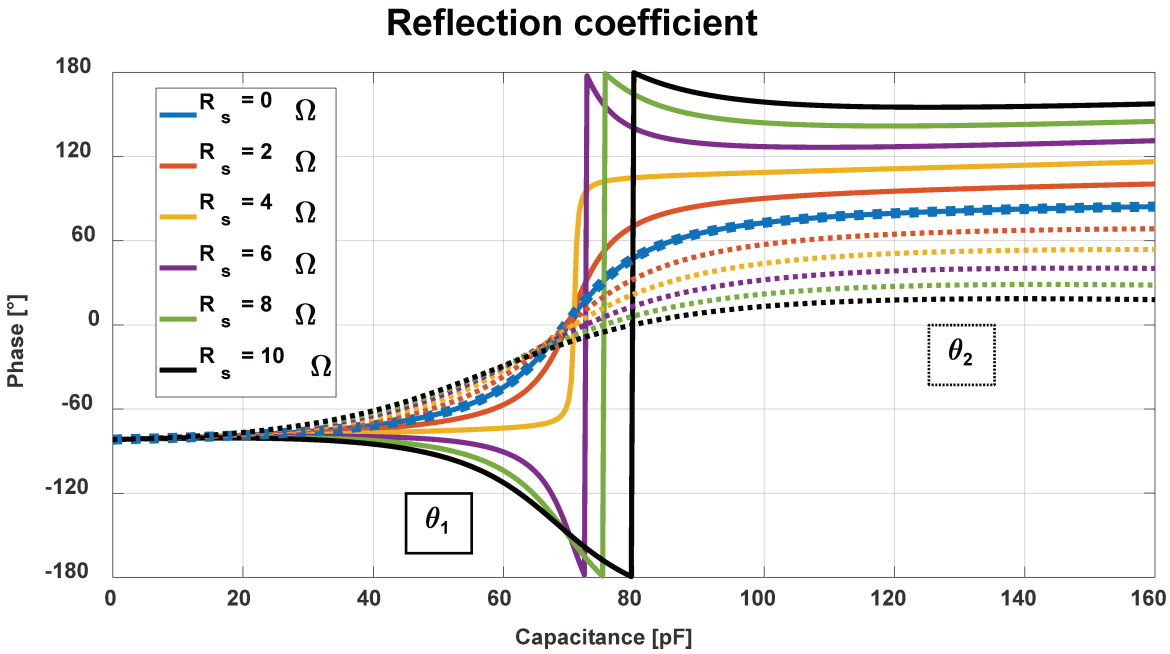

Figure App. 7 : Phase curves for phase functions (solid) θ_1 and (dotted) θ_2 such that $\angle\Gamma = -(\theta_1 + \theta_2)$, for different series resistance values (colors) from an ECM model of a varactor-loaded metasurface-based frequency converter at $f_0 = 300$ MHz using four SMV1249 varactor diodes of series resistor $R_s \in \{0, 2, 4, 6, 8, 10\}$ Ω.

As one may notice, the θ_1 part is the one inducing the phase behavior observed in Figure III.11, while θ_2 is only smoothly varying. Indeed, on the one hand, taking a look at Equation (App.-31)one may notice that θ_2, for a positive real part of Y_{MS}, is a strictly increasing function, finding a root at C_r such that $Im\big(Y_{MS}(C_r)\big) = 1/\omega L_{SC}$. On the other hand, θ_1 from Equation (App.-31), for a positive real part of Y_{MS}, is the arctangent of a function which exhibits both a zero C_r^{Im} and a pole C_r^{Re}, which yield $\theta_1(C_r^{Im}) = 0$ and $\theta_1(C_r^{Re}) = \pm\pi/2$. In fact, from Figure App. 7, one may notice that for low R_s values, curves pass through $\theta_1 = 0$ but never through $\theta_1 = \pm\pi$, but for higher R_s values (roughly $R_s > 4$), all curves go through $\theta_1 = \pm\pi$ but never through $\theta_1 = 0$. To better locate the poles and zeros for different series resistance values and provide an explanation for the

change of variation regime, values of C_r^{Im} and C_r^{Re} are provided in Figure App. 8, along with functions f_1 and f_2 such that $\theta_1(C) = \text{atan}(f_1(C)/f_2(C))$.

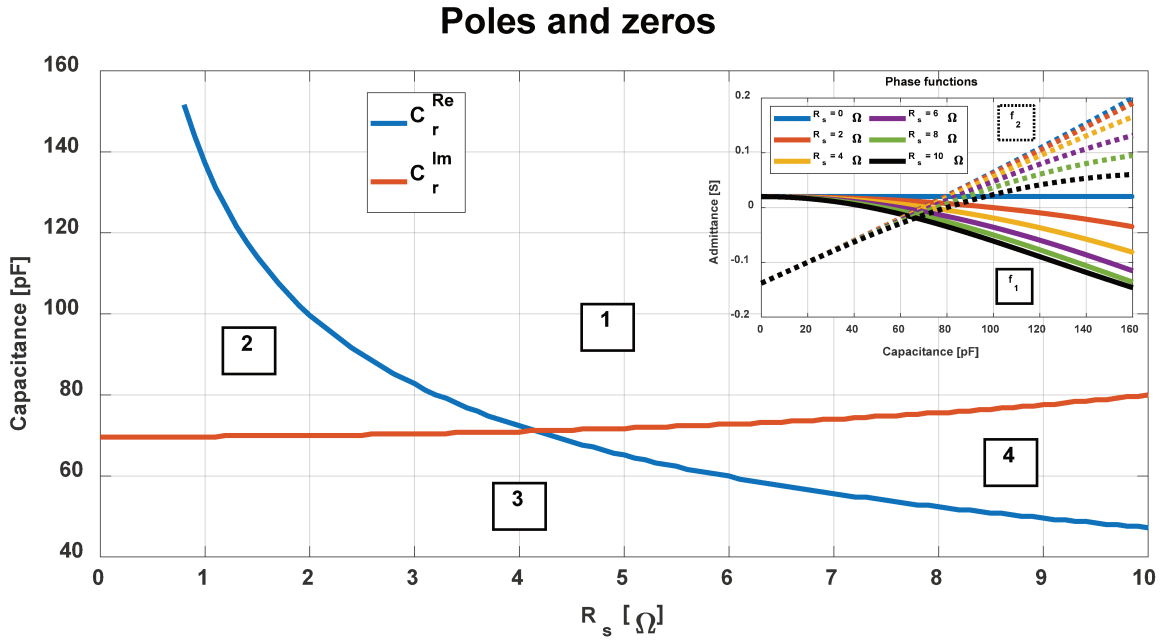

Figure App. 8 : Capacitance (blue) poles and (red) zeros to the phase function θ_1 as a function of the series resistance $R_S \in [0, 10]\ \Omega$, and highlight of the equivalent zones to the four quadrants of the $atan2$ function. (inset) admittance functions (solid) f_1 and (dotted) f_2 such that $\theta_1(C) = \text{atan}(f_1(C)/f_2(C))$ for series resistance values $R_S \in \{0, 2, 4, 6, 8, 10\}\ \Omega$. All from an ECM model of a varactor-loaded metasurface-based frequency converter at $f_0 = 300$ MHz using four SMV1249 varactor diodes.

As previously hinted, the zeros C_r^{Im} and poles C_r^{Re} are not found at the same capacitance values – with an absence of poles for R_S values close to 0 since the MBFC would (largely) be reactive. Furthermore, the tendency is for C_r^{Re} to decrease with increasing resistance, while C_r^{Im} increases with resistance, intersecting at around $(R_S, C) = (4.1\ \Omega, 71.2\ \text{pF})$. One may also notice from the inset in Figure App. 8 that f_1 and f_2 are strictly monotonous with capacitance, and may have equal or opposite signs depending on the relationships between C_r^{Im} and C_r^{Re}, as compiled in Table App. 10.

C	$< C_r^{Im}$	$= C_r^{Im}$	$> C_r^{Im}$		C	$< C_r^{Re}$	$= C_r^{Re}$	$> C_r^{Re}$
$f_1(C)$	< 0	$= 0$	> 0		$f_2(C)$	> 0	$= 0$	< 0

Table App. 10 : Explicit location of the positive and negative values for the functions f_1 and f_2 such that $\theta_1(C) = \text{atan}(f_1(C)/f_2(C))$ where C_r^{Im} is the function's zero and C_r^{Re} the function's pole.

The elements of Table App. 10 lead to define the four quadrants of the $atan2$ function used for the computation of the phase that are located in Figure App. 8 and defined as the intersecting planes specified in Table App. 11.

$f_1(C)$	> 0	> 0	< 0	< 0
$f_2(C)$	< 0	> 0	> 0	< 0

Quadrant	1	2	3	4

Table App. 11 : Definition of the four quadrants of the $atan2$ function depending on the locations of the negative and positive planes of functions f_1 and f_2 such that $\theta(C) = \text{atan}(f_1(C)/f_2(C))$.

Then one may notice, by definition of the $atan2$ function, that depending on the resistance value R_s, the phase variation with capacitance is going to transition quadrants each time a pole or a zero is exceeded. The results are compiled in Table App. 12 by computation of the $atan2$ depending on the sign of functions f_1 and f_2 from Table App. 10 and their associated quadrant.

R_s [Ω]	< 4.2					> 4.2				
C	$< C_r^{Re}$			$= C_r^{Re}$	$> C_r^{Re}$	$< C_r^{Im}$			$= C_r^{Im}$	$> C_r^{Im}$
	$< C_r^{Im}$	$= C_r^{Im}$	$> C_r^{Im}$			$< C_r^{Re}$	$= C_r^{Re}$	$> C_r^{Re}$		
Quadrant	3	0	2	$\pi/2$	1	3	$-\pi/2$	4	π	1

Table App. 12 : Quadrants of the $atan2$ funciton associated to each of the four sign planes of functions f_1 and f_2 such that $\theta(C) = \text{atan}(f_1(C)/f_2(C))$ and the phase value at the transitions, *i.e.* at the pole C_r^{Re} and zero C_r^{Im}.

Therefore, according to Table App. 12, there does exist two phase variation regimes. On the one hand, for low resistance values ($R_s < 4.2$ Ω), the phase is increasing from its origin value (negative because in quadrant 3), passes through its zero then reaches beyond $\pi/2$ values – this is the case for the blue, red and yellow curves of Figure App. 7. On the other hand, for high resistance values ($R_s > 4.2$ Ω), the phase is decreasing from its negative origin value, quickly passes through $-\pi/2$ and must then emerge at π when transitioning from quadrant 4 to 1 – which is observed from the purple, green and black curves of Figure App. 7. One may also distinguish a third phase variation regime that was not accounted for in Figure App. 7 for which $R_s = 4.2$. In that case, $C_r^{Re} = C_r^{Im}$, which enforces a 3 to 1 quadrant transition with a, traditionally, undefined value, but usually set to 0 for an abrupt transition through $\pm\pi$.

This confirms the phase variation regime transition observed in Figure III.11. This phenomenon is strongly dependent on the value of the series resistance, which, at a given frequency, sets the locations of the poles and zeros, enforcing different quadrant transitions to θ_1. The effects on the reflected wave's metrics is an increasing CL, a decreasing R_0, a stronger energy dissipation and more power to the f_0 harmonics with the increasing series resistance. The metrics from an analytical study of this phenomenon are provided in Table App. 13 for which the SMV1249 varactor diode model is used in the 4VCT configuration. It seems increasing R_0 can be obtained for the lowest resistance values, but then decreases from $R_s = 1.5$ Ω but the explanation for this behavior could not be found.

R_s [Ω]	**0**	**0.5**	**1**	**1.5**	**2**	**2.5**	**3**	**3.5**	**4**
CL [dB]	0.101	1.227	2.325	3.424	4.5532	5.751	7.078	8.650	10.831
R_0 [dB]	16.793	20.405	23.490	24.746	18.783	18.291	16.142	15.218	14.477
$\mathcal{E}_{ref}/\mathcal{E}_{inc}$	1	0.778	0.617	0.498	0.407	0.336	0.280	0.234	0.197

Table App. 13 : Conversion loss (CL), spurious free dynamic range ($SFDR$) and energy ratio ($\mathcal{E}_{ref}/\mathcal{E}_{inc}$) from the power spectral densities of the incident and reflected signals from an analytical study of the effects of the varactor diode's series resistance R_s.

F. Finite-Element Time Domain simulation: BDF vs. Generalized-α implicit solvers

For the FETD simulation in COMSOL®, blog articles [125], [126] suggest using implicit solvers, such as the Generalized-α or the BDF. The former is supposedly more robust, but then requires a careful configuration in both the spatial and time discretizations to ensure the Courant-Freiedrichs-Lewy (CFL) criterion is respected [147].

For the Generalized-α solver, I tended to a convergence study on different configurations. I first started by defining that the smallest element h to be discretized is not the smallest wavelength ($\lambda_{min} = 430$ cm at $f = 700$ MHz), but the distance from the short-circuit to the metasurface ($\ell = 20$ mm). A square mesh is then chosen, and a discretization of $N = 5$ is chosen to accurately mesh this dimension, and the entire geometry with an equal mesh size (no variation in size in either length or width). The time step Δt, according to [125], [126], must then be defined as

$$\Delta t = CFL\frac{h}{N} \qquad \text{(App.-32)}$$

with $CFL = 0.1$ considered "near-optimal". The convergence study then confirmed frequency conversion could still be obtained by relaxing the mesh discretization to $N = 1$, leading to a mesh size $h = 20$ cm and time step $\Delta t = 6.67$ fs. Set a to *Manual* step size, the FETD computation is performed at each of these time-steps, ensuring the CFL criterion.

For the BDF solver, the discretization is not as constrained. In order to validate its use, I kept the mesh size, but relaxed the time step. Using an *Intermediate* time-stepping method, which allows to solver to look for the most appropriate time-step, I specified a range of output times regularly spaced by 1 ns. The FETD solver then converged for a variety of time step values, with an average of $\Delta t = 4$ fs, which turned out to be smaller than used in the Generalized-α case.

The frequency conversion of a harmonic wave set at $f_0 = 300$ MHz is well-observed in the PSD of reflected wave from both simulations, as seen in Figure App. 9. One may notice there are only slight discrepancies between both sets of results. For instance, some of the harmonics' power are slightly altered. However, the most striking difference is the asymmetry in the power distribution of the cardinal sine from the incident wave's PSD seen in Figure App. 9(b).

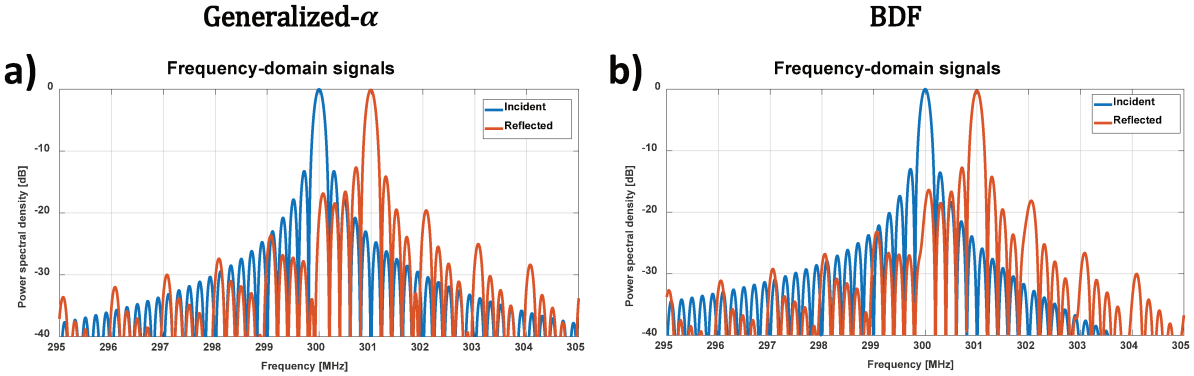

Figure App. 9 : Relative power spectral density of the (blue) incident and (red) reflected electric signals from a 2D axisymmetric numerical study using a 4VCT metasurface with SMV1249 varactor diode for an impinging wave at frequency $f_0 = 300$ MHz for an up-conversion of frequency $f_m = 1$ MHz, using the (a) Generalized-α or (b) BDF implicit solver.

REFERENCES

[1] M. I. Skolnik, *Introduction to Radar Systems*. in International student edition. McGraw-Hill, 1962. [Online]. Available: https://books.google.fr/books?id=XAdTAAAAMAAJ

[2] M. A. Richards, *Fundamentals of Radar Signal Processing*. in Professional Engineering. McGraw-Hill Education, 2005. [Online]. Available: https://books.google.fr/books?id=j91oJ22ldoQC

[3] N. A. W. C. W. D. P. M. CA, *Electronic Warfare and Radar Systems Engineering Handbook*. Storming Media, 1997. [Online]. Available: https://books.google.fr/books?id=7fyVPwAACAAJ

[4] C. Wolff, "radartutorial." [Online]. Available: https://www.radartutorial.eu/index.en.html

[5] J. M. Headrick and M. I. Skolnik, "Over-the-Horizon radar in the HF band," *Proceedings of the IEEE*, vol. 62, no. 6, pp. 664–673, 1974, doi: 10.1109/PROC.1974.9506.

[6] G. T. Ruck, D. E. Barrick, and W. D. Stuart, *Radar Cross Section Handbook*. Peninsula Publishing, 2002. [Online]. Available: https://books.google.fr/books?id=SWVCPgAACAAJ

[7] E. F. Knott, J. F. Schaeffer, and M. T. Tulley, *Radar Cross Section*. Artech House, 1993.

[8] R. B. Dybdal, "Radar cross section measurements," *Proceedings of the IEEE*, vol. 75, no. 4, pp. 498–516, 1987, doi: 10.1109/PROC.1987.13757.

[9] D. A. Bosma, O. A. Krasnov, and A. Yarovoy, "An Advanced Data Processing Algorithm for Extraction of Polarimetric Radar Signatures of Moving Automotive Vehicles Using the H/A/α Decomposition Technique," *Remote Sensing*, vol. 15, no. 4, 2023, doi: 10.3390/rs15041060.

[10] W. Emerson, "Electromagnetic wave absorbers and anechoic chambers through the years," *IEEE Transactions on Antennas and Propagation*, vol. 21, no. 4, pp. 484–490, 1973, doi: 10.1109/TAP.1973.1140517.

[11] F. AUZANNEAU, "Furtivité électromagnétique," *Techniques de l'ingénieur Le traitement du signal et ses applications*, vol. base documentaire : TIP383WEB., no. ref. article : te6712. Editions T.I., 2011. doi: 10.51257/a-v1-te6712.

[12] P. Y. Ufimtsev, "Comments on diffraction principles and limitations of RCS reduction techniques," *Proceedings of the IEEE*, vol. 84, no. 12, pp. 1830–1851, 1996, doi: 10.1109/5.546440.

[13] A. Aytaç, H. İpek, K. Aztekin, and B. Çanakçı, "A review of the radar absorber material and structures," *Scientific Journal of the Military University of Land Forces*, vol. 198, pp. 931–946, Dec. 2020, doi: 10.5604/01.3001.0014.6064.

[14] C. G. Montgomery, R. H. Dicke, and E. M. Purcell, *Principles of Microwave Circuits*. in IEE electromagnetic waves series. Peter Peregrinus, 1987. [Online]. Available: https://books.google.fr/books?id=Sex_282iULMC

[15] A. DE LUSTRAC, "Matériaux composites en électromagnétisme Matériaux absorbants radar," *Techniques de l'ingénieur Plastiques et composites*, vol. base documentaire : TIP100WEB., no. ref. article : e1166. Editions T.I., 2018. doi: 10.51257/a-v2-e1166.

[16] L. K. Neher, "Nonreflecting background for testing microwave equipment." Google Patents, Oct. 20, 1953.

[17] Y. Naito and K. Suetake, "Application of Ferrite to Electromagnetic Wave Absorber and its Characteristics," *IEEE Transactions on Microwave Theory and Techniques*, vol. 19, no. 1, pp. 65–72, 1971, doi: 10.1109/TMTT.1971.1127446.

[18] A. N. Lagarkov, S. M. Matytsin, K. N. Rozanov, and A. K. Sarychev, "Dielectric permittivity of fiber-filled composites: comparison of theory and experiment," *Physica A: Statistical Mechanics and its Applications*, vol. 241, no. 1, pp. 58–63, 1997, doi: https://doi.org/10.1016/S0378-4371(97)00059-9.

[19] W. Dallenbach and W. Kleinsteuber, “Reflection and absorption of decimeter-waves by plane dielectric layers,” *Hochfrequenztechnik und Elektroakustik*, vol. 51.

[20] J. L. Wallace, “Broadband magnetic microwave absorbers: fundamental limitations,” *IEEE Transactions on Magnetics*, vol. 29, no. 6, pp. 4209–4214, 1993, doi: 10.1109/20.280862.

[21] W. W. Salisbury, “Absorbent body for electromagnetic waves.” Google Patents, Jun. 10, 1952.

[22] D. M. Pozar, *Microwave engineering*. John wiley & sons, 2011.

[23] L. J. Du Toit, “The design of Jauman absorbers,” *IEEE Antennas and Propagation Magazine*, vol. 36, no. 6, pp. 17–25, 1994, doi: 10.1109/74.370526.

[24] L. J. Du Toit and J. H. Cloete, “Electric screen Jauman absorber design algorithms,” *IEEE transactions on microwave theory and techniques*, vol. 44, no. 12, pp. 2238–2245, 1996.

[25] J. J. Pesque, D. P. Bouche, and R. Mittra, “Optimization of multilayer antireflection coatings using an optimal control method,” *IEEE Transactions on Microwave Theory and Techniques*, vol. 40, no. 9, pp. 1789–1796, 1992, doi: 10.1109/22.156606.

[26] N. Engheta, “Thin absorbing screens using metamaterial surfaces,” in *IEEE Antennas and Propagation Society International Symposium*, 2002, pp. 392–395 vol.2. doi: 10.1109/APS.2002.1016106.

[27] R. L. Fante and M. T. McCormack, “Reflection properties of the Salisbury screen,” *IEEE Transactions on Antennas and Propagation*, vol. 36, no. 10, pp. 1443–1454, 1988, doi: 10.1109/8.8632.

[28] E. F. Knott and C. D. Lunden, “The two-sheet capacitive Jaumann absorber,” *IEEE Transactions on Antennas and Propagation*, vol. 43, no. 11, pp. 1339–1343, 1995, doi: 10.1109/8.475112.

[29] Y. Shang, Z. Shen, and S. Xiao, “On the Design of Single-Layer Circuit Analog Absorber Using Double-Square-Loop Array,” *IEEE Transactions on Antennas and Propagation*, vol. 61, no. 12, pp. 6022–6029, 2013, doi: 10.1109/TAP.2013.2280836.

[30] M. Li, S. Xiao, Y.-Y. Bai, and B.-Z. Wang, “An ultrathin and broadband radar absorber using resistive FSS,” *IEEE Antennas and Wireless Propagation Letters*, vol. 11, pp. 748–751, 2012.

[31] F. Terracher and G. Berginc, “Thin electromagnetic absorber using frequency selective surfaces,” in *IEEE Antennas and Propagation Society International Symposium. Transmitting Waves of Progress to the Next Millennium. 2000 Digest. Held in conjunction with: USNC/URSI National Radio Science Meeting (C*, IEEE, 2000, pp. 846–849.

[32] R. M. Fano, “Theoretical limitations on the broadband matching of arbitrary impedances,” *Journal of the Franklin Institute*, vol. 249, no. 1, pp. 57–83, 1950, doi: https://doi.org/10.1016/0016-0032(50)90006-8.

[33] K. N. Rozanov, “Ultimate thickness to bandwidth ratio of radar absorbers,” *IEEE Transactions on Antennas and Propagation*, vol. 48, no. 8, pp. 1230–1234, 2000, doi: 10.1109/8.884491.

[34] H. W. Bode, *Network Analysis and Feedback Amplifier Design*. in Bell Telephone Laboratories series. D. Van Nostrand Company, Incorporated, 1945. [Online]. Available: https://books.google.fr/books?id=kSYhAAAAMAAJ

[35] K. Rozanov and S. Starostenko, “Numerical study of bandwidth of radar absorbers,” *The European Physical Journal Applied Physics*, vol. 8, no. 2, pp. 147–151, 1999.

[36] F. Boust and T. Lepetit, “Radar Absorbing Metamaterials: Dreams and Reality,” May 2016.

[37] F. Boust, T. Lepetit, and S. N. Burokur, “Metagrating absorber: design and implementation,” *Optics Letters*, vol. 47, no. 20, pp. 5305–5308, 2022.

[38] J. P. Doane, K. Sertel, and J. L. Volakis, “Matching Bandwidth Limits for Arrays Backed by a Conducting Ground Plane,” *IEEE Transactions on Antennas and Propagation*, vol. 61, no. 5, pp. 2511–2518, 2013, doi: 10.1109/TAP.2013.2243099.

[39] C. Firestein, A. Shlivinski, and Y. Hadad, “Bound and Optimal Design of Dallenbach Absorber Under Finite-Bandwidth Multiple-Angle Illumination.” 2023.

[40] C. L. Holloway, E. F. Kuester, J. A. Gordon, J. O'Hara, J. Booth, and D. R. Smith, "An Overview of the Theory and Applications of Metasurfaces: The Two-Dimensional Equivalents of Metamaterials," *IEEE Antennas and Propagation Magazine*, vol. 54, no. 2, pp. 10–35, 2012, doi: 10.1109/MAP.2012.6230714.

[41] S. B. Glybovski, S. A. Tretyakov, P. A. Belov, Y. S. Kivshar, and C. R. Simovski, "Metasurfaces: From microwaves to visible," *Physics Reports*, vol. 634, pp. 1–72, 2016, doi: https://doi.org/10.1016/j.physrep.2016.04.004.

[42] A. Li, S. Singh, and D. Sievenpiper, "Metasurfaces and their applications," *Nanophotonics*, vol. 7, no. 6, pp. 989–1011, 2018, doi: doi:10.1515/nanoph-2017-0120.

[43] A. K. Zadeh and A. Karlsson, "Capacitive circuit method for fast and efficient design of wideband radar absorbers," *IEEE Transactions on Antennas and Propagation*, vol. 57, no. 8, pp. 2307–2314, 2009.

[44] A. Kazemzadeh, "Nonmagnetic ultrawideband absorber with optimal thickness," *IEEE Transactions on Antennas and propagation*, vol. 59, no. 1, pp. 135–140, 2010.

[45] H. Mosallaei and K. Sarabandi, "A one-layer ultra-thin meta-surface absorber," in *2005 IEEE Antennas and Propagation Society International Symposium*, 2005, pp. 615–618 vol. 1B. doi: 10.1109/APS.2005.1551634.

[46] J. McVay, A. Hoorfar, and N. Engheta, "Thin absorbers using space-filling-curve high-impedance surfaces," in *2005 IEEE Antennas and Propagation Society International Symposium*, IEEE, 2005, pp. 22–25.

[47] D. J. Kern and D. H. Werner, "A genetic algorithm approach to the design of ultra-thin electromagnetic bandgap absorbers," *Microwave and Optical Technology Letters*, vol. 38, no. 1, pp. 61–64, 2003, doi: https://doi.org/10.1002/mop.10971.

[48] F. Ding, Y. Cui, X. Ge, Y. Jin, and S. He, "Ultra-broadband microwave metamaterial absorber," *Applied Physics Letters*, vol. 100, no. 10, p. 103506, Mar. 2012, doi: 10.1063/1.3692178.

[49] A. Kazemzadeh, "Thin wideband absorber with optimal thickness," in *2010 URSI International Symposium on Electromagnetic Theory*, 2010, pp. 676–679. doi: 10.1109/URSI-EMTS.2010.5637290.

[50] Y. Ra'di, C. R. Simovski, and S. A. Tretyakov, "Thin Perfect Absorbers for Electromagnetic Waves: Theory, Design, and Realizations," *Phys. Rev. Applied*, vol. 3, no. 3, p. 037001, Mar. 2015, doi: 10.1103/PhysRevApplied.3.037001.

[51] M. A. Salem and C. Caloz, "Manipulating light at distance by a metasurface using momentum transformation," *Opt. Express*, vol. 22, no. 12, pp. 14530–14543, Jun. 2014, doi: 10.1364/OE.22.014530.

[52] C. Pfeiffer and A. Grbic, "Analysis and synthesis of bianisotropic metasurfaces," in *2014 IEEE Antennas and Propagation Society International Symposium (APSURSI)*, 2014, pp. 19–20. doi: 10.1109/APS.2014.6904341.

[53] K. Achouri, M. A. Salem, and C. Caloz, "General metasurface synthesis based on susceptibility tensors," *IEEE Transactions on Antennas and Propagation*, vol. 63, no. 7, pp. 2977–2991, 2015, doi: 10.1109/TAP.2015.2423700.

[54] Y. Fu *et al.*, "Unleashing the potential: AI empowered advanced metasurface research," *Nanophotonics*, vol. 13, no. 8, pp. 1239–1278, 2024, doi: doi:10.1515/nanoph-2023-0759.

[55] N. I. Landy, S. Sajuyigbe, J. J. Mock, D. R. Smith, and W. J. Padilla, "Perfect Metamaterial Absorber," *Phys. Rev. Lett.*, vol. 100, no. 20, p. 207402, May 2008, doi: 10.1103/PhysRevLett.100.207402.

[56] Y. Cheng, H. Yang, Z. Cheng, and B. Xiao, "A planar polarization-insensitive metamaterial absorber," *Photonics and Nanostructures-Fundamentals and Applications*, vol. 9, no. 1, pp. 8–14, 2011.

[57] B. Zhu, Z. Wang, C. Huang, Y. Feng, J. Zhao, and T. Jiang, "Polarization insensitive metamaterial absorber with wide incident angle," *Progress In Electromagnetics Research*, vol. 101, pp. 231–239, 2010.

[58] O. Luukkonen, F. Costa, C. R. Simovski, A. Monorchio, and S. A. Tretyakov, "A thin electromagnetic absorber for wide incidence angles and both polarizations," *IEEE transactions on antennas and propagation*, vol. 57, no. 10, pp. 3119–3125, 2009.

[59] S. A. Tretyakov and S. I. Maslovski, "Thin absorbing structure for all incidence angles based on the use of a high-impedance surface," *Microwave and Optical Technology Letters*, vol. 38, no. 3, pp. 175–178, 2003, doi: https://doi.org/10.1002/mop.11006.

[60] B. Zhang, C. Jin, and Z. Shen, "Low-Profile Broadband Absorber Based on Multimode Resistor-Embedded Metallic Strips," *IEEE Transactions on Microwave Theory and Techniques*, vol. 68, no. 3, pp. 835–843, 2020, doi: 10.1109/TMTT.2019.2956933.

[61] Z. Tan, J. Yi, Q. Cheng, and S. N. Burokur, "Design of perfect absorber based on metagratings: theory and experiment," *IEEE Transactions on Antennas and Propagation*, vol. 71, no. 2, pp. 1832–1842, 2023.

[62] N. Marcuvitz, *Waveguide Handbook*. in IEE electromagnetic waves series. McGraw-Hill, 1951. [Online]. Available: https://books.google.fr/books?id=Ao34iFuNZgIC

[63] R. J. Langley and E. A. Parker, "Equivalent circuit model for arrays of square loops," *Electronics Letters*, vol. 18, pp. 294–296, 1982.

[64] R. J. Langley and E. A. Parker, "Double-square frequency-selective surfaces and their equivalent circuit," *Electronics Letters*, vol. 17, no. 19, pp. 675–677, 1983.

[65] F. Mesa, R. Rodriguez-Berral, and F. Medina, "Unlocking Complexity Using the ECA: The Equivalent Circuit Model as An Efficient and Physically Insightful Tool for Microwave Engineering," *IEEE Microwave Magazine*, vol. 19, no. 4, pp. 44–65, 2018, doi: 10.1109/MMM.2018.2813821.

[66] T. Lopez, T. Lepetit, and S. N. Burokur, "Equivalent circuit analysis of a mode-converting metacell in a coaxial transmission line at microwave frequencies," *Journal of Applied Physics*, vol. 132, no. 5, p. 054901, 2022, doi: 10.1063/5.0096832.

[67] Y. Han, W. Che, C. Christopoulos, Y. Xiong, and Y. Chang, "A Fast and Efficient Design Method for Circuit Analog Absorbers Consisting of Resistive Square-Loop Arrays," *IEEE Transactions on Electromagnetic Compatibility*, vol. 58, no. 3, pp. 747–757, 2016, doi: 10.1109/TEMC.2016.2524553.

[68] R. Dubrovka and R. Donnan, "Equivalent circuit of FSS loaded with lumped elements using modal decomposition equivalent circuit method," in *Proceedings of the 5th European Conference on Antennas and Propagation (EUCAP)*, 2011, pp. 2250–2253.

[69] R. M. Foster, "A reactance theorem," *The Bell System Technical Journal*, vol. 3, no. 2, pp. 259–267, 1924, doi: 10.1002/j.1538-7305.1924.tb01358.x.

[70] J. G. Linvill, "Transistor Negative-Impedance Converters," *Proceedings of the IRE*, vol. 41, no. 6, pp. 725–729, 1953, doi: 10.1109/JRPROC.1953.274251.

[71] B. P. Bogert, "Some Gyrator and Impedance Inverter Circuits," *Proceedings of the IRE*, vol. 43, no. 7, pp. 793–796, 1955, doi: 10.1109/JRPROC.1955.278142.

[72] D. Sievenpiper, S. Kim, J. Long, and J. Lee, "Advances in nonlinear, active, and anisotropic artificial impedance surfaces," in *2016 46th European Microwave Conference (EuMC)*, 2016, pp. 799–802. doi: 10.1109/EuMC.2016.7824464.

[73] S. E. Sussman-Fort and R. M. Rudish, "Non-Foster Impedance Matching of Electrically-Small Antennas," *IEEE Transactions on Antennas and Propagation*, vol. 57, no. 8, pp. 2230–2241, 2009, doi: 10.1109/TAP.2009.2024494.

[74] J. Mou and Z. Shen, "Design and Experimental Demonstration of Non-Foster Active Absorber," *IEEE Transactions on Antennas and Propagation*, vol. 65, no. 2, pp. 696–704, 2017, doi: 10.1109/TAP.2016.2639012.

[75] P.-Y. Chen, C. Argyropoulos, and A. Alù, "Broadening the Cloaking Bandwidth with Non-Foster Metasurfaces," *Phys. Rev. Lett.*, vol. 111, no. 23, p. 233001, Dec. 2013, doi: 10.1103/PhysRevLett.111.233001.

[76] Y. Li, J. Lin, H. Guo, W. Sun, S. Xiao, and L. Zhou, "A Tunable Metasurface with Switchable Functionalities: From Perfect Transparency to Perfect Absorption," *Advanced Optical Materials*, vol. 8, no. 6, p. 1901548, 2020, doi: https://doi.org/10.1002/adom.201901548.

[77] B. Zhu, Y. Feng, J. Zhao, C. Huang, and T. Jiang, "Switchable Metamaterial Reflector/Absorber for Different Polarized Electromagnetic Waves," *Applied Physics Letters*, vol. 97, Oct. 2010, doi: 10.1063/1.3477960.

[78] M. Yoo and S. Lim, "Electronically switchable metasurface for absorption and reflection modes," in *2014 IEEE Antennas and Propagation Society International Symposium (APSURSI)*, IEEE, 2014, pp. 2102–2103. doi: 10.1109/APS.2014.6905378.

[79] A. de Lustrac, B. Ratni, G.-P. Piau, Y. Duval, and S. N. Burokur, "Tri-state Metasurface-Based Electromagnetic Screen with Switchable Reflection, Transmission, and Absorption Functionalities," *ACS Applied Electronic Materials*, vol. 3, no. 3, pp. 1184–1190, 2021, doi: 10.1021/acsaelm.0c01038.

[80] A. Tennant and B. Chambers, "Adaptive radar absorbing structure with PIN diode controlled active frequency selective surface," *Smart Materials and Structures*, vol. 13, p. 122, Dec. 2003, doi: 10.1088/0964-1726/13/1/013.

[81] J. Zhao, Q. Cheng, J. Chen, M. Q. Qi, W. X. Jiang, and T. J. Cui, "A tunable metamaterial absorber using varactor diodes," *New Journal of Physics*, vol. 15, no. 4, p. 043049, Apr. 2013, doi: 10.1088/1367-2630/15/4/043049.

[82] S. Liu, H.-X. Xu, H. C. Zhang, and T. J. Cui, "Tunable ultrathin mantle cloak via varactor-diode-loaded metasurface," *Opt. Express*, vol. 22, no. 11, pp. 13403–13417, Jun. 2014, doi: 10.1364/OE.22.013403.

[83] Z. Luo, L. Zhao, C. Xue, and D. Sievenpiper, "An electrically tunable absorbing metasurface for surface waves and plane waves," in *2016 Asia-Pacific Microwave Conference (APMC)*, Dec. 2016, pp. 1–4. doi: 10.1109/APMC.2016.7931456.

[84] F. Liu *et al.*, "Intelligent Metasurfaces with Continuously Tunable Local Surface Impedance for Multiple Reconfigurable Functions," *Phys. Rev. Applied*, vol. 11, no. 4, p. 044024, Apr. 2019, doi: 10.1103/PhysRevApplied.11.044024.

[85] B. Chambers and A. Tennant, "A smart radar absorber based on the phase-switched screen," *IEEE Transactions on Antennas and Propagation*, vol. 53, no. 1, pp. 394–403, 2005, doi: 10.1109/TAP.2004.838795.

[86] F. R. Morgenthaler, "Velocity Modulation of Electromagnetic Waves," *IRE Transactions on Microwave Theory and Techniques*, vol. 6, no. 2, pp. 167–172, 1958, doi: 10.1109/TMTT.1958.1124533.

[87] R. L. Fante, "Transmission of Electromagnetic Waves into Time-Varying Media," *IEEE Transactions on Antennas and Propagation*, vol. 19, no. 3, pp. 417–424, 1971, doi: 10.1109/TAP.1971.1139931.

[88] A. A. Oliner and A. Hessel, "Wave Propagation in a Medium with a Progressive Sinusoidal Disturbance," *IRE Transactions on Microwave Theory and Techniques*, vol. 9, no. 4, pp. 337–343, 1961, doi: 10.1109/TMTT.1961.1125340.

[89] G. Ptitcyn, M. S. Mirmoosa, A. Sotoodehfar, and S. A. Tretyakov, "A Tutorial on the Basics of Time-Varying Electromagnetic Systems and Circuits: Historic overview and basic concepts of time-modulation.," *IEEE Antennas and Propagation Magazine*, pp. 2–11, 2023, doi: 10.1109/MAP.2023.3261601.

[90] C. Caloz and Z.-L. Deck-Léger, "Spacetime Metamaterials—Part I: General Concepts," *IEEE Transactions on Antennas and Propagation*, vol. 68, no. 3, pp. 1569–1582, 2020, doi: 10.1109/TAP.2019.2944225.

[91] C. Caloz and Z.-L. Deck-Léger, "Spacetime Metamaterials—Part II: Theory and Applications," *IEEE Transactions on Antennas and Propagation*, vol. 68, no. 3, pp. 1583–1598, 2020, doi: 10.1109/TAP.2019.2944216.

[92] X. Wang, A. Díaz-Rubio, H. Li, S. A. Tretyakov, and A. Alù, "Theory and Design of Multifunctional Space-Time Metasurfaces," *Phys. Rev. Applied*, vol. 13, no. 4, p. 044040, Apr. 2020, doi: 10.1103/PhysRevApplied.13.044040.

[93] C. Firestein, A. Shlivinski, and Y. Hadad, "Absorption and Scattering by a Temporally Switched Lossy Layer: Going beyond the Rozanov Bound," *Phys. Rev. Applied*, vol. 17, no. 1, p. 014017, Jan. 2022, doi: 10.1103/PhysRevApplied.17.014017.

[94] A. Shlivinski and Y. Hadad, "Beyond the Bode-Fano Bound: Wideband Impedance Matching for Short Pulses Using Temporal Switching of Transmission-Line Parameters," *Phys. Rev. Lett.*, vol. 121, no. 20, p. 204301, Nov. 2018, doi: 10.1103/PhysRevLett.121.204301.

[95] H. Li and A. Alù, "Temporal switching to extend the bandwidth of thin absorbers," *Optica*, vol. 8, no. 1, pp. 24–29, Jan. 2021, doi: 10.1364/OPTICA.408399.

[96] V. Pacheco-Peña and N. Engheta, "Antireflection temporal coatings," *Optica*, vol. 7, no. 4, pp. 323–331, Apr. 2020, doi: 10.1364/OPTICA.381175.

[97] K. Ford and B. Chambers, "Smart microwave absorber," *Electronics Letters*, vol. 36, pp. 50–52, Feb. 2000, doi: 10.1049/el:20000115.

[98] A. Mourad, L. Burgnies, and É. Lheurette, "Broadband RCS reduction by means of disordered coding metasurfaces," *Journal of Applied Physics*, vol. 134, no. 12, p. 123105, Sep. 2023, doi: 10.1063/5.0168686.

[99] L. Zhang *et al.*, "Space-time-coding digital metasurfaces," *Nature communications*, vol. 9, no. 1, pp. 1–11, 2018, doi: 10.1038/s41467-018-06802-0.

[100] J. Y. Dai, J. Zhao, Q. Cheng, and T. J. Cui, "Independent control of harmonic amplitudes and phases via a time-domain digital coding metasurface," *Light: Science & Applications*, vol. 7, no. 1, p. 90, Nov. 2018.

[101] J. Zhao *et al.*, "Programmable time-domain digital-coding metasurface for non-linear harmonic manipulation and new wireless communication systems," *National Science Review*, vol. 6, no. 2, pp. 231–238, Nov. 2018, doi: 10.1093/nsr/nwy135.

[102] X. Wang and C. Caloz, "Spread-spectrum selective camouflaging based on time-modulated metasurface," *IEEE Transactions on Antennas and Propagation*, vol. 69, no. 1, pp. 286–295, 2020, doi: 10.1109/TAP.2020.3008621.

[103] M. Liu, A. B. Kozyrev, and I. V. Shadrivov, "Time-varying Metasurfaces for Broadband Spectral Camouflage," *Phys. Rev. Appl.*, vol. 12, no. 5, p. 054052, Nov. 2019, doi: 10.1103/PhysRevApplied.12.054052.

[104] N. Zhang *et al.*, "Spatiotemporal metasurface to control electromagnetic wave scattering," *Physical Review Applied*, vol. 17, no. 5, p. 054001, 2022.

[105] D. Ramaccia, D. L. Sounas, A. Alù, A. Toscano, and F. Bilotti, "Doppler cloak restores invisibility to objects in relativistic motion," *Phys. Rev. B*, vol. 95, no. 7, p. 075113, Feb. 2017, doi: 10.1103/PhysRevB.95.075113.

[106] D. Ramaccia, D. L. Sounas, A. Alù, A. Toscano, and F. Bilotti, "Phase-Induced Frequency Conversion and Doppler Effect With Time-Modulated Metasurfaces," *IEEE Transactions on Antennas and Propagation*, vol. 68, no. 3, pp. 1607–1617, 2020, doi: 10.1109/TAP.2019.2952469.

[107] V. Kozlov, D. Vovchuk, and P. Ginzburg, "Broadband radar invisibility with time-dependent metasurfaces," *Scientific Reports*, vol. 11, no. 1, pp. 1–11, 2021.

[108] B. Liu, Y. He, S.-W. Wong, and Y. Li, "Experimental demonstration of a time-domain digital-coding metasurface for a Doppler cloak," *Opt. Express*, vol. 29, no. 2, pp. 740–750, Jan. 2021, doi: 10.1364/OE.414408.

[109] X. G. Zhang *et al.*, "Smart Doppler cloak operating in broad band and full polarizations," *Advanced Materials*, vol. 33, no. 17, p. 2007966, 2021.

[110] D. J. Gregoire, C. R. White, and J. S. Colburn, "A Coaxial TEM Cell for Direct Measurement of UHF Artificial Magnetic Conductors [AMTA Corner]," *IEEE Antennas and Propagation Magazine*, vol. 54, no. 2, pp. 251–259, 2012, doi: 10.1109/MAP.2012.6230768.

[111] D. J. Gregoire, C. R. White, and J. S. Colburn, "Wideband artificial magnetic conductors loaded with non-Foster negative inductors," *IEEE Antennas and Wireless Propagation Letters*, vol. 10, pp. 1586–1589, 2011.

[112] R. E. Collin, *Field theory of guided waves*, vol. 5. John Wiley & Sons, 1990.

[113] P. McIsaac, "Symmetry-Induced Modal Characteristics of Uniform Waveguides - I: Summary of Results," *IEEE Transactions on Microwave Theory and Techniques*, vol. 23, no. 5, pp. 421–429, 1975, doi: 10.1109/TMTT.1975.1128584.

[114] ANSYS, "An Introductionto HFSS: Fundamental Principles, Concepts, and Use." [Online]. Available: https://athena.ecs.csus.edu/~milica/EEE212/HAND/HFSSintro.pdf

[115] L. F. Chen, C. K. Ong, C. P. Neo, V. V. Varadan, and V. K. Varadan, *Microwave Electronics: Measurement and Materials Characterization*. Wiley, 2004. [Online]. Available: https://books.google.fr/books?id=1vmUdUXlBNIC

[116] R. Cory, "The nuts and bolts of tuning varactors," vol. 8, in High Frequency Electronics, no. 2, vol. 8. , Submit Technical Media, LLC, 2009, pp. 42–51. [Online]. Available: https://www.highfrequencyelectronics.com/Feb09/HFE0209_Cory.pdf

[117] *Varactor SPICE Models for RF VCO Applications*. Skyworks, 2015. [Online]. Available: https://www.skyworksinc.com/-/media/SkyWorks/Documents/Products/1-100/Varactor_SPICE_Model_AN_200315C.pdf

[118] *SMV1247-SMV1255 Series: Hyperabrupt Junction TuningVaractors*. Skyworks, 2020. [Online]. Available: https://www.skyworksinc.com/-/media/SkyWorks/Documents/Products/101-200/SMV1247_SMV1255_Series_200061W.pdf

[119] *SMV123x Series: Hyperabrupt Junction Tuning Varactors*. Skyworks, 2020. [Online]. Available: https://www.skyworksinc.com/-/media/SkyWorks/Documents/Products/101-200/SMV123x_Series_200058AA.pdf

[120] Z. Wu and A. Grbic, "Serrodyne frequency translation using time-modulated metasurfaces," *IEEE Transactions on Antennas and Propagation*, vol. 68, no. 3, pp. 1599–1606, 2019, doi: 10.1109/TAP.2019.2943712.

[121] J. C. Halimeh, R. T. Thompson, and M. Wegener, "Invisibility cloaks in relativistic motion," *Phys. Rev. A*, vol. 93, no. 1, p. 013850, Jan. 2016, doi: 10.1103/PhysRevA.93.013850.

[122] J. S. Jaffe and R. C. Mackey, "Microwave Frequency Translator," *IEEE Transactions on Microwave Theory and Techniques*, vol. 13, no. 3, pp. 371–378, 1965, doi: 10.1109/TMTT.1965.1126002.

[123] R. C. Cumming, "The Serrodyne Frequency Translator," *Proceedings of the IRE*, vol. 45, no. 2, pp. 175–186, 1957, doi: 10.1109/JRPROC.1957.278387.

[124] G. Klein and L. Dubrowsky, "The DIGILATOR, a New Broadband Microwave Frequency Translator," *IEEE Transactions on Microwave Theory and Techniques*, vol. 15, no. 3, pp. 172–179, 1967, doi: 10.1109/TMTT.1967.1126408.

[125] COMSOL, "Resolving Time-Dependent Waves." [Online]. Available: https://www.comsol.com/support/knowledgebase/1118

[126] COMSOL, "BDF, Generalized alpha, and Runge-Kutta Methods." [Online]. Available: https://www.comsol.com/support/knowledgebase/1062

[127] J. woo Hur, H.-J. Maeng, S. J. Kim, J.-E. Han, and D. Kim, "Reconfigurable Intelligent Surface for the Doppler Shift," in *2023 IEEE International Symposium on Antennas and Propagation and USNC-URSI Radio Science Meeting (USNC-URSI)*, IEEE, 2023, pp. 15–16.

[128] S. Taravati and A. A. Kishk, "Space-Time Modulation: Principles and Applications," *IEEE Microwave Magazine*, vol. 21, no. 4, pp. 30–56, 2020, doi: 10.1109/MMM.2019.2963606.

[129] Y. Xiao, D. N. Maywar, and G. P. Agrawal, "Reflection and transmission of electromagnetic waves at a temporal boundary," *Opt. Lett.*, vol. 39, no. 3, pp. 574–577, Feb. 2014, doi: 10.1364/OL.39.000574.

[130] Y. Xiao, G. P. Agrawal, and D. N. Maywar, "Nonlinear pulse propagation: A time–transformation approach," *Opt. Lett.*, vol. 37, no. 7, pp. 1271–1273, Apr. 2012, doi: 10.1364/OL.37.001271.

[131] E. Noether, "Invariante Variationsprobleme," *Nachrichten von der Gesellschaft der Wissenschaften zu Göttingen, Mathematisch-Physikalische Klasse*, vol. 1918, pp. 235–257, 1918.

[132] A. G. Hayrapetyan, J. B. Götte, K. K. Grigoryan, S. Fritzsche, and R. G. Petrosyan, "Electromagnetic wave propagation in spatially homogeneous yet smoothly time-varying dielectric media," *Journal of Quantitative Spectroscopy and Radiative Transfer*, vol. 178, pp. 158–166, 2016, doi: https://doi.org/10.1016/j.jqsrt.2015.12.007.

[133] T. T. Koutserimpas and R. Fleury, "Nonreciprocal Gain in Non-Hermitian Time-Floquet Systems," *Phys. Rev. Lett.*, vol. 120, no. 8, p. 087401, Feb. 2018, doi: 10.1103/PhysRevLett.120.087401.

[134] R. S. Chu and T. Tamir, "Wave propagation and dispersion in space-time periodic media," 1972. [Online]. Available: https://api.semanticscholar.org/CorpusID:122305687

[135] V. Pacheco-Peña and N. Engheta, "Effective medium concept in temporal metamaterials," *Nanophotonics*, vol. 9, no. 2, pp. 379–391, 2020, doi: doi:10.1515/nanoph-2019-0305.

[136] V. Pacheco-Peña and N. Engheta, "Spatiotemporal cascading of dielectric waveguides," *Opt. Mater. Express*, vol. 14, no. 4, pp. 1062–1073, Apr. 2024, doi: 10.1364/OME.516262.

[137] M. Wuttig, H. Bhaskaran, and T. Taubner, "Phase-change materials for non-volatile photonic applications," *Nature Photonics*, vol. 11, pp. 465–476, Aug. 2017, doi: 10.1038/nphoton.2017.126.

[138] K. Shportko, S. Kremers, M. Woda, D. Lencer, J. Robertson, and M. Wuttig, "Resonant bonding in crystalline phase-change materials," *Nature materials*, vol. 7, pp. 653–8, Aug. 2008, doi: 10.1038/nmat2226.

[139] COMSOL, [Online]. Available: https://www.comsol.com/

[140] *RF Module User's Guide*. COMSOL, 2023. [Online]. Available: https://doc.comsol.com/6.2/doc/com.comsol.help.rf/RFModuleUsersGuide.pdf

[141] MathWorks, "Matlab." [Online]. Available: https://ch.mathworks.com/products/matlab.html

[142] *Programmer's Guide*. Agilent Technologies, 2001. [Online]. Available: https://www.keysight.com/fr/en/assets/9018-40048/programming-guides/9018-40048.pdf#E7.Prochain?success=true

[143] *User's Guide*. Agilent Technologies, 2002. [Online]. Available: https://www.keysight.com/fr/en/assets/9018-04436/user-manuals/9018-04436.pdf?success=true

[144] M. A. Leontovich, "Investigations on Radio Wave Propagation. Pt. 2," Ed. B. A. Vvedensky, Ed., 1948, pp. 1–12.

[145] J. H. Beggs, R. J. Luebbers, K. S. Yee, and K. S. Kunz, "Finite-difference time-domain implementation of surface impedance boundary conditions," *IEEE Transactions on Antennas and Propagation*, vol. 40, no. 1, pp. 49–56, 1992, doi: 10.1109/8.123352.

[146] *COMSOL Multiphysics Reference Manual*. COMSOL, 2023. [Online]. Available: https://doc.comsol.com/6.2/doc/com.comsol.help.comsol/COMSOL_ReferenceManual.pdf

[147] R. Courant, K. Friedrichs, and H. Lewy, "On the Partial Difference Equations of Mathematical Physics," *IBM Journal of Research and Development*, vol. 11, no. 2, pp. 215–234, 1967, doi: 10.1147/rd.112.0215.